Fundamental Properties of Single-Photon Sources

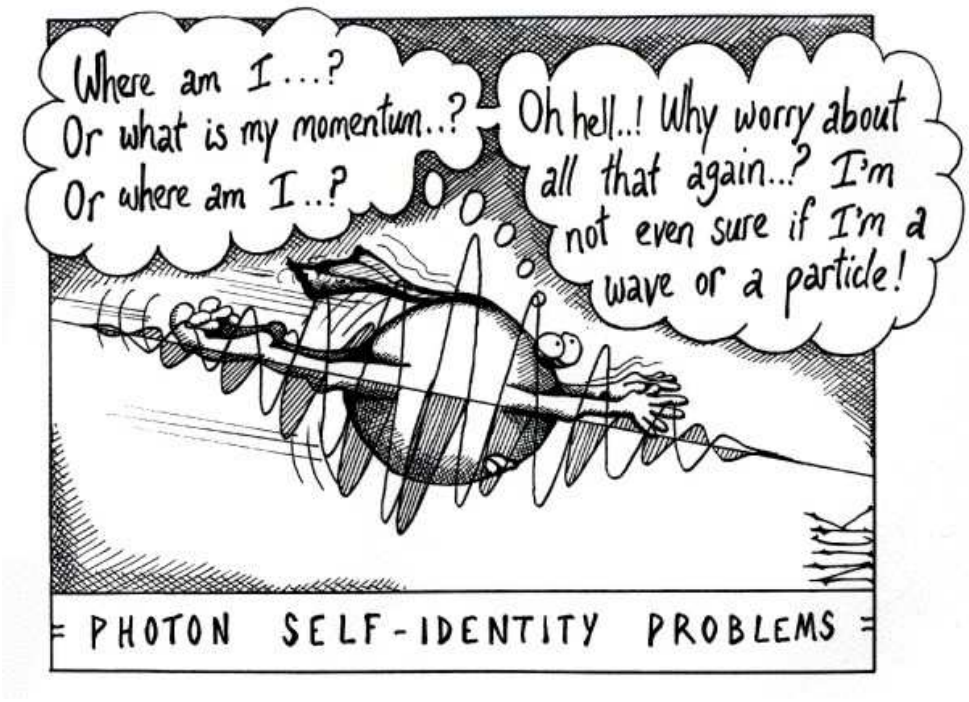

Per Kær Nielsen

August 1, 2008

The cartoon on the front page is taken from the cartoon site: `http://www.nearingzero.net/`

Abstract

In recent years much attention has been focused on the possibility of realizing a single-photon source, due to its possible applications within quantum computing. The efforts have been both experimental and theoretical, and progress has been made on both fronts. However much work still remains to be done, in order to obtain a full understanding of the physics underlying a semiconductor single-photon source, which is a necessity for designing an efficient functional device.

In this thesis we present a theory for describing many-body effects in a semiconductor cavity quantum electrodynamical system, suitable for modeling a semiconductor single-photon source. We employ a non-equilibrium Green's function formalism that is capable of describing the complicated many-body system, which the relevant physical system consists of. Using the Green's function approach we formulated a set of quantum kinetic equations, where we took into account the Coulomb interaction, the interaction between electrons and longitudinal optical (LO) phonons, and the interaction between electrons and photons. Furthermore a model of the electronic states in the semiconductor quantum dots was developed, in terms of which the various interaction matrix elements were calculated.

The quantum kinetic equations were applied to a range of equilibrium and non-equilibrium situations. In equilibrium the interaction with the LO-phonons, was found to dramatically change the properties of the electrons. We investigated the linear absorption spectrum, revealing interesting spectral signatures arising from the LO-phonon coupling, as well as for the Coulomb and photon interaction. The population dynamics for the both electrons and photons was studied in the time domain, where amongst other things the approach to a quasi-equilibrium state and the occurrence of Rabi oscillations was treated.

An attempt to solve for the full two-time Green's functions of the photons was made, however, due to lack of time this part of was not fully completed and more work is needed.

Preface

This thesis is submitted in candidacy for the Master of Science degree from the Technical University of Denmark (DTU). The work was carried out in the period from August 2007 to July 2008 and had an extend of 40 ECTS points. The project supervised by Peter Lodahl, Jesper Mørk, and Torben Roland Nielsen, all at DTU Fotonik, Department of Photonics Engineering, DTU, Denmark.

Acknowledgements

First of all I would like to thank my supervisors. I am grateful to have had as many as three supervisors, enabling me to pursue a project requiring expertise from several different fields. Without these people to discuss the many subtle problems that arose during the project, I would not have come very far. I am looking forward to collaborating more with all of them in the future.

Beside my supervisors several others have contributed to the project in one way or the other. A special tanks goes to Henri Thyrrestrup Nielsen with whom I have had many interesting discussions on all sorts of matters, and who has helped me tremendously in understanding the inner workings of computers in general and MATLAB in particular. I would also like to acknowledge Troels Suhr Jørgensen and Andreas Næsby Rasmussen for many fruit(ful/less) discussions on subjects not concerning my project. From the theory group of DTU Nanotech, I would to thank Antti-Pekka Jauho and Jakob Houmark for several enlightening discussions on technical matters.

I would like to thank Oticon Fonden for financial support, allowing me to focus on my project and not worry about money issues, especially in last few month where I ran out of SU. And for providing me with the opportunity to attend the CLEO/QELS 2008 conference in San Jose, California.

Last, but not least, I would like to thank my girlfriend Solveig for her support throughout my project and for reminding me that there are other things in life than theoretical physics.

Contents

1. Introduction **1**

2. Non-equilibrium Green's Functions **6**
2.1. Introduction and motivation . . . 6
2.2. Basics of contour ordered Green's functions . . . 8
2.2.1. Ensemble averages in non-equilibrium . . . 8
2.2.2. The contour ordered Green's function and Dyson's equation . . . 11
2.3. Real time Green's functions and Langreth rules . . . 14
2.4. Equations of motion . . . 18
2.5. Generalized Kadanoff-Baym Ansatz . . . 21
2.6. Summary . . . 23

3. Fundamental Hamiltonians **24**
3.1. Introduction . . . 24
3.2. Hamiltonians . . . 24
3.2.1. Non-interacting parts . . . 26
3.2.2. Interacting parts . . . 28
3.2.3. Generic semiconductor Hamiltonian . . . 31
3.3. Summary . . . 32

4. Single-Particle States and Matrix Elements **33**
4.1. Introduction . . . 33
4.2. Electronic single-particle states and energies . . . 33
4.2.1. Self-assembled quantum dots . . . 33
4.2.2. Effective mass Schrödinger equation . . . 34
4.2.3. Numerical examples . . . 36
4.3. Coulomb matrix elements . . . 41
4.3.1. Bloch part . . . 42
4.3.2. Representation in separable basis . . . 43
4.3.3. Representation in separable eigenstates . . . 50
4.3.4. Comparison of exact and effective Coulomb matrix elements . . . 51
4.4. Optical dipole matrix elements . . . 54
4.5. Summary . . . 55

5. Equations of Motion **57**
5.1. Introduction . . . 57
5.2. Approximations . . . 57
5.2.1. Hamiltonians . . . 57
5.2.2. Truncation of self-energies . . . 62
5.3. Equilibrium . . . 65
5.3.1. Equilibrium spectral Green's functions . . . 65
5.3.2. The polaron . . . 66
5.3.3. The polariton . . . 73
5.4. Non-equilibrium . . . 74
5.4.1. Electronic equations of motion and scattering terms . . . 74
5.4.2. Photonic equations of motion and scattering terms . . . 81
5.5. Summary . . . 85

6. Results and Discussion **87**
6.1. Introduction . . . 87
6.2. Unphysical populations . . . 87
6.3. Absorption spectra . . . 90
6.3.1. LO-phonons and Coulomb . . . 93
6.3.2. LO-phonons and photons . . . 97
6.4. Time domain . . . 102
6.4.1. LO-phonons . . . 102
6.4.2. LO-phonons and photons . . . 106
6.5. Emission spectra . . . 114
6.5.1. Present stage results . . . 115
6.6. Indistinguishability . . . 117
6.6.1. Present stage results . . . 119
6.7. Summary . . . 120

7. Summary and Outlook **122**
7.1. Outlook . . . 123

A. Appendix **125**
A.1. Second order correlation function for a Hong-Ou-Mandel type experiment . . . 125
A.2. Higher Order Correlation Functions . . . 127
A.3. From $\boldsymbol{A} \cdot \boldsymbol{p}$ to $\boldsymbol{d} \cdot \boldsymbol{E}_{\mathrm{T}}$ interaction . . . 131
A.4. Numerics . . . 133
A.5. Self-energies . . . 134
A.6. Free real-time Green's functions . . . 141
A.7. Analytical basis set for the electronic single-particle states . . . 143
A.8. Semiconductor band parameters . . . 145
A.9. Slowly-varying equations . . . 148
A.9.1. Coherent terms . . . 148
A.9.2. Electronic scattering terms . . . 149
A.9.3. Photonic scattering terms . . . 149

Bibliography **151**

1. Introduction

The emerging field of quantum information technology shows great promise as a possible replacement of the current classical information technology, as it offers opportunities to perform tasks not possible within its classical counterpart. A very central object in this new field is the quantum computer that derives its special properties due to utilization of the qubit. A qubit is a generalization of the classical bit that due to its quantum nature can be in a superposition of the classical "0" and "1", giving it unique properties as a computation device. A promising candidate for a qubit are the two polarization states of a photon. Indeed, ever since it was realized that efficient quantum computing can be performed using single photons and standard linear optical elements [1], there has been an immense international research activity [2, 3] aiming at developing single-photon sources. An ideal single-photon source is a device that can deterministically emit indistinguishable single photons efficiently into a single well defined optical mode. The single photons need to be indistinguishable, as otherwise they will not behave quantum mechanically and therefore not be able to interfere as required by the scheme proposed in Ref. [1]. It is of similar importance that one is able to generate a single photon whenever needed, popularly we speak of single-photons on-demand, as otherwise it will not be possible to effectively interfere the single photons on a beam splitter. Furthermore the collection efficiency, given as the amount of light emitted into the desired mode normalized by the total amount of light emitted, should be as high as possible. To summarize and emphasize these essential facts a good single-photon source should possess

- A high degree of indistinguishability
- The ability to deterministically emit single photons
- A high collection efficiency

The degree of indistinguishability is determined by the amount of decoherence the photonic degrees of freedom experience through various interaction mechanisms, and as these are always present in a physical system, one must be prepared to accept some degree of distinguishability. A detailed understanding of these decoherence processes is needed in order to understand the physics underlying a single-photon source, but also from a more practical point of view to be able to design better single-photon sources.

In this thesis we will focus mainly on describing decoherence processes, and therefore emphasis will be on the indistinguishability aspect of single-photon sources.

Semiconductor single-photon sources

In order for quantum computers, or more generally quantum information technologies, to move outside the laboratory the materials comprising these devices need to practical. Systems such as ultra-cold gases or single atoms are not well suited for eventual commercialization and suffer from poor scalability, even though they are excellent for certain fundamental studies. A material that does not suffer from the same impracticalities is semiconductors, and which for many purposes are highly scalable as witnessed in the microelectronics industry. A huge advantage of employing semiconductors is the very high degree of design control the field has developed over the years, enabling construction of devices structured down to the nanometer scale. It is at these small length scales that quantum effects begin to play a vital role. This control also makes it possible, to a certain degree, to engineer the electronic energy levels in the material and through this controlling the energy of the emitted light. Furthermore, the quality of semiconductor devices grown nowadays is extremely high and various unwanted defects do not pose a serious problem.

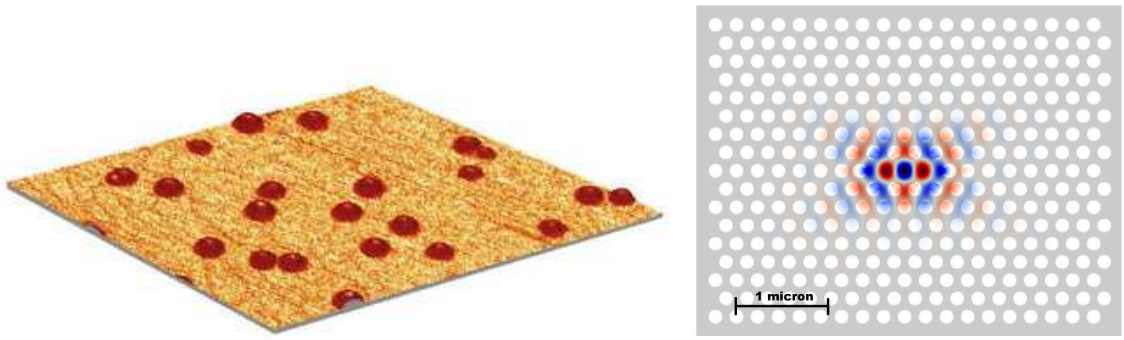

(a) Self-assembled quantum dots grown using the Stranski-Krastanow technique [4]. The diameter of each quantum dot is on the order of a few tens of nanometers.

(b) Simulated electric field mode profile of a cavity created by omitting three holes in a 2D photonic crystal membrane [5].

Figure 1.1.: *Figures of self-assembled QDs and an optical cavity.*

A promising candidate for a semiconductor single-photon source consists of a single[1] self-assembled quantum dot (QD), see figure 1.1(a), placed inside an optical cavity, see figure 1.1(b), which offers control over both the electronic and photonic degrees of freedom. It is this specific system we will deal with in this thesis and a brief overview will therefore be given.

QDs grown using the Stranski-Krastanow technique [6] are made in a three step evaporation process, where due to the physical mechanism behind the formation these QDs are called self-assembled. The first step consists of placing a layer of semiconductor on a substrate, as an example we use GaAs which is a commonly employed material. In the second step a very thin layer, usually only a few monolayers thick, of another kind of semiconductor is evaporated onto the the first. The material forming the second layers should have a slightly different lattice constant than the first, this demand is satisfied by InAs which we will use and which is further commonly employed in connection with GaAs. The lattice mismatch causes a stress field to build in the InAs layer with a subsequent increase in surface energy. To minimize the surface energy small islands of InAs spontaneously form on top of the thin layer of InAs, these islands are denoted self-assembled QDs and the thin layer below them is denoted the wetting layer (WL). This step of the process is illustrated in figure 1.1(a), where a scanning electron microscope image shows how the QDs are randomly distributed on the WL. The last step consists of evaporating a final layer of GaAs on top of the QDs and WL, completely embedding the InAs in GaAs. Now, the bandgap of InAs is significantly lower than that of GaAs, and through band bending effects this creates a confining potential for both electrons and holes, allowing spatially localized states to inside the QDs, see figure 4.3 for a schematic illustration. Regarding the optical cavity we will not go into details with the specific form, as we only require it to have a single well defined optical mode. This mode will be described entirely by parameters, that will be introduced later when needed. For an excellent exposition of different cavity designs we refer to the review article by Vahala et al. [7].

An often performed experiment in solid-state quantum optics is the photoluminescence experiment, where one excites electrons in a given structure and measures the light emitted by the structure. The emitted light carries with it a wealth of information on the various interactions that are present in the structure. It is therefore of great interest to be able to model a photoluminescence experiment accurately, to be able to understand the experimental data. For illustration we have in figure 1.2 sketched a typical photoluminescence experiment. The figure shows an energy diagram of a two-band semiconductor which has a bulk continuum part, arising from the unconfined carriers in the semiconductor bulk, a WL (quasi-) continuum, due to carriers moving in the quasi-2D WL, and a set of discrete states localized in the QD. In the experiment electrons are generated in the conduction band by some external source, that could either be optical or electrical in nature. In the optical case the excitation energy is often tuned to the continuum parts of

[1] In practise it is very difficult to place a single QD inside a cavity, due to the fabrication process. Often several QDs are placed spatially inside the cavity, however, due to size fluctuations and the associated energy fluctuation it is possible to spectrally select a single QD.

the spectrum to, avoid exciting with light of the same energy as one wish to detect. The electrons and holes then undergo a rapid relaxation and dephasing process in the WL or bulk continuum, where the phase space for scattering is large, through the emission of phonons and scattering with other carriers. Once the carriers reach the bottom of the WL continuum, they are captured into the localized QD states. From here on they relax into the ground state of the discrete QD spectrum, and as this part of the relaxation takes place for discrete electron states, the time scales are typically longer than in the continuum case. Often the relaxation to the QD ground state for the electrons and holes, occurs sufficiently fast so that only a very small number of photons are emitted during the process. However, once the the carriers reach their respective ground states, they start interacting efficiently with the quantized electromagnetic field and significant photon emission starts to occur. Depending on the strength of the electron-photon interaction two qualitatively different situation can arise, known as the weak and strong coupling regimes [8, Chap. 7]. In the strong coupling regime the coherent coupling between electrons and photons is stronger than the decay processes, and coherent transfer of energy between the electronic and photonic subsystems is observed through so-called Rabi oscillations. In the weak coupling regime the situation is reversed and the decay processes dominate over the coherent coupling, resulting in an irreversible decay of the excited electron into its ground state while emitting a photon. It is this basic experiment we will set up a theory for in this thesis, as it constitutes the fundamental mechanism in a semiconductor single-photon source.

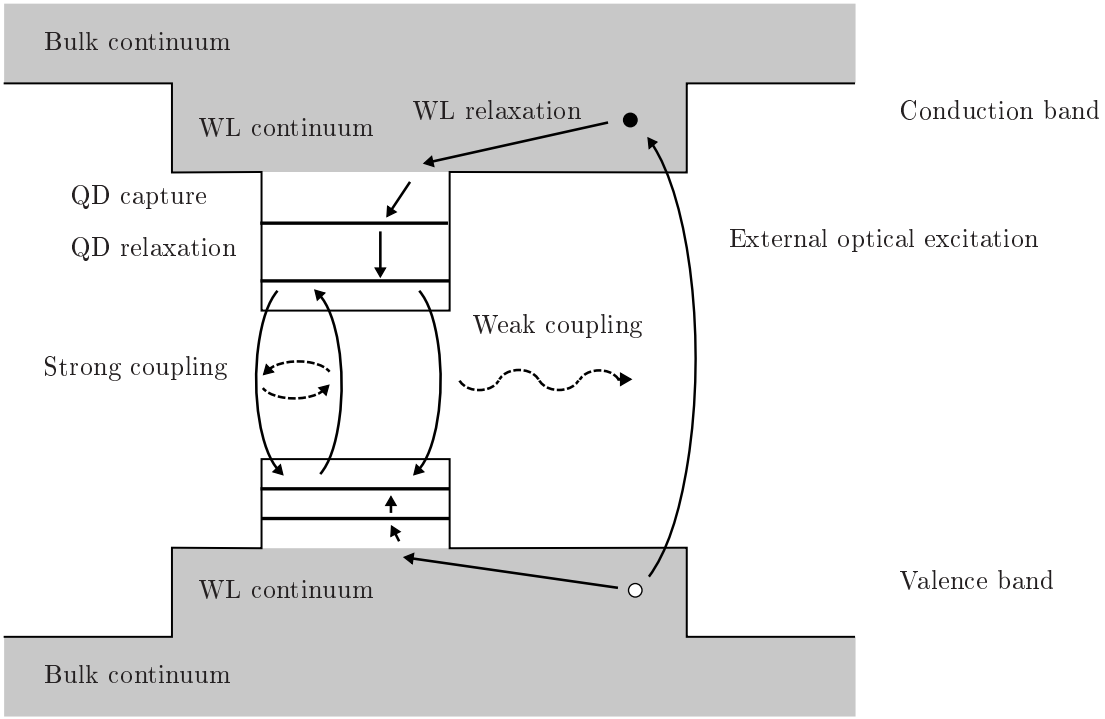

Figure 1.2.: *Schematic energy diagram illustrating the processes involved in a typical photoluminescence experiment, explanations are given in the main text.*

In the context of single-photon sources the weak coupling regime is particular interest due a phenomena known as the Purcell effect [9], where the spontaneous emission rate is altered due to a change in the local density of optical states (LDOS). If the spontaneous emission rate is increased to a value near or above the decoherence rates, it will lead to an increase in the indistinguishability of the emitted photon [10]. Intuitively we can understand this as the photon being emitted before the impact of dephasing has rendered the photons distinguishable. Most exploitations of the Purcell effect have employed an optical cavity to alter the LDOS, however, recently it has been proposed to use a photonic crystal waveguide to alter the LDOS instead of a cavity [11, 12]. This offers several advantages over a spectrally narrow high-Q

cavity. First the Purcell effect in a waveguide can be obtain over a larger range of frequencies and secondly the photon is emitted directly into a strongly directional mode that increases the collection efficiency [13]. We will however only treat cavities and not waveguides in this thesis.

Experimental and theoretical efforts

Much attention is directed towards obtaining a better understanding of the semiconductor cavity quantum electrodynamical (cQED) system described above, both on the experimental and theoretical side. Indeed both measurements of the weak and strong coupling regimes have been realized and we will discuss two such examples. In figure 1.3(a) we show the experimental setup and the result of a coincidence measurement [14], between the two photon counters depicted in the setup, after two single photons have been interfered on the beam splitter. The dip in the count rate at $\tau = 0$ is a signature of two-photon interference and occurs due to the bosonic nature of photons. One can use the area under the suppressed center peak to define a measure for the degree of indistinguishability of the emitted single photons, indeed for perfectly indistinguishable photons the area would vanish [15]. This experiment was performed in the weak coupling regime utilizing the Purcell effect to obtain a higher degree of two-photon interference. An example of a measurement in the strong coupling regime is shown in figure 1.3(b). Here the emission spectra for a photoluminescence experiment is shown at different detunings between between exciton emitter (X) and the cavity (C) [16]. A clear indication that we are in the strong coupling regime is seen through the so-called avoided crossing of the two peaks, revealing the formation of an electron-photon quasi-particle, often called a polariton.

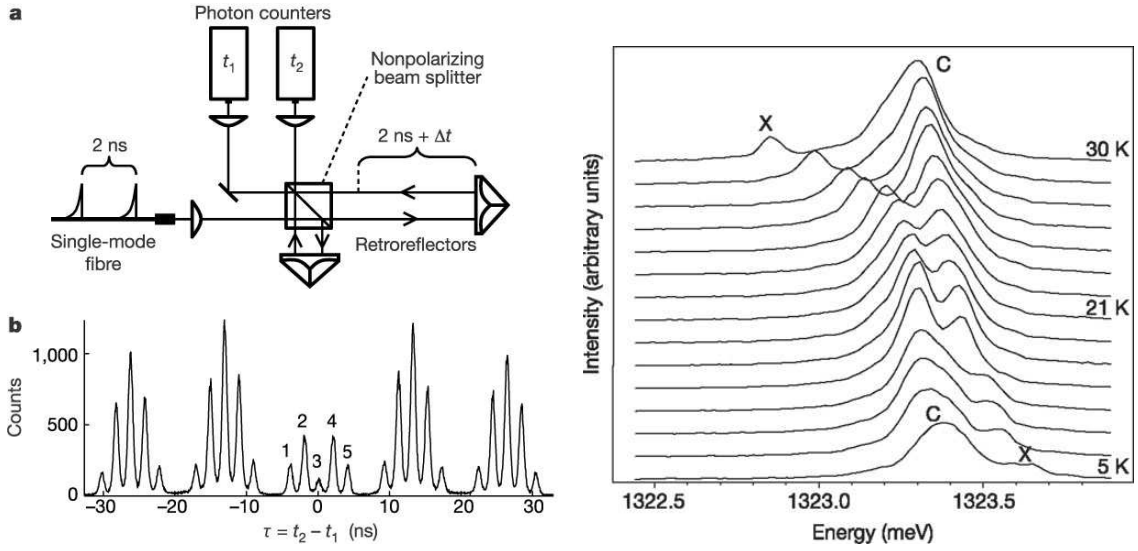

(a) Figures showing the setup for performing a two-photon interference measurement and the corresponding coincidence histogram [14].

(b) Emission spectra for a cQED system in the strong coupling regime [16].

Figure 1.3.: *Figures illustrating examples of weak and strong coupling between electrons and photons.*

The most basic features of these experiments have been reproduced by simple models [15, 17–19], where decay processes are treated in relaxation rate approximations. The rates become fitting parameters and give no understanding or insight into the physics underlying the various decay processes. In order to understand the effects of e.g. temperature, more advanced models are needed that explicitly take into account the interactions giving rise to the temperature features. These interactions have an inherent many-body nature and are therefore notoriously difficult to handle theoretically, and often very computationally demanding, which are some of the reasons why they are not employed more often in the literature. Recently there has been several theoretical papers [20–23] that treat cQED systems and some kind of many-body

interaction, usually phonons. However, they all have the common feature that they use methods[2] that are impossible, or very difficult, to extend to realistic systems, which is the ultimate goal and is a prerequisite for explaining some experiments.

In this thesis we employ a non-equilibrium Green's function formalism and set up a model for a realistic cQED system. We take into account the many-body interactions between electrons, phonons, and photons and go beyond the usual two-level description of the electronic system, in that we consider a multi-level QD scheme rarely done in the literature. The model is analyzed and discussed for several relevant scenarios, with the overall conclusion that in order to accurately describe experiments it is imperative to employ a many-body model, that explicitly describes the various decay mechanisms.

[2] Many employ the so-called independent boson model [24] that only applies to systems with a single electronic level, obviously limiting its usefulness.

2. Non-equilibrium Green's Functions

2.1. Introduction and motivation

The theoretical description of many-body quantum systems is notoriously difficult, and there exists only a very limited understanding of the vast amount of intriguing phenomena arising from the intricate interactions amongst many identical particles. One reason for the limited understanding of many-body systems is due the practical problems associated with solving the fundamental governing equation, namely the time-dependent Schrödinger equation

$$i\hbar\partial_t \left|\Psi(t)\right\rangle = H \left|\Psi(t)\right\rangle . \tag{2.1}$$

In standard wavefunction approaches the Hamiltonian and wavefunction are expanded in a many-particle Hilbert space and the resulting set of linear equations is solved. While this approach is possible and very often used for single or few particles systems, it becomes impossible to proceed down this path once the particle number becomes significant. This is so as the corresponding Hilbert space, increases exponentially in the number of particles and in the number of single-particle states used to expand the many-particle Hilbert space on. To make progress we turn to the Heisenberg representation of quantum theory, in which operators rather than the wavefunctions themselves are the primary objects. This approach does however also have an inherent problem known as the hierarchy problem. The hierarchy problem is nicely illustrated using an concrete example in which we consider the following Hamiltonian

$$H = \hbar\omega_1 c_1^\dagger c_1 + \hbar\omega_2 c_2^\dagger c_2 + \hbar\omega a^\dagger a + \hbar g(c_2^\dagger c_1 a + a^\dagger c_1^\dagger c_2),$$

that represents fermions in two states 1 and 2, interacting with a bosonic mode through the interaction described by the last two terms[1]. In order to get information on the fermions of the system, we would like to know the time evolution of the fermion operators, e.g. $c_2^\dagger$. To obtain the time evolution one needs to solve the Heisenberg equation of motion, see eqs. (2.8) and (2.9), that reads

$$i\hbar\partial_t c_2^\dagger(t) = [c_2^\dagger(t), H(t)].$$

The evaluation of the commutator between $c_2^\dagger$ and H is easily done using the (anti)commutator relations, see eq. (A.33), for the operators and we get the following more explicit equation

$$i\hbar\partial_t c_2^\dagger(t) = -\hbar\omega_2 c_2^\dagger(t) - \hbar g a^\dagger(t) c_1^\dagger(t).$$

The first term on the right hand side (RHS) is identified with the free evolution of $c_2^\dagger(t)$ in the absence of interactions, while the second term is due to the interaction with the bosonic mode. As this equation is not closed in $c_2^\dagger(t)$ we have to set up an equation describing the evolution of the operator product $a^\dagger(t)c_1^\dagger(t)$, doing so one discovers that this equation couples to a new product of three operators. The coupling to higher order products never ends, meaning that a closed set equations is never obtained and therefore the problem is in principle unsolvable. This infinite number of equations is known as the hierarchy problem of many-body theory.

There are different ways one can tackle the hierarchy problem. The two dominating methods both focus on determining the time evolution of expectation values of operators, as here one may focus on obtaining e.g. single-particle information. This should be contrasted to the wavefunction approach, were one obtains

[1] This Hamiltonian is equal to the Jaynes-Cummings model studied in appendix A.2, in the rotating wave approximation, but the point we are trying to make is generic and hence this is not emphasized.

all information available on the system, much of which is often redundant. An example of such a time dependent expectation value is the single-particle density matrix, e.g. $\rho_{11}(t) = \langle c_1^\dagger(t)c_1(t)\rangle$ or its two-time generalization $\rho_{11}^<(t',t) = \langle c_1^\dagger(t)c_1(t')\rangle$. The method relying on one-time density matrices is known as the cluster expansion scheme (for a review see [25]) where, rather intuitively, higher order products are factored into lower ordered ones, which in the end renders the system of equations finite and hence in principle solvable. The method relying on two-time density matrices, or more generally two-time correlation functions, is known as the Green's function approach. In this approach certain contributions in all higher order products are kept, and hence these contributions are taken into account to infinite order. In this thesis we will use the a non-equilibrium version of the Green's function formalism, as it has proven efficient in studying semiconductor many-body system out of equilibrium [26]. For discussions on the differences and similarities of the two methods see [27] and [26, pp. 243-250]

To further motivate the use of Green's functions we now show how these relate to experimentally accessible quantities. We start by considering a general one-body operator B, which describes some observable of a physical system. In creation and annihilation operators B can be written

$$B = \sum_{\alpha\beta} B_{\alpha\beta} O_\alpha^\dagger O_\beta,$$

where O can be either a fermion or boson operator and $B_{\alpha\beta} = \langle\alpha|B|\beta\rangle$ is the single-particle matrix element. What is measured in experiments is the expectation value of B, defined by tracing over the density operator of the system

$$\langle B(t)\rangle = \mathrm{Tr}[B\rho(t)] = \mathrm{Tr}[Bu(t,t_0)\rho(t_0)u^\dagger(t,t_0)] = \mathrm{Tr}[u^\dagger(t,t_0)Bu(t,t_0)\rho(t_0)] = \mathrm{Tr}[B(t)\rho(t_0)]. \tag{2.2}$$

In terms of the expansion of B above we may write

$$\langle B(t)\rangle = \sum_{\alpha\beta} B_{\alpha\beta}\mathrm{Tr}\left[O_\alpha^\dagger(t)O_\beta(t)\rho(t_0)\right] = \sum_{\alpha\beta} B_{\alpha\beta}\left\langle O_\alpha^\dagger(t)O_\beta(t)\right\rangle, \tag{2.3}$$

where $\langle\cdots\rangle$ denotes averaging with respect to the initial state of the system described by $\rho(t_0)$. The entire time-dependent bracket $\langle O_\alpha^\dagger(t)O_\beta(t)\rangle$ is proportional to what is known as the equal-time lesser Green's function, see eq. (2.24b), and plays the role of the single-particle density matrix. Thus with knowledge of the lesser Green's function, the expectation value of any one-body operator can be determined. This makes this object very desirable to obtain, therefore much effort is put into solving the equations for the lesser Green's function and much of this thesis will deal with this issue also. Information on the spectral properties of a system, e.g. density of states, is often wanted and also these are accessible through the Green's functions. One can relate the mean thermal occupation of a state α to the Fourier transform of the so-called spectral function $A_\alpha(\omega)$ as [28, p. 131]

$$\langle O_\alpha^\dagger O_\alpha\rangle = \int_{-\infty}^{\infty} \frac{d(\hbar\omega)}{2\pi} A_\alpha(\hbar\omega) f(\hbar\omega), \tag{2.4}$$

where $f(\hbar\omega)$ is equal to the Fermi-Dirac (Bose-Einstein) distribution function for fermions (bosons) and $A_\alpha(\hbar\omega) = -2\mathrm{Im}[G_\alpha^r(\hbar\omega)]$, see eq. (2.24c). This shows that the spectral function is similar to the usual density of states.

There exists two approaches for generating the equations for the Green's functions. The first is the diagrammatic approach pioneered by Richard Feynman, where one represents the equations in terms of rather intuitive pictograms, that can make it easier to gain an overview of the complicated equations. The second is a more mathematical approach developed by Julian Schwinger, where a functional derivative technique is used to generate the governing equations. The two formulations are identical as showed by Freeman Dyson, but are in practice quite different and we will throughout this thesis employ the diagrammatic approach as the author finds this more intuitive.

This chapter is meant as a brief introduction to the theory of non-equilibrium Green's functions and is a compilation of a number of other texts [24, 26, 28–33], where ref. [33] should be emphasized as

an especially thorough and lucid introduction. Attention should also pointed to the recent release of a textbook by Jørgen Rammer on the subject [34], which seems to fill a gap in the literature for a modern formal introduction to non-equilibrium Green's functions.

2.2. Basics of contour ordered Green's functions

In this section we will introduce the contour ordered Green's function and develop an infinite order perturbation theory for this object. We start by considering the calculation of ensemble averages of physical observables in non-equilibrium situations, this is done to motivate the introduction of the concept of contour time and contour time ordering. Next we define the single-particle contour ordered Green's function for which we develop an infinite order perturbation theory using the diagrammatic technique. The culmination is the arrival at the Dyson equation for the contour ordered Green's function and the concept of self-energy.

2.2.1. Ensemble averages in non-equilibrium

To be able to discuss quantum mechanical problems we first need to introduce a Hamiltonian for the system we are considering. We divide the Hamiltonian into three parts that are fundamentally different and hence write it as

$$H = H_0 + H_{\mathrm{i}} + U(t). \tag{2.5}$$

The non-interacting part is given by H_0, this contains the quadratic (i.e. terms with two operators) parts of all the fermionic and bosonic species of the system, and constitutes the basic system upon which perturbation theory is performed. The interaction part is given by H_{i} and consists of all many-body interactions between the fermionic and bosonic species. Each term in H_{i} is characterized by having more than two operators, and hence gives rise to the hierarchy problem mentioned in the introduction to this chapter. The last part $U(t)$ is the externally applied and explicitly time-dependent disturbance to the system, which drives it into the non-equilibrium state. We assume $U(t)$ to be quadratic, which is normally the case, as this yields a simpler formulation of the theory.

We now proceed by considering the calculation of the expectation of a physical observable described by the operator O in a system governed by the Hamiltonian eq. (2.5)

$$\langle O(t) \rangle = \mathrm{Tr}\left[\rho(t_0) O(t)\right], \tag{2.6}$$

where $\rho(t_0)$ is the initial density matrix, before the time-dependent external potential begins to act. The most natural initial state to consider in a solid-state system is that of thermal equilibrium. The thermal density matrix is given by [28, p. 28]

$$\rho(t_0) = \frac{e^{-\beta[(H_0+H_{\mathrm{i}})-\mu N]}}{\mathrm{Tr}\left[e^{-\beta[(H_0+H_{\mathrm{i}})-\mu N]}\right]} = \frac{e^{-\beta(H_0+H_{\mathrm{i}})}}{\mathrm{Tr}\left[e^{-\beta(H_0+H_{\mathrm{i}})}\right]}, \tag{2.7}$$

where we have chosen our energy scale so that the chemical potential is zero, $\mu = 0$, to avoid having to deal explicitly with the particle number operator, N, and $\beta = (k_{\mathrm{B}}T)^{-1}$ is the inverse thermal energy. For the moment we will postpone the problems associated with thermal density matrix to the end of this section and concentrate on the time development of the expectation value eq. (2.6).

In eq. (2.6) $O(t)$ is the Schrödinger operator O in the Heisenberg picture, also it should be emphasized that $O(t)$ can describe both fermionic or bosonic species. The Heisenberg picture is defined by

$$O(t) = u_H^\dagger(t, t_0) O u_H(t, t_0), \tag{2.8}$$

where $u_H(t,t_0)$ is the time evolution operator which is governed by the Schrödinger equation

$$i\hbar\partial_t u_H(t,t_0) = Hu_H(t,t_0), \tag{2.9}$$

with the initial condition $u_H(t_0,t_0)=1$. This equation is in general very difficult to solve, if not impossible, for most realistic systems. Furthermore as the overall goal is to formulate a perturbation theory, we switch to the interaction picture which facilitates this. In the interaction picture an operators time-dependence is governed by H_0 and is therefore given by

$$\hat{O}(t) = u^\dagger_{H_0}(t,t_0)Ou_{H_0}(t,t_0), \tag{2.10}$$

where $u_{H_0}(t,t_0)$ is the time evolution operator with respect to H_0 and assumed known. However to capture the full time evolution of the system we have to consider Heisenberg time evolution. By using the property $u_{H_0}(t,t_0)u^\dagger_{H_0}(t,t_0)=1$ of unitary operators we rewrite $O(t)$ to a form more suitable for the formulation of a perturbation theory

$$\begin{aligned} O(t) &= u^\dagger_H(t,t_0)Ou_H(t,t_0) = u^\dagger_H(t,t_0)u_{H_0}(t,t_0)u^\dagger_{H_0}(t,t_0)Ou_{H_0}(t,t_0)u^\dagger_{H_0}(t,t_0)u_H(t,t_0) \\ &= v^\dagger_{H_0}(t,t_0)\hat{O}(t)v_{H_0}(t,t_0), \end{aligned} \tag{2.11}$$

where we used eq. (2.10) and defined the very important time evolution operator

$$v_{H_0}(t,t_0) = u^\dagger_{H_0}(t,t_0)u_H(t,t_0).$$

The next step is to obtain an equation of motion for $v_{H_0}(t,t_0)$, which is done by simply differentiating its definition

$$i\hbar\partial_t v_{H_0}(t,t_0) = i\hbar\partial_t\left(u^\dagger_{H_0}(t,t_0)u_H(t,t_0)\right) = \left[i\hbar\partial_t u^\dagger_{H_0}(t,t_0)\right]u_H(t,t_0) + u^\dagger_{H_0}(t,t_0)\left[i\hbar\partial_t u_H(t,t_0)\right].$$

The terms in the square brackets are equal to their respective Schrödinger equations, see eq. (2.9), hence

$$\begin{aligned} i\hbar\partial_t v_{H_0}(t,t_0) &= -H_0u^\dagger_{H_0}(t,t_0)u_H(t,t_0) + u^\dagger_{H_0}(t,t_0)\left(H_0+H_\mathrm{i}+U(t)\right)u_{H_0}(t,t_0)u^\dagger_{H_0}(t,t_0)u_H(t,t_0) \\ &= \left(\hat{H}_\mathrm{i}(t)+\hat{U}(t)\right)v_{H_0}(t,t_0) = \hat{V}(t)v_{H_0}(t,t_0), \end{aligned}$$

where we used that $u^\dagger_{H_0}(t,t_0)H_0u_{H_0}(t,t_0)=H_0$, the definition of $v_{H_0}(t,t_0)$, and introduced $\hat{V}(t)=\hat{H}_\mathrm{i}(t)+\hat{U}(t)$ containing all interactions. To solve this equation we formally integrate once and obtain the following

$$v_{H_0}(t,t_0) = 1 - i\hbar^{-1}\int_{t_0}^{t} dt_1\hat{V}(t_1)v_{H_0}(t_1,t_0),$$

where we have used the initial condition $v_{H_0}(t_0,t_0)=1$. This can now be iterated to yield $v_{H_0}(t,t_0)$ expressed as an infinite sum, namely

$$v_{H_0}(t,t_0) = \sum_{n=0}^{\infty}(-i\hbar^{-1})^n\int_{t_0}^{t}dt_1\int_{t_0}^{t_1}dt_2\cdots\int_{t_0}^{t_{n-1}}dt_n\hat{V}(t_1)\hat{V}(t_2)\cdots\hat{V}(t_n),$$

where the zeroth term is to be taken as 1. If we introduce the time ordering operator[2] T_t we can write the above in a form which allows an easier formulation of the perturbation theory

$$v_{H_0}(t,t_0) = \sum_{n=0}^{\infty}\frac{(-i\hbar^{-1})^n}{n!}\int_{t_0}^{t}dt_1\int_{t_0}^{t}dt_2\cdots\int_{t_0}^{t}dt_nT_t\left\{\hat{V}(t_1)\hat{V}(t_2)\cdots\hat{V}(t_n)\right\}. \tag{2.12}$$

[2]For a textbook introduction to the time ordering operator see the first chapters in any many-body text, e.g. [24, 28].

As this expansion looks like that of an exponential function it is common to define the following short hand notation

$$v_{H_0}(t,t_0) = T_t\left\{e^{-i\hbar^{-1}\int_{t_0}^{t} dt'\hat{V}(t')}\right\},$$

but one should be cautious by treating it as an exponential function in mathematical manipulations. The operator T_t orders operators so that "late times go left", e.g. for a two-operator product we get

$$T_t\left\{\hat{V}(t_1)\hat{V}(t_2)\right\} = \theta(t_1-t_2)\hat{V}(t_1)\hat{V}(t_2) + \theta(t_2-t_1)\hat{V}(t_2)\hat{V}(t_1),$$

which holds for the type of interactions normally considered in solid state physics[3]. When considering time ordered Green's functions in the sections ahead, we will also need to know the action of the time ordering operator on the more fundamental bosonic and fermionic operators, and not just the combinations these occur in in the various interaction Hamiltonians. Here it also holds that operators with "late times go left", so that for a three operator product we for example get [35]

$$T_t\left\{A_1(t_1)A_2(t_2)A_3(t_3)\right\} = (-1)^P A_{i_1}(t_{i_1})A_{i_2}(t_{i_2})A_{i_3}(t_{i_3}), \quad t_{i_1} > t_{i_2} > t_{i_3}, \tag{2.13}$$

where P is the number of interchangings of fermionic operators performed on the original product, while there is no sign changes for bosonic operators. Note that this ordering holds for operators governed in time by any Hamiltonian, both H_0 and H. This is so as eq. (2.13) is basically a definition and not derived from the kind of arguments leading to the introduction of T_t in eq. (2.12), but of course they are consistent.

We are now ready to introduce the concept of contour time which is motivated by the interaction picture expansion of the operator $O(t)$, eq. (2.11), and the expression for the time evolution operator $v_{H_0}(t,t_0)$, eq. (2.12), we have derived. The expression for $v_{H_0}(t,t_0)$ contains an integration from t_0 to t, while $v^\dagger_{H_0}(t,t_0)$ contains one from t to t_0, as seen through the hermitian conjugation procedure

$$\begin{aligned} v^\dagger_{H_0}(t,t_0) &= \sum_{n=0}^{\infty}\frac{(-i\hbar^{-1})^n}{n!}(-1)^n\int_{t_0}^{t}dt_1\int_{t_0}^{t}dt_2\cdots\int_{t_0}^{t}dt_n\left(T_t\left\{\hat{V}(t_1)\hat{V}(t_2)\cdots\hat{V}(t_n)\right\}\right)^\dagger \\ &= \sum_{n=0}^{\infty}\frac{(-i\hbar^{-1})^n}{n!}\int_{t}^{t_0}dt_1\int_{t}^{t_0}dt_2\cdots\int_{t}^{t_0}dt_n T_{at}\left\{\hat{V}(t_1)\hat{V}(t_2)\cdots\hat{V}(t_n)\right\}, \end{aligned} \tag{2.14}$$

where $T_{at}\{\cdots\} = (T_t\{\cdots\})^\dagger$ is called the anti-time ordering operator, as it basically flips the product ordered by T_t. Having made these observations it becomes apparent that we can write

$$O(t) = T_{C_2}\left\{e^{-i\hbar^{-1}\int_{C_2}d\tau'\hat{V}(\tau')}\right\}\hat{O}(t)T_{C_1}\left\{e^{-i\hbar^{-1}\int_{C_1}d\tau'\hat{V}(\tau')}\right\},$$

where C_1 and C_2 are the contours depicted in figure 2.1, and their corresponding time ordering operators $T_{C_1} = T_t$ and $T_{C_2} = T_{at}$, and finally τ is a complex time variable.

Furthermore it is possible [35] to collect the two time evolution operators into one, which is ordered along the entire Keldysh contour $C = C_1 \cup C_2$, so that we obtain

$$\begin{aligned} O(t) &= \sum_{n=0}^{\infty}\frac{(-i\hbar^{-1})^n}{n!}\int_C d\tau_1\int_C d\tau_2\cdots\int_C d\tau_n T_C\left\{\hat{V}(\tau_1)\hat{V}(\tau_2)\cdots\hat{V}(\tau_n)\hat{O}(t)\right\} \\ &= T_C\left\{e^{-i\hbar^{-1}\int_C d\tau'\hat{V}(\tau')}\hat{O}(t)\right\} = T_C\left\{S_C\hat{O}(t)\right\}, \end{aligned} \tag{2.15}$$

[3] For interactions which does not contain an even number of fermionic creation and annihilation operators, and hence does not conserve fermionic particle number, a net sign can occur through interchanging of fermionic operators, see eq. (2.13).

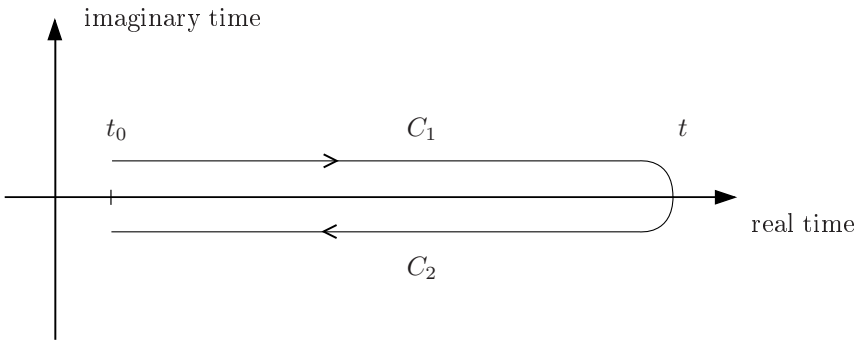

Figure 2.1.: *Schematic illustration of the Keldysh contour consisting of the branches C_1 and C_2. The contour runs on the real axis, but have been shifted slightly for visual clarity.*

where we have defined $S_C = e^{-i\hbar^{-1}\int_C d\tau' \hat{V}(\tau')}$. The contour time ordering operator T_C orders along the Keldysh contour C [35]

$$T_C\left\{A_1(\tau_1)A_2(\tau_2)A_3(\tau_3)\right\} = (-1)^P A_{i_1}(\tau_{i_1})A_{i_2}(\tau_{i_2})A_{i_3}(\tau_{i_3}), \quad \tau_{i_1} >_C \tau_{i_2} >_C \tau_{i_3}, \tag{2.16}$$

where $>_C$ means "greater than" in the contour sense. This for example means that times on the lower contour, C_2, will always be greater than those on the upper contour, C_1. P is again the number of interchanges of fermionic operators. As for the normal time ordering operator T_t, eq. (2.13), the T_C ordering also holds for operators governed by any Hamiltonian. Apart from being a more compact notation eq. (2.15) has the great advantage that all the interactions in $\hat{V}(t)$ are collected in one place, which simplifies the perturbation theory we are aiming at performing.

We have however not completed the task of isolating all the difficult interactions as we still need to address the initial density matrix, eq. (2.7), which performs the thermodynamic averaging. Formally this problem is handled in the same spirit as above, we write a difficult operator as something we know times something we handle perturbatively. The usual way to proceed is to take advantage of the fact that both thermal averaging and time development involves exponential functions, and hence it becomes possible to extend the Keldysh contour into true imaginary time and through this perform the thermal averaging. In equilibrium theory this is known as the Matsubara technique, see e.g. [28]. We will however not dwell at the details[4] as we take the usual approach of letting $t_0 \to -\infty$, corresponding to adiabatically coupling the interactions contained in H_i to the non-interacting H_0 equilibrium system, so that the contribution from the imaginary time branch becomes neglectable. What we end up with is the following expression for the ensemble average of the operator $O(t)$ taking in an arbitrary non-equilibrium state, which has evolved from a non-interacting equilibrium state in the distant past,

$$\langle O(t)\rangle = \mathrm{Tr}\left[\rho(t_0 \to -\infty)O(t)\right] = \frac{\langle T_C\{S_C\hat{O}(t)\}\rangle_0}{\langle T_C\left\{S_C\right\}\rangle_0}, \tag{2.17}$$

where the brackets with subscript "0" denote thermal average with respect to H_0

$$\langle\cdots\rangle_0 = \frac{1}{\mathrm{Tr}\left[e^{-\beta H_0}\right]}\mathrm{Tr}\left[e^{-\beta H_0}\cdots\right]. \tag{2.18}$$

Finally we extend the upper limit on the Keldysh contour from t to ∞ by inserting $v_{H_0}(\infty,t)v^\dagger_{H_0}(\infty,t) = 1$ next to S_C in eq. (2.17), see figure 2.2.

2.2.2. The contour ordered Green's function and Dyson's equation

In the previous section we considered the calculation of the expectation value of a physical observable in a non-equilibrium state, which is often what one is interested in. It has however turned out to be

[4] For a detailed derivation see [33].

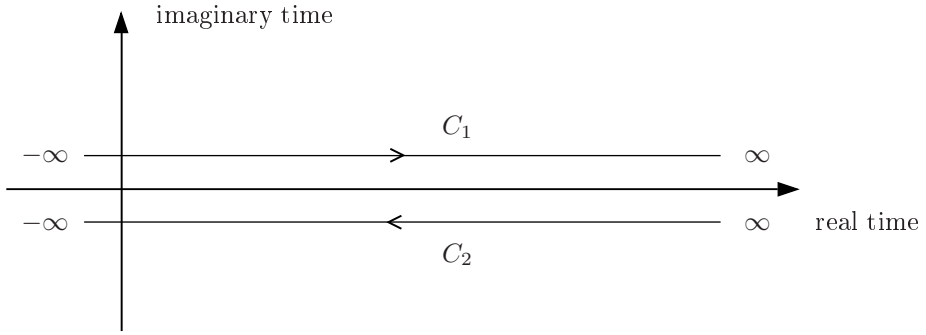

Figure 2.2.: *Schematic illustration of the Keldysh contour with the lower and upper limits extended to $-\infty$ and ∞ respectively.*

very difficult to formulate a closed infinite order perturbation theory for observables, due to the fact that the spatial correlation functions comprising the observables, couple to correlation functions in time also. Sometimes one might be interested in correlation functions in time (even though they are not direct physical observables) themselves, especially for the bosonic photons, as this is what is often measured in experiments. On this basis we define the single-particle contour ordered Green's function by the following

$$G_{\alpha\beta}(\tau,\tau') = -i\hbar^{-1}\left\langle T_C\{O_\alpha(\tau)O^\dagger_\beta(\tau')\}\right\rangle, \tag{2.19}$$

where $O_\alpha(\tau)$ and $O^\dagger_\beta(\tau')$ are either fermionic or bosonic operators in the Heisenberg picture. The reason for introducing this rather strange theoretical object is that it possesses a well defined perturbation expansion, as is hinted by considering the expansion of the time evolution in eq. (2.15). The contour ordered Green's function is defined in terms of contour times that live on the Keldysh contour and therefore its relevance for obtaining observable quantities, which are in real times, might not be clear at the moment. We will consider this issue of going from contour to real times in section 2.3, but for the moment we will keep on working on the contour ordered Green's function.

To make further progress toward a perturbation theory we adopt the result of eq. (2.17) and write the RHS of the contour ordered Green's function in the interaction picture

$$G_{\alpha\beta}(\tau,\tau') = -i\hbar^{-1}\frac{\left\langle T_C\{S_C\hat{O}_\alpha(\tau)\hat{O}^\dagger_\beta(\tau')\}\right\rangle_0}{\left\langle T_C\{S_C\}\right\rangle_0}. \tag{2.20}$$

As seen from eq. (2.15) the time evolution operator S_C in the above equation is an infinite sum of products of operators evolving according the Hamiltonian H_0, this generally results in the generation of higher order contour ordered Green's functions of the following form

$$G^{0,(n)}_{\alpha_1\cdots\alpha_n,\beta_n\cdots\beta_1}(\tau_1,\cdots,\tau_n;\tau'_n,\cdots,\tau'_1) = (-i\hbar^{-1})^n\left\langle T_C\{\hat{O}_{\alpha_1}(\tau_1)\cdots\hat{O}_{\alpha_n}(\tau_n)\hat{O}^\dagger_{\beta_n}(\tau'_n)\cdots\hat{O}^\dagger_{\beta_1}(\tau'_1)\}\right\rangle_0,$$

where n indicates a n'th-particle contour ordered Green's function. These arbitrarily large objects can be calculated, as the time-dependence is known, using the (anti)commutation relations for the (fermionic) bosonic operators, but would be very tedious work. A much more elegant and useful approach is provided by Wick's theorem[5], which states that a n'th-particle contour ordered Green's function can be decomposed into products of single-particle contour ordered Green's functions. It is this decomposition which allows for the formulation of infinite order perturbation theory. The decomposition can be written compactly as follows

$$G^{0,(n)}_{\alpha_1\cdots\alpha_n,\beta_n\cdots\beta_1}(\tau_1,\cdots,\tau_n;\tau'_n,\cdots,\tau'_1) = \begin{vmatrix} G^0_{\alpha_1\beta_1}(\tau_1,\tau'_1) & \cdots & G^0_{\alpha_1\beta_n}(\tau_1,\tau'_n) \\ \vdots & \ddots & \vdots \\ G^0_{\alpha_n\beta_1}(\tau_n,\tau'_1) & \cdots & G^0_{\alpha_n\beta_n}(\tau_n,\tau'_n) \end{vmatrix}_{\pm}, \tag{2.21}$$

[5]A proof of Wick's theorem in contour times can be found in [34].

where + denotes a positive determinant which must be used for bosons and − denotes a regular determinant with minus signs which must be used for fermions. For Wick's theorem to hold the time-dependence and thermal averaging must be governed by H_0, a quadratic Hamiltonian, as in our case.

Applying Wick's theorem to the denominator in eq. (2.20) results in infinitely many disconnected diagrams[6], i.e. diagrams that only involve internal integration variables and not the external (α, τ) and (β, τ') variables. Applying Wick's theorem to the numerator eq. (2.20) results in infinitely many connected diagrams, i.e. diagrams that are connect to the external (α, τ) and (β, τ') points, times (as a factor) all the disconnected diagrams that appeared in the denominator. This means that all disconnected diagrams cancel resulting in a huge simplification and we can write the following perturbative expression for the contour ordered Green's function

$$G_{\alpha\beta}(\tau, \tau') = -i\hbar^{-1} \sum_{n=0}^{\infty} \frac{(-i\hbar^{-1})^n}{n!} \int_C d\tau_1 \int_C d\tau_2 \cdots \int_C d\tau_n \, \langle T_C\{\hat{V}(\tau_1)\hat{V}(\tau_2)\cdots\hat{V}(\tau_n)\hat{O}_\alpha(\tau)\hat{O}^\dagger_\beta(\tau')\}\rangle_{0,\text{con}}, \tag{2.22}$$

where the subscript "con" indicates that we should only keep connected diagrams. Writing out higher and higher orders of the above expression it becomes apparent that the structure somehow repeats itself. One sees that it is possible to perform a resummation to obtain an integral equation for the contour ordered Green's function, also known as a Dyson equation. This resummation is most easily illustrated diagrammatically as shown in figure 2.3. The second term on the RHS describes the interaction with the

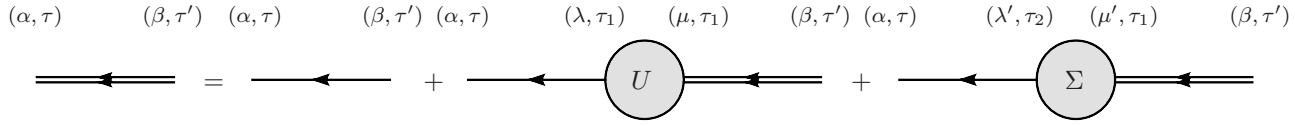

Figure 2.3.: *Diagrammatic representation of the Dyson equation for the full contour ordered Green's function eq.* (2.23)*. The double (single) line represents the full (free) contour ordered Green's function, while the U symbol represents the external potential and the Σ symbol represents the self-energy. For diagrammatical representations of U and Σ see figure 2.4.*

external potential and as this is a one-body interaction it only results in a simple instantaneous scattering from one free Green's function to another with a certain amplitude. This process is illustrated with the dashed line in figure 2.4(b). The third term on the RHS is the so-called (irreducible) self-energy which describes the true many-body interactions of the system and has an infinite number of higher order contributions. A few of the lowest order ones are illustrated in figure 2.4(a). The diagrams in figure 2.4(a) are meant only to serve as an illustration, where for example the straight lines could represent electrons and the wiggly lines phonons. In a system with several many-body interactions each involved specie has its own self-energy dependent on the specific interaction, however the diagrams are topological identical for so it suffices to show one example. If one truncates the self-energy after, say, the two first terms and solves the resulting Dyson equation, these two first order processes have been taken into account to infinite order, which justifies calling this theory infinite order perturbation theory.

In mathematical form the Dyson equation is written as an integral equation in contour time and space

$$\boldsymbol{G}(\tau, \tau') = \boldsymbol{G}^0(\tau, \tau') + \int_C d\tau_1 \boldsymbol{G}^0(\tau, \tau_1)\boldsymbol{U}(\tau_1)\boldsymbol{G}(\tau_1, \tau') + \int_C d\tau_2 d\tau_1 \boldsymbol{G}^0(\tau, \tau_2)\boldsymbol{\Sigma}(\tau_2, \tau_1)\boldsymbol{G}(\tau_1, \tau'), \tag{2.23}$$

where we have transitioned to a matrix notation to reduce the number of sums, i.e. $(\boldsymbol{G}(\tau, \tau'))_{\alpha\beta} = G_{\alpha\beta}(\tau, \tau')$. This is the main equation for the rest of this thesis and will be applied to both fermionic and bosonic particles later on.

[6] Feynman diagrams, or just diagrams, are drawings of the various terms in the expansion of the Green's function that can rigorously be converted to mathematics and vice versa. We will use the term diagram of both the drawings and the mathematical equivalent as they are basically the same. For an introduction to Feynman diagrams see any many-body text book.

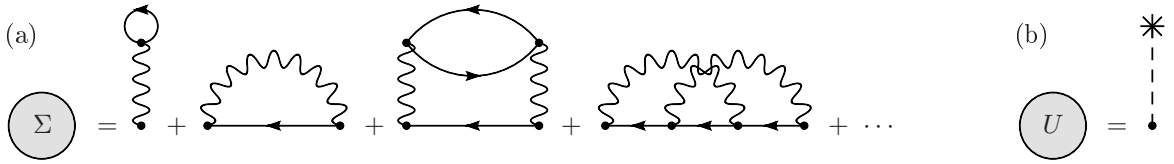

Figure 2.4.: *Diagrammatic representation of (a) a few of the lowest order contributions to the self-energy where, as in figure 2.3, the single lines represent free contour ordered Green's functions and the wiggly lines represent interaction lines and (b) the scattering vertex of the external potential. This self-energy is for fermions, the self-energy for bosons looks slightly different.*

While the contour ordered Green's function possess a nice perturbation expansion it has no direct relation to physical observables and further is expressed in contour time and not real time. The process of translating from contour to real time, known as analytic continuation, and making the connection to more physically relevant correlation functions is carried out in the next section.

2.3. Real time Green's functions and Langreth rules

In the previous sections we introduced the concept of contour time, enabling an relatively easy and compact formulation of the perturbation theory for the contour ordered Green's function. However experiments are performed in real time, so we have to link the contour ordered Green's function to real time Green's functions which have to be the relevant objects for describing physical measurements. It turns out to be convenient to introduce the following four real time Green's functions

$$G^{>}_{\alpha\beta}(t,t') = -i\hbar^{-1}\left\langle O_\alpha(t)O^\dagger_\beta(t')\right\rangle, \tag{2.24a}$$

$$G^{<}_{\alpha\beta}(t,t') = \pm i\hbar^{-1}\left\langle O^\dagger_\beta(t')O_\alpha(t)\right\rangle, \tag{2.24b}$$

$$G^{r}_{\alpha\beta}(t,t') = -i\hbar^{-1}\theta(t-t')\left\langle [O_\alpha(t),O^\dagger_\beta(t')]_\pm\right\rangle = \theta(t-t')(G^{>}_{\alpha\beta}(t,t') - G^{<}_{\alpha\beta}(t,t')), \tag{2.24c}$$

$$G^{a}_{\alpha\beta}(t,t') = i\hbar^{-1}\theta(t'-t)\left\langle [O_\alpha(t),O^\dagger_\beta(t')]_\pm\right\rangle = -\theta(t'-t)(G^{>}_{\alpha\beta}(t,t') - G^{<}_{\alpha\beta}(t,t')), \tag{2.24d}$$

which are called the greater ($>$), lesser ($<$), retarded (r), and advanced (a) Green's function respectively. In the lesser Green's function $+$ is for fermions and $-$ is for bosons. For the retarded and advanced Green's functions the $+$ subscript denotes a anti-commutator which is to be used for fermions and the $-$ denotes a commutator to used for bosons. These Green's functions are directly related to physically measurable quantities. The lesser Green's function can be used to calculate the expectation value of any physical observable in its equal-time limit. The retarded/advanced Green's function contains information on the spectral properties of the system, like the density of states, and can further be used to calculate response functions.

Being defined on the Keldysh contour the contour ordered Green's function, eq. (2.19), contains four real time Green's functions as components, depending on where on the Keldysh contour its time arguments are located. With reference to eqs. (2.16) and (2.19), and figure 2.2 we deduce the following

$$G_{\alpha\beta}(\tau,\tau') = \begin{cases} G^{t}_{\alpha\beta}(t,t'), & \tau,\tau' \in C_1 \\ G^{<}_{\alpha\beta}(t,t'), & \tau \in C_1,\ \tau' \in C_2 \\ G^{>}_{\alpha\beta}(t,t'), & \tau \in C_2,\ \tau' \in C_1 \\ G^{at}_{\alpha\beta}(t,t'), & \tau,\tau' \in C_2, \end{cases} \tag{2.25}$$

where the time ordered Green's function, $G^t_{\alpha\beta}(t,t')$, is given by

$$G^t_{\alpha\beta}(t,t') = -i\hbar^{-1}\left\langle T_t\{O_\alpha(t)O^\dagger_\beta(t')\}\right\rangle = \theta(t-t')G^>_{\alpha\beta}(t,t') + \theta(t'-t)G^<_{\alpha\beta}(t,t') \tag{2.26a}$$
$$= G^<_{\alpha\beta}(t,t') + G^r_{\alpha\beta}(t,t') \tag{2.26b}$$
$$= G^>_{\alpha\beta}(t,t') + G^a_{\alpha\beta}(t,t') \tag{2.26c}$$

and the anti-time ordered Green's function, $G^{at}_{\alpha\beta}(t,t')$, is given by

$$G^{at}_{\alpha\beta}(t,t') = -i\hbar^{-1}\left\langle T_{at}\{O_\alpha(t)O^\dagger_\beta(t')\}\right\rangle = \theta(t'-t)G^>_{\alpha\beta}(t,t') + \theta(t-t')G^<_{\alpha\beta}(t,t') \tag{2.27a}$$
$$= G^<_{\alpha\beta}(t,t') - G^a_{\alpha\beta}(t,t') \tag{2.27b}$$
$$= G^>_{\alpha\beta}(t,t') - G^r_{\alpha\beta}(t,t'). \tag{2.27c}$$

Even though the time and anti-time ordered Green's functions naturally arise through the properties of the T_C operator, these are not practical for calculating physical quantities. For this reason we will formulate the rest of the theory in terms of the retarded and advanced Green's functions (using eqs. (2.26b), (2.26c), (2.27b), and (2.27c)) and the greater and lesser Green's functions. It apparent from the above definitions of the time and anti-time ordered Green's functions that the following relationship holds between the various Green's functions

$$G^r_{\alpha\beta}(t,t') - G^a_{\alpha\beta}(t,t') = G^>_{\alpha\beta}(t,t') - G^<_{\alpha\beta}(t,t'), \tag{2.28}$$

showing that through their definitions there are only three independent Green's functions. One can also show [29, p. 354] that a similar relationship holds between the various components of the self-energy

$$\Sigma^r_{\alpha\beta}(t,t') - \Sigma^a_{\alpha\beta}(t,t') = \Sigma^>_{\alpha\beta}(t,t') - \Sigma^<_{\alpha\beta}(t,t'), \tag{2.29}$$

where

$$\Sigma^r_{\alpha\beta}(t,t') = \theta(t-t')(\Sigma^>_{\alpha\beta}(t,t') - \Sigma^<_{\alpha\beta}(t,t')), \tag{2.30a}$$
$$\Sigma^a_{\alpha\beta}(t,t') = -\theta(t'-t)(\Sigma^>_{\alpha\beta}(t,t') - \Sigma^<_{\alpha\beta}(t,t')). \tag{2.30b}$$

In the equal-time limit of eq. (2.28), one can obtain a very simple relation between the greater and lesser Green's functions, namely

$$G^>_{\alpha\beta}(t,t) = G^<_{\alpha\beta}(t,t) - i\hbar^{-1}\delta_{\alpha\beta}, \tag{2.31}$$

where eqs. (2.24c) and (2.24d) and the fact that, by definition, $\theta(0) = \frac{1}{2}$ have been used. This relation clearly shows the roles of the equal-time lesser and greater Green's functions as occupation factors for electrons and holes, respectively. The relation eq. (2.31) could also have been derived directly from the fundamental (anti)commutator relations in their equal-time limit. Furthermore it is possible to use the relation $\langle\psi|A|\phi\rangle^* = \langle\phi|A^\dagger|\psi\rangle$ to show [32]

$$[G^{\gtrless}_{\alpha\beta}(t,t')]^* = -G^{\gtrless}_{\beta\alpha}(t',t). \tag{2.32}$$

This can be used to prove the following relation between the retarded and advanced Green's function [32]

$$[G^r_{\alpha\beta}(t,t')]^* = G^a_{\beta\alpha}(t',t), \tag{2.33}$$

bringing the final number of independent Green's functions down to two. One might be inclined to think that as the self-energies has a symmetry relation, eq. (2.29), similar to that of the Green's functions, eq. (2.28), that the relations eqs. (2.32) and (2.33) also holds for the various components of the self-energy, but this is unfortunately not the case[7]. The use of both of these symmetry relations for the

[7] It is however claimed in the textbook by Haug and Jauho [36, p. 251] that this is the case, but no proof or reference is made to support this claim. It thus appears to be valid for some self-energies, but whether it holds for all in general is highly doubtful.

Green's functions will yield significant simplifications in the numerical calculations we will be performing in later chapters. This is so as one can calculate either half the Green's functions in the entire (t,t')-plane or all the Green's functions in half the (t,t')-plane. Usually the later is the most economic choice, due to the fact that the number of time steps in the numerical simulation usually is vastly larger than the number of Green's functions.

We will now move on to show the so-called Langreth theorem. This theorem relates a "contour convolution" of the form

$$C(\tau,\tau') = \int_C d\tau_1 A(\tau,\tau_1)B(\tau_1,\tau'), \tag{2.34}$$

to its real time lesser component. These contour integrations of contour time quantities appear, amongst other places, in the Dyson equation eq. (2.23). Maintaining the order the A and B quantities makes the rules derived below applicable to matrix products as well, so this is done. To find the lesser component of eq. (2.34) we know from eq. (2.25) that $\tau \in C_1$ and $\tau' \in C_2$, so that we get

$$\begin{aligned}
C^<(t,t') &= \int_C d\tau_1 A(t,\tau_1)B(\tau_1,t') \\
&= \int_{C_1} d\tau_1 A^t(t,\tau_1)B^<(\tau_1,t') + \int_{C_2} d\tau_1 A^<(t,\tau_1)B^{at}(\tau_1,t') \\
&= \int_{-\infty}^{\infty} dt_1 \left[A^t(t,t_1)B^<(t_1,t') - A^<(t,t_1)B^{at}(t_1,t')\right] \\
&= \int_{-\infty}^{\infty} dt_1 \left[A^r(t,t_1)B^<(t_1,t') + A^<(t,t_1)B^a(t_1,t')\right],
\end{aligned} \tag{2.35}$$

where we have used eqs. (2.26) and (2.27) and obtained the minus sign in third line by flipping the integral limits. The same holds for the greater part, just replace $<$ with $>$. Using this result it possible to find the retarded component of eq. (2.34), where we start by using the definitions eqs. (2.24c) and (2.24d)

$$\begin{aligned}
C^r(t,t') &= \theta(t-t')[C^>(t,t') - C^<(t,t')] \\
&= \theta(t-t') \int_{-\infty}^{\infty} dt_1 \left[A^r(t,t_1)B^>(t_1,t') + A^>(t,t_1)B^a(t_1,t') - A^r(t,t_1)B^<(t_1,t') - A^<(t,t_1)B^a(t_1,t')\right] \\
&= \theta(t-t') \int_{-\infty}^{\infty} dt_1 \left[A^r(t,t_1)\left\{B^>(t_1,t') - B^<(t_1,t')\right\} + \left\{A^>(t,t_1) - A^<(t,t_1)\right\}B^a(t_1,t')\right] \\
&= \int_{-\infty}^{\infty} dt_1 \theta(t-t')\left\{\theta(t-t_1) - \theta(t'-t_1)\right\}\left\{A^>(t,t_1) - A^<(t,t_1)\right\}\left\{B^>(t_1,t') - B^<(t_1,t')\right\}.
\end{aligned}$$

Making a sketch of the product of step functions one can be convinced that the following relation holds

$$\theta(t-t')\left\{\theta(t-t_1) - \theta(t'-t_1)\right\} = \theta(t-t_1)\theta(t_1-t'),$$

from which we arrive at the final result

$$C^r(t,t') = \int_{-\infty}^{\infty} dt_1 A^r(t,t_1)B^r(t_1,t') = \int_{t'}^{t} dt_1 A^r(t,t_1)B^r(t_1,t'). \tag{2.36}$$

A similar calculation can be performed for the advanced part and the result is obtained by replacing r with a and interchanging the integration limits t and t' after the last equal sign. A special kind of "contour convolution" is encountered for some instantaneous self-energies and is of the form

$$D(\tau) = \int_C A(\tau',\tau'^+)B(\tau,\tau'), \tag{2.37}$$

where $\tau^+ = \tau + 0^+$ so that $\tau^+ >_C \tau$. This shift has the consequence that A will always become $A^<$ in real time, for further elaboration see appendix A.5. As this is a one-time object it has no different real time components in the same sense as two-time objects has, but in order to perform calculations we need to express the contour time functions under the contour integral in terms of real time functions. We need to consider the cases of τ being located in both the upper and lower Keldysh branch and we start with $\tau \in C_1$

$$\begin{aligned} D(t) &= \int_{-\infty}^{\infty} dt' A^<(t',t') \left[B^t(t,t') - B^<(t,t')\right] \\ &= \int_{-\infty}^{\infty} dt' A^<(t',t') B^r(t,t') = \int_{-\infty}^{t} dt' A^<(t',t') B^r(t,t'), \end{aligned}$$

where in the first line we used eq. (2.25) to split B into its contributions on both branches and in the last line we used eq. (2.26b). This can be repeated for τ on the lower branch, $\tau \in C_2$, but the result is the same as could have been expected as we deal with a one-time quantity. If the contour times for B in eq. (2.37) happen to be interchanged, the same steps leads to $B^a(t',t)$ instead of $B^r(t,t')$.

Often one encounters, e.g. in the determination of self-energies, products of contour quantities without a contour time integration of the forms

$$\begin{aligned} C_{\leftleftarrows}(\tau,\tau') &= A(\tau,\tau')B(\tau,\tau'), \\ C_{\leftrightarrows}(\tau,\tau') &= A(\tau,\tau')B(\tau',\tau), \end{aligned}$$

called a parallel and an anti-parallel product respectively, due to the arrangement of the time arguments. An example of a parallel product is the second self-energy diagram in figure 2.4(a), for the electron-phonon interaction, while an example of an anti-parallel product occurs in the same figure in the "pair-bubble" in the third term. For the greater and lesser parts of these two quantities we immediately obtain

$$\begin{aligned} C^{\gtrless}_{\leftleftarrows}(t,t') &= A^{\gtrless}(t,t')B^{\gtrless}(t,t'), \\ C^{\gtrless}_{\leftrightarrows}(t,t') &= A^{\gtrless}(t,t')B^{\lessgtr}(t',t), \end{aligned}$$

using eq. (2.25). Again this result is used to find the corresponding retarded components. For $C_{\leftleftarrows}(\tau,\tau')$ we get

$$\begin{aligned} C^r_{\leftleftarrows}(t,t') &= \theta(t-t')[C^>(t,t') - C^<(t,t')] \\ &= \theta(t-t')[A^>(t,t')B^>(t,t') - A^<(t,t')B^<(t,t')] \\ &= \theta(t-t')[\left\{A^<(t,t') + A^r(t,t') - A^a(t,t')\right\}\left\{B^<(t,t') + B^r(t,t') - B^a(t,t')\right\} \\ &\qquad - A^<(t,t')B^<(t,t')] \\ &= A^<(t,t')B^r(t,t') + A^r(t,t')B^r(t,t') + A^r(t,t')B^<(t,t'), \end{aligned}$$

where the relation eq. (2.28) between the four Green's functions was used in going from the second to third line, while in the last line we have taken advantage of the fact that $A^r(t,t')B^a(t,t') \propto \theta(t-t')\theta(t'-t) = 0$ and removed the redundant step function in front. For the advanced part, $C^a_{\leftleftarrows}(t,t')$, all r's should be interchanged with a's and the A^aB^a term gets a minus sign. The same steps can be repeated for the anti-parallel product yielding

$$C^{r(a)}_{\leftrightarrows}(t,t') = A^<(t,t')B^{a(r)}(t',t) + A^{r(a)}(t,t')B^<(t',t).$$

All these various rules for obtaining real time parts of contour quantities we collectively call Langreth rules and they have been summarized in table 2.1. There are of course many more rules that can be derived, e.g. for products of more than two quantities, but we will only need the ones mentioned in this section. Some of these "higher order" rules can be obtained by recursive use of the rules presented in table 2.1. For more exhaustive collections we refer to the references mentioned in the beginning of the chapter.

Contour time	Real time
$C(\tau,\tau') = \int_C d\tau_1 A(\tau,\tau_1)B(\tau_1,\tau')$	$C^{\gtrless}(t,t') = \int_{-\infty}^{\infty} dt_1 \left[A^r(t,t_1)B^{\gtrless}(t_1,t') + A^{\gtrless}(t,t_1)B^a(t_1,t')\right]$ $C^{r(a)}(t,t') = \int_{-\infty}^{\infty} dt_1 A^{r(a)}(t,t_1)B^{r(a)}(t_1,t')$
$D_{\leftarrow}(\tau) = \int_C A(\tau',\tau'^+)B(\tau,\tau')$ $D_{\rightarrow}(\tau) = \int_C A(\tau',\tau'^+)B(\tau',\tau)$	$D_{\leftarrow}(t) = \int_{-\infty}^{t} dt' A^<(t',t')B^r(t,t')$ $D_{\rightarrow}(t) = \int_{-\infty}^{t} dt' A^<(t',t')B^a(t',t)$
$C_{\Leftarrow}(\tau,\tau') = A(\tau,\tau')B(\tau,\tau')$	$C^{\gtrless}_{\Leftarrow}(t,t') = A^{\gtrless}(t,t')B^{\gtrless}(t,t')$ $C^{r}_{\Leftarrow}(t,t') = A^<(t,t')B^r(t,t') + A^r(t,t')B^r(t,t') + A^r(t,t')B^<(t,t')$ $C^{a}_{\Leftarrow}(t,t') = A^<(t,t')B^a(t,t') - A^a(t,t')B^a(t,t') + A^a(t,t')B^<(t,t')$
$C_{\leftrightarrows}(\tau,\tau') = A(\tau,\tau')B(\tau',\tau)$	$C^{\gtrless}_{\leftrightarrows}(t,t') = A^{\gtrless}(t,t')B^{\lessgtr}(t',t)$ $C^{r(a)}_{\leftrightarrows}(t,t') = A^<(t,t')B^{a(r)}(t',t) + A^{r(a)}(t,t')B^<(t',t)$

Table 2.1.: *Summary of the Langreth rules derived in section 2.3.*

2.4. Equations of motion

In the previous sections we have provided the theory which is needed to solve a non-equilibrium problem, that is the Dyson equation and the Langreth rules for analytical continuation. For some practical calculations it however turns out to be more advantageous to solve a differential[8] equation instead of an integral equation. It is thus the object of this section to derive the equations of motion, usually called the kinetic equations, for the various relevant Green's functions introduced in the previous sections.

In deriving the equations of motion we use the same approach as in the above sections, namely first derive in contour time and then afterward take the real time components one may need. We start out by defining two operators which are used to denote differentiation with respect to the two contour times τ and τ', these are

$$(\overrightarrow{\boldsymbol{G}}^0(\tau))^{-1} = i\hbar\partial_\tau \boldsymbol{I} - \boldsymbol{H}_0(\tau) \Rightarrow (\overrightarrow{\boldsymbol{G}}^0(\tau))^{-1}_{\alpha\beta} = (i\hbar\partial_\tau - \hbar\omega_\alpha)\delta_{\alpha\beta}, \tag{2.38}$$

for the first time argument and

$$(\overleftarrow{\boldsymbol{G}}^0(\tau'))^{-1} = -i\hbar\partial_{\tau'} \boldsymbol{I} - \boldsymbol{H}_0(\tau') \Rightarrow (\overleftarrow{\boldsymbol{G}}^0(\tau'))^{-1}_{\alpha\beta} = (-i\hbar\partial_{\tau'} - \hbar\omega_\beta)\delta_{\alpha\beta}, \tag{2.39}$$

for the second time argument[9], where $\boldsymbol{I}$ is the identity matrix. The arrows indicate on what side they operate, e.g. $(\overrightarrow{\boldsymbol{G}}^0(\tau))^{-1}$ operate on the left side. Defining contour time differentiation this way gives the following nice property when operating on $\boldsymbol{G}^0(\tau,\tau')$

$$(\overrightarrow{\boldsymbol{G}}^0(\tau))^{-1}\boldsymbol{G}^0(\tau,\tau') = \boldsymbol{G}^0(\tau,\tau')(\overleftarrow{\boldsymbol{G}}^0(\tau'))^{-1} = \delta(\tau-\tau')\boldsymbol{I}, \tag{2.40}$$

where $\delta(\tau-\tau')$ is the contour delta function. The real time properties of this function can be determined by performing actual real time differentiations on the free Green's functions of the system, which are known, and we obtain

$$(\delta(\tau-\tau'))^{\gtrless} = 0, \quad (\delta(\tau-\tau'))^r = \delta(t-t'), \tag{2.41}$$

[8] We do not obtain a ordinary differential equation, but rather a integro-differential equation containing memory integrals. One time integral in the Dyson equation is exchanged for a time derivative.

[9] Note that the notation $\boldsymbol{H}_0(\tau)$ is not meant to signify any time-dependence in H_0, but is merely meant as a notational device to indicate that one should take the H_0 energy corresponding to the first or second time argument. Also note that eqs. (2.38) and (2.39) assumes H_0 to be written in diagonal form.

for the greater/lesser and retarded parts, respectively. For notational and interpretive purposes we introduce the singular self-energy in the following way

$$\boldsymbol{\Sigma}^{\mathrm{s}}(\tau) = \boldsymbol{U}(\tau) + (\text{single time parts of } \boldsymbol{\Sigma}). \tag{2.42}$$

It is called singular as it can formally be multiplied by a delta function, $\boldsymbol{\Sigma}^{\mathrm{s}}(\tau_1)\delta(\tau_1 - \tau_2)$, and put under the double integral along with the two-time self-energy and hence would appear as a singular contribution to this. A well known single-time self-energy is the Hartree-Fock self-energy arising from electron-electron interaction, which acts as a instantaneous renormalization to the single-particle energies and external potential.

To get the equation of motion in the first time argument, τ, the Dyson equation in the form of eq. (2.23) is used

$$\boldsymbol{G}(\tau,\tau') = \boldsymbol{G}^0(\tau,\tau') + \int_C d\tau_1 \boldsymbol{G}^0(\tau,\tau_1)\boldsymbol{\Sigma}^{\mathrm{s}}(\tau_1)\boldsymbol{G}(\tau_1,\tau') + \int_C d\tau_2 d\tau_1 \boldsymbol{G}^0(\tau,\tau_2)\boldsymbol{\Sigma}(\tau_2,\tau_1)\boldsymbol{G}(\tau_1,\tau'),$$

which we now let $(\overrightarrow{\boldsymbol{G}}^0(\tau))^{-1}$, eq. (2.38), operate on and on applying eq. (2.40) we obtain

$$(\overrightarrow{\boldsymbol{G}}^0(\tau))^{-1}\boldsymbol{G}(\tau,\tau') = \delta(\tau-\tau')\boldsymbol{I} + \boldsymbol{\Sigma}^{\mathrm{s}}(\tau)\boldsymbol{G}(\tau,\tau') + \int_C d\tau_1 \boldsymbol{\Sigma}(\tau,\tau_1)\boldsymbol{G}(\tau_1,\tau'). \tag{2.43}$$

This is the differential form of the Dyson equation. To get the equation of motion in second time argument, τ', we reiterate the Dyson equation to the following form, where $\boldsymbol{G}$ and $\boldsymbol{G}^0$ has switched places under the integrals,

$$\boldsymbol{G}(\tau,\tau') = \boldsymbol{G}^0(\tau,\tau') + \int_C d\tau_1 \boldsymbol{G}(\tau,\tau_1)\boldsymbol{\Sigma}^{\mathrm{s}}(\tau_1)\boldsymbol{G}^0(\tau_1,\tau') + \int_C d\tau_2 d\tau_1 \boldsymbol{G}(\tau,\tau_2)\boldsymbol{\Sigma}(\tau_2,\tau_1)\boldsymbol{G}^0(\tau_1,\tau').$$

Operating with $(\overleftarrow{\boldsymbol{G}}^0(\tau'))^{-1}$, eq. (2.39), on this Dyson equation yields the equation of motion in τ'

$$\boldsymbol{G}(\tau,\tau')(\overleftarrow{\boldsymbol{G}}^0(\tau'))^{-1} = \delta(\tau-\tau')\boldsymbol{I} + \boldsymbol{G}(\tau,\tau')\boldsymbol{\Sigma}^{\mathrm{s}}(\tau') + \int_C d\tau_1 \boldsymbol{G}(\tau,\tau_1)\boldsymbol{\Sigma}(\tau_1,\tau'). \tag{2.44}$$

Having determined the equations of motion for the contour ordered Green's function, the Langreth rules presented in section 2.3 can be used to acquire real time equations, and with the appropriate initial conditions the relevant Green's functions can be calculated in the (t,t')-plane. However, in order to compare with experimental results or apply certain approximation schemes (or both), it is often advantageous to transform to another set of time variables, instead of the original ones. For this purpose it is customary to form the sum and difference of the two governing equations, eqs. (2.43) and (2.44), resulting in the following equations

$$\begin{aligned} i\hbar(\partial_\tau \mp \partial_{\tau'})\boldsymbol{G}(\tau,\tau') - [\boldsymbol{H}_0(\tau)\boldsymbol{G}(\tau,\tau') \pm \boldsymbol{G}(\tau,\tau')\boldsymbol{H}_0(\tau')] &= (1\pm 1)\delta(\tau-\tau')\boldsymbol{I} \\ &+ \boldsymbol{\Sigma}^{\mathrm{s}}(\tau)\boldsymbol{G}(\tau,\tau') \pm \boldsymbol{G}(\tau,\tau')\boldsymbol{\Sigma}^{\mathrm{s}}(\tau') + \int_C d\tau_1 \left[\boldsymbol{\Sigma}(\tau,\tau_1)\boldsymbol{G}(\tau_1,\tau') \pm \boldsymbol{G}(\tau,\tau_1)\boldsymbol{\Sigma}(\tau_1,\tau')\right]. \end{aligned}$$

Using the Langreth rules, eqs. (2.35) and (2.41), we obtain two equations of motion for the greater/lesser Green's function

$$\begin{aligned} i\hbar(\partial_t \mp \partial_{t'})\boldsymbol{G}^{\gtrless}(t,t') &= [\boldsymbol{H}_0(t) + \boldsymbol{\Sigma}^{\mathrm{s}}(t)]\,\boldsymbol{G}^{\gtrless}(t,t') \pm \boldsymbol{G}^{\gtrless}(t,t')\,[\boldsymbol{H}_0(t') + \boldsymbol{\Sigma}^{\mathrm{s}}(t')] \\ &+ \int_{-\infty}^{\infty} dt_1 \left[\boldsymbol{\Sigma}^r(t,t_1)\boldsymbol{G}^{\gtrless}(t_1,t') + \boldsymbol{\Sigma}^{\gtrless}(t,t_1)\boldsymbol{G}^a(t_1,t') \pm \boldsymbol{G}^r(t,t_1)\boldsymbol{\Sigma}^{\gtrless}(t_1,t') \pm \boldsymbol{G}^{\gtrless}(t,t_1)\boldsymbol{\Sigma}^a(t_1,t')\right], \end{aligned} \tag{2.45}$$

and likewise, using eqs. (2.36) and (2.41), equations for the retarded Green's function can be produced

$$\begin{aligned} i\hbar(\partial_t \mp \partial_{t'})\boldsymbol{G}^r(t,t') &= (1\pm 1)\delta(t-t')\boldsymbol{I} + [\boldsymbol{H}_0(t) + \boldsymbol{\Sigma}^{\mathrm{s}}(t)]\,\boldsymbol{G}^r(t,t') \pm \boldsymbol{G}^r(t,t')\,[\boldsymbol{H}_0(t') + \boldsymbol{\Sigma}^{\mathrm{s}}(t')] \\ &+ \int_{-\infty}^{\infty} dt_1 \left[\boldsymbol{\Sigma}^r(t,t_1)\boldsymbol{G}^r(t_1,t') \pm \boldsymbol{G}^r(t,t_1)\boldsymbol{\Sigma}^r(t_1,t')\right]. \end{aligned} \tag{2.46}$$

The new set of time variables most practical for our purposes are given by the transformations

$$\tilde{t} = t, \quad \tau = t - t' \quad \Rightarrow \quad \partial_t = \partial_{\tilde{t}} + \partial_\tau, \quad \partial_{t'} = -\partial_\tau, \tag{2.47}$$

where the difference or delay time[10] τ measures the distance from the time diagonal, and for the case $\tau = 0$ the absolute time $\tilde{t}$ sets the position on the time diagonal. Due to the many-body interactions, the Green's functions are expected to decay when moving away from the time diagonal, making this specific set of time variables natural to employ.

The equation of motion for the greater/lesser Green's function with respect to $\tilde{t}$ is found by taking the difference part of eq. (2.45) and applying the transformation eq. (2.47)

$$\begin{aligned} i\hbar\partial_t \boldsymbol{G}^{\gtrless}(t, t-\tau) &= [\boldsymbol{H}_0(t) + \boldsymbol{\Sigma}^{\mathrm{s}}(t)]\, \boldsymbol{G}^{\gtrless}(t, t-\tau) - \boldsymbol{G}^{\gtrless}(t, t-\tau)\, [\boldsymbol{H}_0(t-\tau) + \boldsymbol{\Sigma}^{\mathrm{s}}(t-\tau)] \\ &+ \int_{-\infty}^{\infty} dt_1 \left[\boldsymbol{\Sigma}^r(t, t_1)\boldsymbol{G}^{\gtrless}(t_1, t-\tau) + \boldsymbol{\Sigma}^{\gtrless}(t, t_1)\boldsymbol{G}^a(t_1, t-\tau) - \boldsymbol{G}^r(t, t_1)\boldsymbol{\Sigma}^{\gtrless}(t_1, t-\tau) - \boldsymbol{G}^{\gtrless}(t, t_1)\boldsymbol{\Sigma}^a(t_1, t-\tau) \right], \end{aligned} \tag{2.48}$$

where we have relabeled $\tilde{t} \to t$ to lighten the notation. The new set of times (t, τ) defined in eq. (2.47) appear in eq. (2.48) merely as placeholders for the old set (t, t') and no true mathematical transformation has been applied. Whether the full transformation should be performed, also including the time integral, depends on what further approximations that are to be made and the numerical solution scheme. For more on transformation of the time integral see e.g. [29, p. 357]. For certain approximation schemes it advantageous to replace all retarded and advanced quantities with their greater and lesser counterparts, this is done using eqs. (2.24c), (2.24d), and (2.30), resulting in

$$\begin{aligned} i\hbar\partial_t \boldsymbol{G}^{\gtrless}(t, t-\tau) &= [\boldsymbol{H}_0(t) + \boldsymbol{\Sigma}^{\mathrm{s}}(t)]\, \boldsymbol{G}^{\gtrless}(t, t-\tau) - \boldsymbol{G}^{\gtrless}(t, t-\tau)\, [\boldsymbol{H}_0(t-\tau) + \boldsymbol{\Sigma}^{\mathrm{s}}(t-\tau)] \\ &+ \int_{-\infty}^{t} dt_1 \left[\left\{ \boldsymbol{\Sigma}^{>}(t, t_1) - \boldsymbol{\Sigma}^{<}(t, t_1) \right\} \boldsymbol{G}^{\gtrless}(t_1, t-\tau) - \left\{ \boldsymbol{G}^{>}(t, t_1) - \boldsymbol{G}^{<}(t, t_1) \right\} \boldsymbol{\Sigma}^{\gtrless}(t_1, t-\tau) \right] \\ &- \int_{-\infty}^{t-\tau} dt_1 \left[\boldsymbol{\Sigma}^{\gtrless}(t, t_1) \left\{ \boldsymbol{G}^{>}(t_1, t-\tau) - \boldsymbol{G}^{<}(t_1, t-\tau) \right\} - \boldsymbol{G}^{\gtrless}(t, t_1) \left\{ \boldsymbol{\Sigma}^{>}(t_1, t-\tau) - \boldsymbol{\Sigma}^{<}(t_1, t-\tau) \right\} \right], \end{aligned} \tag{2.49}$$

where the step function in the definition of the retarded and advanced functions, have been used on the upper limit in the time integrals. With reference to the discussion below eq. (2.47) these equation take care of the propagation along the time diagonal for the greater/lesser Green's function. A particular important special case of eqs. (2.48) and (2.49) is the equal-time limit, $\tau = 0$, as the equal-time lesser Green's function is proportional to the single-particle density matrix, see section 2.1. Taking this limit in eq. (2.49) for the lesser Green's function we obtain the following very important equation

$$\begin{aligned} i\hbar\partial_t \boldsymbol{G}^{<}(t, t) &= [\boldsymbol{H}_0(t) + \boldsymbol{\Sigma}^{\mathrm{s}}(t)]\, \boldsymbol{G}^{<}(t, t) - \boldsymbol{G}^{<}(t, t)\, [\boldsymbol{H}_0(t) + \boldsymbol{\Sigma}^{\mathrm{s}}(t)] \\ &+ \int_{-\infty}^{t} dt_1 \left[\boldsymbol{\Sigma}^{>}(t, t_1)\boldsymbol{G}^{<}(t_1, t) - \boldsymbol{\Sigma}^{<}(t, t_1)\boldsymbol{G}^{>}(t_1, t) - \boldsymbol{G}^{>}(t, t_1)\boldsymbol{\Sigma}^{<}(t_1, t) + \boldsymbol{G}^{<}(t, t_1)\boldsymbol{\Sigma}^{>}(t_1, t) \right], \end{aligned} \tag{2.50}$$

where several terms under the time integral has canceled compared to eq. (2.49). Even though we have put $\tau = 0$ we do not have a closed set of equations for the equal-time lesser[11] Green's function. This is due to the fact that the time integral still goes outside the time diagonal, and hence in general we still need the lesser Green's function in the full two-time plane. There exists however an approximation scheme which to some degree can circumvent this problem, for which the specific form of eq. (2.50) (only

[10] This time variable should not be confused with the contour time, which uses the same symbol, and as the relative time only is used in connection with real time Green's functions the notation should be unambiguous.

[11] The equal-time greater is related to the equal-time lesser through eq. (2.31), and therefore only the lesser needs to be considered.

greater and lesser quantities occurring) is particularly useful. The scheme is known as the Generalized Kadanoff-Baym Ansatz (GKBA) and is treated in more detail in section 2.5. The equation of motion with respect to τ is found by simply taking the lesser component of eq. (2.44) and applying the transformation eq. (2.47)

$$i\hbar\partial_\tau \boldsymbol{G}^{\gtrless}(t,t-\tau) = \boldsymbol{G}^{\gtrless}(t,t-\tau)\left[\boldsymbol{H}_0(t-\tau)+\boldsymbol{\Sigma}^{\mathrm{s}}(t-\tau)\right] + \int_{-\infty}^{\infty} dt_1 \left[\boldsymbol{G}^r(t,t_1)\boldsymbol{\Sigma}^{\gtrless}(t_1,t-\tau)+\boldsymbol{G}^{\gtrless}(t,t_1)\boldsymbol{\Sigma}^a(t_1,t-\tau)\right],$$

and further replacing all retarded and advanced functions with greater and lesser ones we get

$$\begin{aligned} i\hbar\partial_\tau \boldsymbol{G}^{\gtrless}(t,t-\tau) &= \boldsymbol{G}^{\gtrless}(t,t-\tau)\left[\boldsymbol{H}_0(t-\tau)+\boldsymbol{\Sigma}^{\mathrm{s}}(t-\tau)\right] \\ &+ \int_{-\infty}^{t} dt_1 \left[\left\{\boldsymbol{G}^{>}(t,t_1)-\boldsymbol{G}^{<}(t,t_1)\right\}\boldsymbol{\Sigma}^{\gtrless}(t_1,t-\tau)\right] \\ &- \int_{-\infty}^{t-\tau} dt_1 \left[\boldsymbol{G}^{\gtrless}(t,t_1)\left\{\boldsymbol{\Sigma}^{>}(t_1,t-\tau)-\boldsymbol{\Sigma}^{<}(t_1,t-\tau)\right\}\right]. \end{aligned}$$

As for the t equation which version to use, depends on what approximations schemes that are to be employed. This equation can be interpreted as propagating the greater/lesser Green's function away from the time diagonal. Applying essentially the same steps with eq. (2.46), the equations of motion for the retarded Green's function can be found. The t equation becomes

$$i\hbar\partial_t \boldsymbol{G}^r(t,t-\tau) = \left[\boldsymbol{H}_0(t)+\boldsymbol{\Sigma}^{\mathrm{s}}(t)\right]\boldsymbol{G}^r(t,t-\tau) - \boldsymbol{G}^r(t,t-\tau)\left[\boldsymbol{H}_0(t-\tau)+\boldsymbol{\Sigma}^{\mathrm{s}}(t-\tau)\right] + \int_{-\infty}^{\infty} dt_1 \left[\boldsymbol{\Sigma}^r(t,t_1)\boldsymbol{G}^r(t_1,t-\tau)-\boldsymbol{G}^r(t,t_1)\boldsymbol{\Sigma}^r(t_1,t-\tau)\right],$$

while the τ equation becomes

$$i\hbar\partial_\tau \boldsymbol{G}^r(t,t-\tau) = \delta(\tau)\boldsymbol{I} + \boldsymbol{G}^r(t,t-\tau)\left[\boldsymbol{H}_0(t-\tau)+\boldsymbol{\Sigma}^{\mathrm{s}}(t-\tau)\right] + \int_{-\infty}^{\infty} dt_1 \boldsymbol{G}^r(t,t_1)\boldsymbol{\Sigma}^r(t_1,t-\tau). \tag{2.51}$$

It should be noted that for both the equations of motion for the retarded Green's function, the infinite integrals can be reduced to finite limits as $\int_{-\infty}^{\infty} dt \to \int_{t-\tau}^{t} dt$. For reasons that will be elaborated in section 5.4.2 only the equation of motion in t is needed to cover the entire two-time plane, assuming that the solution is known in a sufficiently wide strip around the time diagonal up to some t. It is natural to obtain the Green's functions on this strip in equilibrium, where they only depend in the difference time τ, see section 5.3, and hence only the equations of motion in τ will be needed. Furthermore, due to the symmetry relations eqs. (2.28) and (2.33) only two of the four Green's functions are independent, and one is free to choose these according to what is most appropriate in the present situation. Previous studies have employed the lesser/retarded Green's functions [37, 38] and greater/lesser Green's functions [39].

The equations derived in this section will be applied to more specific situations in chapter 5.

2.5. Generalized Kadanoff-Baym Ansatz

As mentioned in the previous section the equation of motion for the equal-time lesser Green's function, eq. (2.50), is not a closed equation as the scattering integral requires the values of the Green's function beyond the time diagonal. In many situations the full two-time lesser Green's function is not needed, as only the equal-time lesser Green's function is required to determine expectation values, see eq. (2.3). It would therefore be nice if some reasonable approximation could allow us to avoid dealing explicitly with

the full two-time plane. Such an approximation does fortunately exists and is known as the Generalized Kadanoff-Baym Ansatz (GKBA) [40].

The basis for obtaining the GKBA is an exact relation obeyed by the greater/lesser Green's function, which is [35]

$$\begin{aligned}\boldsymbol{G}^{\gtrless}(t,t') &= i\hbar\left[\boldsymbol{G}^{r}(t,t')\boldsymbol{G}^{\gtrless}(t',t') - \boldsymbol{G}^{\gtrless}(t,t)\boldsymbol{G}^{a}(t,t')\right] \\ &+ \theta(t-t')\int_{t'}^{t} dt_1 \int_{-\infty}^{t'} dt_2 \boldsymbol{G}^{r}(t,t_1)\left[\boldsymbol{\Sigma}^{r}(t_1,t_2)\boldsymbol{G}^{\gtrless}(t_2,t') + \boldsymbol{\Sigma}^{\gtrless}(t_1,t_2)\boldsymbol{G}^{a}(t_2,t')\right] \\ &+ \theta(t'-t)\int_{t}^{t'} dt_1 \int_{-\infty}^{t} dt_2 \left[\boldsymbol{G}^{\gtrless}(t,t_2)\boldsymbol{\Sigma}^{a}(t_2,t_1) + \boldsymbol{G}^{r}(t,t_2)\boldsymbol{\Sigma}^{\gtrless}(t_2,t_1)\right]\boldsymbol{G}^{a}(t_1,t'). \quad (2.52)\end{aligned}$$

What should be noted about this relation is that the first term on the RHS contains only equal-time greater/lesser Green's functions, multiplied by two-time retarded/advanced Green's functions. The full two-time greater/lesser Green's functions only enter in the more complicated double time integrals on the second and third lines. The GKBA consists of neglecting the second and third lines containing the two-time greater/lesser Green's functions, after which one obtains

$$\boldsymbol{G}^{\gtrless}(t,t') = i\hbar\left[\boldsymbol{G}^{r}(t,t')\boldsymbol{G}^{\gtrless}(t',t') - \boldsymbol{G}^{\gtrless}(t,t)\boldsymbol{G}^{a}(t,t')\right] = \begin{cases} i\hbar\boldsymbol{G}^{r}(t,t')\boldsymbol{G}^{\gtrless}(t',t'), & t > t' \\ -i\hbar\boldsymbol{G}^{\gtrless}(t,t)\boldsymbol{G}^{a}(t,t'), & t' > t \end{cases} \quad (2.53)$$

This now allows one to form a closed set of equations in the equal-time lesser Green's function through the use of the equal-time identity eq. (2.31), that can be written in the following matrix form

$$\boldsymbol{G}^{>}(t,t) = \boldsymbol{G}^{<}(t,t) - i\hbar^{-1}\boldsymbol{I}, \quad (2.54)$$

All this assumes that the retarded and advanced Green's functions are somehow known quantities, which in general they are not. The range of validity of the GKBA is by no means fully understood in a rigorous sense [26, p. 95], but it is possible to give a simple naive justification for its use which we will briefly do. The exact relation eq. (2.52) can be used to generate an expansion to arbitrarily high order in the self-energy, of the two-time greater/lesser Green's function in terms of the equal-time greater/lesser Green's function. If we then assume that the self-energy contains some small parameter, it makes sense to truncate this series at some point, where the GKBA is the lowest order approximation of this expansion. Thus we can expect the GKBA to yield reasonable results in the limit of a weak coupling self-energy, which has indeed been verified numerically for a few specific systems [37, 38].

Up to now we have assumed that the retarded and advanced Green's functions appearing in the GKBA were known, which of course is not true and they represent another issue when applying the GKBA. In the GKBA these appear in their full two-time non-equilibrium form, and as such obey their own two-time Dyson equations. However, if these Dyson equations were to solved there would be no idea in applying the GKBA in the first place, as presumably no computationally advantage would be obtained. We therefore have to find an appropriate approximation to the spectral Green's functions, that still yields satisfactory results. The simplest choice is to use the free Green's functions of the system as these are always known on the onset. The free Green's functions do however not contain any form of decay and will therefore often yield incorrect or even unphysical results. Another approach that has been applied successfully in the literature [41, 42] is to employ the equilibrium spectral Green's functions of the system. These will contain the renormalized single-particle properties including both energy renormalizations and finite lifetimes, appropriate for the given system. We have followed this path in all uses of the GKBA in this thesis.

If for some reason, either exactly or approximately, we can argue that only the diagonal elements of the spectral Green's functions are significant, the sums implied in the matrix form of eq. (2.53) reduce to a

single term and get the following simpler version of the GKBA

$$G^{\gtrless}_{\alpha\beta}(t,t') = i\hbar\left[G^{r}_{\alpha\alpha}(t,t')G^{\gtrless}_{\alpha\beta}(t',t') - G^{\gtrless}_{\alpha\beta}(t,t)G^{a}_{\beta\beta}(t,t')\right] = \begin{cases} i\hbar G^{r}_{\alpha\alpha}(t,t')G^{\gtrless}_{\alpha\beta}(t',t'), & t > t' \\ -i\hbar G^{\gtrless}_{\alpha\beta}(t,t)G^{a}_{\beta\beta}(t,t'), & t' > t \end{cases} \tag{2.55}$$

which will be employed throughout this thesis. For further discussion of the GKBA see e.g. [31, pp. 288-291] and [32, pp. 44-46].

2.6. Summary

In this chapter we have given a brief introduction the non-equilibrium Green's function formalism, which will be the main theoretical tool in the rest of the thesis. We started out by showing how setting up the Heisenberg equation of motion for an electronic operator, led to an infinite hierarchy of coupled equations, yielding a problem that even in principle is unsolvable. The occurrence of this infinite set of equations is often referred to as the many-body hierarchy problem. In order to tackle the hierarchy problem, we introduced the contour ordered Green's function, for which we formulated an integral equation, known as the Dyson equation, written in terms of the so-called self-energy. Obtaining the Dyson equation is a huge achievement, as it allows one solve parts of the problem to infinite order. To make the theory more practical we further introduced the real time Green's functions, in terms of which the final governing equations were formulated. In the last section we briefly discussed an important approximation scheme known as the GKBA, which will be applied throughout the thesis.

3. Fundamental Hamiltonians

3.1. Introduction

In this chapter we will deal with the formulation of the general form of the Hamiltonian operator entering the Schrödinger equation, eq. (2.1). The motivation is to gain an understanding of the origin, and a general overview of the many different Hamiltonians that appear in many-body physics. This is important in order to know the range of validity of the various Hamiltonians, but also to be sure that one deals with a consistent set operators. Even though we will attempt to make the exposition as general as possible, we should emphasize that the theory is developed for a solid-state system, more specifically a semiconductor heterostructure, which will sometimes be (implicitly) assumed.

3.2. Hamiltonians

In this section we derive the Hamiltonian for the system described in chapter 1. We start by writing down the general Hamiltonian for a system of charged particles interacting with a classical and quantized electromagnetic field[1]. Using the Coulomb gauge, $\boldsymbol{\nabla} \cdot \boldsymbol{A}(\boldsymbol{r}, t) = 0$ and in the Schrödinger picture the Hamiltonian reads

$$H(\{\boldsymbol{r}_i\}) = \sum_i \frac{1}{2m_i} \left(\boldsymbol{p}_i - q_i \boldsymbol{A}(\boldsymbol{r}_i, t)\right)^2 + \sum_{i<j} \frac{q_i q_j}{4\pi\varepsilon} \frac{1}{|\boldsymbol{r}_i - \boldsymbol{r}_j|} + \frac{1}{2} \int d\boldsymbol{r} \left(\varepsilon |\boldsymbol{E}_{\mathrm{T}}(\boldsymbol{r})|^2 + \frac{1}{\mu_0} |\boldsymbol{B}(\boldsymbol{r})|^2\right). \tag{3.1}$$

The indexes i and j run over all valence electrons and ions of the system, $\boldsymbol{p}_i = -i\hbar\boldsymbol{\nabla}_i$ is the momentum operator, q_i is the charge, and m_i is the mass of the particles. For notational simplicity we assume that the i and j indexes also contain a spin index. The first term in eq. (3.1) describes the kinetic energy of the particles and the interaction with the vector potential $\boldsymbol{A}(\boldsymbol{r}, t)$. We will be considering interactions with both classical and quantized electromagnetic fields, the vector potential must be a sum of these and it is therefore written as $\boldsymbol{A}(\boldsymbol{r}, t) = \boldsymbol{A}_{\mathrm{cl}}(\boldsymbol{r}, t) + \boldsymbol{A}_{\mathrm{qm}}(\boldsymbol{r})$. In the Coulomb gauge the transverse electric and magnetic fields are obtained from the vector potential through the following relations

$$\boldsymbol{B}(\boldsymbol{r}, t) = \boldsymbol{\nabla} \times \boldsymbol{A}(\boldsymbol{r}, t), \tag{3.2}$$

$$\boldsymbol{E}_{\mathrm{T}}(\boldsymbol{r}, t) = -\partial_t \boldsymbol{A}(\boldsymbol{r}, t), \tag{3.3}$$

for these relations to hold for the quantized fields, they must be written in the Heisenberg picture where they are time-dependent. The second term in eq. (3.1) describes the Coulomb interaction between the various charged particles, which is mediated by the longitudinal component of the electric field, $\boldsymbol{E}_{\mathrm{L}}(\boldsymbol{r}) = -\boldsymbol{\nabla}\varphi(\boldsymbol{r})$, where $\varphi(\boldsymbol{r})$ is the scalar potential. Note that the vacuum permittivity, ε_0, has been replaced by a background dielectric constant, $\varepsilon = \varepsilon_{\mathrm{r}}\varepsilon_0$, where ε_{r} is the relative dielectric constant. The background dielectric constant contains non-resonant contributions to screening [31, p. 44] and it has to replace ε_0 everywhere as it is originates from the Maxwell equations. The last term in eq. (3.1) describes the energy of the quantized transverse electromagnetic fields, the energy of the classical field is neglected [44].

The two first terms in eq. (3.1) are by far the most difficult and a few approximations and rearrangements are needed in order to proceed. Due to the large mass of the ions, compared to the electrons, and the

[1] See for example sec. 2.2 in [31], sec. 1.5 in [24], or sec. 4.8 in [43].

relatively weak electromagnetic fields we are considering, the response of the ions to the fields will be much smaller than that of the electrons. This means that we can neglect the interaction between the ions and the photons, hence the first term becomes

$$\sum_i \frac{1}{2m_i}\left(\boldsymbol{p}_i - q_i\boldsymbol{A}(\boldsymbol{r}_i,t)\right)^2 \approx \sum_{\substack{\text{electrons}\\ i}} \frac{1}{2m}\left(\boldsymbol{p}_i + e\boldsymbol{A}(\boldsymbol{r}_i,t)\right)^2 + \sum_{\substack{\text{ions}\\ j}} \frac{\boldsymbol{p}_j^2}{2m_j}, \quad q_{\text{electron}} = -e, \tag{3.4}$$

which is a sum of the electrons kinetic energy and interaction with the fields and the kinetic energy of the ions. Another simplification becomes apparent if we expand the squared parentheses for the electrons

$$\begin{aligned}\sum_{\substack{\text{electrons}\\ i}} \frac{1}{2m}\left(\boldsymbol{p}_i + e\boldsymbol{A}(\boldsymbol{r}_i,t)\right)^2 &= \sum_{\substack{\text{electrons}\\ i}} \frac{1}{2m}\left[\boldsymbol{p}_i^2 + e\left[\boldsymbol{p}_i\cdot\boldsymbol{A}(\boldsymbol{r}_i,t) + \boldsymbol{A}(\boldsymbol{r}_i,t)\cdot\boldsymbol{p}_i\right] + e^2\boldsymbol{A}^2(\boldsymbol{r}_i,t)\right]\\ &\approx \sum_{\substack{\text{electrons}\\ i}} \left[\frac{\boldsymbol{p}_i^2}{2m} + \frac{e}{m}\boldsymbol{A}(\boldsymbol{r}_i,t)\cdot\boldsymbol{p}_i\right],\end{aligned} \tag{3.5}$$

where in the second line we have neglected the $\boldsymbol{A}^2$ term as it is assumed small[2] [44, p. 150] and further we have used the fact that[3] $[\boldsymbol{p}_i, \boldsymbol{A}(\boldsymbol{r}_i,t)] = 0$ to obtain the well known $\boldsymbol{A}\cdot\boldsymbol{p}$ interaction.

The Coulomb interaction, second term in eq. (3.1), between the charged particles, produces three qualitatively different interactions even though fundamentally they are all of a Coulombic nature. The three different combinations of the indexes i and j have been written out below for illustration

$$\sum_{i<j}\frac{q_iq_j}{4\pi\varepsilon}\frac{1}{|\boldsymbol{r}_i-\boldsymbol{r}_j|} = \underbrace{\frac{1}{2}\sum_{i\neq j}\frac{e^2}{4\pi\varepsilon}\frac{1}{|\boldsymbol{r}_i-\boldsymbol{r}_j|}}_{\{i,j\}=\{\text{e,e}\}} + \underbrace{\frac{1}{2}\sum_{i\neq j}\frac{q_iq_j}{4\pi\varepsilon}\frac{1}{|\boldsymbol{R}_i-\boldsymbol{R}_j|}}_{\{i,j\}=\{\text{ion,ion}\}} + \underbrace{\sum_{ij}\frac{(-e)q_j}{4\pi\varepsilon}\frac{1}{|\boldsymbol{r}_i-\boldsymbol{R}_j|}}_{\{i,j\}=\{\text{e,ion}\}}. \tag{3.6}$$

The first term is the usual electron-electron interaction, which will be kept in its present form. The second term is the interaction between the positively charged ions. As mentioned above, the ions are much heavier than the electrons and thus move much slower. This means that a full dynamical analysis is not necessary and further approximations will be performed on this term, discussed further in section 3.2.1. The third term involves the interaction between the electrons and ions. This term can be simplified considerably by first writing the ionic position vector as

$$\boldsymbol{R}_j = \boldsymbol{R}_j^{(0)} + \boldsymbol{u}_j, \tag{3.7}$$

where $\boldsymbol{R}_j^{(0)}$ is the equilibrium position of the ions, the static lattice, and $\boldsymbol{u}_j$ is the displacement from equilibrium. The approximation then consists of Taylor expanding the electron-ion interaction to first order in $\boldsymbol{u}_j$, which results in

$$\sum_{ij}\frac{(-e)q_j}{4\pi\varepsilon}\frac{1}{|\boldsymbol{r}_i-\boldsymbol{R}_j|} \approx \sum_{ij}\frac{(-e)q_j}{4\pi\varepsilon}\left(\frac{1}{|\boldsymbol{r}_i-\boldsymbol{R}_j^{(0)}|} - \boldsymbol{u}_j\cdot\boldsymbol{\nabla}_{\boldsymbol{r}_i}\left[\frac{1}{|\boldsymbol{r}_i-\boldsymbol{R}_j^{(0)}|}\right]\right), \tag{3.8}$$

notice that there is no factor 1/2 in front of the sum, as there is no double counting for the different particles. The zeroth order part of this expansion is the well known interaction between electrons and a static lattice, which for a single crystal resulting in Bloch states for the electrons. The first order term is what becomes the electron-phonon interaction after the field quantization has been performed, see section 3.2.2.

[2] In the context of single-photon sources the neglection the $\boldsymbol{A}^2$ term is well justified both for the quantized and classical case. For the quantized case the magnitude of $\boldsymbol{A}$ is obviously small as the goal is to produce a single photon. For the classical contribution, here the excitation pulse, we are in the extremely low excitation limit as ultimately we are only interested in the excitation of a single electron.

[3] The commutator between $\boldsymbol{p}$ and $\boldsymbol{A}$ is $[\boldsymbol{p},\boldsymbol{A}] = -i\hbar\boldsymbol{\nabla}\cdot\boldsymbol{A}$, which is zero in the Coulomb gauge. See p. 311 in [45].

This concludes the initial discussion of the Hamiltonian of the total system. In the following sections we will consider non-interacting and interacting parts of the Hamiltonian separately and perform the field quantization procedure, second quantization for the particles and actual field quantization for the ionic displacement field. The radiation field is already quantized. The field quantization procedure is discussed in detail in many textbooks, e.g. [24, 28, 31].

3.2.1. Non-interacting parts

In this section we will consider the non-interacting parts from the discussion of the Hamiltonian, eq. (3.1), in the previous section. It is important to specify what precisely is meant by a non-interacting Hamiltonian, as this forms the basis for the many-body perturbation theories we will apply, see chapter 2. A non-interacting Hamiltonian has no terms with products of more than two operators (often referred to as quadratic Hamiltonians and denoted H_0) and must be time-independent in the Schrödinger picture. Below we will go through the quadratic contributions from the three fields we are considering, namely the electronic, photonic, and phononic fields.

Electrons

The non-interacting contributions from the electrons are the kinetic energy, first term in eq. (3.5), and the interaction with the static lattice, first term in eq. (3.8)

$$H_{0,\mathrm{e}}(\{\boldsymbol{r}_i\}) = \sum_i \frac{\boldsymbol{p}_i^2}{2m} + \sum_{ij} \frac{(-e)q_j}{4\pi\varepsilon} \frac{1}{|\boldsymbol{r}_i - \boldsymbol{R}_j^{(0)}|} = \sum_i H_{0,\mathrm{e}}(\boldsymbol{r}_i).$$

The transition to the second quantization representation of the electronic field is done using the standard formulae

$$H_{0,\mathrm{e}} = \int d\boldsymbol{r} \psi^\dagger(\boldsymbol{r}) H_{0,\mathrm{e}}(\boldsymbol{r}) \psi(\boldsymbol{r}),$$

where $\psi(\boldsymbol{r}) = \sum_\nu \langle \boldsymbol{r}|\nu\rangle\, c_\nu$ is a field annihilation operator, written in a single-particle basis $\{|\nu\rangle\}$ which consists of spatial part $|\alpha\rangle$ and a spin part $|\sigma\rangle$, $|\nu\rangle = |\alpha\rangle \otimes |\sigma\rangle$. The real space/spin representation of $|\nu\rangle$ is given by $\langle \boldsymbol{r}|\nu\rangle = \phi_\alpha(\boldsymbol{r})\chi_\sigma$, where $\phi_\alpha(\boldsymbol{r})$ is the wave function of the electron in the spatial state α and χ_σ is a spin function. If we choose the eigenstates of $H_{0,\mathrm{e}}$ as the single-particle basis $\{|\nu\rangle\}$, we obtain a simple diagonal form of the quadratic contribution from the electrons

$$H_{0,\mathrm{e}} = \sum_\nu \hbar\omega_\nu c_\nu^\dagger c_\nu. \tag{3.9}$$

If the sum over the static ions runs over a single crystal, then the states $|\nu\rangle$ would become Bloch states producing the usual band structure energy diagrams. This is however not the case for the nanostructures we are considering. We use band gap bending to create the confining potentials for the electrons and holes, that make up the QD, and hence we do not have a single crystal and thus no pure Bloch states. Due to the large difference in length scales of the QDs and the lattice unit cells, it is fortunately possible to formulate an effective theory simplifying the calculation of the eigenstates of $H_{0,\mathrm{e}}$ immensely. We will employ this effective mass approach in later chapters, when specific structures are considered.

Photons

The quadratic contributions from the photons originate solely from the last term in eq. (3.1), the total energy of the transverse electromagnetic, or simply radiation, field

$$H_{0,\mathrm{rad}} = \frac{1}{2} \int d\boldsymbol{r} \left(\varepsilon |\boldsymbol{E}_\mathrm{T}(\boldsymbol{r})|^2 + \frac{1}{\mu_0} |\boldsymbol{B}(\boldsymbol{r})|^2 \right). \tag{3.10}$$

There exist several ways to quantize the radiation field, depending on what level of sophistication one may wish, all resulting in the same result. We will not go further into the quantization procedure, as this is standard textbook material, but simply proceed with the following[4] form of the transverse electric field

$$\boldsymbol{E}_{\mathrm{T}}(\boldsymbol{r}) = \sum_m \mathcal{E}_m (a_m^\dagger + a_m)\boldsymbol{u}_m(\boldsymbol{r}). \tag{3.11}$$

In the above the mode functions satisfy the orthonormality relation $\int d\boldsymbol{r}\boldsymbol{u}_m(\boldsymbol{r}) \cdot \boldsymbol{u}_{m'}(\boldsymbol{r}) = \delta_{m,m'}$ and $\mathcal{E}_m = (\frac{\hbar\omega_m}{2\varepsilon})^{1/2}$, where ω_m is the frequency of mode m. This choice of normalization means that the quantization volume, V, is contained in the mode functions and further these are real quantities found by solving the classical wave equation for the transverse electric field. The magnetic field can be obtained by combining eqs. (3.2) and (3.3) to $-\partial_t \boldsymbol{B}(\boldsymbol{r},t) = \boldsymbol{\nabla} \times \boldsymbol{E}_{\mathrm{T}}(\boldsymbol{r},t)$. Inserting the quantized radiation field into eq. (3.10) and performing the integral we get the following result

$$H_{0,\mathrm{rad}} = \sum_m \hbar\omega_m \left(a_m^\dagger a_m + \frac{1}{2} \right), \tag{3.12}$$

where the composite quantum number m contains the spatial, κ, and polarization, λ, quantum numbers.

Phonons

The non-interacting contributions from the phonons comes from the kinetic energy of the ions, second term in eq. (3.4), and the ion-ion Coulomb interaction, second term in eq. (3.6),

$$H_{0,\mathrm{ph}}(\{\boldsymbol{R}_j\}) = \sum_j \frac{\boldsymbol{p}_j^2}{2m_j} + \frac{1}{2}\sum_{i\neq j} \frac{q_i q_j}{4\pi\varepsilon} \frac{1}{|\boldsymbol{R}_i - \boldsymbol{R}_j|} \tag{3.13}$$

This interaction is in principle the same as the electron-electron interaction and hence should be treated as a pair interaction and not a quadratic term. The ions are however much heavier than the electrons and hence react much slower to external perturbations and further they are positioned in a periodic lattice only exhibiting small oscillations about their equilibrium positions. On this basis we will assume the usual harmonic approximation for the ions, where the interaction term in eq. (3.13) is Taylor expanded to second order in the ionic displacement vector, $\boldsymbol{u}_j$, see eq. (3.7). The coefficients in this second order expansion are elements in the so-called dynamical matrix of the ion system[5]. The determination of the dynamical matrix is in general a very complicated task. Values can be obtained for example by fitting models to experiments or calculated using first principles methods like Density Functional Theory. The remaining Hamiltonian in the harmonic approximation is then quantized according to the standard procedure[6], resulting in the following Hamiltonian for the phonons

$$H_{0,\mathrm{ph}} = \sum_\mu \hbar\omega_\mu \left(b_\mu^\dagger b_\mu + \frac{1}{2} \right). \tag{3.14}$$

The quantum number μ is composed of the quasi-momentum[7], $\boldsymbol{q}$, of the phonon and branch index, λ, which runs over the various optical and acoustic polarizations (TA, LA, TO, LO). It should be noted that formally the $\boldsymbol{q} = 0$ should be left out of the sum, as this term corresponds to a uniform translation of the entire crystal [24]. By writing the phonon Hamiltonian this way we assume bulk phonons, that is phonons which live in a system where the periodicity is given by the static lattice. Even though present day semiconductor

[4] For a derivation of this specific form of the quantized transverse electric field see chap. 19 in [45].
[5] See e.g. sec. 3.4 in [28] or sec. 11.2.1 in [31].
[6] See e.g. sec. 1.1 in [24].
[7] Restricted to the first Brillouin zone.

nanostructures are rarely pure bulk system, the system of Stranski-Krastanow grown QDs we are considering, can to a certain extent be considered as a bulk material from the phonons point of view. The WL is only a few nanometers thick and the QDs are very small compared to the rest of the structure, composed of the barrier material. We will therefore assume that the phonon modes existing in the barrier material will pervade the low band gap material justifying the use of bulk phonons.

3.2.2. Interacting parts

In this section we will consider the interaction terms in the Hamiltonian eq. (3.1). Interacting terms are Hamiltonians containing products of three or more operators, describing the interactions amongst the various fields. Interacting contributions are fundamentally different from the non-interacting ones discussed in the previous section. The reason for this is that the self-energy they give rise to contains infinitely many diagrams and hence has to be truncated and can therefore not be treated exactly. Below we will go trough the interactions between the various fields separately.

Electron-electron

The Coulomb interaction between the electrons is given by the first term in eq. (3.6)

$$H_{\mathrm{e-e}}(\{\boldsymbol{r}_i\}) = \frac{1}{2}\sum_{i\neq j}\frac{e^2}{4\pi\varepsilon}\frac{1}{|\boldsymbol{r}_i-\boldsymbol{r}_j|} = \frac{1}{2}\sum_{i\neq j}H_{\mathrm{e-e}}(\boldsymbol{r}_i,\boldsymbol{r}_j). \tag{3.15}$$

The second quantized form of the interaction is given by

$$H_{\mathrm{e-e}} = \frac{1}{2}\int d\boldsymbol{r}d\boldsymbol{r}'\psi^\dagger(\boldsymbol{r})\psi^\dagger(\boldsymbol{r}')H_{\mathrm{e-e}}(\boldsymbol{r},\boldsymbol{r}')\psi(\boldsymbol{r}')\psi(\boldsymbol{r}) \tag{3.16}$$

$$= \frac{1}{2}\sum_{\substack{\nu_1\nu_2\\ \nu_3\nu_4}} V_{\nu_4\nu_3,\nu_1\nu_2}c^\dagger_{\nu_4}c^\dagger_{\nu_3}c_{\nu_2}c_{\nu_1}, \tag{3.17}$$

where the interaction matrix element is given by

$$V_{\nu_4\nu_3,\nu_1\nu_2} = \langle\nu_4,\nu_3|H_{\mathrm{e-e}}|\nu_1,\nu_2\rangle = \int d\boldsymbol{r}d\boldsymbol{r}'\phi^*_{\alpha_4}(\boldsymbol{r})\phi^*_{\alpha_3}(\boldsymbol{r}')H_{\mathrm{e-e}}(\boldsymbol{r},\boldsymbol{r}')\phi_{\alpha_1}(\boldsymbol{r})\phi_{\alpha_2}(\boldsymbol{r}')\delta_{\sigma_4,\sigma_1}\delta_{\sigma_3,\sigma_2}, \tag{3.18}$$

the Kronecker deltas in the spin indexes appear as the Coulomb interaction is diagonal in spin. For illustration, a Coulomb scattering event, a single term in eq. (3.17), between two electrons is presented in figure 3.1.

Electron-photon

The interaction between the electrons and photons is given by the second term in eq. (3.5), the so-called $\boldsymbol{A}\cdot\boldsymbol{p}$ interaction,

$$\sum_i \frac{e}{m}\boldsymbol{A}(\boldsymbol{r}_i,t)\cdot\boldsymbol{p}_i,$$

We will start by applying the electric dipole approximation, which is commonly used in optics. The approximation consists of evaluating the space dependent radiation field, $\boldsymbol{A}(\boldsymbol{r},t)$, at the position of the electronic system it is interacting with [44]. This can be justified by considering the spatial part of the exponential function arising from a Fourier decomposition of $\boldsymbol{A}(\boldsymbol{r},t)$, $\exp(\boldsymbol{k}\cdot\boldsymbol{r})$. The function $\exp(\boldsymbol{k}\cdot\boldsymbol{r})$ can now be Taylor expanded to lowest order as we assume $\boldsymbol{k}\cdot\boldsymbol{r}\ll 1$, which is usually the case for optical

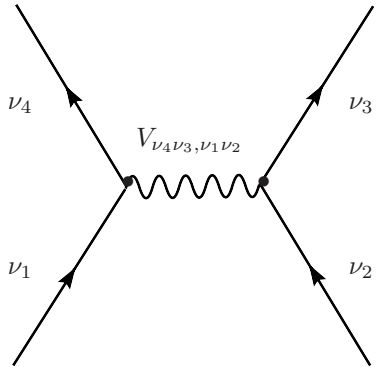

Figure 3.1.: *Diagrammatic illustration of an electron-electron Coulomb scattering event, a single term from eq.* (3.17)*, where two electrons in the states* ν_1 *and* ν_2 *are scattered to the states* ν_3 *and* ν_4 *with a scattering amplitude of* $V_{\nu_4\nu_3,\nu_1\nu_2}$*.*

wave vectors. If we further assume that the electrons are located near the origin, all electron positions can henceforth be evaluated at the origin in the above interaction term.

Next we will replace the $\boldsymbol{A}\cdot\boldsymbol{p}$ interaction with a $\boldsymbol{D}\cdot\boldsymbol{E}_{\mathrm{T}}$ form, where $\boldsymbol{D}=-e\boldsymbol{r}$ is the electron dipole operator, for practical reasons[8] in connection with the numerical solution later on. The transformation between the two interactions can be performed more or less rigorously. We choose a simple heuristic approach, carried out in appendix A.3, more advanced treatments can be found in [31, 43, 46]. According to this derivation we can write the interaction in the following way

$$-\sum_i \boldsymbol{D}_i\cdot\boldsymbol{E}_{\mathrm{T}}(0,t).$$

The total transverse electric field consists of a quantized and an externally applied classical part

$$\boldsymbol{E}_{\mathrm{T}}(0,t)=\boldsymbol{E}_{\mathrm{T,qm}}(0)+\boldsymbol{E}_{\mathrm{T,cl}}(0,t),$$

the resulting interaction Hamiltonians differ significantly and will therefore be treated separately. The quantized field is given by eq. (3.11), so that the field quantized form of the interaction becomes

$$\begin{aligned} H_{\mathrm{e-rad}} &= \int d\boldsymbol{r}\psi^\dagger(\boldsymbol{r})e\boldsymbol{r}\cdot\boldsymbol{E}_{\mathrm{T,qm}}(0)\psi(\boldsymbol{r}) \\ &= \sum_{\nu\nu' m}\hbar g^m_{\nu\nu'}c^\dagger_\nu c_{\nu'}(a^\dagger_m+a_m), \end{aligned} \tag{3.19}$$

where the coupling strength is given by

$$\hbar g^m_{\nu\nu'}=u_m(0)\mathcal{E}_m\int d\boldsymbol{r}\phi^*_\alpha(\boldsymbol{r})e\boldsymbol{r}\cdot\boldsymbol{e}_{\boldsymbol{u}_m}\phi_{\alpha'}(\boldsymbol{r})\delta_{\sigma,\sigma'}. \tag{3.20}$$

For an illustration of the emission and absorption processes originating from the interaction eq. (3.19) see figure 3.2(a) and (b), respectively. The interaction between the electrons and the classical field depends explicitly on time, even in the Schrödinger picture, and is therefore very special in many-body perturbation

[8] Keeping the electron-photon interaction on the $\boldsymbol{A}\cdot\boldsymbol{p}$ form causes no problems for the quantized field, but it is does however for the external classical excitation pulse. The excitation pulse is known in its electric field form, but in the $\boldsymbol{A}\cdot\boldsymbol{p}$ interaction the corresponding $\boldsymbol{A}$ should be calculated through the relation $\boldsymbol{E}_{\mathrm{T}}=-\partial_t\boldsymbol{A}$, which for most fields should be done numerically. The is indeed possible and the approach could be followed in situations where the $\boldsymbol{D}\cdot\boldsymbol{E}_{\mathrm{T}}$ interaction problematic, this is however not the case for our model. Also it is always advisable to work with gauge-independent physical fields, rather than the gauge-dependent potentials, see e.g. chapter 7 in [35] or the discussion [45, p. 359], especially when doing perturbation theory in the electromagnetic fields.

theory. The field quantized form of this semi-classical interaction is

$$\begin{aligned} U(t) &= \int d\boldsymbol{r}\psi^\dagger(\boldsymbol{r})e\boldsymbol{r}\cdot\boldsymbol{E}_{\mathrm{T,cl}}(0,t)\psi(\boldsymbol{r}) \\ &= \sum_{\nu\nu'} d_{\nu\nu'}E_{\mathrm{cl}}(t)c_\nu^\dagger c_{\nu'}, \end{aligned} \tag{3.21}$$

where the notation for the classical field has been simplified and the projected dipole matrix element is given by

$$d_{\nu\nu'} = \int d\boldsymbol{r}\phi_\alpha^*(\boldsymbol{r})e\boldsymbol{r}\cdot\boldsymbol{e}_{\boldsymbol{E}_{\mathrm{cl}}}\phi_{\alpha'}(\boldsymbol{r})\delta_{\sigma,\sigma'}. \tag{3.22}$$

Note that $U(t)$ has Heisenberg picture notation, but it is not in the Heisenberg picture. For an illustration of the electron scattering provided by this semi-classical interaction see figure 3.2(c).

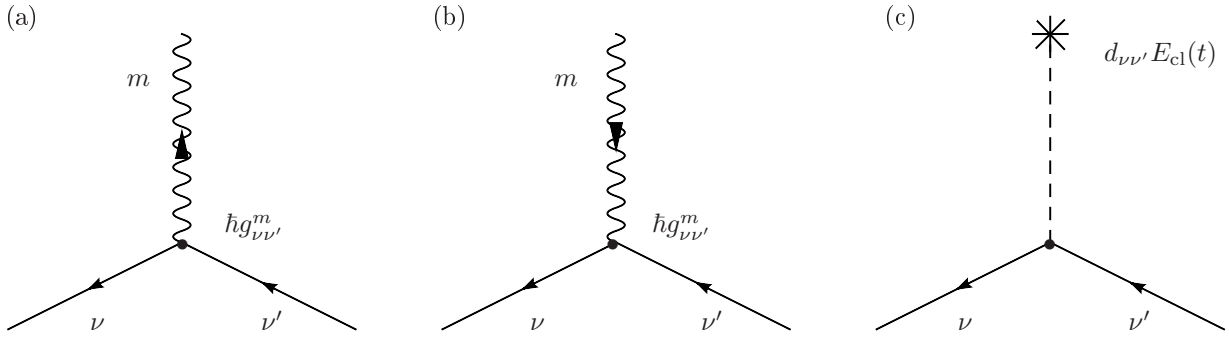

Figure 3.2.: *Diagrammatic illustrations of electron-photon scattering events, described by terms from eq.* (3.19) *and eq.* (3.21)*. In (a) and (b) we show the scattering of an electron from state ν' to ν through the emission, (a), or absorption, (b), of an photon in mode m, both with a scattering amplitude of $\hbar g^m_{\nu\nu'}$. In (c) we show the scattering of an electron from state ν' to ν through the interaction with the classical field, with an amplitude of $d_{\nu\nu'}E_{\mathrm{cl}}(t)$.*

Electron-phonon

The interaction between the electrons and phonons is given by the second term in eq. (3.8)

$$H_{\mathrm{e-ph}}(\{\boldsymbol{r}_i\}) = \sum_{ij}\boldsymbol{u}_j\cdot\boldsymbol{\nabla}_{\boldsymbol{r}_i}\left[\frac{eq_j}{4\pi\varepsilon}\frac{1}{|\boldsymbol{r}_i-\boldsymbol{R}_j^{(0)}|}\right] = \sum_i H_{\mathrm{e-ph}}(\boldsymbol{r}_i).$$

As discussed in section 3.2.1 on the non-interacting phonons, the ionic displacement vector $\boldsymbol{u}_j$ is quantized according the standard procedure[9] and the quantized displacement vector takes the form

$$\boldsymbol{u}_j = \sum_\mu i\tilde{U}_\mu\boldsymbol{\xi}_\mu e^{i\boldsymbol{q}\cdot\boldsymbol{R}_j^{(0)}}(b_{\bar{\mu}}^\dagger + b_\mu),$$

where $\bar{\mu} = (-\boldsymbol{q},\lambda)$, $\tilde{U}_\mu$ is an unspecified[10] expansion coefficient, and $\boldsymbol{\xi}_\mu$ is a polarization vector. As noted below eq. (3.14) the $\boldsymbol{q}=0$ term should should formally be omitted. Using the above, the field quantized expression is obtained as

$$\begin{aligned} H_{\mathrm{e-ph}} &= \int d\boldsymbol{r}\psi^\dagger(\boldsymbol{r})H_{\mathrm{e-ph}}(\boldsymbol{r})\psi(\boldsymbol{r}) \\ &= \sum_{\nu\nu'\mu} M^\mu_{\nu\nu'}c_\nu^\dagger c_{\nu'}(b_{\bar{\mu}}^\dagger + b_\mu), \end{aligned} \tag{3.23}$$

[9] See e.g. sec. 1.1 in [24].

[10] We are not going to use the explicit form of $\tilde{U}_\mu$. Instead we adapt an effective form of this interaction where tabulated parameters account for different materials.

where the coupling strength is given by the expression

$$M^{\mu}_{\nu\nu'} = i\tilde{U}_{\mu} \sum_j e^{i\boldsymbol{q}\cdot\boldsymbol{R}^{(0)}_j} \int d\boldsymbol{r} \phi^*_{\alpha}(\boldsymbol{r}) \boldsymbol{\xi}_{\mu} \cdot \boldsymbol{\nabla}_{\boldsymbol{r}} \left[\frac{eq_j}{4\pi\varepsilon} \frac{1}{|\boldsymbol{r} - \boldsymbol{R}^{(0)}_j|} \right] \phi_{\alpha'}(\boldsymbol{r}) \delta_{\sigma,\sigma'}.$$

As the electron-phonon and electron-photon interaction are formally identical the emission and absorption processes illustrated in figure 3.2(a) and (b) also apply for phonons, with the appropriate replacement of symbols.

3.2.3. Generic semiconductor Hamiltonian

The full Hamiltonian can be written as three parts that are qualitatively different

$$H = H_0 + H_{\mathrm{i}} + U(t). \tag{3.24}$$

The non-interacting (quadratic) part, H_0, has three contribution, one from each of the quantized fields we are considering

$$H_0 = H_{0,\mathrm{e}} + H_{0,\mathrm{rad}} + H_{0,\mathrm{ph}},$$

where the explicit forms are given by

$$\begin{aligned} H_{0,\mathrm{e}} &= \sum_{\nu} \hbar\omega_{\nu} c^{\dagger}_{\nu} c_{\nu}, \\ H_{0,\mathrm{rad}} &= \sum_{m} \hbar\omega_m \left(a^{\dagger}_m a_m + \frac{1}{2} \right), \\ H_{0,\mathrm{ph}} &= \sum_{\mu} \hbar\omega_{\mu} \left(b^{\dagger}_{\mu} b_{\mu} + \frac{1}{2} \right), \end{aligned}$$

see eqs. (3.9), (3.12), and (3.14) respectively. The non-interacting system constitutes the basis upon which we perform perturbation theory. The interacting part, H_{i}, contains the Hamiltonians having three or four basic operators, namely

$$H_{\mathrm{i}} = H_{\mathrm{e-e}} + H_{\mathrm{e-rad}} + H_{\mathrm{e-ph}},$$

where the explicit forms are given by

$$\begin{aligned} H_{\mathrm{e-e}} &= \frac{1}{2} \sum_{\substack{\nu_1\nu_2 \\ \nu_3\nu_4}} V_{\nu_4\nu_3,\nu_1\nu_2} c^{\dagger}_{\nu_4} c^{\dagger}_{\nu_3} c_{\nu_2} c_{\nu_1}, \\ H_{\mathrm{e-rad}} &= \sum_{\nu\nu' m} \hbar g^m_{\nu\nu'} c^{\dagger}_{\nu} c_{\nu'} (a^{\dagger}_m + a_m), \\ H_{\mathrm{e-ph}} &= \sum_{\nu\nu'\mu} M^{\mu}_{\nu\nu'} c^{\dagger}_{\nu} c_{\nu'} (b^{\dagger}_{\bar{\mu}} + b_{\mu}), \end{aligned}$$

see eqs. (3.17), (3.19), and (3.23) respectively. These are the contributions to the Hamiltonian giving rise to infinitely many terms in their respective self-energies. The last part of the Hamiltonian is the interaction between the electrons and the externally applied electric field,

$$U(t) = \sum_{\nu\nu'} d_{\nu\nu'} E_{\mathrm{cl}}(t) c^{\dagger}_{\nu} c_{\nu'},$$

given by eq. (3.21). The term is singled out as it has an explicit time-dependence, unlike the other terms[11], making it very special in many-body perturbation theory.

[11] We remind the reader that we are currently operating in the Schrödinger picture.

The full Hamiltonian eq. (3.24) is illustrated in figure 3.3, with each subsystem represented by an oval and with arrows indicating the various interactions between the subsystems. The figure emphasizes the central role electrons play in semiconductor dynamics as this particle specie interact with all other constituents.

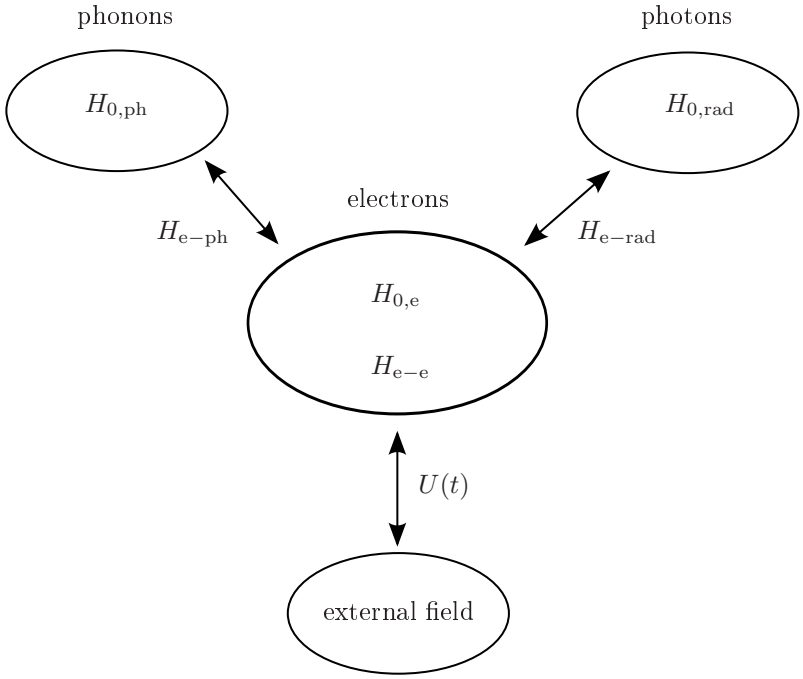

Figure 3.3.: *Schematic illustration of the Hamiltonian eq.* (3.24)*, indicating the individual subsystems and their respective interactions.*

3.3. Summary

In this chapter we have attempted to give an overview of the many different Hamiltonian operators entering many-body physics. We started from a very basic form of the full Hamiltonian of a solid-state system, and gradually performed standard approximations to come closer to a form, that would be applicable in practical calculations. For each contribution, both non-interacting and interacting, to the full Hamiltonian, the general second quantized version was presented in a form that is ready for the application of the Green's function formalism, derived in the previous chapter.

4. Single-Particle States and Matrix Elements

4.1. Introduction

As was made apparent in the previous chapters, one needs to know the matrix elements of a number of operators in order to be able to evaluate a many-body theory, where the basic building blocks for calculating these matrix elements, are the free single-particle states of the involved species. Our focus is on many-body simulations and as the name indicates, one often has to evaluate a very large number of matrix elements. This can be a quite formidable task in itself, even when the single-particle states are known, especially for two-particle interactions such as the Coulomb interaction, where a 6D integral has to be evaluated. This calls for a fast and efficient method of evaluating the great number of matrix elements, which we will develop in the coming sections. However, a first requirement for being able to perform the calculation of the matrix elements is to have a suitable set of single-particle states. As our focus is on many-body effects, we will choose a simple description of our electronic single-particle states, and neglect subtleties introduced by more elaborate methods such as $\boldsymbol{k} \cdot \boldsymbol{p}$, tight-binding, Density Functional Theory or other advanced methods.

The outline of this chapter is as follows: In the first section, section 4.2, we describe the model and method used to obtain the electronic single-particle states, where a simple effective mass model is applied. In section 4.3 we describe two methods for evaluating the computationally demanding Coulomb matrix elements, one efficient approximate formulation and a more accurate, but significantly slower method. In the last section, section 4.4, we describe how to calculate the matrix elements entering the light-matter interaction in the dipole approximation.

4.2. Electronic single-particle states and energies

In this section we will briefly discuss the model of, and the method used to calculate, the electronic single-particle states and energies introduced in section 3.2.1. The approach is very basic and provides the simplest way of consistently including both bound states in the QD and unbound states in the WL.

4.2.1. Self-assembled quantum dots

As mentioned in chapter 1 we are interested in self-assembled semiconductor quantum dots grown using the Stranski-Krastanow technique [6]. These form as small islands on top of a WL, as seen in figure 1.1(a), where the entire WL and QD is embedded in a barrier material. For simplicity we model the QD as a rotationally symmetric truncated cone, which roughly agrees with what is found experimentally [47, 48], sitting on an in principle infinite WL. A few scanning tunneling microscope images of self-assembled quantum dots are shown in figure 4.1, illustrating the rough resemblance with a truncated cone. This setup is shown schematically in figure 4.2 where cylindrical coordinates have been used to exploit the rotational symmetry, furthermore various geometrical parameters are indicated.

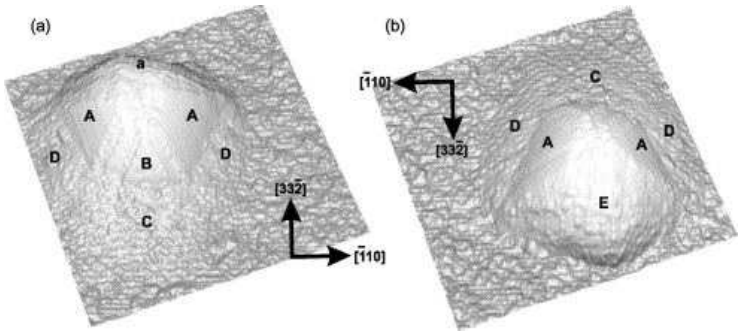

Figure 4.1.: *Scanning tunneling microscope image of a few self-assembled quantum dots [49].*

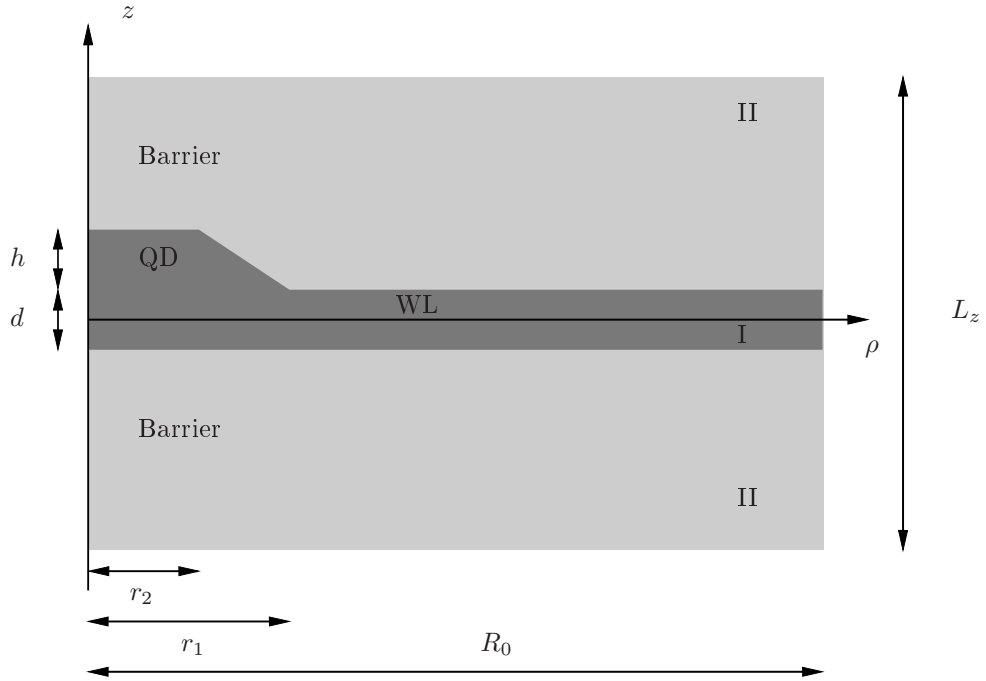

Figure 4.2.: *Schematic of the effective 2D computational domain used for solving the effective mass Schrödinger equation, eq.* (4.4)*. The figure shows the high (II) and low (I) bandgap materials, creating the electronic confinement, along with the relevant lengths entering the model.*

4.2.2. Effective mass Schrödinger equation

For the theoretical description of the electronic states, we will assume the validity of a two-band semiconductor model with a single valence and conduction band, as is often done in the literature [50–52]. For the wavefunctions the envelope function approximation will be employed, in which the full wavefunction is written as [53, pp. 488-490]

$$\phi(\boldsymbol{r}) = u(\boldsymbol{r})F(\boldsymbol{r}), \tag{4.1}$$

where $u(\boldsymbol{r})$ is the lattice periodic Bloch function and $F(\boldsymbol{r})$ is the envelope function. The Bloch function does not need to be determined explicitly, while the envelope function is found from a one-band effective mass Schrödinger equation

$$\left(-\frac{\hbar^2}{2}\boldsymbol{\nabla}\cdot\left[\frac{1}{m^*(\boldsymbol{r})}\boldsymbol{\nabla}\right]+V(\boldsymbol{r})\right)F(\boldsymbol{r}) = EF(\boldsymbol{r}). \tag{4.2}$$

Here $V(\boldsymbol{r})$ is the confining potential, created by bandbending effects through the embedding of the low bandgap material (I) in the high bandgap material (II), see figure 4.2, and $m^*(\boldsymbol{r})$ is the position dependent effective mass. The envelope function $F(\boldsymbol{r})$ is subject to the conditions that

$$F(\boldsymbol{r}) \quad \text{and} \quad \frac{1}{m^*(\boldsymbol{r})}\boldsymbol{n}\cdot\boldsymbol{\nabla}F(\boldsymbol{r}) \tag{4.3}$$

must be continuous and differentiable at every point and further that $F(\boldsymbol{r})$ must be finite. Here $\boldsymbol{n}$ is an arbitrary unit vector. These conditions arise from the fact that the particle number must be conserved [54, p. 74]. Due to the rotational symmetry, the Hamiltonian commutes with the generator for rotations about the z-axis, the z-component of the angular momentum operator L_z (not to be confused with the length L_z in figure 4.2). This has the consequence that the z-component of the angular momentum is a conserved quantity, and therefore the envelope can be written as a product of the eigenfunction for L_z, defined as $L_z\Phi_m(\varphi) = \hbar m\Phi_m(\varphi)$, and a part independent of φ

$$F(\boldsymbol{r}) = \Phi_m(\varphi)f(\rho,z) = \frac{1}{\sqrt{2\pi}}e^{im\varphi}f(\rho,z),$$

where eq. (4.3) dictates that m must be an integer, see e.g. [45, sec. 7.3]. Inserting this into eq. (4.2) we obtain the following eigenvalue equation for $f(\rho,z)$

$$\left(-\frac{\hbar^2}{2\rho}\partial_\rho\left[\frac{\rho}{m^*}\partial_\rho\right] - \frac{\hbar^2}{2}\partial_z\left[\frac{1}{m^*}\partial_z\right] + \frac{\hbar^2m^2}{2m^*\rho^2} + V(\rho,z)\right)f(\rho,z) = Ef(\rho,z), \tag{4.4}$$

where $m^* = m^*(\rho,z)$ and we immediately see that E is degenerate in m following from the rotational symmetry. Eq. (4.4) must also be supplied with a set of boundary conditions for the new function $f(\rho,z)$, which can be derived from eq. (4.3). On the internal boundaries between the domains I and II $f(\rho,z)$ must satisfy eq. (4.3) directly, while on the external boundaries and on the z-axis we must be a bit more careful. Due to the third term in eq. (4.4) one must distinguish between cases of m equal to zero or different from zero. For $m \neq 0$ the third term diverges as $\rho \to 0$, therefore $f(\rho,z)$ must go to zero on the z-axis. For $m = 0$ the third term does not cause any problems, but now the derivative $\partial_\rho f(\rho,z)$ must be zero on the z-axis, otherwise $f(\rho,z)$ would get a non-differentiable kink. Mathematically these conditions can be written

$$f(\rho = 0, z) = 0, \quad m \neq 0, \tag{4.5a}$$
$$\partial_\rho f(\rho = 0, z) = 0, \quad m = 0. \tag{4.5b}$$

The boundaries at $z = \pm L_z/2$ and $\rho = R_0$ are artificial boundaries introduced to be able to solve the equation numerically, and therefore the solutions must ideally be independent of the position of the boundaries. For the boundaries at $z = \pm L_z/2$ there is no practical problem. This is the case as we are only interested in states bound in the QD or in the WL and hence we expect the states to decay exponentially as we move in the z-direction from material I into material II. For this reason L_z should simply be chosen large enough that $f(\rho, z = \pm L_z)$ has approached zero. For the boundary at $\rho = R_0$ the problem is more subtle. We are interested in describing the delocalized states in the WL which we know form an energy continuum. The energy continuum arises from the unbounded nature of the WL and is an essential feature to maintain in the theoretical description. The effect of introducing a zero boundary condition at $\rho = R_0$, is that the WL energy continuum becomes discreetly sampled, in the way that the large R_0 the finer the sampling. One can then systematically increase R_0 until the physical result one is considering no longer depends on this artificial boundary. We state these conditions mathematically as

$$f(\rho \neq 0, z = \pm L_z/2) = 0, \tag{4.6a}$$
$$f(\rho = R_0, z) = 0. \tag{4.6b}$$

The position dependent effective mass and confinement potential are constants within each domain (I and II) and jump whenever an internal boundary is crossed, hence

$$m^*(\rho,z) = \begin{cases} m_{\mathrm{I}}, & (\rho,z) \in \mathrm{I} \\ m_{\mathrm{II}}, & (\rho,z) \in \mathrm{II}, \end{cases}$$

and

$$V(\rho,z) = \begin{cases} \Delta E_{\mathrm{I}}, & (\rho,z) \in \mathrm{I} \\ \Delta E_{\mathrm{II}}, & (\rho,z) \in \mathrm{II}. \end{cases}$$

A schematic illustration of the energy landscape experienced by the electrons is shown figure 4.3.

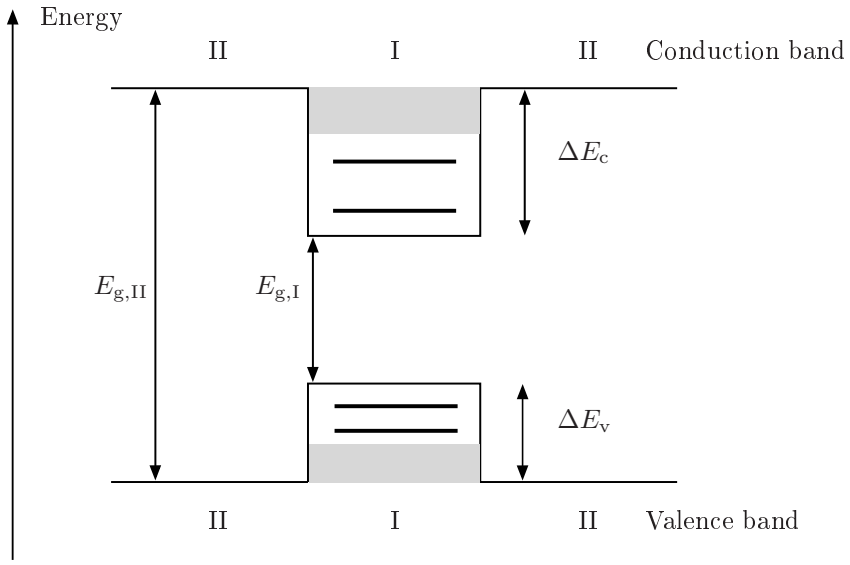

Figure 4.3.: *Schematic illustration of the energy landscape in the QD/WL system. In the potential well the horizontal lines indicate bound QD states, while the grey boxes indicate the WL energy continuum.*

The mathematical model for obtaining the electronic states is now fully specified and eq. (4.4) is ready to be solved for electrons in the conduction band and holes in the valence band. For the numerical values of the various band parameters, and a small discussion of these, we refer to appendix A.8. The full identification of a state needs three indexes (when neglecting spin which is not important here), a band index (b), the z angular momentum (m), and a final index counting the states within each m subspace (N). An envelope state can now be written as

$$F^b_{m,N}(\boldsymbol{r}) = \Phi_m(\varphi) f^b_{|m|,N}(\rho,z), \tag{4.7}$$

which, when properly normalized and combined with its respective Bloch function (eq. (4.1)), satisfies the orthonormality condition

$$\langle u^b F^b_{m,N} | u^{b'} F^{b'}_{m',N'} \rangle = \delta_{m,m'} \delta_{N,N'} \delta_{b,b'}.$$

Usually all spatial quantum numbers will be collected into a single one, normally denoted α, to lighten the notation. Then the orthonormality condition e.g. can be written compactly as: $\langle \alpha | \alpha' \rangle = \delta_{\alpha,\alpha'}$.

For most geometries it is not possible to solve eq. (4.4) analytically, therefore we have to resort to numerical methods. In our simulations we used the finite element package COMSOL[1], which provides an easy implementation and relatively stable and accurate solutions [52].

4.2.3. Numerical examples

For illustration of the solutions of eq. (4.4) we will in this section present a set of solutions for a typical system. The geometrical parameters of the QD and WL system were chosen to yield a representative

[1] For more information: `http://www.comsol.com/`

Quantity	Value	Unit
h	1.25	nm
d	1.25	nm
r_1	20	nm
r_2	10	nm
R_0	300	nm
L_z	60	nm

Table 4.1.: *Numerical values of the geometrical parameters used in section 4.2.3, see figure 4.2.*

selection of states that one would typically encounter, these parameters are given in table 4.1. The band parameters for the InGaAs system we employ for our heterostructure are discussed and presented in appendix A.8.

We start out by providing an overview of the energy eigenstates obtained by solving eq. (4.4) in terms of the energy density of states (DOS), the DOS for the conduction band is shown in figure 4.4(a) and for the valence band in figure 4.4(b). An alternative overview, slightly more informative, is given in figure 4.5 showing the energy levels as a function of the angular momentum m. We have defined the DOS[2] as

$$d(E) = \sum_{\alpha} \delta(E - E_\alpha),$$

but for practical numerical reasons we use a broadened delta function in the form of a Lorentzian with a width w, so that for the figures the DOS is

$$d(E) = \sum_{\alpha} L_w(E - E_\alpha), \quad L_w(x) = \frac{w}{\pi} \frac{1}{x^2 + w^2}. \tag{4.8}$$

The values of the DOS will depend on w and should therefore only be considered as an illustration. By comparing figures (4.4) and (4.5) for the conduction and valence band, we notice that the overall level structure is very much alike, which is a consequence of our choice of band parameters, see A.8. The envelope functions are therefore also very similar for the two bands and for that reason we will focus on the conduction band states. In the DOS for the conduction band states, the peaks below the onset of the WL continuum correspond to states bound mainly to the QD, while the states in the continuum are a mixture of so-called quasi-bound states and WL states. We will elaborate on these different types of states below. Henceforth the notation (b, m, N) will be employed when referring to $f^b_{|m|,N}(\rho, z)$.

We start by considering the bound states. The first peak reflects the non-degenerate state $(\mathrm{c}, 0, 1)$, this state has zero angular momentum and can therefore be found very close to the z-axis, as seen in figure 4.6(a). As this state has the lowest energy, it is also the one most strongly bound to the QD. The second peak is the degenerate pair of states $(\mathrm{c}, \pm 1, 1)$, where the degeneracy gives twice the DOS of the first peak. Having an angular momentum of ± 1, the electron is forced a bit further away from the z-axis than the state $(\mathrm{c}, 0, 1)$ and therefore less localized in the QD, see figure 4.6(c). The third peak stems from the degenerate pair of states $(\mathrm{c}, \pm 2, 1)$, where the one unit higher angular momentum forces the electrons further out of the QD, see figure 4.6(d). The fourth peak has zero angular momentum, seen from its max value, and is the non-degenerate state $(\mathrm{c}, 0, 2)$. This state is still located mainly in the QD, but has acquired a node in the radial direction to stay orthogonal to the states spatial near it, see figure 4.6(b). The fifth peak is the degenerate $(\mathrm{c}, \pm 3, 1)$ pair of states, which has an envelope similar to states $(\mathrm{c}, \pm 1, 1)$ and $(\mathrm{c}, \pm 2, 1)$, but is pushed even further out of the QD due to its higher angular momentum, see figure 4.6(e). The last visible peak originates from the degenerate $(\mathrm{c}, \pm 1, 2)$ pair and is similar in nature to the state $(\mathrm{c}, 0, 2)$, which also has a node in the radial direction, see figure 4.6(f).

[2] The degeneracy in the spin quantum number is not taken into account here. To include it, one should simply multiply by a factor of 2.

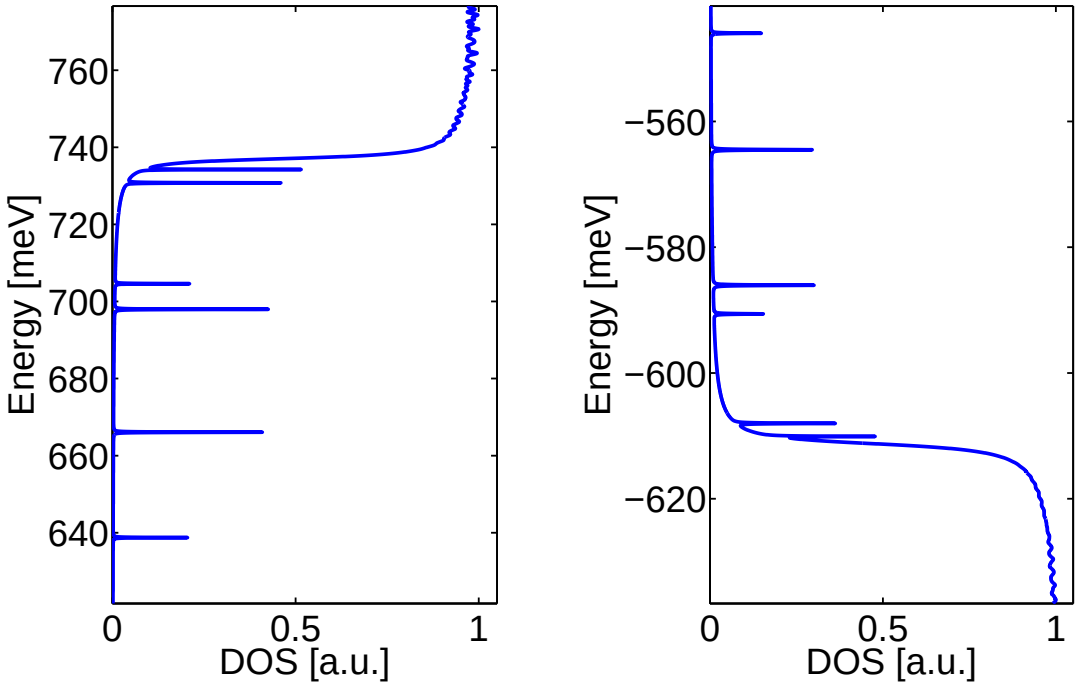

(a) DOS for the conduction band.

(b) DOS for the valence band.

Figure 4.4.: *Figures illustrating the energy density of states, eq.* (4.8)*, for (left) the electrons in the conduction band and (right) the electrons in the valence band. The DOS plots are on the same energy scale, with the zero point placed in the middle of the gap for material I, see figure 4.3. For illustrative reasons a different width was used for the discrete and continuous part of the spectrum,* $w_{\text{discreete}} = 0.05$ meV *and* $w_{\text{continuous}} = 0.8$ meV*, the larger width of the continuum part reflects the sampling in energy that is needed in the numerical simulation. This trick is needed in order to reproduce the well-known step-like DOS of 2D structures, otherwise the 2D plateau would be very spiky and not flat.*

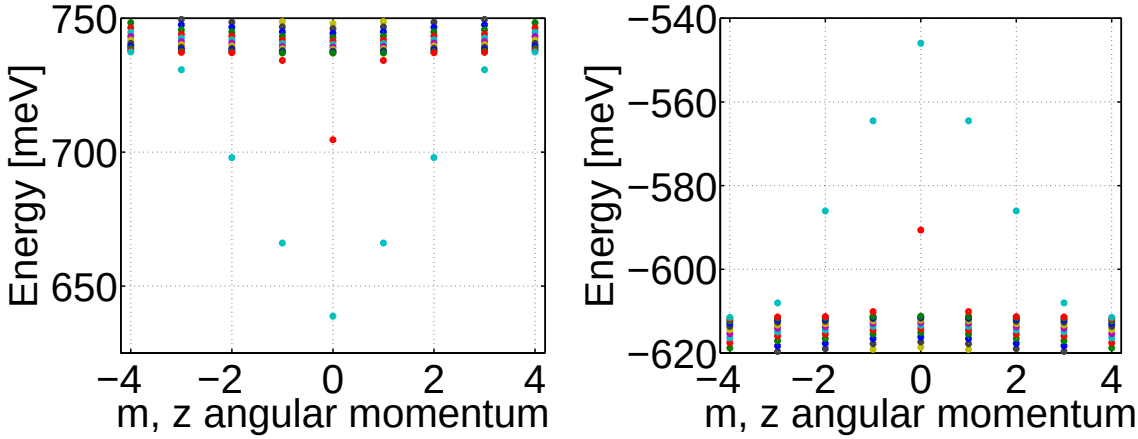

(a) Energies for the conduction band.

(b) Energies for the valence band.

Figure 4.5.: *Representation of the energies obtained from solving eq.* (4.4)*. To the left is the conduction band with* m *on the horizontal axis and* N *counting up upwards in energy, while to the right the valence band is shown with* N *counting up downwards in energy. The color coding of the dots is arbitrary.*

To be able to discuss the quasi-bound states effectively it is helpful to have been through the WL states first, as the quasi-bound states are intermediates between the strongly localized and delocalized states. We will refer to a state as being a WL state when it is basically unaffected by the presence of the QD potential[3]. It is of course true that all states in the continuum are affected by the QD potential, but in practice it turns out that many of these are unaffected (within our numerical accuracy) and therefore it safe to regard them as pure WL states. This fact becomes very visible when expanding a WL state on the eigenstates of a pure WL (or quantum well) system as is done in section 4.3.3. Three examples are shown figures 4.7(b), 4.7(c), and 4.7(d), where it is clearly seen that none of these envelopes are spatially near the QD, and hence they need not change in order to be orthogonal to the bound QD states. One also notices that the number of nodes in the radial direction is correlated with N, and is equal to $N-1$. These three states are all part of the energy continuum that has its onset at around 737 meV, and displays the familiar step shape known from 2D systems, which is what the WL effectively is. The tail that extends from the continuum part of the DOS is due to the finite width of our Lorentzian, eq. (4.8), and therefore artificial, the transition should be sharp as we have no broadening mechanisms yet.

Having discussed both the bound and unbound states, we move on to an intermediate between these two, namely what we will refer to as quasi-bound states. These are states which are not clearly bound to the QD and yet not clearly part of the WL continuum of delocalized states either. An example is shown figure 4.6(g), where we clearly see that the envelope of the state $(\mathrm{c}, 0, 3)$ is located both in the QD and is delocalized in the full WL; Fig. 4.6(h) shows a zoom in on the QD area. In figure 4.7(a) we show the states $(\mathrm{c}, \pm 2, 2)$ which in very large parts is located in the WL, but there is still a small probability of finding it in the QD. Energetically they usually form near the onset of the energy continuum and a bit into this, depending on the geometry of the system. What is very special about these states is that they have a significant amplitude both in the QD and WL, and can therefore overlap both with pure bound and WL states. This means that effective scattering can take place between the spectrally and spatially well separated QD and WL states, with the mediator being the quasi-bound states.

It should be emphasized that the present approach for obtaining the electronic states, treats the bound, quasi-bound, and WL states on the same footing, as they originate from the same differential equation. This has the consequence that properties such as orthogonality and relative energy difference between different states are automatically fulfilled. This is in contrast to another commonly used scheme for describing electronic states in many-body calculations, the so-called Orthogonalized Plane Wave (OPW) procedure (see e.g. [32, 55]). In the OPW procedure plane waves are made orthogonal to some predefined bound states, often harmonic oscillator states, and these are then used as the single-particle basis. The energies are taken as a combination of the unperturbed parabolic dispersion of the plane waves, the energies of the bound states, and an user chosen offset between these. The OPW approach has the huge advantage of being semi-analytical, which speeds up calculations considerably, but suffers from the above mentioned fundamental problem. A study of the significance of various descriptions of the electronic states has been performed in [51] and shows that it is important to treat the qualitatively different states on the same footing.

[3] It should be noted that for certain geometries we experienced QD resonances in the WL continuum. These appear for otherwise pure WL states that are far from the localized QD states, both spectrally and spatially, but which at some energy rather suddenly become localized in the QD. We expect that these states occur due to the fulfilment of a resonance conditions for the delocalized WL states, much like the transmission spectra for 1D quantum wells in introductory textbooks on quantum mechanics.

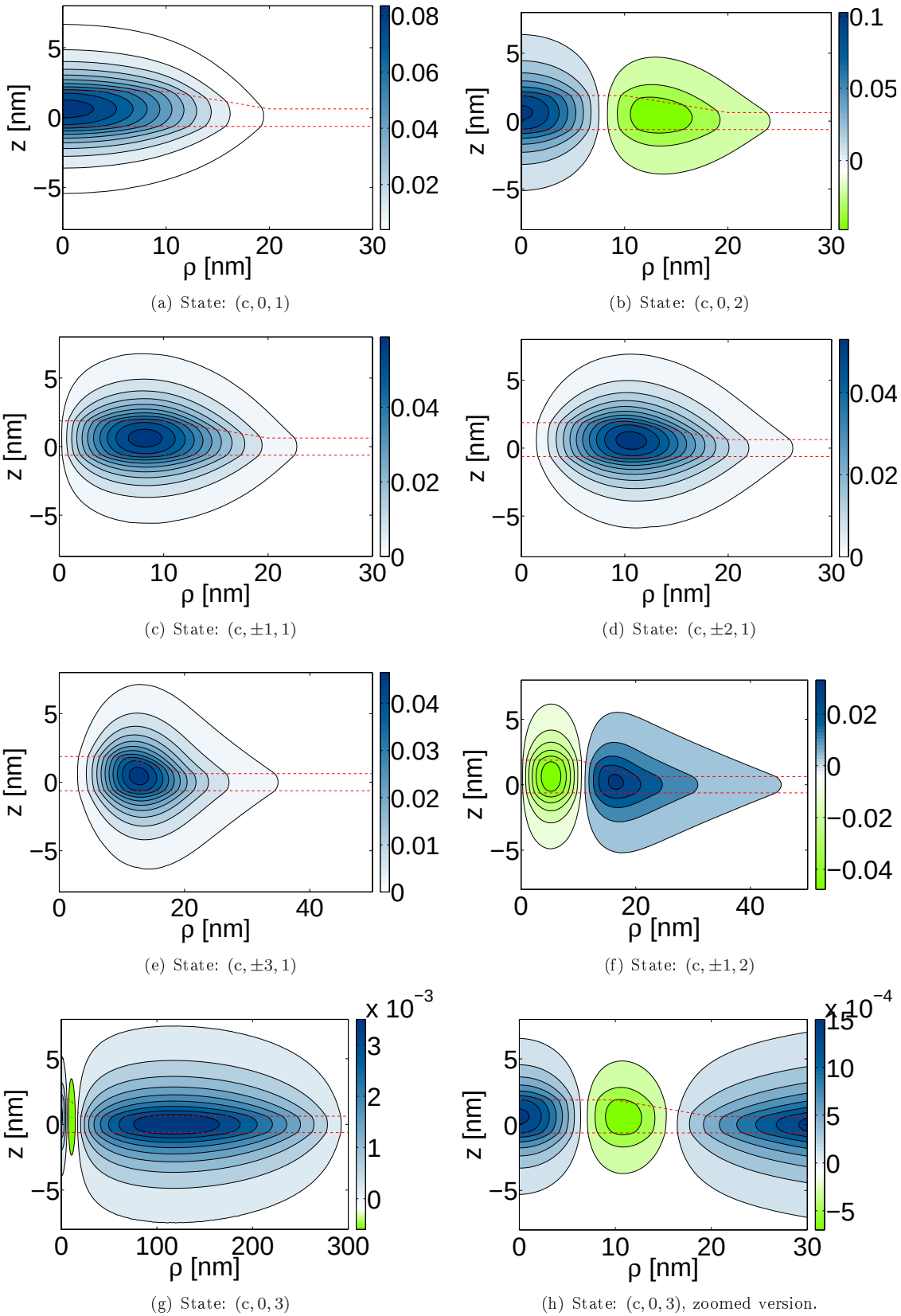

(a) State: $(c, 0, 1)$

(b) State: $(c, 0, 2)$

(c) State: $(c, \pm 1, 1)$

(d) State: $(c, \pm 2, 1)$

(e) State: $(c, \pm 3, 1)$

(f) State: $(c, \pm 1, 2)$

(g) State: $(c, 0, 3)$

(h) State: $(c, 0, 3)$, zoomed version.

Figure 4.6.: *Figures showing various solutions to eq.* (4.4)*, namely the envelopes* $f^b_{|m|,N}(\rho, z)$*, for electrons in the conduction band. We use the notation* (b, m, N) *when referring to* $f^b_{|m|,N}(\rho, z)$*. Notice that one must carefully inspect the values on the colorbar in each plot, especially for negative values.*

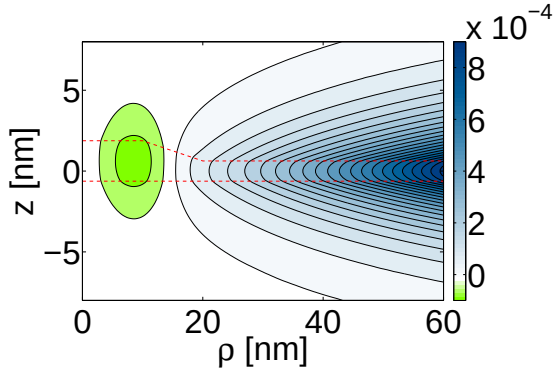

(a) State: $(c, \pm 2, 2)$. Notice that the ratio between the minimum and maximum value is around 60, meaning that there is only a very very small chance of finding the electron in the QD.

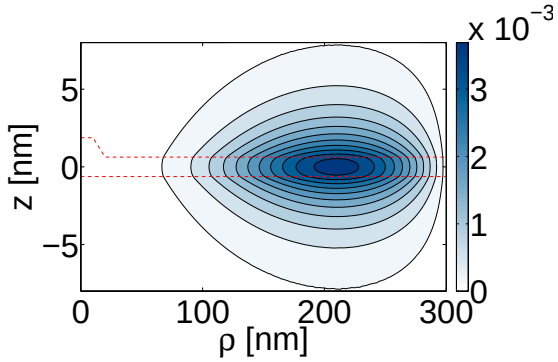

(b) State: $(c, \pm 4, 1)$

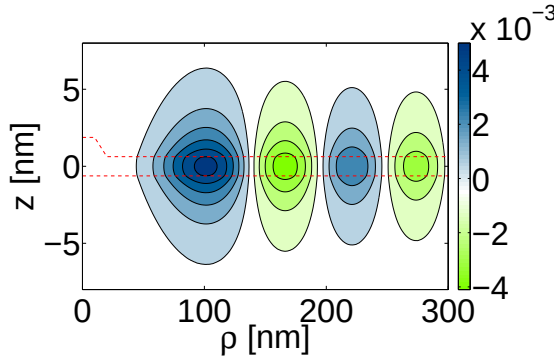

(c) State: $(c, \pm 5, 4)$

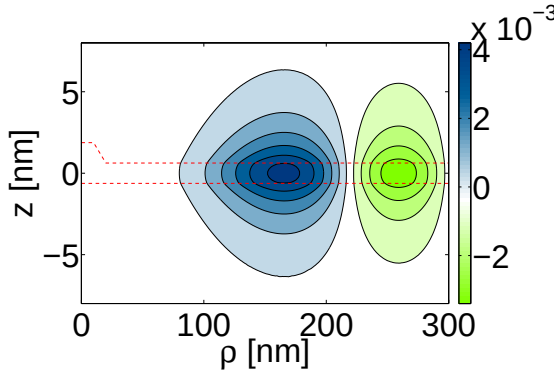

(d) State: $(c, \pm 6, 2)$

Figure 4.7.: *Figures showing various solutions to eq.* (4.4)*, namely the envelopes* $f^b_{|m|,N}(\rho, z)$*, for electrons in the conduction band. We use the notation* (b, m, N) *when referring to* $f^b_{|m|,N}(\rho, z)$*. Notice that one must carefully inspect the values on the colorbar in each plot, especially for negative values.*

4.3. Coulomb matrix elements

The Coulomb matrix element, eq. (3.18), is one of the central numerical quantities which has to be evaluated in order to be able to perform many-body calculations[4]. We will therefore in this section, discuss various properties and strategies for its evaluation, as it is not a trivial task.

To reduce the amount of computation time needed, it is advantageous to make use of the symmetries the Coulomb matrix elements possess. These can easily be derived from the definition, eq. (3.18), and by using the fact that $H_{\mathrm{e-e}}(\boldsymbol{r}, \boldsymbol{r}') = H_{\mathrm{e-e}}(\boldsymbol{r}', \boldsymbol{r})$. The symmetries are

$$V_{\nu_4\nu_3,\nu_1\nu_2} = V^*_{\nu_1\nu_2,\nu_4\nu_3} = V_{\nu_3\nu_4,\nu_2\nu_1} = V^*_{\nu_2\nu_1,\nu_3\nu_4}. \tag{4.9}$$

The spatial part of the Coulomb matrix element, eq. (3.18), is given by

$$V_{\alpha_4\alpha_3,\alpha_1\alpha_2} = \int d\boldsymbol{r} d\boldsymbol{r}' \phi^*_{\alpha_4}(\boldsymbol{r}) \phi^*_{\alpha_3}(\boldsymbol{r}') H_{\mathrm{e-e}}(\boldsymbol{r}, \boldsymbol{r}') \phi_{\alpha_1}(\boldsymbol{r}) \phi_{\alpha_2}(\boldsymbol{r}'), \tag{4.10}$$

which is the computationally demanding part as the spin overlaps are trivially evaluated. To facilitate the evaluation of the Coulomb matrix element, and for formal reasons, it is convenient to 3D Fourier transform

[4] It turns out that also for the interaction between electrons and dispersionless LO phonons, the matrix elements entering the self-energy can be reformulated in terms of the Coulomb matrix element section 5.2.2.

$H_{\mathrm{e-e}}(\boldsymbol{r},\boldsymbol{r}')$ yielding

$$H_{\mathrm{e-e}}(\boldsymbol{r}-\boldsymbol{r}') = \frac{1}{V}\sum_{\boldsymbol{q}} V_q e^{i\boldsymbol{q}\cdot(\boldsymbol{r}-\boldsymbol{r}')}, \quad V_q = \frac{e^2}{\varepsilon}\frac{1}{q^2}, \tag{4.11}$$

where V is the quantization volume and $\boldsymbol{q} = (q_x, q_y, q_z)$ is the 3D wavevector. We use the Fourier transform defined by [28]

$$f(\boldsymbol{r}) = \frac{1}{V}\sum_{\boldsymbol{q}} f_{\boldsymbol{q}} e^{i\boldsymbol{q}\cdot\boldsymbol{r}}, \quad f_{\boldsymbol{q}} = \int_V d\boldsymbol{r} f(\boldsymbol{r}) e^{-i\boldsymbol{q}\cdot\boldsymbol{r}}. \tag{4.12}$$

Depending on the system under consideration it can be advantageous to perform the q_z integration explicitly in eq. (4.11) ending up with the 2D Fourier transform of the Coulomb interaction. Performing this integration [56, p. 122] yields

$$H_{\mathrm{e-e}}(\boldsymbol{r}-\boldsymbol{r}') = \frac{1}{A}\sum_{\boldsymbol{q}_\parallel} V_{q_\parallel} e^{i\boldsymbol{q}_\parallel\cdot(\boldsymbol{\rho}-\boldsymbol{\rho}')} e^{-q_\parallel|z-z'|}, \quad V_{q_\parallel} = \frac{e^2}{2\varepsilon}\frac{1}{q_\parallel}, \tag{4.13}$$

where A is the quantization area, $\boldsymbol{q}_\parallel = (q_x, q_y)$ is the 2D or in-plane wavevector, and $\boldsymbol{\rho} = (x, y)$ is the in-plane position vector. The reason for expanding the Coulomb interaction in plane-waves, and not evaluating eq. (4.10) directly, is due to the problems generated by the $1/|\boldsymbol{r}-\boldsymbol{r}'|$ singularity, which are difficult to handle numerically.

If one inserts the 3D Fourier transform of the Coulomb interaction into eq. (4.10), the integrations over $\boldsymbol{r}$ and $\boldsymbol{r}'$ can be separated as follows

$$V_{\alpha_4\alpha_3,\alpha_1\alpha_2} = \frac{1}{V}\sum_{\boldsymbol{q}} V_q \int d\boldsymbol{r}\phi^*_{\alpha_4}(\boldsymbol{r}) e^{i\boldsymbol{q}\cdot\boldsymbol{r}}\phi_{\alpha_1}(\boldsymbol{r}) \int d\boldsymbol{r}'\phi^*_{\alpha_3}(\boldsymbol{r}') e^{-i\boldsymbol{q}\cdot\boldsymbol{r}'}\phi_{\alpha_2}(\boldsymbol{r}'), \tag{4.14}$$

so that the integrals which need to be evaluated are all of the form

$$\langle\alpha_5|e^{\pm i\boldsymbol{q}\cdot\boldsymbol{r}}|\alpha_6\rangle = \int d\boldsymbol{r}\phi^*_{\alpha_5}(\boldsymbol{r}) e^{\pm i\boldsymbol{q}\cdot\boldsymbol{r}}\phi_{\alpha_6}(\boldsymbol{r}). \tag{4.15}$$

This separation is made for formal reasons, the result is needed in the next section, while for the actual evaluation the 2D transform, eq. (4.13), is used.

4.3.1. Bloch part

In the effective mass envelope approximation for the electrons, the wavefunctions in eq. (4.10) are all of the following form

$$\phi_\alpha(\boldsymbol{r}) = F^b_\alpha(\boldsymbol{r}) u_b(\boldsymbol{r}), \tag{4.16}$$

where $F^b_\alpha(\boldsymbol{r})$ is the envelope function and $u_b(\boldsymbol{r})$ is the Bloch function for the static lattice, both for band b. Normally the band index b is contained in the general spatial quantum number α, but here we display it explicitly in the envelope function for clarity. The envelope function is determined from the effective mass Schrödinger equation, see section 4.2.2, while the Bloch function is generally not known. Below we will show that for the class of Coulomb matrix elements we are considering, it is not necessary to know the Bloch function, which is very fortunate as this function is very hard to obtain.

In a semiconductor scattering processes where an electron is scattered from one band and to the other, can occur due to the Coulomb interaction between the electrons in the semiconductor. However, for a relatively wide bandgap semiconductor this process will be very non-resonant in nature, with the consequence that the probability for it to happen will be very small, and for this reason we will neglect such processes in our

model [56, p. 212]. This approximation does not mean that the carriers do not interact across the bandgap. There are strong interactions between electrons in the valence and conduction band as their wavefunctions overlap spatially, giving rise to the excitonic effects that are in general very important. A consequence of the approximation, which must be kept in mind, is that the number of carriers in each band is conserved, hence no recombination takes place due to the Coulomb interactions. For the Coulomb integrals, eq. (4.15), this means that the band index in the wavefunctions is the same

$$\begin{aligned}\langle\alpha_5|e^{\pm i\boldsymbol{q}\cdot\boldsymbol{r}}|\alpha_6\rangle &= \int d\boldsymbol{r}\phi^*_{\alpha_5}(\boldsymbol{r})e^{\pm i\boldsymbol{q}\cdot\boldsymbol{r}}\phi_{\alpha_6}(\boldsymbol{r})\delta_{b_5,b_6}\\ &= \int d\boldsymbol{r}\left[F^b_{\alpha_5}(\boldsymbol{r})u_b(\boldsymbol{r})\right]^* e^{\pm i\boldsymbol{q}\cdot\boldsymbol{r}}F^b_{\alpha_6}(\boldsymbol{r})u_b(\boldsymbol{r}).\end{aligned}$$

By assumption the envelope functions are slowly-varying compared to the Bloch functions. If we further assume that only components of the Coulomb interaction with relatively small wavevectors are needed, the exponentials $e^{\pm i\boldsymbol{q}\cdot\boldsymbol{r}}$ also become slowly-varying compared to the Bloch part. A more quantitative requirement would be that $q_{\max}a_{\mathrm{uc}} \ll 1$, where $q_{\max}$ is the largest wavevector needed in the expansion of the Coulomb potential and a_{uc} is the typical size of the unit cell. For the InGaAs systems we will be considering we have $a_{\mathrm{uc}} \approx 5$ Å [53] leading to $q_{\max} \ll 2\times 10^9$ m^{-1}. This value of $q_{\max}$ limits us to the vicinity of the band edges, which is consistent with the fundamental assumption of the effective mass theory we have employed for the electronic states. Having argued that both the envelopes and exponentials are slowly-varying compared to the Bloch function, we may follow [53, p. 120] and write the integral over the entire structure as a sum over all unit cells and an integral over a single periodic[5] unit cell

$$\begin{aligned}\langle\alpha_5|e^{\pm i\boldsymbol{q}\cdot\boldsymbol{r}}|\alpha_6\rangle &\approx \sum_{\mathrm{uc}\ i} V_{\mathrm{uc}}\left[F^b_{\alpha_5}(\boldsymbol{r}_i)\right]^* e^{\pm i\boldsymbol{q}\cdot\boldsymbol{r}_i}F^b_{\alpha_6}(\boldsymbol{r}_i)\underbrace{\left(\frac{1}{V_{\mathrm{uc}}}\int_{\mathrm{uc}} d\boldsymbol{r}u^*_b(\boldsymbol{r})u_b(\boldsymbol{r})\right)}_{\langle u_b|u_b\rangle=1}\\ &= \int d\boldsymbol{r}\left[F^b_{\alpha_5}(\boldsymbol{r})\right]^* e^{\pm i\boldsymbol{q}\cdot\boldsymbol{r}}F^b_{\alpha_6}(\boldsymbol{r}),\end{aligned} \tag{4.17}$$

where in the last line the sum was converted into an integral. This leads to the fact that the Coulomb matrix elements can be evaluated with out explicitly knowing the Bloch functions and we end up with [32, p. 86]

$$V_{\alpha_4\alpha_3,\alpha_1\alpha_2} = \int d\boldsymbol{r}d\boldsymbol{r}'F^*_{\alpha_4}(\boldsymbol{r})F^*_{\alpha_3}(\boldsymbol{r}')H_{\mathrm{e-e}}(\boldsymbol{r},\boldsymbol{r}')F_{\alpha_1}(\boldsymbol{r})F_{\alpha_2}(\boldsymbol{r}')\times\delta_{b_4,b_1}\delta_{b_3,b_2}. \tag{4.18}$$

4.3.2. Representation in separable basis

The geometry of the QD/WL system we intent to use for practical calculations later in the thesis, will all be for relatively shallow QDs, that is with a large width to height ratio, as those presented in section 4.2.1. Due to the shallowness of the QDs, it becomes a good approximation to write the entire envelope function $F(\boldsymbol{r})$ on a separable form, see section 4.3.3. However, to set the stage for performing this approximation we first formulate an exact procedure for calculating the Coulomb matrix elements. This procedure is based expanding the numerical envelope functions on an analytical basis set, that is separable in each of the cylindrical coordinates ρ, φ, and z, and furthermore this exact formulation will serve as a benchmark for the approximative formulation.

Denoting the separable basis as $\{B_\beta(\boldsymbol{r})\}$ we may write the expansion of the envelope function as follows

$$F_\alpha(\boldsymbol{r}) = \sum_\beta A^\alpha_\beta B_\beta(\boldsymbol{r}), \quad A^\alpha_\beta = \langle\beta|\alpha\rangle = \int d\boldsymbol{r}B^*_\beta(\boldsymbol{r})F_\alpha(\boldsymbol{r}), \tag{4.19}$$

[5] We will assume that the argument still holds, even though the system under consideration has different kinds of unit cells.

where the basis states are of the specific form, see appendix A.7,

$$B_\beta(\boldsymbol{r}) = \Phi_m(\varphi)R_{|m|l}(\rho)Z_{n_z}(z) = g_\beta(\boldsymbol{\rho})Z_\beta(z), \quad \beta = (m, l, n_z), \tag{4.20}$$

and where $g_\beta(\boldsymbol{\rho}) = \Phi_m(\varphi)R_{|m|l}(\rho)$ has been introduced for notational simplicity. Using the result eq. (4.18), the 2D transform of the Coulomb potential, eq. (4.13), and the newly introduced basis, a Coulomb matrix element can be written as

$$\begin{aligned} V_{\alpha_4\alpha_3,\alpha_1\alpha_2} &= \sum_{\substack{\beta_1\beta_2\\ \beta_3\beta_4}} \left[A^{\alpha_4}_{\beta_4}\right]^* \left[A^{\alpha_3}_{\beta_3}\right]^* A^{\alpha_1}_{\beta_1} A^{\alpha_2}_{\beta_2} \times \delta_{b_4,b_1}\delta_{b_3,b_2} \\ &\quad \times \left\{ \frac{1}{A}\sum_{\boldsymbol{q}_\parallel} V_{q_\parallel} \int d\boldsymbol{\rho} g^*_{\beta_4}(\boldsymbol{\rho}) e^{i\boldsymbol{q}_\parallel\cdot\boldsymbol{\rho}} g_{\beta_1}(\boldsymbol{\rho}) \int d\boldsymbol{\rho}' g^*_{\beta_3}(\boldsymbol{\rho}') e^{-i\boldsymbol{q}_\parallel\cdot\boldsymbol{\rho}'} g_{\beta_2}(\boldsymbol{\rho}') \right. \\ &\quad \left. \times \int dz dz' Z^*_{\beta_4}(z) Z^*_{\beta_3}(z') e^{-q_\parallel|z-z'|} Z_{\beta_1}(z) Z_{\beta_2}(z') \right\} \\ &= \sum_{\substack{\beta_1\beta_2\\ \beta_3\beta_4}} \left[A^{\alpha_4}_{\beta_4}\right]^* \left[A^{\alpha_3}_{\beta_3}\right]^* A^{\alpha_1}_{\beta_1} A^{\alpha_2}_{\beta_2} \times \delta_{b_4,b_1}\delta_{b_3,b_2} \times V_{\beta_4\beta_3,\beta_1\beta_2}. \end{aligned} \tag{4.21}$$

In the last line we have introduced the Coulomb matrix element for a basis state, $V_{\beta_4\beta_3,\beta_1\beta_2}$, defined as the content in the curly brackets on the second and third line. From this formula it is seen that the challenging task apparently is to calculate $V_{\beta_4\beta_3,\beta_1\beta_2}$, as the rest consists of simple summations. For this reason the following will focus on simplifying the expression for $V_{\beta_4\beta_3,\beta_1\beta_2}$.

In the expression for $V_{\beta_4\beta_3,\beta_1\beta_2}$ two types of integrals occur, one involving the $\boldsymbol{\rho}$ coordinate and one involving z and z', for which we define short hand notations in the following way

$$I^\pm_{\boldsymbol{\rho}}(\beta_5, \beta_6 : \boldsymbol{q}_\parallel) = \int d\boldsymbol{\rho} g^*_{\beta_5}(\boldsymbol{\rho}) e^{\pm i\boldsymbol{q}_\parallel\cdot\boldsymbol{\rho}} g_{\beta_6}(\boldsymbol{\rho}), \tag{4.22}$$

$$I_z(\beta_4, \beta_3, \beta_1, \beta_2 : q_\parallel) = \int dz dz' Z^*_{\beta_4}(z) Z^*_{\beta_3}(z') e^{-q_\parallel|z-z'|} Z_{\beta_1}(z) Z_{\beta_2}(z'). \tag{4.23}$$

We start by considering the integral $I^\pm_{\boldsymbol{\rho}}$. Using the definition of $g_\beta(\boldsymbol{\rho})$ $I^\pm_{\boldsymbol{\rho}}$ can be written as

$$I^\pm_{\boldsymbol{\rho}}(\beta_5, \beta_6 : \boldsymbol{q}_\parallel) = \int_0^{R_0} d\rho\rho R^*_{\beta_5}(\rho) R_{\beta_6}(\rho) \left[\frac{1}{2\pi}\int_0^{2\pi} d\varphi e^{i([m_6-m_5]\varphi \pm q_\parallel\rho\cos(\varphi-\varphi_\parallel))}\right],$$

where we have used $\boldsymbol{q}_\parallel\cdot\boldsymbol{\rho} = q_\parallel\rho\cos(\varphi-\varphi_\parallel)$, with $\varphi_\parallel$ being the angle of $\boldsymbol{q}_\parallel$ with respect to the x-axis. The angular integral in square brackets can be rewritten to an expression involving Bessel functions, like those in the ρ integral. For this we use the following integral representation of the Bessel function [57, p. 684]

$$J_m(x) = \frac{i^{-m}}{2\pi}\int_0^{2\pi} d\gamma e^{i[m\gamma + x\cos(\gamma)]}, \quad m = 0, 1, 2, 3, \ldots$$

and the fact that the integrand in the angular integral is 2π-periodic. From this we obtain

$$\frac{1}{2\pi}\int_0^{2\pi} d\varphi e^{i([m_6-m_5]\varphi \pm q_\parallel\rho\cos(\varphi-\varphi_\parallel))} = e^{i(m_6-m_5)\varphi_\parallel} i^{|m_6-m_5|} J_{|m_6-m_5|}(\pm q_\parallel\rho).$$

Finally using the series representation of the Bessel function [57, p. 670] one can show that $J_m(-x) = (-1)^m J_m(x)$ and we arrive at

$$I^\pm_{\boldsymbol{\rho}}(\beta_5, \beta_6 : \boldsymbol{q}_\parallel) = 1_\pm e^{i(m_6-m_5)\varphi_\parallel} i^{|m_6-m_5|} \int_0^{R_0} d\rho\rho R^*_{\beta_5}(\rho) J_{|m_6-m_5|}(q_\parallel\rho) R_{\beta_6}(\rho), \tag{4.24}$$

where

$$1_{\pm} = \begin{cases} 1, & +q_{\parallel}\rho \\ (-1)^{|m_6-m_5|}, & -q_{\parallel}\rho. \end{cases}$$

The most demanding part can now be identified as the integral

$$I_J(\beta_5, \beta_6 : q_{\parallel}) = \int_0^{R_0} d\rho\rho R^*_{\beta_5}(\rho) J_{|m_6-m_5|}(q_{\parallel}\rho) R_{\beta_6}(\rho), \tag{4.25}$$

which has to be evaluated numerically. It should be noted that an analytical expression exists for this integral when $R_0 \to \infty$, see eq. ([1.] 6.578) in [58]. This is not the case for our system, but it could possibly yield an excellent approximation under certain conditions, this has however not been investigated further.

The $\boldsymbol{q}_{\parallel}$ sum in eq. (4.21) can be transformed into an integral, assuming that the quantization area is large. Hence we make the substitution [28, p. 38]

$$\frac{1}{A}\sum_{\boldsymbol{q}_{\parallel}} \to \frac{1}{(2\pi)^2}\int d\boldsymbol{q}_{\parallel} = \frac{1}{(2\pi)^2}\int_0^{2\pi} d\varphi_{\parallel}\int_0^{\infty} dq_{\parallel} q_{\parallel}. \tag{4.26}$$

Due to our choice of basis set the only place $\varphi_{\parallel}$ enters is through the exponential in eq. (4.24), therefore it is possible to perform this integration analytically which is a nice simplification. Applying the rule eq. (4.26) we can write $V_{\beta_4\beta_3,\beta_1\beta_2}$ as

$$\begin{aligned} V_{\beta_4\beta_3,\beta_1\beta_2} = \frac{1}{2\pi}\int_0^{\infty} dq_{\parallel} q_{\parallel} V_{q_{\parallel}} \\ \times i^{|m_1-m_4|} I_J(\beta_4, \beta_1 : q_{\parallel})(-1)^{|m_2-m_3|} i^{|m_2-m_3|} I_J(\beta_3, \beta_2 : q_{\parallel}) I_z(\beta_4, \beta_3, \beta_1, \beta_2 : q_{\parallel}) \\ \times \underbrace{\frac{1}{2\pi}\int_0^{2\pi} d\varphi_{\parallel} e^{i[(m_1-m_4)+(m_2-m_3)]\varphi_{\parallel}}}_{=\delta_{m_1+m_2,m_3+m_4}}, \end{aligned} \tag{4.27}$$

where the integral in the last line provides us with a selection rule in the angular momentum quantum number m. The selection rule in the m's reflects the underlying symmetry of the basis functions, and basically tells us that the total angular momentum (the sum of the two participating particles) in the z-direction is conserved. The delta function can further be used on the exponents of i and -1 in the second line to yield unity

$$i^{|m_1-m_4|}(-1)^{|m_2-m_3|} i^{|m_2-m_3|}\delta_{m_1+m_2,m_3+m_4} = 1 \times \delta_{m_1+m_2,m_3+m_4}.$$

Going back to eq. (4.27) we can insert $V_{q_{\parallel}}$ from eq. (4.13), where the $1/q_{\parallel}$ singularity is canceled by the volume element in the $q_{\parallel}$ integral, and we obtain a simplified expression for the Coulomb matrix element of a basis state

$$V_{\beta_4\beta_3,\beta_1\beta_2} = \frac{e^2}{4\pi\varepsilon}\int_0^{\infty} dq_{\parallel} I_J(\beta_4, \beta_1 : q_{\parallel}) I_J(\beta_3, \beta_2 : q_{\parallel}) I_z(\beta_4, \beta_3, \beta_1, \beta_2 : q_{\parallel}) \times \delta_{m_1+m_2,m_3+m_4}. \tag{4.28}$$

Next we take a closer look at some of the properties of the integrals I_J and I_z, which constitute the basic building blocks for calculating the Coulomb matrix elements.

Properties of I_J

From eq. (4.28) it is apparent that the integration parameter $q_{\parallel}$ in principle should be varied continuously from 0 to ∞, this is however impossible to do numerically and in practise not necessary either. The electronic states we consider are all relatively low in energy and hence we will be able to limit the size of

the Hilbert space for the basis states used in the expansion eq. (4.19). This means that we can define some upper cut-off for the quantum number, β, characterizing the basis. Having put an upper limit on β we can make some qualitative statements on the integral I_J, eq. (4.25), as a function of $q_\parallel$, more specifically on the limiting cases of very small and very large $q_\parallel$.

For very small $q_\parallel$ the Bessel function in eq. (4.25) containing $q_\parallel$ will have the following dependency on $q_\parallel$: $J_{|m|}(q_\parallel\rho \to 0) \propto (q_\parallel\rho)^{|m|}$, which is seen from its series representation [57, p. 670]. This tells us that for $|m| \neq 0$, I_J will always give zero, while for $|m| = 0$ we get $J_{|m|}(q_\parallel\rho \to 0) \to 1$ and hence the value of I_J will depend on the mutual orthogonality of the g_β's. These two observations can be written collectively as

$$I_J(\beta_5, \beta_6 : q_\parallel \to 0) \to \delta_{m_5,m_6}\delta_{l_5,l_6}. \tag{4.29}$$

For very large $q_\parallel$ the Bessel function $J_{|m|}(q_\parallel\rho)$ will oscillate much more rapidly than the other two Bessel functions, and hence the integral will average to zero

$$I_J(\beta_5, \beta_6 : q_\parallel \to \infty) \to 0. \tag{4.30}$$

These two statements are illustrated in figure 4.8, where relatively low energy basis states are shown in figures 4.8(a) and 4.8(c) and a relatively high energy basis states are shown in figures 4.8(b) and 4.8(d). The first thing ones notices, when comparing the high and low energy cases, is that the cut-off in $q_\parallel$ seems to come at a lower value for the low energy states than for the high energy states. This is understandable in the light of eq. (4.30), as $J_{|m|}(q_\parallel\rho)$ faster becomes highly oscillatory compared to the low energy states than compared to the high energy states, and hence the integral will average to zero at a lower $q_\parallel$ for the low energy states than for the high energy ones. The cut-off value in $q_\parallel$ depends highly on R_0, see figure 4.2, but in a very simple way and scales basically linearly with R_0, as can be seen by introducing a unitless radial coordinate, $\tilde{\rho} = \rho/R_0$, in eq. (4.25). It is also apparent that the high energy states have more structure below their cut-off and therefore require a finer sampling in $q_\parallel$ in order to yield correct results. This makes the high energy states much more challenging numerically, for which reason it is important to make sure that ones performs the minimum amount of numerical calculations required. One way to minimize this number is to make use of the symmetries I_J possesses in its β quantum numbers, these symmetries will be discussed next.

From its definition, eq. (4.25),

$$I_J(m_5l_5, m_6l_6 : q_\parallel) = \int_0^{R_0} d\rho\rho R^*_{|m_5|l_5}(\rho)J_{|m_6-m_5|}(q_\parallel\rho)R_{|m_6|l_6}(\rho),$$

we have deduced the symmetries of I_J

$$\begin{aligned}
I_J(m_5l_5, m_6l_6 : q_\parallel) &= I^*_J(m_6l_6, m_5l_5 : q_\parallel) && \text{(4.31a)}\\
&= I_J(m_6l_6, m_5l_5 : q_\parallel),\ \text{sign}(m_5) = \text{sign}(m_6), && \text{(4.31b)}\\
I_J(\mp m_5l_5, \pm m_6l_6 : q_\parallel) &= I^*_J(\mp m_6l_6, \pm m_5l_5 : q_\parallel) && \text{(4.31c)}\\
&= I_J(\mp m_6l_6, \pm m_5l_5 : q_\parallel),\ \text{sign}(m_5) \neq \text{sign}(m_6). && \text{(4.31d)}
\end{aligned}$$

The sign of the m's matters as there appears a difference in m_5 and m_6 in I_J. The number of different permutations of m and l in I_J equals $(2 \times m_{\max} + 1)^2 l^2_{\max}$, this times the numbers of sampling points of $q_\parallel$, which is usually a few hundreds, is the number of integrals needed to be calculated numerically. For illustration we choose the numbers $m_{\max} = 10$ and $l_{\max} = 50$, which are reasonable for a typical QD/WL system. Plugging in these numbers we get $(2 \times m_{\max} + 1)^2 l^2_{\max} = 1102500$, while application of eq. (4.31) reduces this number to 276775, roughly a factor of 4 lower. This factor of 4 is however not representative for the computation time spend. This is so as high energy states are more oscillatory than low energy ones, and thus the sampling in ρ, used in the numerical quadrature, needs to be correspondingly finer, leading to longer computation time. The factor of 4 is thus a lower bound for the speed up in computation time. Parallelization is possible for each I_J and hence leads to further efficiency, but the calculation of all the integrals I_J is still a considerable numerical task.

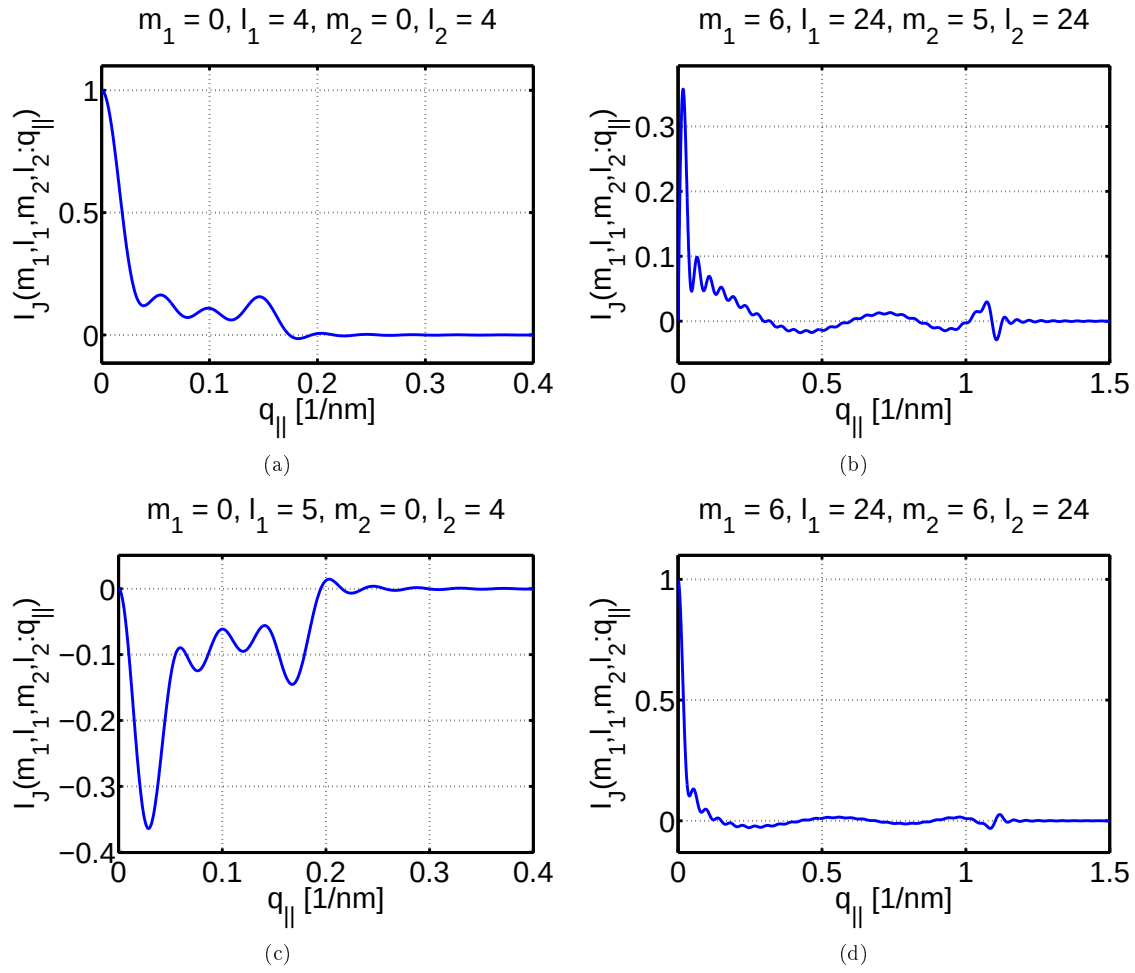

Figure 4.8.: *Examples of the integral I_J, eq. (4.25), illustrating the behavior stated in eqs. (4.29) and (4.30). It should be noticed that I_J is dependent on R_0, see figure 4.2, as the basis functions also depend on this. For these illustrations we used $R_0 = 150$ nm.*

Properties of I_z

As for I_J the in-plane wavevector $q_\parallel$ must be varied between 0 and ∞ in the integral I_z, and as for I_J we can give some general statements in these two limits. From eq. (4.23)

$$I_z(n_{z4}, n_{z3}, n_{z1}, n_{z2} : q_\parallel) = \int dz dz' Z^*_{n_{z4}}(z) Z^*_{n_{z3}}(z') e^{-q_\parallel |z-z'|} Z_{n_{z1}}(z) Z_{n_{z2}}(z'),$$

it is clearly seen that for $q_\parallel \to 0$, the exponential $e^{-q_\parallel |z-z'|}$ will tend toward unity and the 2D integral can be separated into two 1D integrals. Due to the orthogonality of the Z_n's we obtain the following simple result

$$I_z(n_{z4}, n_{z3}, n_{z1}, n_{z2} : q_\parallel \to 0) \to \delta_{n_{z4}, n_{z1}} \delta_{n_{z3}, n_{z2}}, \tag{4.32}$$

similar to the $q_\parallel \to 0$ limit for I_J. For very large $q_\parallel$ the exponential $e^{-q_\parallel |z-z'|}$ will dampen the integrand so strongly that it will give zero for sufficiently large $q_\parallel$. On the diagonal in the (z, z')-plane we have $z - z' = 0$ and hence the exponential will always be 1 regardless of the value of $q_\parallel$, however this infinitely thin line has integral measure zero and will therefore not contribute to a finite value of the entire integral.

Hence for $q_{\|} \to \infty$ we have

$$I_z(n_{z4}, n_{z3}, n_{z1}, n_{z2} : q_{\|} \to \infty) \to 0. \tag{4.33}$$

To illustrate eqs. (4.32) and (4.33) we show in figure 4.9 three examples of I_z. One immediately notices

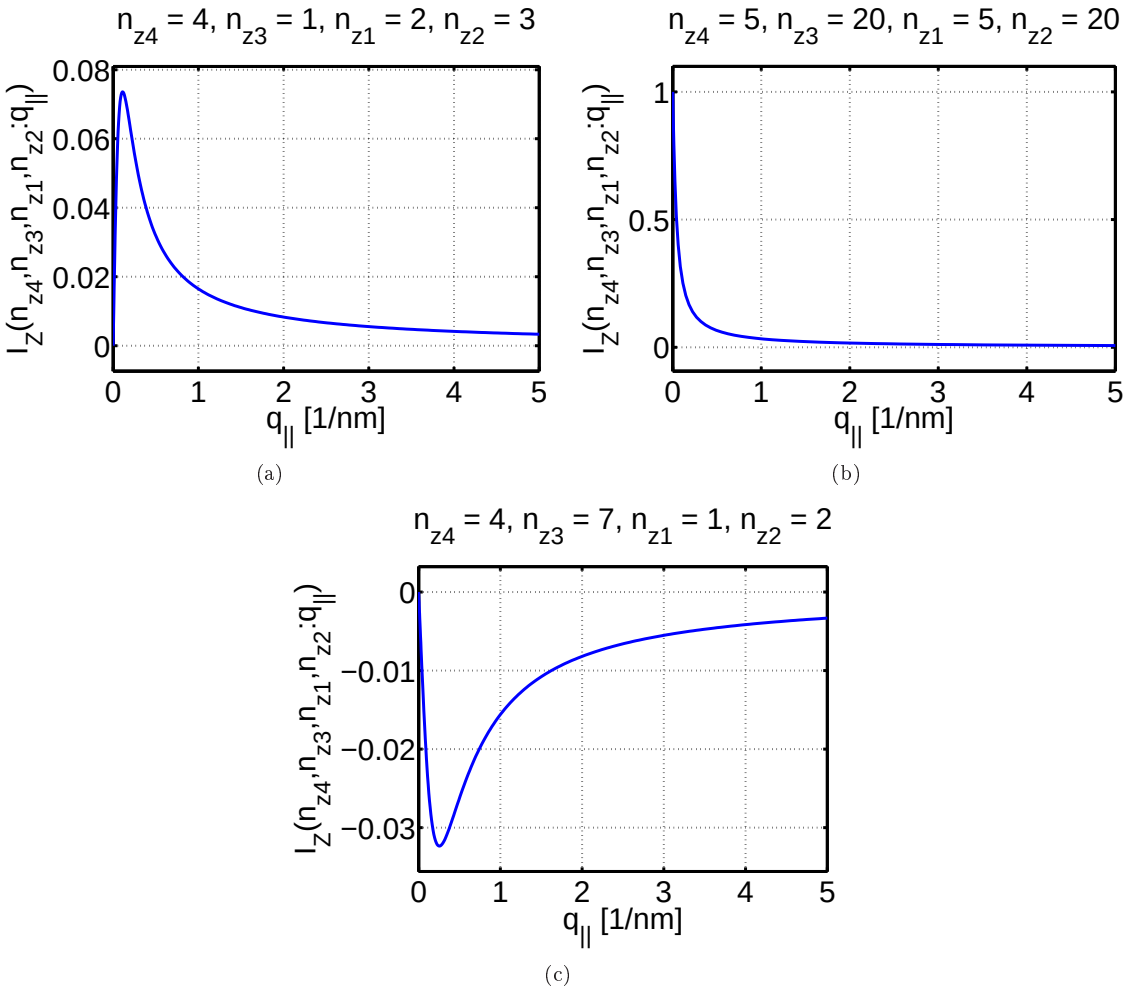

Figure 4.9.: *Examples of the integral I_z, eq. (4.23), illustrating the behavior stated in eqs. (4.32) and (4.33). It should be noticed that I_z is dependent on L_z, see figure 4.2, as the basis functions also depend on this. For these illustrations we used $L_z = 60$ nm.*

that all three curves are remarkably similar, except for the dips at $q_{\|} = 0$, when comparing to I_J. In fact all I_z's that have been manually inspected display one of these three kinds of qualitative behavior as a function of $q_{\|}$. The slow convergence towards zero for large $q_{\|}$ is also characteristic for I_z, but this is usually not a problem as I_J often has the smallest cut-off and therefore the long tail of I_z does not need to be determined. The absolute value of the cut-off depends on L_z, see figure 4.2. Comparing again to I_J, I_z shows very little structure as a function of $q_{\|}$, which is very good news as much fewer sampling points are needed and interpolation can be used for obtaining the values corresponding to the more dense sampling required by I_J.

The values of I_z are obtained by performing 2D integrals numerically, which is much more demanding than performing 1D integrals, from which I_J is calculated. To give an idea of the magnitude, consider a 1D function that needs N function evaluations in order to meet some tolerance set on its integrated value, the corresponding 2d integration would then need roughly N^2 evaluations to yield the same accuracy,

N^3 for 3D and so on. If the function values are computationally expensive to obtain, higher dimensional integrals can be very very demanding to calculate numerically. This is also one of the reasons for choosing the current approach for evaluation of the Coulomb matrix elements, that initially is determined from a 6D integral.

From the discussion above it is apparent that it is very important to exploit potential symmetries and selection rules of I_z, even more than for I_J. We will now address this issue. From eq. (4.23) one can show the following symmetries for the integral I_z

$$I_z(n_{z4}, n_{z3}, n_{z1}, n_{z2} : q_\parallel) = I_z^*(n_{z1}, n_{z2}, n_{z4}, n_{z3} : q_\parallel) = I_z(n_{z1}, n_{z2}, n_{z4}, n_{z3} : q_\parallel) \tag{4.34a}$$

$$= I_z(n_{z3}, n_{z4}, n_{z2}, n_{z1} : q_\parallel) \tag{4.34b}$$

$$= I_z^*(n_{z2}, n_{z1}, n_{z3}, n_{z4} : q_\parallel) = I_z(n_{z2}, n_{z1}, n_{z3}, n_{z4} : q_\parallel), \tag{4.34c}$$

note the similarity with eq. (4.9). Furthermore it is possible to determine a selection rule for I_z by making the following coordinate transformation

$$z \to -z, \quad z' \to -z',$$

which does not change the value of the integral, but yields the following relation in the n_z's

$$I_z(n_{z4}, n_{z3}, n_{z1}, n_{z2} : q_\parallel) = (-1)^{n_{z4}+n_{z3}+n_{z1}+n_{z2}+4} I_z(n_{z4}, n_{z3}, n_{z1}, n_{z2} : q_\parallel).$$

Here we have used the parity of $Z_{n_z}(z)$, $Z_{n_z}(-z) = (-1)^{1+n_z} Z_{n_z}(z)$ see appendix A.7, and the fact that $e^{-q_\parallel|z-z'|}$ is even under inversion in the (z, z')-plane[6]. This tells us that unless the sum of the quantum numbers n_z is an even number, the integral I_z is identically zero. This can be formulated mathematically using the modulus operation as follows

$$I_z(n_{z4}, n_{z3}, n_{z1}, n_{z2} : q_\parallel) = I_z(n_{z4}, n_{z3}, n_{z1}, n_{z2} : q_\parallel)\delta_{\mathrm{mod}(n_{z4}+n_{z3}+n_{z1}+n_{z2},2),0}. \tag{4.35}$$

This condition simply means that the product of the four Z_{n_z}'s in I_z must be an even function, like $e^{-q_\parallel|z-z'|}$, in order for the integral to yield a non-zero value, which could have been intuitively expected. The fact that the integrand has even inversion symmetry means one can limit the integration domain to half the (z, z')-plane, resulting in a significant speed up, roughly a factor of 2, in terms of cpu time. To give an idea of the reduction in computation time achieved by applying the symmetries eq. (4.34) and the selection rule eq. (4.35), consider a cut-off of $n_{z,\max} = 25$. This gives $n_{z,\max}^4 = 390625$ permutations of n_z in I_z, using the symmetries and selection rule this number reduces to 49297, almost a factor of 8. Similar to the calculation of I_J, calculation of I_z with high energy states is more time consuming and thus the factor of 8 is the minimum gain. On top of the number of permutations in the basis indices the sampling of $q_\parallel$ adds another dimesion. For I_z usually around 50 sampling point of $q_\parallel$ are needed, with the majority clustered near $q_\parallel = 0$. Again, as for I_J, parallelization is possible for each I_z.

Collecting everything we arrive at the final simplified expression for the Coulomb matrix element

$$V_{\alpha_4\alpha_3,\alpha_1\alpha_2} = \sum_{\substack{\beta_1\beta_2 \\ \beta_3\beta_4}} \left[A_{\beta_4}^{\alpha_4}\right]^* \left[A_{\beta_3}^{\alpha_3}\right]^* A_{\beta_1}^{\alpha_1} A_{\beta_2}^{\alpha_2} \times \delta_{b_4,b_1}\delta_{b_3,b_2} \times V_{\beta_4\beta_3,\beta_1\beta_2}$$
$$\times \delta_{m_1+m_2,m_3+m_4} \times \delta_{\mathrm{mod}(n_{z4}+n_{z3}+n_{z1}+n_{z2},2),0}, \tag{4.36}$$

with $V_{\beta_4\beta_3,\beta_1\beta_2}$ being given by

$$V_{\beta_4\beta_3,\beta_1\beta_2} = \frac{e^2}{4\pi\varepsilon} \int_0^\infty dq_\parallel I_J(\beta_4, \beta_1 : q_\parallel) I_J(\beta_3, \beta_2 : q_\parallel) I_z(\beta_4, \beta_3, \beta_1, \beta_2 : q_\parallel)$$
$$\times \delta_{\mathrm{mod}(n_{z4}+n_{z3}+n_{z1}+n_{z2},2),0} \times \delta_{m_1+m_2,m_3+m_4}. \tag{4.37}$$

[6] This result could also have been reached using the more formal methods of group theory. Here one would introduce the (z, z')-plane parity operator $P_{zz'}$, defined by $P_{zz'}f(z, z') = f(-z, -z')$, and look for the eigenvalues of $P_{zz'}$ with the involved functions.

4.3.3. Representation in separable eigenstates

For very shallow, that is small height, QDs it becomes a good approximation to assume that the electronic envelope function can be factored into a function for each spatial direction [55]. The philosophy is that for shallow QDs, the effective envelope for the z-direction is very similar for the various types of states we encounter: bound QD states, quasi-bound states, and unbound WL states. And hence ultimately one can use the same z-envelope for all states, yielding faster computation times and hopefully fairly accurate results (see section 4.3.4). In this approximation we write the envelope as follows

$$F_\alpha^{\text{eff}}(\boldsymbol{r}) = \Phi_m(\varphi)R_\alpha^{\text{eff}}(\rho)Z_\alpha^{\text{eff}}(z) = g_\alpha^{\text{eff}}(\boldsymbol{\rho})Z_\alpha^{\text{eff}}(z), \quad \alpha = (b, m, N), \tag{4.38}$$

where due to symmetry the angular part is exact. One possible definition of the effective functions is described in the next subsection. Inserting eq. (4.38) into eq. (4.18), with the Coulomb potential Fourier transformed, we obtain

$$\begin{aligned} V_{\alpha_4\alpha_3,\alpha_1\alpha_2} = \frac{1}{A}\sum_{\boldsymbol{q}_\parallel} V_{q_\parallel} \times \delta_{b_4,b_1}\delta_{b_3,b_2} \\ \times \int d\boldsymbol{\rho}[g_{\alpha_4}^{\text{eff}}(\boldsymbol{\rho})]^* e^{i\boldsymbol{q}_\parallel\cdot\boldsymbol{\rho}} g_{\alpha_1}^{\text{eff}}(\boldsymbol{\rho}) \int d\boldsymbol{\rho}'[g_{\alpha_3}^{\text{eff}}(\boldsymbol{\rho}')]^* e^{-i\boldsymbol{q}_\parallel\cdot\boldsymbol{\rho}'} g_{\alpha_2}^{\text{eff}}(\boldsymbol{\rho}') \\ \times \int dz dz'[Z_{\alpha_4}^{\text{eff}}(z)]^*[Z_{\alpha_3}^{\text{eff}}(z')]^* e^{-q_\parallel|z-z'|} Z_{\alpha_1}^{\text{eff}}(z) Z_{\alpha_2}^{\text{eff}}(z'). \end{aligned}$$

The procedure executed in section 4.3.2 can now be repeated here and the end result is

$$\begin{aligned} V_{\alpha_4\alpha_3,\alpha_1\alpha_2} = \frac{e^2}{4\pi\varepsilon}\int_0^\infty dq_\parallel I_J^{\text{eff}}(\alpha_4,\alpha_1 : q_\parallel) I_J^{\text{eff}}(\alpha_3,\alpha_2 : q_\parallel) I_z^{\text{eff}}(\alpha_4,\alpha_3,\alpha_1,\alpha_2 : q_\parallel) \\ \times \delta_{b_4,b_1}\delta_{b_3,b_2} \times \delta_{m_1+m_2,m_3+m_4}. \end{aligned} \tag{4.39}$$

In analogy with eqs. (4.23) and (4.25) we have introduced the following notation

$$\begin{aligned} I_J^{\text{eff}}(\alpha_5,\alpha_6 : q_\parallel) &= \int_0^{R_0} d\rho\rho[R_{\alpha_5}^{\text{eff}}(\rho)]^* J_{|m_6-m_5|}(q_\parallel\rho) R_{\alpha_6}^{\text{eff}}(\rho), \\ I_z^{\text{eff}}(\alpha_4,\alpha_3,\alpha_1,\alpha_2 : q_\parallel) &= \int dz dz'[Z_{\alpha_4}^{\text{eff}}(z)]^*[Z_{\alpha_3}^{\text{eff}}(z')]^* e^{-q_\parallel|z-z'|} Z_{\alpha_1}^{\text{eff}}(z) Z_{\alpha_2}^{\text{eff}}(z'). \end{aligned}$$

One definition of the effective functions

Our starting point for defining the effective functions in eq. (4.38) is the general expansion of the envelope function, eq. (4.19), in terms of the basis given by eq. (4.20)

$$F_\alpha(\boldsymbol{r}) = \sum_\beta A_\beta^\alpha B_\beta(\boldsymbol{r}).$$

The spatial quantum number characterizing an envelope function is written as

$$\alpha = (b, m, N),$$

where m is the eigenvalue of the z component of the angular momentum operator (see appendix A.7), N is a quantum number describing the (ρ, z)-plane, and b is a band index. The spatial quantum number characterizing a basis state is

$$\beta = (m, l, n_z),$$

see appendix A.7 for details. It should be emphasized that for a rotationally symmetric system, the z component of the angular momentum operator is a conserved quantity and m is therefore a good

quantum number. We will always consider such systems and therefore the angular part of the envelope and basis function will always be same. More specifically, we write the expansion of the envelope as follows

$$F^b_{m,N}(\boldsymbol{r}) = \sum_{ln_z} A^b_m(N : l, n_z) B_{mln_z}(\boldsymbol{r}). \tag{4.40}$$

To motivate the definition of the effective functions one can consider an explicit set of coefficients, e.g. as shown in figure 4.10 for a typical QD ground state; this specific state has the label $(b, m, N) = (\mathrm{c}, 0, 1)$. The geometry is the same as in section 4.2.3, except for R_0 which is 75 nm in these calculations. The first thing one notices is that the coefficients decay as we go to higher and higher quantum numbers in both the radial and z direction, as is expected when considering a localized state. Next it is very apparent how rows for even n_z have a much less amplitude than those for odd n_z, this is simply a manifestation of the fact that the wavefunction is almost symmetric about the (x, y)-plane. To define the effective function it seems intuitively correct to focus on the coefficients that have large amplitudes, as these must be the most significant. For this purpose we identify the coefficient with the largest amplitude and denote its indexes with stars as superscripts: (l^*, n_z^*). We now propose to define the effective functions $R^{b,\mathrm{eff}}_{|m|,N}(\rho)$ and $Z^{b,\mathrm{eff}}_{|m|,N}(z)$ in the following way

$$R^{b,\mathrm{eff}}_{|m|,N}(\rho) = \sum_l C^{R,b}_l(m, N) R_{|m|,l}(\rho), \quad C^{R,b}_l(m, N) = \xi \frac{A^b_m(N : l, n_z^*)}{\sqrt{\sum_l |A^b_m(N : l, n_z^*)|^2}},$$

$$Z^{b,\mathrm{eff}}_{|m|,N}(\rho) = \sum_{n_z} C^{Z,b}_l(m, N) Z_{n_z}(z), \quad C^{Z,b}_{n_z}(m, N) = \xi \frac{A^b_m(N : l^*, n_z)}{\sqrt{\sum_{n_z} |A^b_m(N : l^*, n_z)|^2}},$$

where $\xi = \mathrm{sign}[A^b_m(N : l^*, n_z^*)]$ is a phase factor that ensures that the effective functions have the same phase as as the original function. Notice that the effective coefficients have been renormalized in order for the effective functions to be normalized to unity. The coefficients used in the effective functions are shown graphically in figure 4.10, where the horizontal line indicates those used for R^{eff} while the vertical line indicates those used for Z^{eff}. In order for this approximation to be good, the two lines should cover as much "weight" as possible, that is $\sum_\perp |A^b_m(N : l, n_z)|^2$ should be as close to unity as possible, where $\perp$ indicate the black lines in figure 4.10. A limiting case where this approximation is exact is for the pure WL state, where no dot potential is present in the geometry. For this system the eigenstates are completely separable and for the radial direction the solutions are Bessel functions, the same ones as we use as our basis (see appendix A.7), hence by definition the factorization procedure is exact for these states.

This specific definition of the effective functions suffers from a potentially very serious drawback, namely that the mutual orthogonality of the effective functions is not guarantied in this simple minded separation procedure. This is however only an issue when considering the overlap between states of equal m, for different m the integration over the exact angular functions ensures the orthogonality. But for equal m we have the situation

$$\langle F^{\mathrm{eff}}_\alpha | F^{\mathrm{eff}}_{\alpha'} \rangle = \langle R^{\mathrm{eff}}_\alpha | R^{\mathrm{eff}}_{\alpha'} \rangle \langle Z^{\mathrm{eff}}_\alpha | Z^{\mathrm{eff}}_{\alpha'} \rangle \neq 0, \quad N \neq N', \quad m = m', \quad b = b'.$$

The importance of having orthogonal wavefunctions depends on what should be calculated using these wavefunctions. In the case of Coulomb matrix elements orthogonality is crucial, as seen from e.g. figure 4.8 where the point $q_\parallel = 0$ corresponds to the pure overlap of two effective radial functions and thus it must always be zero for different functions. The actual impact of this non-orthogonality will be investigated in the next subsection.

4.3.4. Comparison of exact and effective Coulomb matrix elements

In this subsection we will perform a numerical comparison between the Coulomb matrix elements calculated using the exact expression eq. (4.36) and those obtained through the effective expression eq. (4.39). The

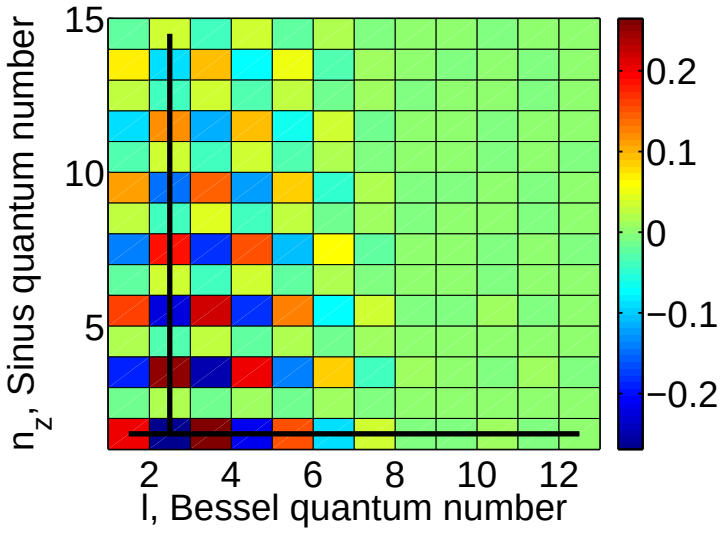

Figure 4.10.: *Plot showing the coefficient* $A_0^c(1:l,n_z)$ *in the expansion eq.* (4.40). *The vertical and horizontal black lines indicate which coefficients that are used in the definition of the effective functions in eq.* (4.38).

comparison is performed to estimate the validity of the factorization procedure described in section 4.3.3. More specifically we test whether the separated wavefunctions provide a good description and how big a role the non-orthogonality of the separated wavefunctions play.

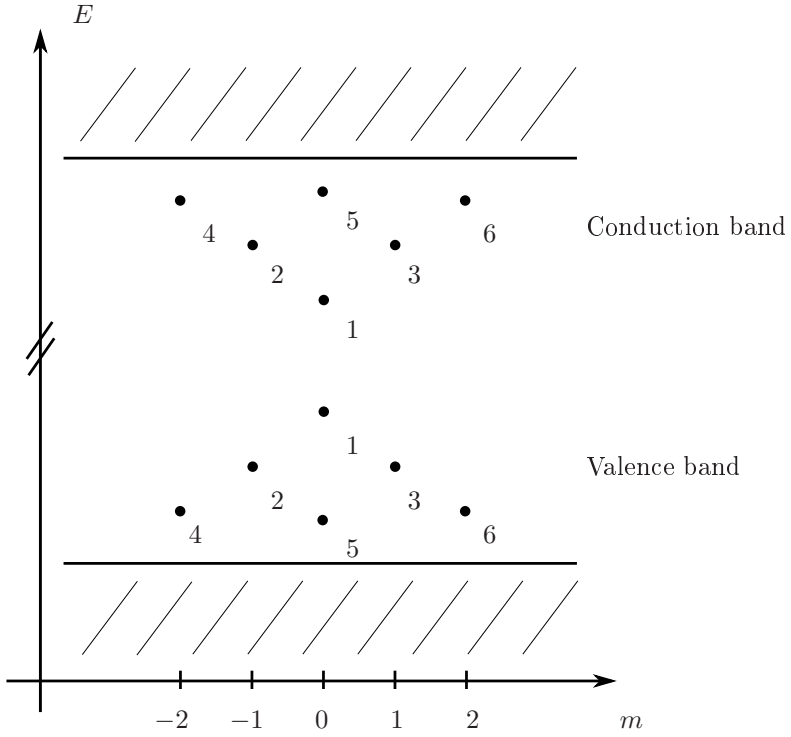

Figure 4.11.: *Schematic illustration of the level structure of the QD presented in section 4.2.3.*

We focus on the same QD/WL geometry as in section 4.2.3, with the exception that $R_0 = 75$ nm in these calculations. A schematic of the level structure is shown in figure 4.11 where the level notation is indicated, a more detailed version can be found in figure 4.5. We only perform the comparison for the clearly bound QD states, as the factorization approximation is expected to be worst for these states, and

therefore attention is not payed to the delocalized WL states, where the factorization approximation is expected to be much better.

A representative selection of Coulomb elements is shown in table 4.2, where four different classes of elements are presented, separated by the horizontal lines. The first class is that of two electrons in the same spatial state scattering with each other into the same state and can be thought of as a classical electrostatic interaction energy between two (equal) charge distributions given by the wavefunction squared. The second class is similar to the first, but now the electrons are in different spatial states and hence these elements can be expected to be smaller than the first class, as the spatial overlap between the two charge distributions is smaller. The two first classes of elements, which can be interpreted classically, are usually called direct elements. The third class contains elements of true quantum mechanical scattering events, that is where the electrons are scattered to new states and hence this process can not be thought of classically as the interaction of two charge distributions. These elements are usually called exchange elements, due to their quantum nature. The fourth class comprises elements giving rise to excitonic effects, as these describe the repulsion of electrons in the conduction band with electrons in the valence band. For the first three classes we only consider processes in the conduction band, as those for the valence band are very similar in magnitude, due to our choice of band parameters, which provide very similar wavefunctions for the two bands, see appendix A.8. For each set of elements we have calculated the absolute and relative error of the effective description, defined in the following way

$$\text{absolute error } = |V_{\text{exact}} - V_{\text{eff}}|, \quad \text{relative error } = \frac{|V_{\text{exact}} - V_{\text{eff}}|}{|V_{\text{exact}}|}.$$

In general we observe values ranging from 1 to 14 meV, with the direct elements being clearly larger than the exchange elements. This is an effect easily understood mathematically in terms of the overlap integrals, but it also makes sense physically since electrons that are closer spatially interact more strongly. For almost all the elements considered here the relative error is below one percent, which is perhaps a bit surprising considering the rather simple definition of the effective wavefunctions we have employed. It should be noted that none of the elements in classes one, two, and four suffer from the non-orthogonality issues described in the previous section, as they are either direct elements or exchange elements arising from scattering between states of different angular momentum (and thus orthogonality is ensured). The exchange element in the third class does, however, describe a scattering event between states of equal angular momentum and here the non-orthogonality is expected to play a role. This element also has a significantly higher relative error than any of the other considered elements, which is in part expected to originate from the non-orthogonality. To test this presumption a Gram-Schmidt orthogonalization algorithm was applied to the $m = 0$ subspace which states (c,1) and (c,5) belong to, to make sure that the states where orthogonal. This lowered the relative error on V_{5313}^{cccc} to around 6 % from 8.3 % indicating that non-orthogonality does indeed have an effect. A fundamental problem does, however, arise when applying various orthogonalization procedures to non-orthogonal quantum states. The issue is that the procedure is unconstrained, in the sense that it has no connection to the underlying physical equation and hence it is not ensured that the orthogonalized states continues to be eigenstates of the physical equation. Due to this issue and the fact that only a small number of the exchange elements, which typically have a small magnitude compared to other elements, are seriously affected by the non-orthogonality the states were left not orthogonalized.

$V^{b_4b_3b_1b_2}_{\alpha_4\alpha_3\alpha_1\alpha_2}$	Exact [meV]	Effective [meV]	Absolute error [μeV]	Relative error [%]
V^{cccc}_{1111}	13.6855	13.6621	23.4464	0.171
V^{cccc}_{5555}	9.80818	9.63959	168.590	1.72
V^{cccc}_{3333}	10.7314	10.6882	43.2419	0.403
V^{cccc}_{6666}	9.33722	9.27056	66.6584	0.714
V^{cccc}_{1515}	10.9611	10.8305	130.671	1.20
V^{cccc}_{1313}	11.5185	11.4823	36.1249	0.314
V^{cccc}_{1616}	9.94670	9.89138	55.3118	0.556
V^{cccc}_{5353}	9.63071	9.53662	94.0926	0.977
V^{cccc}_{5656}	8.89239	8.80978	82.6087	0.929
V^{cccc}_{3636}	9.79372	9.73499	58.7227	0.600
V^{cccc}_{5313}	1.13377	1.03971	94.0645	8.30
V^{cvcv}_{1331}	3.15866	3.14862	10.0423	0.318
V^{cvcv}_{1111}	13.6236	13.6005	23.1121	0.170
V^{cvcv}_{1515}	10.8932	10.7954	97.8453	0.898

Table 4.2.: *Table for comparison of Coulomb matrix elements calculated using the exact expression given by eq.* (4.36) *and the effective expression given by eq.* (4.39)*. For these calculations a background dielectric constant of* $\varepsilon/\varepsilon_0 = 13.6$ *was used.*

4.4. Optical dipole matrix elements

In this section we briefly describe the calculation of the matrix elements entering the quantum and classical light-matter interaction Hamiltonians, eqs. (3.19) and (3.21) respectively. According to eqs. (3.20) and (3.22) the matrix element is mainly determined by an apparently simple overlap integral over the position operator (projected onto the electric field direction)

$$\int d\boldsymbol{r}[\phi^b_\alpha(\boldsymbol{r})]^* \boldsymbol{r}\cdot\boldsymbol{e_E}\phi_{\alpha'}(\boldsymbol{r}).$$

The integral can, however, not be calculated directly due to the fact that we are working in the effective mass approximation, and therefore do not know the Bloch part of the product wavefunction, eq. (4.16),

$$\phi^b_\alpha(\boldsymbol{r}) = F^b_\alpha(\boldsymbol{r})u_b(\boldsymbol{r}),$$

explicitly. To proceed we wish to take advantage of the different length scales governing the Bloch and envelope parts, as done with the Coulomb matrix elements in section 4.3.1, and separate the integral into parts that can be handled. This separation is much easier to perform in the $\boldsymbol{A}\cdot\boldsymbol{p}$ form of the electron-photon interaction. Therefore we remind the reader of the relation between a dipole and momentum matrix elements, see eq. (A.13),

$$\langle\phi^b_\alpha|\boldsymbol{D}\cdot\boldsymbol{e_E}|\phi^{b'}_{\alpha'}\rangle = i\frac{1}{\omega^{bb'}_{\alpha\alpha'}}\frac{e}{m}\langle\phi^b_\alpha|\boldsymbol{p}\cdot\boldsymbol{e}|\phi^{b'}_{\alpha'}\rangle, \tag{4.41}$$

showing proportionality between the two quantities. Using the full product form of the wavefunction a momentum matrix element may now be written as [53, p. 119]

$$\begin{aligned}\langle\phi^b_\alpha|\boldsymbol{p}\cdot\boldsymbol{e_E}|\phi^{b'}_{\alpha'}\rangle &= \int d\boldsymbol{r}\left[F^b_\alpha(\boldsymbol{r})u_b(\boldsymbol{r})\right]^*\boldsymbol{p}\cdot\boldsymbol{e_E}F^{b'}_{\alpha'}(\boldsymbol{r})u_{b'}(\boldsymbol{r})\\ &= \int d\boldsymbol{r}\left[F^b_\alpha(\boldsymbol{r})u_b(\boldsymbol{r})\right]^*\left\{F^{b'}_{\alpha'}(\boldsymbol{r})[\boldsymbol{p}\cdot\boldsymbol{e_E}u_{b'}(\boldsymbol{r})] + u_{b'}(\boldsymbol{r})[\boldsymbol{p}\cdot\boldsymbol{e_E}F^{b'}_{\alpha'}(\boldsymbol{r})]\right\}\\ &\approx \langle F^b_\alpha|F^{b'}_{\alpha'}\rangle\langle u_b|\boldsymbol{p}\cdot\boldsymbol{e_E}|u_{b'}\rangle + \langle F^b_\alpha|\boldsymbol{p}\cdot\boldsymbol{e_E}|F^{b'}_{\alpha'}\rangle\langle u_b|u_{b'}\rangle,\end{aligned}$$

where on the second line we used that $\boldsymbol{p}$ is a differential operator and therefore the chain rule must be applied on products, and further on the last line we separated out the slowly-varying envelope part as in eq. (4.17). If we restrict our attention to inter-band transitions, which we will only consider in this thesis, the second term vanish due to the orthogonality of the Bloch functions, i.e. $\langle u_{\mathrm{c}}|u_{\mathrm{v}}\rangle = 0$, and we are left with

$$\langle \phi^{\mathrm{c}}_{\alpha}|\boldsymbol{p}\cdot\boldsymbol{e_E}|\phi^{\mathrm{v}}_{\alpha'}\rangle = \langle F^{\mathrm{c}}_{\alpha}|F^{\mathrm{v}}_{\alpha'}\rangle \langle u_{\mathrm{c}}|\boldsymbol{p}\cdot\boldsymbol{e_E}|u_{\mathrm{v}}\rangle . \tag{4.42}$$

The part involving the Bloch function and momentum operator can be measured and is tabulated in the literature, while the simple overlap integral between the envelopes can be calculated within our effective mass theory. Fixing the polarization to the y-direction and using the formulaes of [53, appendix A 8.3] one can obtain the following expression for the momentum matrix element

$$\langle u_{\mathrm{c}}|p_y|u_{\mathrm{v}}\rangle = -i\frac{|M|}{\sqrt{2}}, \tag{4.43}$$

which holds for a typical III-V semiconductor with a single conduction band and where the valence band is taken to be the heavy hole band. For the material system we consider,$\mathrm{In}_x\mathrm{Ga}_{x-1}\mathrm{As}_x$, the parameter $|M|$ can be parameterized according to the formulae [53, p. 121]

$$|M| = \frac{m}{2}\sqrt{28.8 - 6.6x}\ [\mathrm{eV}^{\frac{1}{2}}],$$

where x is the composition fraction and the $\left[\mathrm{eV}^{\frac{1}{2}}\right]$ means the unit $\mathrm{eV}^{\frac{1}{2}}$. Inserting now eqs. (4.41), (4.42), and (4.43) into the expressions for a matrix element of the interaction Hamiltonian as derived in appendix A.3, eqs. (A.14) and (A.15), we get

$$\langle \phi^{\mathrm{c}}_{\alpha}|H_{\mathrm{i}}|\phi^{\mathrm{v}}_{\alpha'}\rangle = \frac{e|M|}{\sqrt{2}m\omega}\langle F^{\mathrm{c}}_{\alpha}|F^{\mathrm{v}}_{\alpha'}\rangle \frac{E_{0,y}}{2}.$$

We note that the only quantity left that depend on the electronic states, is the pure overlap between the involved states, the electronic transition frequency that entered eq. (4.41) has canceled. As mentioned in section 4.2.3 the electronic envelopes for conduction and valence band states are often very similar in nature, meaning that we to a good approximation can assume the following

$$\langle F^{\mathrm{c}}_{\alpha}|F^{\mathrm{v}}_{\alpha'}\rangle = \delta_{\alpha,\alpha'}. \tag{4.44}$$

This has the consequence that we only consider "direct" or "vertical" optical transitions. This yields very significant simplifications in the numerical solution of the equations of motion for the electronic density matrix, as one can neglect "indirect" optical off-diagonal elements of the density matrix as discussed in section 5.4.1.

The conclusion that can be drawn after this long series of approximations, is that all non-zero dipole matrix elements has the same value independent of which transition they refer to. For the quantized fields the dipole matrix element has to be multiplied with a few other constants that are not calculated explicitly, see eq. (3.20), and hence we might as well treat the entire coupling constant as a parameter. This will not over parameterize the equations, as often we only consider a single quantized mode. For the semi-classical interaction, eq. (3.21), the dipole matrix element is multiplied by the externally applied field and it will therefore only be this effective product, often denoted the Rabi energy, that enters the equations. For these reasons we will not explicitly evaluate the values of the dipole matrix elements, but simply refer to the effective numbers that enter the Hamiltonian.

4.5. Summary

In this chapter we considered the electronic single-particle states and the subsequent calculation of various matrix elements using these states. In the first section we setup a simplified model for describing the

single-particle electronic states bound in the QD and WL. We employed a simple effective mass model, that treats the bound and unbound states on the same footing, and solved this model for a realistic geometry using the commercial finite element package COMSOL. To illustrate the model we presented solutions for a specific geometry and discuss the nature of the different states obtained. In the second part of the chapter we discussed how to calculate the computationally demanding Coulomb matrix elements, using the numerically obtained single-particle states. We presented two ways of performing this calculation, an exact but slow formulation and an approximative but much faster method. The two approaches were compared for a specific geometry, and for most elements the fast methods yielded relative errors below 1%. In the last section calculation of matrix elements of the dipole interaction were discussed. We argued why it to a good approximation was not necessary to perform any actual numerical calculations of the elements, but rather obtain the numbers needed only using known and tabulated parameters.

5. Equations of Motion

5.1. Introduction

In this chapter we present approximate forms of the general theory derived in the two first chapters and develop the final equations of motion describing our cQED system. Selecting the appropriate approximative forms of the Hamiltonians, and subsequently the truncation of the self-energies, is really the essential part of doing theoretical many-body physics, as in general there is no chance of including all physical effects. Our choices in this process will all be guided by previous studies in the literature, with the exception of the electron-photon interaction which is not often treated in the literature. The end goal of this chapter is to formulate a set of equations describing the time evolution of our non-equilibrium system. This will be done in two steps: First we consider the equations governing the cQED system in equilibrium, as these provide the initial conditions for the general non-equilibrium system and are important input parameters in the GKBA. Secondly the actual non-equilibrium equations are developed. We treat two cases of these, namely one where the GKBA is applied to both the electronic and photonic Green's functions and one where the full two-time Green's function for the photon is treated. To our knowledge it is the first time that the two-time photon Green's function is being treated within a many-body semiconductor formalism.

5.2. Approximations

In this section we will discuss various approximations to the general semiconductor Hamiltonian presented in section 3.2.3, so that it in a feasible way describes the cQED system we wish to examine, see chapter 1. The system contains three kinds of particles, electrons, phonons, and photons, that interact. Below, we describe first the free systems, the quadratic parts of the Hamiltonian, and second the interaction parts of the Hamiltonian. In the last part we consider the truncation of the self-energies, where the actual derivation of these is performed in appendix A.5.

5.2.1. Hamiltonians

Non-interacting Hamiltonians

The electrons constitute a very important part of the system and hence a good description is needed for the single-particle states and energies. The basic QD-WL system of the electrons has already been described in section 4.2 and the band parameters in appendix A.8, hence technical details will be omitted here. To sum up the most important facts, we operate within a decoupled two-band model, with a conduction and a valence band. The localized QD states and the delocalized WL states are found from the same effective mass Schrödinger equation and hence treated on equal footing. This automatically ensures that orthogonality between the states fulfilled and that the energies are correctly described. The free Hamiltonian for the electrons is still as in eq. (3.9)

$$H_{0,\mathrm{e}} = \sum_{\nu} \hbar\omega_{\nu} c_{\nu}^{\dagger} c_{\nu},$$

but now we can elaborate on the general quantum number ν. It can be written as $\nu = (b, \alpha, \sigma)$, where b is the band index that can be either conduction (c) or valence (v), α contains other spatial quantum numbers within each band, and finally the spin is denoted by σ.

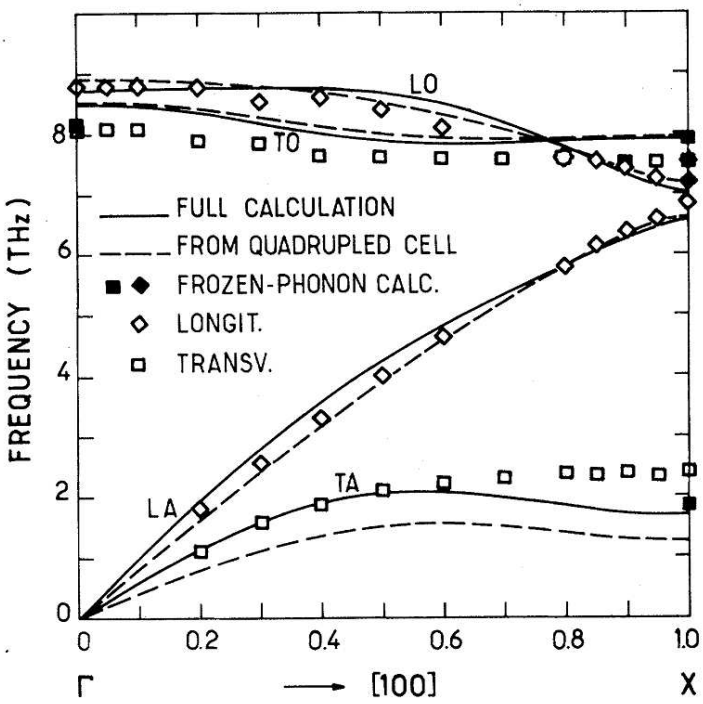

Figure 5.1.: *Model calculation of the dispersion of the various phonon branches in bulk GaAs. Taken from [59].*

Next we will discuss the free phonon Hamiltonian. In a III-V semiconductor like GaAs there exist several different kinds of lattice vibrations which eigenmodes are called phonons. These are divided into transverse and longitudinal polarizations, usually called branches with reference to their band structure diagram. Furthermore we divide them into so-called acoustical and optical phonons, where acoustical phonons in general have a linear dispersion for long wavelengths, while the optical ones have a finite energy for long wavelengths, often with very weak dispersion. To illustrate these facts regarding the dispersion of the different phonon branches, we show in figure 5.1 a model calculation for bulk GaAs. It is a textbook fact, e.g. [31, p. 325], that only longitudinal phonons set up strong polarization fields inside a crystal on which electrons can scatter efficiently, therefore only longitudinal phonons will be considered. Furthermore for scattering between discrete states in QDs, which is of the primary concern in this thesis, only longitudinal optical (LO) phonons need be considered, as longitudinal acoustical (LA) phonons do not have a large enough energy to provide efficient scattering [60, 61]. For larger wavevectors where the LA-phonon energy becomes comparable to the energy separation between the QD states (typically 20-40 meV), the scattering amplitude for the transition goes to zero[1] and therefore do not contribute either. It has however been pointed out [62, 63] that in the low temperature regime, below 150 K, LA-phonons dominate the dephasing dynamics in QD systems. Based on these arguments and facts we will restrict our attention to LO-phonons and only consider temperatures above 150 K. The LO-phonons will further be taken as dispersionless in their long wavelength limit, seen to be reasonable from figure 5.1, which is a commonly adopted approximation yielding huge computational simplifications. The free LO-phonon

[1] This tendency can be seen in figure 4.8, where the integral I_J is proportional to the amplitude for electron-phonon scattering event for both LO- and LA-phonons.

Hamiltonian can then be written as

$$H_{0,\mathrm{LO}} = \sum_{\boldsymbol{q}} \hbar\omega_{\mathrm{LO}} b^\dagger_{\boldsymbol{q}} b_{\boldsymbol{q}},$$

where $\boldsymbol{q}$ is the phonon wavevector and the zero-point energy appearing in the general form eq. (3.14) has been dropped as it is without importance in the calculations. The value of $\hbar\omega_{\mathrm{LO}}$ for GaAs is approximately 37 meV. In practice ω_{LO} is often replaced by $\omega_{\mathrm{LO}} - i\tau^{-1}_{\mathrm{LO}}$, where τ_{LO} is a phenomenological lifetime for the LO-phonons, that arise due to anharmonic processes going beyond linear spring model that is normally assumed [64]. Formally one should not simply insert a complex energy into the Hamiltonian as suggested above. This makes the Hamiltonian non-Hermitian and does not in general result in the correct dynamics, one should rather consider a dressed LO-phonon Green's function that decay with the introduced lifetime. Values of τ_{LO} found in the literature are typically in the range 1-5 ps [41, 65]. We will not consider any temperature dependence of either ω_{LO} or τ_{LO}.

In the case of the free photons we are interested in modeling a cavity with a finite lifetime. The density of states for such a cavity is characterized by having a certain width centered around the main cavity energy. The cavity peak is made up by summing over many modes supported by the photonic structure and therefore many equations would be generated to treat the photons correctly. However, as our main focus is not to provide a highly accurate description of the photonic modes and energies, we will adopt another approach that enables us to consider only a single quasi-mode of the cavity with a finite lifetime. To motivate this formally we replace the Hamiltonian eq. (3.12) for the free photons by the following

$$H_{0,\mathrm{rad}} = \hbar\omega_{\mathrm{cav}} a^\dagger_{\mathrm{c}} a_{\mathrm{c}} + \sum_l \hbar\omega_l a^\dagger_l a_l + \sum_l \left(T_l a^\dagger_{\mathrm{c}} a_l + T^*_l a^\dagger_l a_{\mathrm{c}} \right),$$

which is inspired by the tight-binding model used for electrons. This Hamiltonian describes a system of a localized mode, denoted c, and a continuum of delocalized leaky modes, denoted by l, where an amplitude exists, T^*_l, for the process where a photon can "tunnel" from the localized mode and into the continuum and of course also the reverse process. We are interested in the effect the leaky modes have on the lifetime of an excitation in the localized cavity mode. To this end one should look for the spectral Green's functions of the system, e.g. the retarded Green's function defined by

$$A^r_{\mathrm{cc}}(\tau) = -i\hbar^{-1}\theta(\tau) \left\langle [a_{\mathrm{c}}(\tau), a^\dagger_{\mathrm{c}}] \right\rangle,$$

where we have used that the system is assumed to be in equilibrium and hence the Green's functions only depend on a single time (actually the time difference $\tau = t - t'$), see e.g. [28, p. 89]. As the Hamiltonian only contains quadratic terms, and thus does not generate the infinite hierarchy of coupled equations, $A^r_{\mathrm{cc}}(\tau)$ can be determined exactly using the Heisenberg equation of motion. This is a textbook exercise (see e.g. [28, p. 143] for the same model for electrons) and will therefore not be repeated. For one-time functions, as $A^r_{\mathrm{cc}}(\tau)$, it is often advantageous to go into the frequency domain and we employ the following time Fourier transform definition

$$f(\omega) = \int_{-\infty}^{\infty} dt e^{i(\omega + i\eta)t} f(t), \quad f(t) = \int_{-\infty}^{\infty} \frac{d\omega}{2\pi} e^{-i\omega t} f(\omega), \tag{5.1}$$

where $\eta = 0^+$ is a positive infinitesimal that ensures the existence of the Fourier transform. Physically it can be seen as adding artificial damping to the system motivated by the fact that in real physical systems no correlations lasts forever. It will however be replaced by a damping mechanisms in the physical model. The retarded Green's function for the cavity mode is given by

$$A^r_{\mathrm{cc}}(\omega) = \frac{1}{\hbar\omega - \hbar\omega_{\mathrm{cav}} - \Sigma^r_{\mathrm{cc}}(\omega)}, \quad \Sigma^r_{\mathrm{cc}}(\omega) = \sum_l \frac{|T_l|^2}{\hbar(\omega - \omega_l + i\eta)},$$

where $\Sigma^r_{\mathrm{cc}}(\omega)$ is the retarded self-energy. The self-energy can be written in terms of its real and imaginary parts $\Sigma^r_{\mathrm{cc}}(\omega) = \hbar\Lambda^r_{\mathrm{cc}}(\omega) - i\hbar\Gamma^r_{\mathrm{cc}}(\omega)$, where $\hbar\Lambda^r_{\mathrm{cc}}(\omega)$ corresponds to an energy shift and $\Gamma^r_{\mathrm{cc}}(\omega)$ to an inverse

lifetime. If we assume the self-energy to be frequency independent a Fourier transform back to the time domain yields

$$A^r_{\rm cc}(\tau) = -i\hbar^{-1}\theta(\tau)e^{-i(\omega_{\rm cav}+\Lambda^r_{\rm cc})\tau}e^{-\Gamma^r_{\rm cc}\tau},$$

clearly showing a renormalization of the energy and the acquisition of a finite lifetime when comparing to its free counterpart given by $A^{0,r}_{\rm cc}(\tau) = -i\hbar^{-1}\theta(\tau)\exp(-i\omega_{\rm cav}\tau)$. If we further assume that only the new quasi-cavity mode is spatially resonant with the electronic transitions in the QD, we can neglect the leaky modes and only treat them implicitly as a reservoir for the quasi-cavity mode and simply use the quasi-cavity mode with a finite lifetime (neglecting the unimportant energy shift). The free Hamiltonian for the cavity photons thus reduces to

$$H_{0,\rm rad} = \hbar\omega_{\rm cav}a^\dagger a, \tag{5.2}$$

where the subscript c has been dropped on the operators. To take into account the finite lifetime of the photons in the cavity, all cavity photon Green's functions should be dressed with the decay rate given by $\omega_{\rm cav}/Q$, with $Q = \omega_{\rm cav}/\Gamma^r_{\rm cc}$ being the usual Q-factor of the cavity. In the density of states picture this series of approximations yields a Lorentzian shaped cavity with a width proportional to $\hbar\omega_{\rm cav}/Q$ in energy units. This approach is commonly used in the literature, see e.g. [66].

Interacting Hamiltonians

Now we move on to discuss the many-body interaction Hamiltonians of the system. We start with electron-electron Coulomb interaction given in general by eq. (3.16). The only limitation we will put on this Hamiltonian is the inability to scatter particles across the band gap, which has already been discussed in section 4.3.1. We neglect these processes due to their very non-resonant nature and hence the Coulomb matrix element acquire two delta functions in the band indexes

$$V_{\nu_4\nu_3,\nu_1\nu_2} = V^{b_4b_3,b_1b_2}_{\alpha_4\alpha_3,\alpha_1\alpha_2} \times \delta_{b_4,b_1}\delta_{b_3,b_2}, \tag{5.3}$$

where the spin index, σ, has been absorbed into the spatial index, α. It is illustrative to write out the sums over the band indexes in the expression for $H_{\rm e-e}$ explicitly

$$H_{\rm e-e} = \frac{1}{2}\sum_{\substack{\alpha_1\alpha_2\\ \alpha_3\alpha_4}} \left\{V^{\rm cc,cc}_{\alpha_4\alpha_3,\alpha_1\alpha_2}c^\dagger_{{\rm c},\alpha_4}c^\dagger_{{\rm c},\alpha_3}c_{{\rm c},\alpha_2}c_{{\rm c},\alpha_1} + V^{\rm vv,vv}_{\alpha_4\alpha_3,\alpha_1\alpha_2}c^\dagger_{{\rm v},\alpha_4}c^\dagger_{{\rm v},\alpha_3}c_{{\rm v},\alpha_2}c_{{\rm v},\alpha_1}\right.$$
$$\left. + V^{\rm cv,cv}_{\alpha_4\alpha_3,\alpha_1\alpha_2}c^\dagger_{{\rm c},\alpha_4}c^\dagger_{{\rm v},\alpha_3}c_{{\rm v},\alpha_2}c_{{\rm c},\alpha_1} + V^{\rm vc,vc}_{\alpha_4\alpha_3,\alpha_1\alpha_2}c^\dagger_{{\rm v},\alpha_4}c^\dagger_{{\rm c},\alpha_3}c_{{\rm c},\alpha_2}c_{{\rm v},\alpha_1}\right\}.$$

The two first terms describe intra-band processes occurring in the conduction and valence bands respectively. The two last terms describe inter-band processes where particles in each band scatter on each other, but remains in their respective bands. The inter-band processes give rise to excitonic effects well known for their importance in semiconductor optics. It should also be noted that this form of the Coulomb interaction conserves the number of particles in each band, hence it does not cause recombination of electrons and holes.

As argued in the previous section, we need only consider LO phonons in the interaction between electrons and phonons. The interaction Hamiltonian between electrons and dispersionless long-wavelength LO phonons is often described by the so-called Frölich Hamiltonian [24, p. 44]

$$H_{\rm e-LO} = \sum_{\boldsymbol{q}} \frac{M}{qV^{\frac{1}{2}}}\rho(\boldsymbol{q})(b^\dagger_{-\boldsymbol{q}} + b_{\boldsymbol{q}}), \tag{5.4}$$

where $\boldsymbol{q}$ is the phonon wavevector, $\rho(\boldsymbol{q})$ is the Fourier transformed of the electron density operator, and V is the quantization volume. The square of the coupling constant M is given by

$$M^2 = \frac{e^2\hbar\omega_{\rm LO}}{2}\left(\frac{1}{\varepsilon_\infty} - \frac{1}{\varepsilon}\right) = \frac{e^2\hbar\omega_{\rm LO}}{2}\frac{1}{\varepsilon^*},$$

where $\hbar\omega_{\mathrm{LO}}$ is the LO phonon energy and ε (ε_∞) is the low frequency/background (high frequency) dielectric constant. This interaction Hamiltonian can be derived from the fundamental form, eq. (3.23), but this will not be done here, interested readers can consult refs. [24, 31]. The Fourier transformed of the electron density operator is obtained from its definition $\rho(\boldsymbol{r}) = \psi^\dagger(\boldsymbol{r})\psi(\boldsymbol{r})$ and using the spatial Fourier transform in eq. (4.12), giving

$$\rho(\boldsymbol{q}) = \int d\boldsymbol{r} e^{-i\boldsymbol{q}\cdot\boldsymbol{r}}\rho(\boldsymbol{r}) = \sum_{\nu\nu'} \langle\nu|e^{-i\boldsymbol{q}\cdot\boldsymbol{r}}|\nu'\rangle\, c^\dagger_\nu c_{\nu'}.$$

Inserting this into eq. (5.4) yields

$$H_{\mathrm{e-LO}} = \sum_{\nu\nu'\boldsymbol{q}} M^{\boldsymbol{q}}_{\nu\nu'} c^\dagger_\nu c_{\nu'}(b^\dagger_{-\boldsymbol{q}} + b_{\boldsymbol{q}}), \quad M^{\boldsymbol{q}}_{\nu\nu'} = \frac{M}{qV^{\frac{1}{2}}}\langle\nu|e^{-i\boldsymbol{q}\cdot\boldsymbol{r}}|\nu'\rangle\,,$$

which is the desired form of the interaction. As with the Coulomb interaction between electrons we limit the LO phonons to only cause intra-band transitions, which is justified due to the non-resonant nature of an inter-band transition caused by a LO phonon. This does however not mean that the LO phonons cannot affect electronic inter-band quantities, such as the optical polarization.

The interaction between the electrons and cavity photons is given by eq. (3.19), which for the quasi-cavity mode introduced in eq. (5.2) reduces to

$$H_{\mathrm{e-rad}} = \sum_{\nu\nu'} \hbar g_{\nu\nu'} c^\dagger_\nu c_{\nu'}(a^\dagger + a). \tag{5.5}$$

We can simplify this interaction further by applying the rotating wave approximation (RWA), in which terms describing very non-resonant processes where an electron is excited across the bandgap and a photon is emitted (and the opposite) are neglected. This approximation is well justified when the coupling constants $\hbar g_{\nu\nu'}$ are small compared to the cavity energy $\hbar\omega_{\mathrm{cav}}$. In the RWA we get the following Hamiltonian

$$H_{\mathrm{e-rad}} = \sum_{\alpha\alpha'} \hbar g_{\alpha\alpha'}(c^\dagger_{\mathrm{c},\alpha} c_{\mathrm{v},\alpha'} a + a^\dagger c^\dagger_{\mathrm{v},\alpha} c_{\mathrm{c},\alpha'}), \tag{5.6}$$

where we have assumed that $g^{\mathrm{cv}}_{\alpha\alpha'} = g^{\mathrm{vc}}_{\alpha\alpha'} = g_{\alpha\alpha'}$ and again the spin index has been absorbed into the spatial index. The RWA is investigated further in appendix A.2.

The interaction Hamiltonian for the classical excitation pulse is given by eq. (3.21) which can be used in this general form. The RWA can however also be applied to this interaction, to which end we write the classical field as

$$E_{\mathrm{cl}}(t) = \frac{1}{2}E_0(t)(e^{i\omega_0 t} + e^{-i\omega_0 t}),$$

where $E_0(t)$ is an envelope function and the exponentials set the carrier frequency of the pulse. Unless otherwise stated the pulse envelope will be a Gaussian of the form $E_0(t) = E_0 \exp(-((t-t_0)/\Delta t)^2)$, with Δt being the temporal width and t_0 the peak position. The positive and negative exponentials in $E_{\mathrm{cl}}(t)$ basically correspond to the photon operators discussed above, i.e. emission and absorption of photons, hence the same arguments apply and we can immediately write down $U(t)$ in the RWA

$$U(t) = \sum_{\alpha\alpha'} d_{\alpha\alpha'} \frac{E_0(t)}{2}(e^{-i\omega_0 t} c^\dagger_{\mathrm{c},\alpha} c_{\mathrm{v},\alpha'} + e^{i\omega_0 t} c^\dagger_{\mathrm{v},\alpha} c_{\mathrm{c},\alpha'}), \tag{5.7}$$

where again we assume that $d^{\mathrm{cv}}_{\alpha\alpha'} = d^{\mathrm{vc}}_{\alpha\alpha'} = d_{\alpha\alpha'}$ and absorb the spin index into the spatial.

The reason for applying the RWA to the Hamiltonians involving the various optical fields is purely practical. If the RWA was not applied, there would appear terms in the equations of motion oscillating on timescales on the order of two times the inverse optical frequencies, which in our case are tuned to the band gap of around 1 eV. These timescales are much smaller than any other in the system and hence set the lower limit in the time discretization. Furthermore the effect of including these highly non-resonant contributions is usually small. Thus it is of great practical importance to apply the RWA and this will be done for most calculations in this thesis.

5.2.2. Truncation of self-energies

Approximations applied to the Hamiltonians are the most fundamental restrictions one can impose on a given model of a physical system, and these approximations will set the ultimate limit for the validity of our physical model. Unfortunately, we are not done with applying approximations. Any many-body interaction Hamiltonian will generate infinitely many terms in its corresponding self-energy, a situation that cannot be handled in practice and hence a truncation of the self-energy is needed. The truncation of the self-energy decreases the accuracy of the quantities calculated using the Green's functions, as oppose to the exact quantities obtained through exact diagonalization of the Hamiltonian. The challenge is then to select the appropriate self-energy, so that ones results has the desired accuracy needed in a given application. The selection process is often guided by physical intuition, experience, and certain fundamental conservation laws. However it is not always obvious which self-energy diagrams should be used.

Notation is a rather important aspect of performing many-body calculations due to the many different quantities one has to keep track of. We will therefore at this point fix the symbols used for the various self-energies in a hopefully meaningful fashion. The electrons interact with every other constituent of the system, including themselves, and therefore we need a total of four self-energies which we will denote by the following symbols

$$\Sigma^{\mathrm{LO},x}_{\nu\nu'}(t,t'), \quad \Sigma^{\mathrm{rad},x}_{\nu\nu'}(t,t'), \quad \Sigma^{\mathrm{ee},x}_{\nu\nu'}(t,t'), \quad U_{\nu\nu'}(t).$$

The superscripts LO, rad, and ee refer to interactions with phonons, photons, and other electrons (Coulomb) respectively and $U_{\nu\nu'}(t)$ is the singular self-energy due to the classical excitation pulse. The self-energies are presented in their real-time form and x refers to one of the four components greater, lesser, retarded or advanced. The photons in the cavity only interact with electrons, and as we only consider a single quasi-cavity mode, only a single symbol is needed for this self-energy and we will use the following

$$\sigma^x(t,t').$$

The phonons will be assumed to be in thermal equilibrium at all times and therefore a self-energy is not needed.

Below, we explicitly go through all the self-energies mentioned above, but first we make a comment on some general features of the self-energies. All the considered self-energies are of lowest order in their respective coupling strengths, however they are all made self-consistent as dictated by the conservation laws[2] of particle number, momentum, and energy [30]. The procedure of making a self-energy self-consistent consists of replacing free Green's functions by the corresponding full one, as illustrated diagrammatically in appendix A.5. A justification for considering only lowest order contributions will be given for each self-energy below.

The lowest order contribution to the self-energy from the electronic Coulomb interaction is given by eq. (A.21) and is a singular contribution, in the sense that it does not depend on two times, but rather a single time see eq. (2.42). This has the effect, that it acts as an effective one-body interaction and not a true many-body interaction. As such it gives rise to instantaneous renormalizations in the single-particle energies and external fields, but does not cause broadening of spectral features. In its self-consistent form it is equal to the well-known mean-field Hartree-Fock (HF) approximation, which is exactly the form we will use

$$\Sigma^{\mathrm{ee,HF}}_{\nu\nu'}(t) = i\hbar \sum_{\nu_1\nu_2} \left(V_{\nu\nu_2,\nu_1\nu'} - V_{\nu\nu_2,\nu'\nu_1}\right) [G^{<}_{\nu_1\nu_2}(t,t) - i\hbar^{-1}\delta_{b_1,\mathrm{v}}\delta_{b_2,\mathrm{v}}\delta_{\nu_1,\nu_2}]. \tag{5.8}$$

Notice that the contribution from the full valence band has been subtracted from this self-energy, for which reason only diagonal Green's functions should be subtracted ensured by δ_{ν_1,ν_2} [26, p. 260]. This

[2] Of course a quantity is only conserved if the corresponding symmetry is present in the system. In general in a non-relativistic non-equilibrium system particle number is the only conserved quantity.

is done as it is included in the band structure of the single-particle energies we are using, basically it is contained in the experimentally measured parameters discussed in appendix A.8. This subtraction has the consequence that in equilibrium (the unexcited semiconductor) the electronic Coulomb interaction will not contribute, it will only give contributions for non-equilibrium situations. The regime of validity for the HF self-energy is that of low excitation, where only a small number of electrons are optically excited. Beyond the low-excitation regime one has to include higher order contributions to the self-energy to account for complicated effects like screening and true Coulomb scattering. It should also be noted that the HF mean-field theory does not account for two-pair or higher order correlations as e.g. biexcitons, see [27, p. 451]. For completeness we mention that the HF self-energy satisfy the following symmetry

$$[\Sigma^{\mathrm{ee,HF}}_{\nu\nu'}(t)]^* = \Sigma^{\mathrm{ee,HF}}_{\nu'\nu}(t), \tag{5.9}$$

which be shown using the symmetry relations for the lesser Green's function eq. (2.32) and those of the Coulomb matrix element eq. (4.9). This symmetry can be useful for formal arguments as well as for saving computation time in the numerics.

In the low excitation regime it is a well established fact [56, p. 222] that the dominant scattering mechanism is provided by phonons and therefore these are the main sources of intra-band relaxation and inter-band, as well as intra-band, dephasing. The two lowest order self-consistent contributions to the self-energy are given by eqs. (A.30) and (A.29). However as discussed in the previous subsection we can to a good approximation limit our attention to LO-phonons if we keep the temperature above 150 K [63], which yields very significant simplifications as will be discussed next.

We can make some simplifications on the self-energy arising from the LO-phonon interaction, due to the simple fact that we assume the LO-phonons to be dispersionless. Both contributions to the self-energy, eqs. (A.30) and (A.29), contain a sum over $\boldsymbol{q}$ and a product of two $M^{\boldsymbol{q}}_{\nu\nu'}$s multiplied by the free phonon Green's function. Due to the dispersionlessness of the LO-phonons, their corresponding free Green's function will not depend on energy and therefore not on $\boldsymbol{q}$ either, meaning that it can be taken outside the $\boldsymbol{q}$ sum. The wavevector sum is therefore limited to run over the $M^{\boldsymbol{q}}_{\nu\nu'}$s giving a quantity which can be considered an effective matrix element in four electron indices. Inserting the definition of $M^{\boldsymbol{q}}_{\nu\nu'}$ into this quantity gives the following

$$\sum_{\boldsymbol{q}} M^{\boldsymbol{q}}_{\nu_1\nu'_1} M^{-\boldsymbol{q}}_{\nu_2\nu'_2} = M^2 \frac{1}{V} \sum_{\boldsymbol{q}} \frac{1}{q^2} \langle \nu_2 | e^{i\boldsymbol{q}\cdot\boldsymbol{r}} | \nu'_2 \rangle \langle \nu_1 | e^{-i\boldsymbol{q}\cdot\boldsymbol{r}} | \nu'_1 \rangle ,$$

by comparing this to the Coulomb matrix element in the form of eq. (4.14), we see that these quantities are equal[3], apart from a few multiplicative constants[4]. We end up being able to write [32, p. 72]

$$\sum_{\boldsymbol{q}} M^{\boldsymbol{q}}_{\nu_1\nu'_1} M^{-\boldsymbol{q}}_{\nu_2\nu'_2} = \frac{M^2\varepsilon}{e^2} V_{\nu_2\nu_1,\nu'_2\nu'_1} = \frac{\hbar\omega_{\mathrm{LO}}}{2\varepsilon^*/\varepsilon} V_{\nu_2\nu_1,\nu'_2\nu'_1}. \tag{5.10}$$

This result saves a lot of computation time in two aspects. Firstly we only need to calculate the Coulomb matrix elements, and not the phonon matrix elements, which is very fortunate as these two are the most time consuming of all the input matrix elements. Secondly, and more importantly, the $\boldsymbol{q}$ sum does not have to be carried out explicitly in the numerical solution of the equations of motion for the Green's functions, which results in a very significant speed up. With this simplification we write the Fock

[3] However, it should be noted that formally the wavevector sum for the phonons is restricted to the first Brillouin zone, but we will assume the matrix elements $M^{\boldsymbol{q}}_{\nu\nu'}$ decay sufficiently fast so that we may extend the sum to all wavevectors.

[4] In the actual simulations one should be mindful of the fact that the two dielectric constants in eq. (5.10) are for the bulk material in which the LO-phonons live, whereas the electronics wavefunctions are often calculated for another material as usually we consider heterostructures. This means that the pure Coulomb matrix elements are often calculated with a different dielectric constant and hence a simple rescaling is needed.

contribution using the contour version eq. (A.30) and the appropriate Langreth rule from table 2.1 as follows[5]

$$\Sigma^{\mathrm{LO,F},\gtrless}_{\nu\nu'}(t,t') = i\hbar \sum_{\nu_1\nu_2} \frac{\hbar\omega_{\mathrm{LO}}}{2\varepsilon^*/\varepsilon} V_{\nu_2\nu,\nu'\nu_1} G^{\gtrless}_{\nu_1\nu_2}(t,t') D^{0,\gtrless}_{\mathrm{LO}}(t,t'), \tag{5.11}$$

where $D^{0,\gtrless}_{\mathrm{LO}}(t,t')$ is free LO-phonon Green's function defined in eq. (A.35). This self-energy has the following symmetry under complex conjugation

$$\left[\Sigma^{\mathrm{LO,F},\gtrless}_{\nu\nu'}(t,t')\right]^* = -\Sigma^{\mathrm{LO,F},\gtrless}_{\nu'\nu}(t',t),$$

shown using the same relations as eq. (5.9). This relation is useful for simplifying the scattering terms arising from the electron-LO-phonon interaction, as done in section 5.4.1, or to relate values of the self-energy above and below the time diagonal, which could save some computational effort. The second first order self-energy is the Hartree contribution, which from eq. (A.29) and using the Langreth rules, see table 2.1, has the following real time expression

$$\Sigma^{\mathrm{LO,H}}_{\nu\nu'}(t) = -i\hbar \int_{-\infty}^{t} dt' \sum_{\nu_1\nu_2} \frac{\hbar\omega_{\mathrm{LO}}}{2\varepsilon^*/\varepsilon} V_{\nu_2\nu,\nu_1\nu'} \left[G^{<}_{\nu_1\nu_2}(t',t') - i\hbar^{-1}\delta_{b_1,\mathrm{v}}\delta_{b_2,\mathrm{v}}\delta_{\nu_1,\nu_2}\right] D^{0,r}_{\mathrm{LO}}(t,t'), \tag{5.12}$$

where $D^{0,r}_{\mathrm{LO}}(t,t')$ is the free retarded Green's function of the LO-phonons and where the contribution from the full valence band has been subtracted for the same reasons as with eq. (5.8). As with the singular self-energy for the electron-electron interaction this singular self-energy satisfy a symmetry relation similar to eq. (5.9), namely that under under complex conjugation we get

$$[\Sigma^{\mathrm{LO,H}}_{\nu\nu'}(t)]^* = \Sigma^{\mathrm{LO,H}}_{\nu'\nu}(t),$$

which is useful in the numerics and for certain formal arguments. The justification for neglecting higher order self-energies in the electron-LO-phonon coupling, is that we restrict ourselves to treating materials with weak coupling constants, such as GaAs [26, p. 262].

We will now consider the electronic self-energies arising from the electron-photon interaction. Due to the formal equivalence of the electron-photon and electron-phonon interaction Hamiltonians, see section 3.2.3, their corresponding self-energies will also be equal, with the appropriate replacement of symbols of course. We will therefore simply state these, as basically all the comments made to the phonon case applies to the photon case as well. From the Hamiltonian eq. (5.5) and eq. (A.23) we obtain the Fock contribution for the photons

$$\Sigma^{\mathrm{rad,F},\gtrless}_{\nu\nu'}(t,t') = i\hbar \sum_{\nu_1\nu_2} \hbar g_{\nu\nu_1} \hbar g_{\nu_2\nu'} G^{\gtrless}_{\nu_1\nu_2}(t,t') \mathcal{A}^{\gtrless}(t,t'), \tag{5.13}$$

which as for the phonons has the following symmetry

$$\left[\Sigma^{\mathrm{rad,F},\gtrless}_{\nu\nu'}(t,t')\right]^* = -\Sigma^{\mathrm{rad,F},\gtrless}_{\nu'\nu}(t',t). \tag{5.14}$$

The Hartree contribution from the photons is obtained from eq. (A.22)

$$\Sigma^{\mathrm{rad,H}}_{\nu\nu'}(t) = -i\hbar \int_{-\infty}^{t} dt' \sum_{\nu_1\nu_2} \hbar g_{\nu\nu'} \hbar g_{\nu_2\nu_1} \left[G^{<}_{\nu_1\nu_2}(t',t') - i\hbar^{-1}\delta_{b_1,\mathrm{v}}\delta_{b_2,\mathrm{v}}\delta_{\nu_1,\nu_2}\right] \mathcal{A}^{r}(t,t'), \tag{5.15}$$

with the symmetry relation

$$[\Sigma^{\mathrm{rad,H}}_{\nu\nu'}(t)]^* = \Sigma^{\mathrm{rad,H}}_{\nu'\nu}(t).$$

[5] In this section we only present the greater and lesser real time components of the self-energies, as it is these that are used in the non-equilibrium simulations which are the main focus. If other real components are needed, as in equilibrium, they will be presented in their respective sections.

Restricting ourselves to the lowest order self-energies for the electron-photon interaction we limit the validity of our theory to relatively weak electron-photon coupling constants.

Now we turn to the photonic self-energy arising from the interaction with the electrons. To stay consistent with the electronic self-energies described above, we keep only the lowest order self-energy diagram in the expansion of the photonic Dyson equation. This is called the pair-bubble diagram due to its diagrammatic appearance, see figure A.8. The contour version is given by eq. (A.27) and with the use of the Langreth rules we get the real time components

$$\sigma^{\gtrless}(t,t') = -i\hbar \sum_{\substack{\nu_1\nu_1' \\ \nu_2\nu_2'}} \hbar g_{\nu_1\nu_1'} \hbar g_{\nu_2\nu_2'} G^{\gtrless}_{\nu_2'\nu_1}(t,t') G^{\lessgtr}_{\nu_1'\nu_2}(t',t), \tag{5.16}$$

which satisfy a symmetry relation similar to that of the electronic self-energies

$$\left[\sigma^{\gtrless}(t,t')\right]^* = -\sigma^{\gtrless}(t',t). \tag{5.17}$$

5.3. Equilibrium

In this section we deal with the Green's function theory describing the equilibrium properties of our system. It is important to know these for two reasons. The first and most relevant for the present thesis is the need to supply the GKBA, section 2.5, with suitable retarded and advanced Green's functions. Even though one may employ free Green's functions in the GKBA, the result is often very poor and indeed for our system it resulted in unphysical populations for all considered situations. Fortunately it turns out [37, 38, 41] that the equilibrium Green's functions provide excellent approximations for the retarded and advanced Green's functions entering the GKBA. More generally the solution of the equilibrium system is needed in order to provide any set of non-equilibrium equations with the correct initial conditions, which is the second reason for considering the equilibrium Green's functions. The correct set of initial conditions is needed in order for the initial/equilibrium correlations to enter in the non-equilibrium time development, as otherwise these will be missing for the rest of the time evolution [26].

5.3.1. Equilibrium spectral Green's functions

A general consequence of a system being in thermal equilibrium is that its Green's functions become functions of a single effective time (the time difference), rather than the two-time dependence in non-equilibrium. This is indeed expected on an intuitive level, as a system in thermal equilibrium cannot depend more on one time than the other, and hence the only "real" time coordinate must be the time difference. This is easily shown formally, as for a time-independent Hamiltonian the Heisenberg time-dependence is given explicitly by $O(t) = e^{iHt/\hbar} O e^{-iHt/\hbar}$. For a greater-like quantity we may write

$$\begin{aligned}
\langle O_\alpha(t) O_\beta^\dagger(t')\rangle &= \frac{1}{\mathrm{Tr}[e^{-\beta H}]} \mathrm{Tr}\left[e^{-\beta H} e^{iHt/\hbar} O_\alpha e^{-iHt/\hbar} e^{iHt'/\hbar} O_\beta^\dagger e^{-iHt'/\hbar}\right] \\
&= \frac{1}{\mathrm{Tr}[e^{-\beta H}]} \mathrm{Tr}\left[e^{-\beta H} e^{iH(t-t')/\hbar} O_\alpha e^{-iH(t-t')/\hbar} O_\beta^\dagger\right] \\
&= \langle O_\alpha(t-t') O_\beta^\dagger\rangle\,,
\end{aligned} \tag{5.18}$$

where we used that the trace operation is invariant under cyclic permutations, $\mathrm{Tr}[AB] = \mathrm{Tr}[BA]$, and that the thermal and time operators commute, also the chemical potential is assumed to be zero. The same can be shown for a lesser-like quantity and hence all the various Green's functions can be written as functions of the difference time, $G(t,t') = G(t-t') = G(\tau)$.

In the following we will focus on the retarded Green's function as this object is directly related to the spectral properties of an equilibrium system, further it is known from the equilibrium Green's function formalism that only a single Green's function is needed[6] and this is often chosen to be the retarded one. We will therefore aim for a formulation in terms of the retarded Green's function within the non-equilibrium formalism. A natural starting point is the difference (equilibrium) time limit of the equation of motion for the retarded Green's function, eq. (2.51),

$$i\hbar\partial_\tau G^r_{\nu\nu'}(\tau) = \delta(\tau)\delta_{\nu\nu'} + \hbar\omega_{\nu'}G^r_{\nu\nu'}(\tau) + \int_{t-\tau}^{t} dt_1 \sum_{\nu_1} G^r_{\nu\nu_1}(t-t_1)\Sigma^r_{\nu_1\nu'}(\tau - [t-t_1]). \tag{5.19}$$

In the equation of motion above the step function from the definition of the retarded quantities has been used to limit the memory integral. In this version we do not consider any contributions from the singular self-energy. This is correct for the external potential as this is not present in equilibrium. Furthermore, the instantaneous self-energy from the Coulomb interaction is by construction zero in equilibrium[7], see eq. (5.8) and so are the singular contributions arising from the Hartree self-energies from the LO-phonons and cavity photons, eqs. (5.12) and (5.15) respectively. We can simplify a bit further by introducing the following transformation of the memory time t_1

$$\tau_1 = t - t_1 \Rightarrow d\tau_1 = -dt_1, \quad \int_{t_1=t-\tau}^{t_1=t} dt_1 = -\int_{\tau_1=\tau}^{\tau_1=0} d\tau_1 = \int_0^\tau d\tau_1,$$

through which we may write the above equation as

$$i\hbar\partial_\tau G^r_{\nu\nu'}(\tau) = \delta(\tau)\delta_{\nu\nu'} + \hbar\omega_{\nu'}G^r_{\nu\nu'}(\tau) + \int_0^\tau d\tau_1 \sum_{\nu_1} G^r_{\nu\nu_1}(\tau_1)\Sigma^r_{\nu_1\nu'}(\tau - \tau_1). \tag{5.20}$$

This equation will form the starting point for all spectral functions considered in the rest of the report.

5.3.2. The polaron

In this section we will formulate the theory for the situation where the self-energy in eq. (5.20) describes the interaction between electrons and dispersionless LO-phonons. The quasi-particle that forms from this interaction is usually called a polaron [24, p. 497].

LO-phonons cause only intra-band transitions and as no inter-band polarizations are induced otherwise, all Green's functions must be diagonal in the band index. It has further been found [41, 61] to be a good approximation to only include Green's functions fully diagonal in both band and all other indices. This is a huge simplification computationally and further we can simplify the notation for all quantities to only contain a single index (two in practise as we write the band explicitly), hence we can perform the following replacement everywhere

$$G^{bb',x}_{\alpha\alpha'}(\tau) = G^{b,x}_{\alpha}(\tau)\delta_{bb'}\delta_{\alpha\alpha'}, \quad \Sigma^{bb',r}_{\alpha\alpha'}(\tau) = \Sigma^{b,r}_{\alpha}(\tau)\delta_{bb'}\delta_{\alpha\alpha'}, \tag{5.21}$$

where b is the band index and α contains all other quantum numbers. The fact that the self-energy also becomes diagonal in its outer indices is a consequence of the matrix structure of the Dyson equation eq. (5.20).

We consider only the Fock contribution to the lowest order self-energy, as the Hartree term is zero as mentioned in the discussion below eq. (5.19). From eq. (A.30) and the appropriate Langreth rule from

[6] The fact that only a single Green's function is needed in equilibrium can be realized using the fluctuation-dissipation theorem that links the different Green's functions together [26, p. 45].

[7] The equal-time lesser Green's function that appears in eq. (5.8) becomes proportional to the mean thermal occupation in equilibrium, which is zero for the conduction band and unity for the valence band so that $\langle c^\dagger_{b,\alpha}c_{b,\alpha}\rangle - \delta_{b,\mathrm{v}} = 0$.

table 2.1 we get

$$\Sigma_\alpha^{b,\mathrm{LO,F},r}(t,t') = i\hbar \sum_{\alpha_1} \frac{\hbar\omega_{\mathrm{LO}}}{2\varepsilon^*/\varepsilon} V^{bbbb}_{\alpha_1\alpha\alpha\alpha_1} \times \left\{ G^{b,<}_{\alpha_1}(t,t') D^{0,r}_{\mathrm{LO}}(t,t') + G^{b,r}_{\alpha_1}(t,t') D^{0,r}_{\mathrm{LO}}(t,t') + G^{b,r}_{\alpha_1}(t,t') D^{0,<}_{\mathrm{LO}}(t,t') \right\},$$

where we have used eq. (5.21) and eq. (5.3) to remove most of the sums. To proceed further we will make the assumption that no electrons are thermally excited across the bandgap, hence we consider what is sometimes referred to as an electron-hole vacuum. This assumption is well satisfied for the class of III-V semiconductors we are considering all having band gaps well above thermal energies typically used in experiments (26 meV for room temperature). This allows us to assume that [26, p. 296]

$$G_\alpha^{\mathrm{c},<}(t,t') = 0, \tag{5.22}$$

as $G_\alpha^{\mathrm{c},<}(t,t')$ is related to the probability of detecting an electron in the same state at time t and t', and in an empty band this probability is zero. More formally this can be realized by considering the definition of the above Green's function which is $G_\alpha^{\mathrm{c},<}(t,t') = i\hbar^{-1} \langle c^\dagger_{\mathrm{c},\alpha}(t') c_{\mathrm{c},\alpha}(t) \rangle$, this Green's function is proportional to the probability of removing an electron in state α in the conduction band at time t and putting it back at time t', where $t' < t$ might be the case. By assumption the brackets describe a system where no electrons are present in the conduction band, hence the annihilation operator at time t will see a vacuum and the probability for this process will be zero. For the electrons in the valence band it must similarly hold that

$$G_\alpha^{\mathrm{v},>}(t,t') = 0,$$

as the $G_\alpha^{\mathrm{v},>}(t,t')$ is related to the probability of detecting a hole at times t and t' which is zero in a full band. As above a more reason can be seen by considering the definition of the greater Green's function $G_\alpha^{\mathrm{v},>}(t,t') = -i\hbar^{-1} \langle c_{\mathrm{v},\alpha}(t) c^\dagger_{\mathrm{v},\alpha}(t') \rangle$, where an electron is created in the valence band at time t' and removed at time t. By assumption the probability for this process is zero in our full valence band due to the Pauli principle. From this conclusion and from the definition of the retarded Green's function, eq. (2.24c), we get

$$G_\alpha^{\mathrm{v},<}(t,t') = -G_\alpha^{\mathrm{v},r}(t,t'). \tag{5.23}$$

Considering now the retarded self-energy for the conduction band: The first term is zero through eq. (5.22), for the second term we use the relation[8] $D^r = D^> - D^<$ for the LO phonon Green's functions, which after a cancelation yields

$$\Sigma_\alpha^{\mathrm{c,LO,F},r}(t,t') = \sum_{\alpha_1} G^{\mathrm{c},r}_{\alpha_1}(t,t') D^{\mathrm{cc},>}_{\alpha\alpha_1}(t,t').$$

For the valence band simply use eq. (5.23) in the first term after which this and the second one cancels giving

$$\Sigma_\alpha^{\mathrm{v,LO,F},r}(t,t') = \sum_{\alpha_1} G^{\mathrm{v},r}_{\alpha_1}(t,t') D^{\mathrm{vv},<}_{\alpha\alpha_1}(t,t').$$

In both of the above self-energies we have introduced an effective LO-phonon Green's function given by

$$\begin{aligned} D^{bb',\gtrless}_{\alpha\alpha_1}(t,t') &= i\hbar \frac{\hbar\omega_{\mathrm{LO}}}{2\varepsilon^*/\varepsilon} V^{b'bb'b}_{\alpha_1\alpha\alpha\alpha_1} D^{0,\gtrless}_{\mathrm{LO}}(t,t') \\ &= \frac{\hbar\omega_{\mathrm{LO}}}{2\varepsilon^*/\varepsilon} V^{b'bb'b}_{\alpha_1\alpha\alpha\alpha_1} \left\{ N_{\mathrm{LO}} e^{\pm i\omega_{\mathrm{LO}}(t-t')} + (N_{\mathrm{LO}}+1) e^{\mp i\omega_{\mathrm{LO}}(t-t')} \right\}, \end{aligned} \tag{5.24}$$

[8] Even though the phonon Green's function is not defined in exactly the same way as the electronic Green's functions, this relation still holds as it does for electrons in the retarded Green's function definition eq. (2.24c). See [24, p. 121].

where $D^{0,\gtrless}_{\mathrm{LO}}(t,t')$ is found from eq. (A.35), $\hbar\omega_{\mathrm{LO}}$ is the constant LO phonon energy, and $N_{\mathrm{LO}} = 1/(\exp(\hbar\omega_{\mathrm{LO}}/k_{\mathrm{B}}T) - 1)$ is the thermal occupation factor of the LO-phonons. In the actual simulations this Green's function is multiplied with a decaying exponential $\exp(-\tau_{\mathrm{LO}}^{-1}|t-t'|)$, to simulate the finite lifetime of the LO-phonons, see section 5.2.1. For completeness and later use we mention that $D^{bb',\gtrless}_{\alpha\alpha_1}(t,t')$ satisfies the following symmetry relations

$$D^{bb',\gtrless}_{\alpha\alpha_1}(t,t') = D^{bb',\lessgtr}_{\alpha\alpha_1}(t',t), \tag{5.25}$$

and under complex conjugation

$$\left[D^{bb',\gtrless}_{\alpha\alpha_1}(t,t')\right]^* = D^{bb',\lessgtr}_{\alpha_1\alpha}(t,t') = D^{b'b,\lessgtr}_{\alpha\alpha_1}(t,t'), \tag{5.26}$$

shown using the symmetries of the Coulomb matrix element, see eq. (4.9), and those of $D^{0,\gtrless}_{\mathrm{LO}}(t,t')$, see eq. (A.36). We can now write down the equation of motion for the retarded Green's function

$$i\hbar\partial_\tau G^{b,r}_\alpha(\tau) = \delta(\tau) + \hbar\omega^b_\alpha G^{b,r}_\alpha(\tau) + \int_0^\tau d\tau_1 G^{b,r}_\alpha(\tau_1) \sum_{\alpha_1} G^{b,r}_{\alpha_1}(\tau-\tau_1) D^{bb,\lambda_b}_{\alpha\alpha_1}(\tau-\tau_1), \tag{5.27}$$

where $\lambda_{\mathrm{c}} = >$ and $\lambda_{\mathrm{v}} = <$ is a band specific index. We note that in the present approximation the bands decouple completely and can be solved independently simplifying the numerics and interpretation. The initial condition for $G^{b,r}_\alpha(\tau)$ can be determined from its definition eq. (2.24c) as follows

$$G^{b,r}_\alpha(0) = -i\hbar^{-1}\theta(0)\left\langle [c_{b,\alpha}(t), c^\dagger_{b,\alpha}(t)]_+ \right\rangle = -i\hbar^{-1}/2, \tag{5.28}$$

where the equal-time anti-commutator has been evaluated to unity and we used that $\theta(0) = 1/2$ per definition.

Eq. (5.27) is in its present form not very suitable for numerical solution, this is due to the presence of the delta function in the first term and the free energy in the second term. The delta function is hard to represent numerically while maintaining its essential features and the underlying fast oscillations from the free evolution will require a very fine time discretization. To avoid having to deal with these issues we perform a transformation of the retarded Green's function [67] given by the following

$$G^{b,r}_\alpha(\tau) = -i\hbar^{-1}\theta(\tau)e^{-i\omega^b_\alpha\tau}\mathcal{G}^b_\alpha(\tau), \tag{5.29}$$

which eliminates the fast oscillations through the exponential and the delta function through the step function. The transformation is just a slowly-varying envelope representation used in many areas of physics. The initial condition for $\mathcal{G}^b_\alpha(\tau)$ is found from that of $G^{b,r}_\alpha(\tau)$ and we simply get

$$\mathcal{G}^b_\alpha(0) = 1.$$

Transformation of the equation of motion, eq. (5.27), is done using simple substitution, the chainrule for the time derivative, and the fact that $\partial_\tau(\theta(\tau)) = \delta(\tau)$. This yields the following equation[9]

$$\partial_\tau \mathcal{G}^b_\alpha(\tau) = -\hbar^{-2}\int_0^\tau d\tau_1 \mathcal{G}^b_\alpha(\tau_1) \sum_{\alpha_1} e^{i[\omega^b_\alpha - \omega^b_{\alpha_1}](\tau-\tau_1)} \mathcal{G}^b_{\alpha_1}(\tau-\tau_1) D^{bb,\lambda_b}_{\alpha\alpha_1}(\tau-\tau_1). \tag{5.30}$$

Numerical examples

To illustrate the effect LO phonons has on the spectral properties of the electrons, we give a numerical example which further serves as future reference for the non-equilibrium simulations performed later in

[9] The time derivative in eq. (5.30) has a step function multiplied onto it, $\theta(\tau)\partial_\tau\mathcal{G}^{b,r}_\alpha(\tau)$, from the transformation. However as it is only different from 1 for $\tau < 0$, which we do not consider, and for $\tau = 0$, where the RHS of zero, we have removed it from the equation.

Quantity	Value	Unit	Quantity	Value	Unit	Quantity	Value	Unit
h	1	nm	$\hbar\omega_1^{\mathrm{c}}$	665.9697	meV	$\hbar\omega_{\mathrm{LO}}$	36.8	meV
d	1.25	nm	$\hbar\omega_2^{\mathrm{c}}$	702.1410	meV	$\varepsilon_\infty/\varepsilon_0$	10.9	1
r_1	15	nm	$\hbar\omega_3^{\mathrm{c}}$	702.1410	meV	$\varepsilon/\varepsilon_0$	12.5	1
r_2	7.5	nm	$\hbar\omega_1^{\mathrm{v}}$	-563.8878	meV	τ_{LO}	5	ps
R_0	50	nm	$\hbar\omega_2^{\mathrm{v}}$	-588.3320	meV			
L_z	60	nm	$\hbar\omega_3^{\mathrm{v}}$	-588.3320	meV			

Table 5.1.: *Table presenting various parameters: (left) geometrical parameters of the QD, (mid) free single-particle of the bound states in the QD, and (right) parameters describing LO-phonons in a bulk GaAs system.*

the thesis. For simplicity we focus on a QD with few bound states and to further simplify we neglect the WL continuum. We stress that the neglection of the WL is not justified for the temperature range we will be considering, namely the range above 150 K where acoustic phonons can be neglected [63], which are not included in the present theory. For temperatures near room temperature it can be expected, and has been demonstrated [42], that electrons will be thermally excited into the WL continuum and hence these states will become important for the dynamics. In the low temperature regime it is, on the other hand, expected to be a much better approximation to neglect the WL continuum, as here the thermal excitation is expected to be smaller [68].

To obtain only a few bound states, the size of the QD has to be relatively small and it turns out that the geometric parameters shown in table 5.1 (left) (compare with figure 4.2) produces a QD with three clearly bound states in both conduction and valence band. The energies of these states are shown in table 5.1 (mid), while the corresponding wavefunctions are very similar to those presented in section 4.2. All matrix elements used in the simulations to come are calculated using these states. A schematic of the level structure is shown in figure 5.2 where also the notation of the states is indicated, the crossed areas above and below the dots represents the WL continuum which we neglect. We note that the spin degrees of freedom of the electron are omitted in the following, this is not an approximation as the electron-phonon interaction we are considering is diagonal in spin and hence does not couples the spin up and down subspaces. The parameters describing the LO-phonons are shown in table 5.1 (right) and are taken as those of a bulk GaAs system, as this is what our embedding barrier material consists of [31], the LO-phonon lifetime has been taken from the literature [41, 42].

The governing equation eq. (5.30) was solved in the time domain using the methods described in appendix A.4, but the results are presented in the frequency domain as this domain is usually more familiar when discussing spectral properties. We use the Fourier transform defined in eq. (5.1) with $\eta = 0$. It should be noted that the system consisting of a single electronic state coupled to a continuum of phonon modes can be solved exactly. This model is known as the independent boson model (IBM) [24, p. 285], and we will sometimes refer to this model in the following discussion, as it can be useful in the interpretation and verification of the theory developed here.

In figure 5.3 the spectral functions of the various states are shown at four different temperatures, for the conduction band in the top figure and the valence band in the bottom figure. The spectral function (or spectral density) is defined as

$$A_\alpha^b(\omega) = -2\mathrm{Im}\left[G_\alpha^{b,r}(\omega)\right], \tag{5.31}$$

where $G_\alpha^{b,r}(\omega)$ is the Fourier transformed of $G_\alpha^{b,r}(\tau)$. The spectral function is very similar to the usual density of states, see eq. (2.4), and therefore has a rather physically intuitive interpretation which is the reason for showing this quantity. When comparing the polaron densities to that of a free particle, $A_\alpha^{0,b}(\omega) = 2\pi\delta(\hbar\omega - \hbar\omega_\alpha^b)$ marked by the vertical lines, the difference is very significant. The most striking difference when comparing to normal Lorentzian lineshapes is the formation of the phonon sidebands situated approximately one LO-phonon energy apart. These form due to the constant energy of the LO-phonons and are signatures of states where a number phonons have been absorbed or emitted. A small

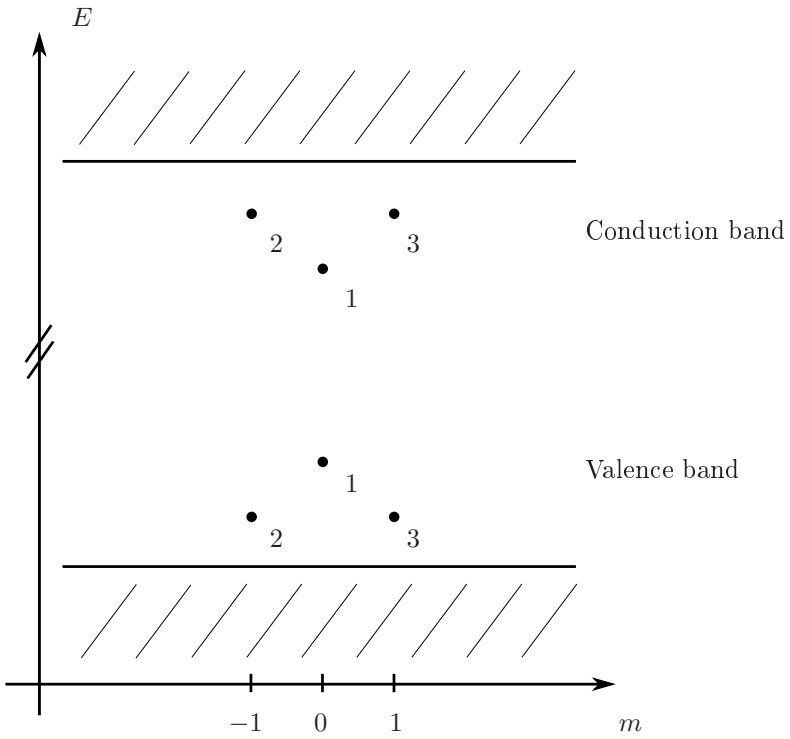

Figure 5.2.: *Schematic illustration of the level structure of the QD used in the polaron simulations.*

energy renormalization is also induced by the phonons, usually called the polaron shift, it is negative for conduction band states and positive for the valence band states. This difference of sign is expected arise from the fact that for the conduction band states we are really considering holes (unoccupied states), while for the valence band we are considering electrons (occupied states) so a difference is definitely expected.

Another peculiar feature is the multipeak clusters near each of the main peaks, as oppose to just a single peak at each LO-phonon energy separation that would naively be expected from the IBM. It turns out that these multipeak structure are due to the coupling between the bound states in the QD, mediated by the LO-phonons and as such it is an hybridization effect. To support this claim the spectral functions have also been calculated for the uncoupled system, i.e. where there is no intra-band coupling between states due to phonons, the result is shown in figure 5.4 and we observe a simple series of single peaks as expected on the grounds of the IBM. The relatively large difference in the spectrum for the conduction and valence band is solely due to the difference in transition energies within each band, as the phonon matrix elements are very similar for the two. For the conduction band the transition energy is $\hbar\omega_{21}^{\mathrm{c}} = 36.17$ meV while for the valence band we obtain $\hbar\omega_{12}^{\mathrm{v}} = 24.44$ meV. This shows that the electronic transitions in the conduction band are very close to resonant with an LO-phonon energy, while the valence band transition is not nearly as resonant. Thus a stronger interaction between the conduction band states and the LO-phonons is expected, which is manifested in the three-peak structure many of the main peaks exhibits. The center peak is the one which is also present without coupling to other states, while the "shoulder" peaks arise due to a hybridization splitting seen many places in quantum physics. The three-peak structure is completely absent for the valence band spectrum, where the hybridization peak is well separate from the phonon peak, due to the lack of resonance. The main phonon peaks in the valence band all have a small "shoulder" on one of their sides, this is not a sign of hybridization as it also appears in the decoupled spectra in figure 5.4. From the IBM we know that the decoupled solutions should no exhibit any "shoulders" but should simply be a series of Lorentzians, we therefore take the presence of these "shoulders" as unphysical artifacts present due to the approximations we have performed [69]. The lack of resonance is also seen through the width of the peaks in the valence band, these are more narrow than those in the conduction, indicating a longer lifetime as they do not couple as efficiently to the phonon reservoir.

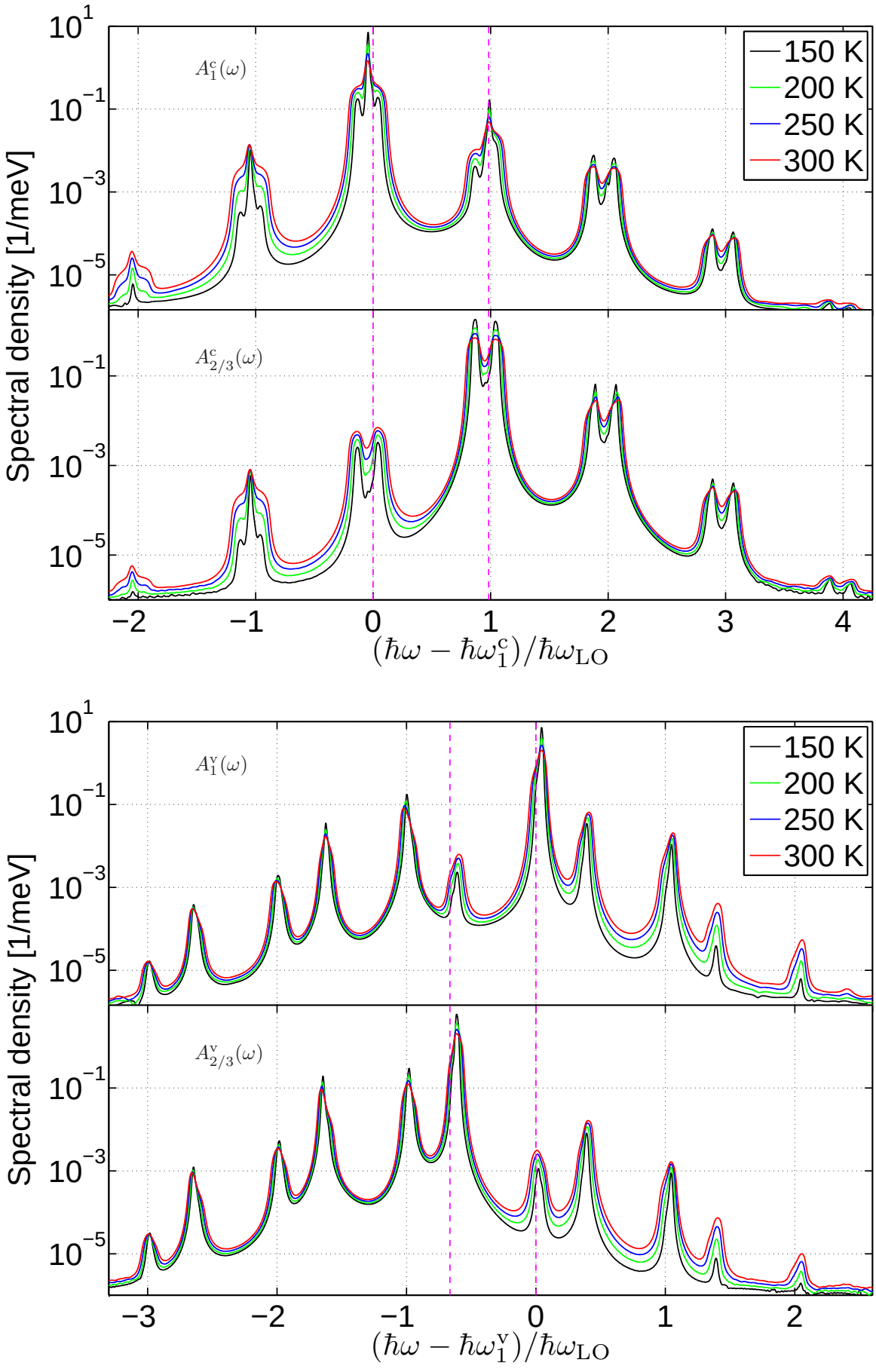

Figure 5.3.: *Plots of the spectral function, eq.* (5.31)*, for the electronic states.*

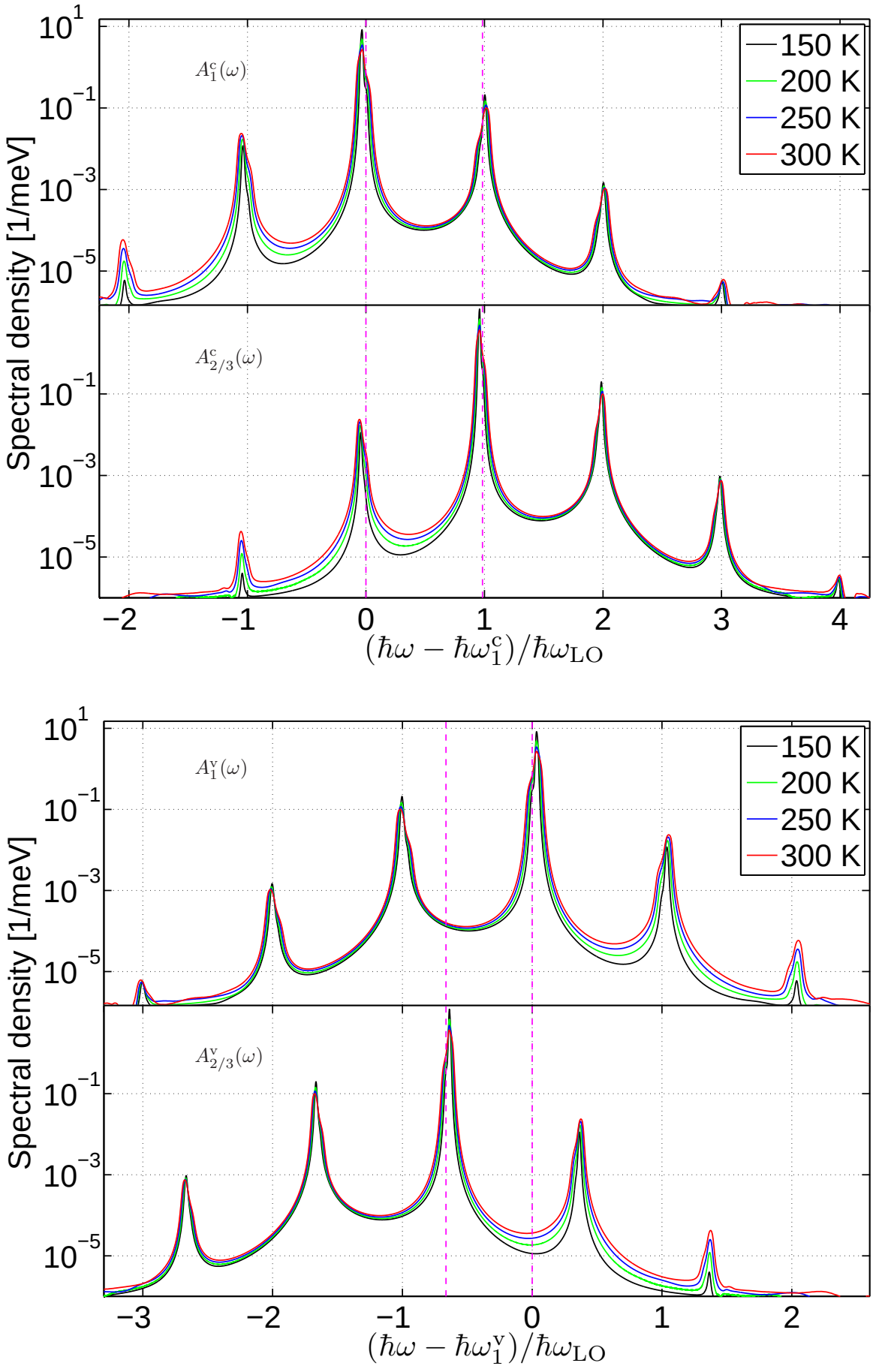

Figure 5.4.: *Plots of the spectral function, eq.* (5.31)*, for the electronic states, but in the uncoupled system.*

As we go through the various series for decreasing temperatures we notice that the peak height either increases or decreases, depending on whether we consider the high or low energy side with respect to the free energy, further the trend is reversed when going between bands. For the valence band the high energy side peaks decrease and the low energy side peaks increase in height, while generally narrowing in width. This observation is taken as evidence that the high energy side corresponds to absorption of LO-phonons, as generally lowering the temperature decreases the number of phonons, correspondingly the low energy side must correspond to emission of LO-phonons. The reason why the emission peaks do not decrease in height as the temperature is lowered, is due to the contribution from the vacuum field, i.e. spontaneous phonon emission. This overall picture of the peaks agrees well with the physical intuition that if an electron absorbs a LO-phonon its energy must increase, while emission must lower its energy. For the conduction band the situation is reversed, which is expected to arise from the fact that we are dealing with holes (unoccupied states) rather than electrons. It is easily seen formally that we consider hole properties when solving for the retarded Green's function, this is so as for the conduction band $G^< = 0$, eq. (5.22), and hence per definition $G^r = G^>$, where $G^>$ describes the properties of unoccupied states, i.e. holes. A more intuitive physical reason has however not been found.

When comparing the above results to similar calculations in the literature [41] we find excellent agreement on the overall structure of the spectrum. Furthermore it seems that the main effect of including a WL, is to broaden all spectral features and many of the fine structure features survives inclusion of the WL. As a further verification of our implementation, we compared the results of our numerical code to a numerically exact solution, that can be obtained in the case of a free (non-self-consistent) self-energy. The result of the comparison was an excellent agreement between the two approaches, verifying the numerical code. As a closing note we mention that all the considered spectral functions satisfy the sum rule [28, p. 130]

$$\int \frac{d(\hbar\omega)}{2\pi} A^b_\alpha(\hbar\omega) = 1,$$

which provides further verification of our implementation and confirms that the particle number is conserved after turning on the LO-phonon interaction, by virtue of the self-consistent self-energy we have employed.

5.3.3. The polariton

In this section we will formulate the theory where the self-energy in eq. (5.20) describes the interaction between electrons and photons in a single cavity mode.

For the case of the LO-phonon interaction treated using non-equilibrium Green's functions much literature is available, but this is not the case for the photon, at least to the knowledge of the author. This means that we must take a more explicit approach for finding out which elements of the retarded Green's function we need to solve for. Our starting point is the Fock self-energy arising due to the electron-photon interaction, which in the RWA and contour time is given by eq. (A.25). It should be noted that the Hartree self-energy is zero, as we assume all optical inter-band polarizations to vanish[10] in equilibrium, see eq. (A.26) or eq. (5.41). The cavity photons we consider have energies near the band gap hence we will assume that they only cause inter-band transitions, i.e. are band off-diagonal in their matrix element. Furthermore we will assume that pairs of states in the conduction and valence band exists, which are spatially similar, so that the optical matrix elements become diagonal in the in-band quantum number α, see section 4.4. All in all we may write the optical matrix element $g^{bb'}_{\alpha\alpha'} = g_\alpha \delta_{\alpha,\alpha'}(1-\delta_{b,b'})$, further suggesting that it may be a good approximation to only treat Green's functions diagonal in the in-band quantum number α. This simplification is further supported by the observation that only fully diagonal retarded Green's functions

[10] Although this statement might seem trivial, it in fact amounts to showing that $\rho^{\mathrm{cv}}_\alpha(t) = \langle c^\dagger_{\mathrm{v},\alpha}(t)c_{\mathrm{c},\alpha}(t)\rangle = \langle c^\dagger_{\mathrm{v},\alpha}(t-t)c_{\mathrm{c},\alpha}\rangle = \langle c^\dagger_{\mathrm{v},\alpha}c_{\mathrm{c},\alpha}\rangle = \frac{1}{\mathrm{Tr}\{e^{-\beta H}\}}\mathrm{Tr}\left\{e^{-\beta H}c^\dagger_{\mathrm{v},\alpha}c_{\mathrm{c},\alpha}\right\}$ is zero. In the presence of interaction mechanisms that operate across the band, such as the electron-photon interaction, this is not possible and it will remain an assumption, but for most wide band gap semi-conductors a rather good one.

do initially have a non-zero value and hence source terms are needed for these to become non-zero, which are small or zero according to the arguments given above. With the use of these arguments, eq. (A.25), and the Langreth rules of table 2.1 we may write the retarded self-energy as

$$\Sigma_\alpha^{bb',\mathrm{rad,F},r}(t,t') = i\hbar|\hbar g_\alpha|^2 \times \{ \\ \left[G_\alpha^{\mathrm{vv},<}(t,t')A^r(t,t') + G_\alpha^{\mathrm{vv},r}(t,t')A^r(t,t') + G_\alpha^{\mathrm{vv},r}(t,t')A^<(t,t')\right]\delta_{b,\mathrm{c}} \\ + \left[G_\alpha^{\mathrm{cc},<}(t,t')A^a(t',t) + G_\alpha^{\mathrm{cc},r}(t,t')A^<(t',t)\right]\delta_{b,\mathrm{v}} \}\,\delta_{b,b'}.$$

As for the phonons we will assume that no electrons are thermally excited and hence that eqs. (5.22) and (5.23) continue to be valid when considering photons also, therefore we may simplify this self-energy to

$$\Sigma_\alpha^{bb',\mathrm{rad,F},r}(t,t') = i\hbar|\hbar g_\alpha|^2 \times \left[G_\alpha^{\mathrm{vv},r}(t,t')A^<(t,t')\delta_{b,\mathrm{c}} + G_\alpha^{\mathrm{cc},r}(t,t')A^<(t',t)\delta_{b,\mathrm{v}}\right]\delta_{b,b'}.$$

We now observe that all contributions to this self-energy are proportional to the lesser cavity photon Green's function, which in its equal time limit is proportional to the photon number in the cavity and from appendix A.5 we get that its free version is equal to $A^{0,<}(t,t') = -i\hbar^{-1}e^{-i\omega(t-t')}n_B(\hbar\omega)$. Regardless of whether we consider the full or free photon Green's function it is very fair to assume that its envelope will mainly be given by its thermal occupation $n_B(\hbar\omega)$ factor. For a 1 eV photon at room temperature the thermal occupation is equal to $n_B(\hbar\omega) = 1/(\exp(1/0.026) - 1) \approx \exp(-38) \approx 10^{-17}$ and therefore we may put this equal to zero.

After this series of approximations we have arrived at the conclusion that the photons will not affect the equilibrium properties of the electrons, or vice versa. This means that the electronic spectral Green's functions in equilibrium, will be completely determined by the polaron functions discussed in the previous section. Also, the equilibrium properties of the photons are described by the free photons, as we have assumed that the photons only interact with electrons. The photons do of course have an influence on the dynamics of the electrons, and vice versa, but this influence will be limited to non-equilibrium situations which will be treated later in the next section.

5.4. Non-equilibrium

In this section we will derive the final form of the equations of motion governing our non-equilibrium cQED system. For the electronic Green's functions the GKBA will be applied in all cases, which is expected to be the main limitation of our theory, however it enables us to save vast amounts of computation time. For the photonic Green's functions we present equations of motion both with and without the GKBA applied. The reason for not applying the GKBA to the photon Green's functions, is that in some cases the full two-time lesser Green's functions is needed in order to give sensible results as shown in section 6.5. The two-time theory is however significantly more complicated and much more demanding to solve numerically, as will be discussed in the next chapter.

5.4.1. Electronic equations of motion and scattering terms

In this section we will derive the equations of motion describing the electronic degrees of freedom in our non-equilibrium system, where we are interested in observable quantities like populations and polarizations. These quantities are described by the equal-time lesser Green's function for the electrons, where the fact that we are only interested in equal-time Green's functions means that we can apply the GKBA, see section 2.5, which simplifies the solution process immensely. A natural step when considering the equal-time lesser Green's function, is to formulate the equations of motion in terms of the reduced density matrix of the electronic system, which the equal-time lesser Green's function is proportional to, see section 2.1. Next we will discuss an approximation regarding which elements of the density matrix are considered in

the calculations. In a two-band model of a semiconductor the density matrix may be written in matrix form as follows

$$\boldsymbol{\rho}(t) = \begin{bmatrix} \boldsymbol{\rho}^{\mathrm{cc}}(t) & \boldsymbol{\rho}^{\mathrm{cv}}(t) \\ \boldsymbol{\rho}^{\mathrm{vc}}(t) & \boldsymbol{\rho}^{\mathrm{vv}}(t) \end{bmatrix}. \tag{5.32}$$

If we assume an equal number N of single-particle states in each band has $(2N)^2$ elements, that each has their own equation of motion. For a standard quantum kinetic simulation where the dynamics is mainly confined to the bound states of a QD and where parts of the WL continuum are also included, one could easily have $N = 100$ leading to $(2N)^2 = 40000$ elements of the density matrix. Even on the supercomputers of today this is a very difficult computational task that is often not pursuable in practice, hence we need to consider a reduced number of elements in the density matrix. A number of different approaches are possible depending on what kind of experiment one is looking to describe. The critical factor is how the system is excited by external sources.

In the standard experiment of optical inter-band excitation of electrons from the valence to the conduction band, with subsequent intra-band relaxation and recombination by photons, a large reduction in the number of elements is possible. For this particular experiment it has turned out [38, 42] to be a good approximation to only consider diagonal elements in each of the four sub-matrices in eq. (5.32). For the band diagonal sub-matrices this has the consequence that we only describe populations and no intra-band polarizations, while for the off-diagonal (in the band index) sub-matrices it means that we only describe "vertical" or "optical" polarizations. Again assuming an equal number of single-states in each band, this reduces the considered number of density matrix elements to $3N$, which for $N = 100$ results in $3N = 300$ elements, a much more feasible number compared to 40000. It should however be noted that this approximation is only well-defined in certain systems. There need to exist pairs of states in the two bands, that are similar in their spatial form so that it is possible to define what is meant by a diagonal element in e.g. $\boldsymbol{\rho}^{\mathrm{cv}}(t)$. Only systems where such diagonal elements[11] can be unambiguously defined will be treated in the thesis.

We will proceed the derivations in the approximation described above and hence we make the replacement $\rho^{bb'}_{\alpha\alpha'}(t) = \rho^{bb'}_{\alpha}(t)\delta_{\alpha\alpha'}$ in all equations henceforth. The index b is a band index and α describes all other indexes. The fundamental forms of our equations of motion from section 2.4 are all formulated in terms of Green's functions, so first we present the transformation between the equal-time lesser Green's function and the density matrix

$$G^{bb',<}_{\alpha}(t,t) = i\hbar^{-1}\left\langle c^{\dagger}_{b',\alpha}(t)c_{b,\alpha}(t)\right\rangle = i\hbar^{-1}\rho^{bb'}_{\alpha}(t), \tag{5.33a}$$

$$G^{bb',>}_{\alpha}(t,t) = -i\hbar^{-1}\left\langle c_{b,\alpha}(t)c^{\dagger}_{b',\alpha}(t)\right\rangle = -i\hbar^{-1}[\delta_{b,b'} - \rho^{bb'}_{\alpha}(t)], \tag{5.33b}$$

where also the transformation of the greater Green's function has been presented as this will be needed later. These equations serve as our definition of the density matrix elements. Transformation of eq. (2.50) according to eq. (5.33) yields the equation of motion for the density matrix, which we write in the following compact form

$$\partial_t \rho^{bb'}_{\alpha}(t) = \partial_t \rho^{bb'}_{\alpha}(t)|_{\mathrm{coh}} + \partial_t \rho^{bb'}_{\alpha}(t)|_{\mathrm{scatt}}, \tag{5.34}$$

where $\partial_t \rho^{bb'}_{\alpha}(t)|_{\mathrm{coh}}$ describes terms giving rise to coherent time evolution and $\partial_t \rho^{bb'}_{\alpha}(t)|_{\mathrm{scatt}}$ describes terms giving rise to time evolution due to many-body processes, each of which will be described below.

Coherent terms

The coherent term becomes

$$\partial_t \rho^{bb'}_{\alpha}(t)|_{\mathrm{coh}} = -i\omega^{bb'}_{\alpha}\rho^{bb'}_{\alpha}(t) - i\hbar^{-1}\sum_{b_1}\left[\Sigma^{bb_1,\mathrm{s}}_{\alpha}(t)\rho^{b_1b'}_{\alpha}(t) - \rho^{bb_1}_{\alpha}(t)\Sigma^{b_1b',\mathrm{s}}_{\alpha}(t)\right]. \tag{5.35}$$

[11] One possible definition could be the transition where the overlap integral $\langle \mathrm{c}, \alpha | \mathrm{v}, \alpha' \rangle$ is the largest.

The first contribution is that from the free evolution, in the absence of any interactions, where the transition frequency is written as $\omega_\alpha^{bb'} = \omega_\alpha^b - \omega_\alpha^{b'}$. This term is not very interesting and we move on to the singular self-energy. By definition, eq. (2.42), the singular self-energy contains the interaction with the external fields and any one-time self-energy that might result from the many-body interactions. In our system we have the following contributions

$$\Sigma_\alpha^{bb',\mathrm{s}}(t) = U_\alpha^{bb'}(t) + \Sigma_\alpha^{bb',\mathrm{ee,HF}}(t) + \Sigma_\alpha^{bb',\mathrm{LO,H}}(t) + \Sigma_\alpha^{bb',\mathrm{rad,H}}(t), \tag{5.36}$$

which will be described below, but first we discuss some general features of the singular self-energy. Due to the simple structure of the singular source term in eq. (5.35), we can make some general conclusions on what effect a singular self-energy has depending on whether it is strictly diagonal or off-diagonal in the band indexes. To this end we decompose the singular self-energy into a diagonal (d) and an off-diagonal (od) part

$$\boldsymbol{\Sigma}_\alpha^{\mathrm{s}}(t) = \boldsymbol{\Sigma}_\alpha^{\mathrm{d}}(t) + \boldsymbol{\Sigma}_\alpha^{\mathrm{od}}(t),$$

where matrix notation with respect to the band indexes has been employed. For the diagonal part we get the following source term

$$\partial_t \rho_\alpha^{bb'}(t)|_{\mathrm{coh}}^{\mathrm{d}} = -i\hbar^{-1}\left[\Sigma_\alpha^{bb,\mathrm{d}}(t) - \Sigma_\alpha^{b'b',\mathrm{d}}(t)\right]\rho_\alpha^{bb'}(t)(1-\delta_{b,b'}),$$

which shows that a diagonal singular self-energy leads to a time-dependent renormalization of the single-particle energies. For the off-diagonal part we choose the two following cases as illustration

$$\partial_t \rho_\alpha^{\mathrm{cv}}(t)|_{\mathrm{coh}}^{\mathrm{od}} = -i\hbar^{-1}[\rho_\alpha^{\mathrm{vv}}(t) - \rho_\alpha^{\mathrm{cc}}(t)]\Sigma_\alpha^{\mathrm{cv,od}}(t), \tag{5.37a}$$

$$\partial_t \rho_\alpha^{\mathrm{cc}}(t)|_{\mathrm{coh}}^{\mathrm{od}} = -2\hbar^{-1}\mathrm{Im}\left[\rho_\alpha^{\mathrm{cv}}(t)\Sigma_\alpha^{\mathrm{vc,od}}(t)\right], \tag{5.37b}$$

which show that an off-diagonal singular self-energy gives rise to source terms identical to those of an external field operating on an interband transition [31, p. 89], hence it will renormalize any such field.

The first term describes the interaction with the external electric field which in its RWA form is given given by eq. (5.7), where the matrix elements we use are written as

$$U_\alpha^{bb'}(t) = \begin{cases} 0, & b = b' = \mathrm{c,v} \\ d_\alpha^{\mathrm{cv}}\frac{E_0(t)}{2}e^{-i\omega_0 t}, & b = \mathrm{c}, \quad b' = \mathrm{v} \\ d_\alpha^{\mathrm{vc}}\frac{E_0(t)}{2}e^{i\omega_0 t}, & b = \mathrm{v}, \quad b' = \mathrm{c} \end{cases} \tag{5.38}$$

The dipole matrix elements are written as $d_\alpha^{\mathrm{cv}} = d_{\alpha\alpha}^{\mathrm{cv}} = \langle \mathrm{c},\alpha|d|\mathrm{v},\alpha\rangle$, in the spirit of our main approximation discussed in the beginning of section 5.4.1. Actually it turns out, see section 4.4, that in the dipole approximation for inter-band optical transitions, the dipole matrix element is proportional to the pure overlap between the involved states in each band, $\langle \mathrm{c},\alpha|\mathrm{v},\alpha'\rangle$. Hence in systems where these are very similar in nature $d_{\alpha\alpha}^{\mathrm{cv}}$ is much larger than $d_{\alpha\neq\alpha'}^{\mathrm{cv}}$ and consequently the direct optical transitions are driven much more strongly that the indirect ($\alpha \neq \alpha'$) ones, which is the main reason why it is a good approximation to only consider the diagonal part of $\boldsymbol{\rho}^{\mathrm{cv}}(t)$. In general there are other sources, such as the excitonic Coulomb interaction, to the off-diagonal elements in $\boldsymbol{\rho}^{\mathrm{cv}}(t)$, but these are usually of only minor importance.

The second term is the mean-field HF energy, eq. (5.8), arising from the Coulomb interaction between the electrons. In terms of density matrices the HF term is written as

$$\Sigma_\alpha^{bb',\mathrm{ee,HF}}(t) = \sum_{\substack{b_1 b_2 \\ \alpha_1}}\left(V_{\alpha\alpha_1\alpha\alpha_1}^{bb_2b'b_1} - V_{\alpha\alpha_1\alpha_1\alpha}^{bb_2b_1b'}\right)\left[\rho_{\alpha_1}^{b_1b_2}(t) - \delta_{b_1,\mathrm{v}}\delta_{b_2,\mathrm{v}}\right]. \tag{5.39}$$

Being a singular self-energy $\Sigma^{\mathrm{ee,HF}}$ with both band diagonal and off-diagonal terms it will give rise to instantaneous renormalizations in the free energies as well as in the external electric field, the latter giving rise to the well-known excitonic features in various spectra.

The third term is the Hartree self-energy from the LO-phonon interaction, eq. (5.12), which in our present notation may be written as

$$\Sigma_{\alpha}^{bb',\mathrm{LO,H}}(t) = \int_{-\infty}^{t} dt' \sum_{b_1\alpha_1} \frac{\hbar\omega_{\mathrm{LO}}}{2\varepsilon^*/\varepsilon} V_{\alpha_1\alpha\alpha_1\alpha}^{b_1bb_1b} \left[\rho_{\alpha_1}^{b_1b_1}(t') - \delta_{b_1,\mathrm{v}}\right] D_{\mathrm{LO}}^{0,r}(t,t')\delta_{b,b'}, \tag{5.40}$$

where $D_{\mathrm{LO}}^{0,r}(t,t')$ is free retarded Green's function of the LO-phonons. It can be found from the relation $D^r(t,t') = \theta(t-t')[D^>(t,t') - D^<(t,t')]$ and explicitly reads

$$D_{\mathrm{LO}}^{0,r}(t,t') = -2\hbar^{-1}\theta(t-t')\sin(\omega_{\mathrm{LO}}[t-t'])e^{-|t-t'|/\tau_{\mathrm{LO}}},$$

where the equations in eq. (A.35) were used. This self-energy is band diagonal and hence thus it will only renormalize the free energies of the electrons. The sums in eq. (5.40) only involve electronic populations, where further the contribution from the full valence band has been subtracted. Thus it can already at this point be expected, that this self-energy will be of little significance in the low excitation regime[12] where we will primarily be operating.

The fourth term is the Hartree contribution from the electron-photon interaction. From now on we will employ the RWA version of the electron-photon interaction, eq. (5.6). This unfortunately means that the notation cannot be kept as compact as it has been up to this point, this is so because when applying the RWA one has to perform the band summation in order to remove the non-resonant contributions. The contour version of the RWA Hartree self-energy is given by eq. (A.26) and with the use of the Langreth rules we get

$$\Sigma_{\alpha}^{bb',\mathrm{rad,H}}(t) = \int_{-\infty}^{t} dt' \sum_{\alpha_1} \hbar g_{\alpha}\hbar g_{\alpha_1} \left[\rho_{\alpha_1}^{\mathrm{cv}}(t')A^r(t,t')\delta_{b,\mathrm{c}}\delta_{b',\mathrm{v}} + \rho_{\alpha_1}^{\mathrm{vc}}(t')[A^r(t,t')]^*\delta_{b,\mathrm{v}}\delta_{b',\mathrm{c}}\right]. \tag{5.41}$$

This self-energy is purely band off-diagonal and hence it will renormalize the external field and further drive the system as an internal field, which it actually is.

Scattering terms

We now move on to consider many-body scattering contributions to the density matrix equation of motion. The correct description of the various decay processes, be it relaxation or dephasing, that occur in a semiconductor nanostructure is the main motivation for employing the non-equilibrium Green's function formalism to our system. The scattering term in eq. (5.34) can in general be written as

$$\begin{aligned}\partial_t\rho_{\alpha}^{bb'}(t)|_{\mathrm{scatt}} = \\ -\int_{-\infty}^{t} dt_1 \sum_{b_1} \Big[&\Sigma_{\alpha}^{bb_1,>}(t,t_1)G_{\alpha}^{b_1b',<}(t_1,t) - \Sigma_{\alpha}^{bb_1,<}(t,t_1)G_{\alpha}^{b_1b',>}(t_1,t) \\ &-G_{\alpha}^{bb_1,>}(t,t_1)\Sigma_{\alpha}^{b_1b',<}(t_1,t) + G_{\alpha}^{bb_1,<}(t,t_1)\Sigma_{\alpha}^{b_1b',>}(t_1,t)\Big].\end{aligned} \tag{5.42}$$

It is apparent from this form that the values of the electronic Green's functions are needed away from the time diagonal in the (t,t')-plane and hence it is in general not possible to formulate a theory entirely in terms of equal-time Green's functions, that per definition live on the time diagonal. As we do not wish to solve for the Green's functions in the two-time plane an approximation is needed that provides us with a closed set of equations for the equal-time electronic Green's functions. Fortunately one such approximation exits and it is know as the GKBA, see section 2.5. We will employ a version of the GKBA where diagonal

[12] Rather surprisingly it turns out that the effects of the LO Hartree self-energy remains small even at high excitation conditions. This is expected to be connected to the fact that the sine function in the retarded LO-phonon Green's function, oscillates with a relatively fast period ($T_{\mathrm{LO}} = 2\pi/\omega_{\mathrm{LO}} \approx 0.11$ ps in GaAs) and hence will tend to average the integral to zero, unless the populations change significantly within this time span.

spectral Green's functions have been assumed, eq. (2.55), (see the discussion above eq. (5.21)) and in terms of the density matrix the GKBA may be written as

$$G_\alpha^{bb',\gtrless}(t,t') = \begin{cases} -G_\alpha^{b,r}(t,t')\rho_\alpha^{bb'}(t'), & < \text{ and } t > t' \\ G_\alpha^{b,r}(t,t')[\delta_{b,b'} - \rho_\alpha^{bb'}(t')], & > \text{ and } t > t' \\ \rho_\alpha^{bb'}(t)G_\alpha^{b',a}(t,t'), & < \text{ and } t < t' \\ -[\delta_{b,b'} - \rho_\alpha^{bb'}(t)]G_\alpha^{b',a}(t,t'), & > \text{ and } t < t' \end{cases} \tag{5.43}$$

The spectral Green's functions that occur in the GKBA are for the general non-equilibrium system and as such obey their respective Dyson equations, in both times. However, if these were to be used not much (if any) computational time would be saved and it would be a better strategy to simply solve the original two-time equations of motion for $G^{\gtrless}$. However, it turns out to be a good approximation [37, 38] for a weak coupling self-energy to use the equilibrium spectral Green's functions in the GKBA, that further only depends on the time difference in the two times. This is a huge simplification as the equilibrium spectral Green's functions can be calculated in advance and simply used as an input to the non-equilibrium calculation, and they only have to be recalculated if any parameters characterizing the equilibrium system are changed.

The scattering term is linear in the self-energy and the self-energy itself is a sum of each of its contributions, hence it is possible to write down a scattering term for each interaction and corresponding contribution to its self-energy. This is a very practical feature of the non-equilibrium Green's function formalism, as taking into account new interactions or going to higher orders simply amounts to adding more scattering terms to already existing equations. This is in contrast to many other methods that depend on expansion in basis states of the combined system, and not in the individual subsystems as in the non-equilibrium Green's function formalism, where inclusion of another kind bosonic interaction would result in a complete reformulation of the derived equations.

We start off by considering the scattering terms due to the interaction of the electrons and LO-phonons. The Fock contribution to the lowest order self-energy, eq. (5.11), is in our main approximation given by

$$\begin{aligned} \Sigma_\alpha^{bb',\mathrm{LO,F},\gtrless}(t,t') &= i\hbar \sum_{\alpha_1} \frac{\hbar\omega_{\mathrm{LO}}}{2\varepsilon^*/\varepsilon} V_{\alpha_1\alpha\alpha\alpha_1}^{b'bb'b} G_{\alpha_1}^{bb',\gtrless}(t,t') D_{\mathrm{LO}}^{0,\gtrless}(t,t') \\ &= \sum_{\alpha_1} D_{\alpha\alpha_1}^{bb',\gtrless}(t,t') G_{\alpha_1}^{bb',\gtrless}(t,t'), \end{aligned}$$

where the effective LO-phonon Green's function, $D_{\alpha\alpha_1}^{bb',\gtrless}(t,t')$, is defined in eq. (5.24). Plugging this into eq. (5.42) and employing the GKBA we obtain the following scattering term

$$\begin{aligned} &\partial_t \rho_\alpha^{bb'}(t)|_{\mathrm{scatt}}^{\mathrm{LO,F}} = \\ &\int_{-\infty}^{t} dt_1 \sum_{b_1\alpha_1} \Big(G_{\alpha_1}^{b,r}(t,t_1) \left[G_\alpha^{b',r}(t,t_1)\right]^* \\ &\times \left\{ -D_{\alpha\alpha_1}^{bb_1,>}(t,t_1)[\delta_{b,b_1} - \rho_{\alpha_1}^{bb_1}(t_1)]\rho_\alpha^{b_1b'}(t_1) + D_{\alpha\alpha_1}^{bb_1,<}(t,t_1)\rho_{\alpha_1}^{bb_1}(t_1)[\delta_{b_1,b'} - \rho_\alpha^{b_1b'}(t_1)] \right\} \\ &+ G_\alpha^{b,r}(t,t_1) \left[G_{\alpha_1}^{b',r}(t,t_1)\right]^* \\ &\qquad \times \left\{ [\delta_{b,b_1} - \rho_\alpha^{bb_1}(t_1)]\rho_{\alpha_1}^{b_1b'}(t_1) D_{\alpha\alpha_1}^{b_1b',>}(t,t_1) - \rho_\alpha^{bb_1}(t_1)[\delta_{b_1,b'} - \rho_{\alpha_1}^{b_1b'}(t_1)] D_{\alpha\alpha_1}^{b_1b',<}(t,t_1) \right\} \Big), \end{aligned} \tag{5.44}$$

where eq. (2.33) has been used to formulate it in terms of the retarded Green's function only and eq. (5.25) to flip the time arguments in the LO-phonon Green's function. We can exploit the symmetries under complex conjugation of the Green's functions, see eqs. (2.32) and (5.26), to simplify the band diagonal

scattering terms, that is population relaxation, to the following form

$$\partial_t \rho_\alpha^{bb}(t)|_{\text{scatt}}^{\text{LO,F}} = \\ 2\text{Re}\Big[\int_{-\infty}^{t} dt_1 \sum_{b_1\alpha_1} \Big(G_{\alpha_1}^{b,r}(t,t_1)\left[G_\alpha^{b,r}(t,t_1)\right]^* \\ \times \left\{-D_{\alpha\alpha_1}^{bb_1,>}(t,t_1)[\delta_{b,b_1} - \rho_{\alpha_1}^{bb_1}(t_1)]\rho_\alpha^{b_1 b}(t_1) + D_{\alpha\alpha_1}^{bb_1,<}(t,t_1)\rho_{\alpha_1}^{bb_1}(t_1)[\delta_{b_1,b} - \rho_\alpha^{b_1 b}(t_1)]\right\}\Big)\Big].$$

This simplification applies to 2/3 of all scattering terms and saves around 50 % computation time on each, thus leading to an approximate 33.3 % speed up.

Next we consider the scattering terms arising due to the interaction between the electrons and cavity photons. In the RWA the Fock contribution to the contour self-energy is given by eq. (A.25) and with the help of the Langreth rules we obtain the following real time components

$$\Sigma_\alpha^{bb',\text{rad,F},\gtrless}(t,t') = i\hbar|\hbar g_\alpha|^2 \left[G_\alpha^{\text{vv},\gtrless}(t,t')A^{\gtrless}(t,t')\delta_{b,\text{c}} + G_\alpha^{\text{cc},\gtrless}(t,t')A^{\lessgtr}(t',t)\delta_{b,\text{v}}\right]\delta_{b,b'}, \tag{5.45}$$

where we have assumed $g_{\alpha\alpha'} = g_\alpha\delta_{\alpha\alpha'}$, see section 4.4. Below we will present two versions of the electronic scattering terms due to the cavity photons, in the first version in which the GKBA has been applied to the photon Green's function, and a second version in which we keep the photon Green's function in its general two-time form. The GKBA has been applied to the electronic Green's functions in both versions, as we are only interested in equal-time properties for these. For the photons we are, however, interested in the full two-time Green's function[13] as this allows for the calculation of quantities such as emission spectra and indistinguishability, see sections 6.5 and 6.6, while the GKBA is assumed to yield a sufficiently correct equal-time dynamics.

The GKBA for the photons is given by eq. (5.53), where we have also made use of the relations eq. (5.52) to express everything in terms of the number of photons in the cavity $A(t)$. We are now ready to determine the scattering term eq. (5.42) with self-energy given by eq. (5.45) in the GKBA for the electrons and photons. After straight forward insertion the band diagonal term becomes

$$\partial_t \rho_\alpha^{bb}(t)|_{\text{scatt}}^{\text{rad,F}} = -2\text{Re}\Big[\int_{-\infty}^{t} dt_1 \Big(\\ G_\alpha^{\text{v},r}(t,t_1)\left[G_\alpha^{\text{c},r}(t,t_1)\right]^* \left(i\hbar|\hbar g_\alpha|^2 A^r(t,t_1)\right)\left\{[1-\rho_\alpha^{\text{vv}}(t_1)][1+A(t_1)]\rho_\alpha^{\text{cc}}(t_1) - \rho_\alpha^{\text{vv}}(t_1)A(t_1)[1-\rho_\alpha^{\text{cc}}(t_1)]\right\}\delta_{b,\text{c}} \\ -G_\alpha^{\text{c},r}(t,t_1)\left[G_\alpha^{\text{v},r}(t,t_1)\right]^* \left(i\hbar|\hbar g_\alpha|^2 [A^r(t,t_1)]^*\right)\left\{[1-\rho_\alpha^{\text{cc}}(t_1)]A(t_1)\rho_\alpha^{\text{vv}}(t_1) - \rho_\alpha^{\text{cc}}(t_1)[1+A(t_1)][1-\rho_\alpha^{\text{vv}}(t_1)]\right\}\delta_{b,\text{v}}\Big)\Big],$$

where we have used the symmetry relations of the Green's functions and self-energy, eq. (5.14), to simplify as done above with the LO-phonon scattering terms. It is possible to simplify further due to the fact that we only need the real part of the integral, and after a few cancelations we end up with

$$\partial_t \rho_\alpha^{bb}(t)|_{\text{scatt}}^{\text{rad,F}} = -2\text{Re}\Big[\int_{-\infty}^{t} dt_1 G_\alpha^{\text{v},r}(t,t_1)\left[G_\alpha^{\text{c},r}(t,t_1)\right]^* \left(i\hbar|\hbar g_\alpha|^2 A^r(t,t_1)\right) \\ \times \left\{A(t_1)\left[\rho_\alpha^{\text{cc}}(t_1) - \rho_\alpha^{\text{vv}}(t_1)\right] + \rho_\alpha^{\text{cc}}(t_1)\left[1-\rho_\alpha^{\text{vv}}(t_1)\right]\right\}\left(\delta_{b,\text{c}} - \delta_{b,\text{v}}\right)\Big]. \tag{5.46}$$

We have grouped contributions due to stimulated and spontaneous processes under the integral. Furthermore note that the sign of the conduction and valence band contributions are opposite, similarly to what would be expected in a two-level system. This is indeed expected as we only consider diagonal transitions in the in-band quantum number α, hence we consider effective two-level systems for each α. Indeed if

[13] Naively one might expect that the GKBA would yield an approximately valid two-time Green's function, in the full two-time plane, however when one employs equilibrium retarded Green's functions in it these seem to determine the spectral properties. This severely limits its use in calculating e.g. emission spectra as will be discussed further in section 6.5.

no other interactions were present, the set of equations for each α would decouple and could be solved independently. The band off-diagonal term becomes

$$\partial_t \rho_\alpha^{\mathrm{cv}}(t)|_{\mathrm{scatt}}^{\mathrm{rad,F}} = -\int_{-\infty}^{t} dt_1 \left(i\hbar|\hbar g_\alpha|^2 A^r(t,t_1)\right) \Big(\\ |G_\alpha^{\mathrm{v},r}(t,t_1)|^2 \left\{[1-\rho_\alpha^{\mathrm{vv}}(t_1)][1+A(t_1)]\rho_\alpha^{\mathrm{cv}}(t_1) + \rho_\alpha^{\mathrm{vv}}(t_1)A(t_1)\rho_\alpha^{\mathrm{cv}}(t_1)\right\} \\ + |G_\alpha^{\mathrm{c},r}(t,t_1)|^2 \left\{\rho_\alpha^{\mathrm{cv}}(t_1)\rho_\alpha^{\mathrm{cc}}(t_1)[1+A(t_1)] + \rho_\alpha^{\mathrm{cv}}(t_1)[1-\rho_\alpha^{\mathrm{cc}}(t_1)]A(t_1)\right\}\Big),$$

and after a few cancelations we obtain the following simplified version

$$\partial_t \rho_\alpha^{\mathrm{cv}}(t)|_{\mathrm{scatt}}^{\mathrm{rad,F}} = -\int_{-\infty}^{t} dt_1 \left(i\hbar|\hbar g_\alpha|^2 A^r(t,t_1)\right) \Big(\\ |G_\alpha^{\mathrm{v},r}(t,t_1)|^2 \left\{A(t_1)\rho_\alpha^{\mathrm{cv}}(t_1) + \rho_\alpha^{\mathrm{cv}}(t_1)[1-\rho_\alpha^{\mathrm{vv}}(t_1)]\right\} + |G_\alpha^{\mathrm{c},r}(t,t_1)|^2 \left\{A(t_1)\rho_\alpha^{\mathrm{cv}}(t_1) + \rho_\alpha^{\mathrm{cv}}(t_1)\rho_\alpha^{\mathrm{cc}}(t_1)\right\}\Big). \tag{5.47}$$

Again we can group stimulated and spontaneous processes contributing to the electronic dephasing and we note that $\partial_t \rho_\alpha^{\mathrm{vc}}(t)|_{\mathrm{scatt}}^{\mathrm{rad,F}}$ can be obtained through complex conjugation.

Next we treat the same scattering terms as above, but now we do not apply the GKBA for the photonic Green's function. The structure of the terms will be similar, however, a bit more complicated as we cannot anymore make use of the equal-time relation between the greater and lesser photon Green's function, eq. (5.52), and hence no cancelations occur. We introduce a new photon Green's function $\tilde{A}^{\gtrless}(t,t')$ by the following definition

$$i\hbar A^{\gtrless}(t,t') = e^{-i\omega_{\mathrm{cav}}(t-t')}\tilde{A}^{\gtrless}(t,t'), \tag{5.48}$$

which is slowly-varying outside the time diagonal. The retarded electronic Green's functions play a similar role in the GKBA for the electrons as the exponential in the above definition, except here we kept the slowly-varying envelope in its two-time form, whereas for the electrons we only consider the equal-time envelope. The new photon Green's functions satisfy the following symmetry relation

$$[\tilde{A}^{\gtrless}(t,t')]^* = \tilde{A}^{\gtrless}(t',t), \tag{5.49}$$

derived from eqs. (5.48) and (2.32), which will be used to limit the numerical solution to the subdiagonal halfplane in the two-time plane, and for other simplifications. The band diagonal scattering term becomes

$$\partial_t \rho_\alpha^{bb}(t)|_{\mathrm{scatt}}^{\mathrm{rad,F}} = -2\mathrm{Re}\Big[\int_{-\infty}^{t} dt_1 |\hbar g_\alpha|^2 \Big(\\ G_\alpha^{\mathrm{v},r}(t,t_1)\left[G_\alpha^{\mathrm{c},r}(t,t_1)\right]^* e^{-i\omega_{\mathrm{cav}}(t-t_1)} \left\{[1-\rho_\alpha^{\mathrm{vv}}(t_1)]\tilde{A}^{>}(t,t_1)\rho_\alpha^{\mathrm{cc}}(t_1) - \rho_\alpha^{\mathrm{vv}}(t_1)\tilde{A}^{<}(t,t_1)[1-\rho_\alpha^{\mathrm{cc}}(t_1)]\right\}\delta_{b,\mathrm{c}} \\ + G_\alpha^{\mathrm{c},r}(t,t_1)\left[G_\alpha^{\mathrm{v},r}(t,t_1)\right]^* e^{-i\omega_{\mathrm{cav}}(t_1-t)} \left\{[1-\rho_\alpha^{\mathrm{cc}}(t_1)]\tilde{A}^{<}(t_1,t)\rho_\alpha^{\mathrm{vv}}(t_1) - \rho_\alpha^{\mathrm{cc}}(t_1)\tilde{A}^{>}(t_1,t)[1-\rho_\alpha^{\mathrm{vv}}(t_1)]\right\}\delta_{b,\mathrm{v}}\Big)\Big],$$

which can be simplified, for the same reasons as in the GKBA case (and using eq. (5.49)), to

$$\partial_t \rho_\alpha^{bb}(t)|_{\mathrm{scatt}}^{\mathrm{rad,F}} = -2\mathrm{Re}\Big[\int_{-\infty}^{t} dt_1 |\hbar g_\alpha|^2 G_\alpha^{\mathrm{v},r}(t,t_1)\left[G_\alpha^{\mathrm{c},r}(t,t_1)\right]^* e^{-i\omega_{\mathrm{cav}}(t-t_1)} \\ \times \left\{[1-\rho_\alpha^{\mathrm{vv}}(t_1)]\tilde{A}^{>}(t,t_1)\rho_\alpha^{\mathrm{cc}}(t_1) - \rho_\alpha^{\mathrm{vv}}(t_1)\tilde{A}^{<}(t,t_1)[1-\rho_\alpha^{\mathrm{cc}}(t_1)]\right\}(\delta_{b,\mathrm{c}} - \delta_{b,\mathrm{v}})\Big]. \tag{5.50}$$

For the band off-diagonal terms we get

$$\partial_t \rho_\alpha^{\mathrm{cv}}(t)|_{\mathrm{scatt}}^{\mathrm{rad,F}} = -\int_{-\infty}^{t} dt_1 |\hbar g_\alpha|^2 e^{-i\omega_{\mathrm{cav}}(t-t_1)} \Big(\\ |G_\alpha^{\mathrm{v},r}(t,t_1)|^2 \left\{[1-\rho_\alpha^{\mathrm{vv}}(t_1)]\tilde{A}^{>}(t,t_1)\rho_\alpha^{\mathrm{cv}}(t_1) + \rho_\alpha^{\mathrm{vv}}(t_1)\tilde{A}^{<}(t,t_1)\rho_\alpha^{\mathrm{cv}}(t_1)\right\} \\ + |G_\alpha^{\mathrm{c},r}(t,t_1)|^2 \left\{\rho_\alpha^{\mathrm{cv}}(t_1)\rho_\alpha^{\mathrm{cc}}(t_1)\tilde{A}^{>}(t,t_1) + \rho_\alpha^{\mathrm{cv}}(t_1)[1-\rho_\alpha^{\mathrm{cc}}(t_1)]\tilde{A}^{<}(t,t_1)\right\}\Big), \tag{5.51}$$

where $\partial_t \rho_\alpha^{\mathrm{vc}}(t)|_{\mathrm{scatt}}^{\mathrm{rad,F}}$ can be obtained through complex conjugation.

5.4.2. Photonic equations of motion and scattering terms

In this section we will derive the equations of motion governing the Green's functions describing the photonic degrees of freedom. In the electronic case we were primarily interested in the equal-time lesser Green's function, as this describes electronic populations and polarizations. The full two-time electronic Green's functions were only of secondary interest in themselves, needed only in order to solve the inherent two-time equations of motion for the Green's functions correctly. This enabled us to apply the GKBA for the electronic Green's functions, which simplified all aspects of both the formal theory and numerical solution immensely. In many quantum optical experiments the main task is to perform time correlated measurements or record emission spectra, to obtain information on the properties of the photons emitted from some excited structure. Both of these quantities require the full two-time photonic Green's function in order to be calculated theoretically, thus making the two-time photonic Green's function of primary interest in itself, and not just as an device enabling one to obtain equal-time Green's functions. The full two-time formulation of the equation of motion is a complicated affair, and we will therefore start by describing the equal-time GKBA version of the photonic equations of motion first, which are indeed interesting in their own right, and in the end of the section consider the more general two-time version.

In the GKBA the fundamental governing equation is the equation of motion for the equal-time lesser Green's function, eq. (2.50), which for the single mode cavity reduces to

$$i\hbar\partial_t A^<(t,t) = -i\hbar\gamma_{\mathrm{cav}} A^<(t,t) + 2\mathrm{Re}\left\{\int_{-\infty}^{t} dt_1 \left[\sigma^>(t,t_1)A^<(t_1,t) - \sigma^<(t,t_1)A^>(t_1,t)\right]\right\}.$$

To simplify the symmetry relation eq. (5.17) has been used for the self-energy, also a decay term has been added to take into account the finite photon lifetime in the cavity, with the decay rate being given by $\gamma_{\mathrm{cav}} = \omega_{\mathrm{cav}}/Q$, see the discussion above eq. (5.2). The equal-time lesser Green's function, $A^<(t,t)$, is proportional to the number of photons in the cavity, $A(t)$, which we will eventually formulate the equation of motion in terms of. To write the GKBA in terms of $A(t)$ we use eq. (2.31) to obtain the following equal-time relations between the lesser and greater Green's function

$$A^<(t,t) = -i\hbar^{-1}\langle a^\dagger(t)a(t)\rangle = -i\hbar^{-1}A(t), \tag{5.52a}$$
$$A^>(t,t) = -i\hbar^{-1}\langle a(t)a^\dagger(t)\rangle = -i\hbar^{-1}[1+A(t)]. \tag{5.52b}$$

Now we may write the GKBA[14], eq. (2.55), in terms of the photon density

$$A^{\gtrless}(t,t') = \begin{cases} A^r(t,t')[1+A(t')], & > \text{ and } t>t' \\ A^r(t,t')A(t'), & < \text{ and } t>t' \\ -[1+A(t)]A^a(t,t'), & > \text{ and } t<t' \\ -A(t)A^a(t,t'), & < \text{ and } t<t' \end{cases} \tag{5.53}$$

where we will take the retarded and advanced Green's functions in their equilibrium forms. To proceed we need the self-energy of the photons due to the electron-photon interaction. In the RWA and at the pair-bubble level this is given in the contour version by eq. (A.28), with the following real time components

$$\sigma^{\gtrless}(t,t') = -i\hbar\sum_{\alpha_1}|\hbar g_{\alpha_1}|^2 G_{\alpha_1}^{\mathrm{cc},\gtrless}(t,t')G_{\alpha_1}^{\mathrm{vv},\lessgtr}(t',t). \tag{5.54}$$

[14] Whether we use the full GKBA, eq. (2.53), or the GKBA assuming diagonal spectral functions, eq. (2.55), is indifferent in the present case due to the fact that we only consider a single mode.

Using this self-energy, the GKBA for both the electrons, eq. (5.43), and photons, eq. (5.53), we obtain the equation of motion for the photon density $A(t)$

$$\begin{aligned}\partial_t A(t) &= -\gamma_{\rm cav} A(t) \\ &+ 2{\rm Re}\Big\{ \int_{-\infty}^{t} dt_1 \sum_{\alpha_1} G^{{\rm c},r}_{\alpha_1}(t,t_1) \left[G^{{\rm v},r}_{\alpha_1}(t,t_1)\right]^* \left(i\hbar|\hbar g_{\alpha_1}|^2 [A^r(t,t_1)]^*\right) \\ &\qquad \times \left\{[1-\rho^{\rm cc}_{\alpha_1}(t_1)]\rho^{\rm vv}_{\alpha_1}(t_1)A(t_1) - \rho^{\rm cc}_{\alpha_1}(t_1)[1-\rho^{\rm vv}_{\alpha_1}(t_1)][1+A(t_1)]\right\}\Big\},\end{aligned}$$

that can be simplified to the following by a few cancelations

$$\begin{aligned}\partial_t A(t) &= -\gamma_{\rm cav} A(t) \\ &- 2{\rm Re}\Big\{ \int_{-\infty}^{t} dt_1 \sum_{\alpha_1} G^{{\rm c},r}_{\alpha_1}(t,t_1) \left[G^{{\rm v},r}_{\alpha_1}(t,t_1)\right]^* \left(i\hbar|\hbar g_{\alpha_1}|^2 [A^r(t,t_1)]^*\right) \\ &\qquad \times \left\{A(t_1)\left[\rho^{\rm cc}_{\alpha_1}(t_1) - \rho^{\rm vv}_{\alpha_1}(t_1)\right] + \rho^{\rm cc}_{\alpha_1}(t_1)\left[1-\rho^{\rm vv}_{\alpha_1}(t_1)\right]\right\}\Big\}. \quad (5.55)\end{aligned}$$

Notice the strong similarity between this scattering term and that of electronic population, eq. (5.46), hinting that we have chosen a consistent set of self-energies for the two interacting subsystem.

Now we will consider the equations of motion for the two-time photonic Green's functions, $A^{\gtrless}(t,t-\tau)$, only applying the GKBA to the electronic Green's functions. The equation of motion for the two-time Green's functions is eq. (2.49). We note that we need to solve for both the greater and lesser Green's function, as these couple through the scattering terms in their respective equations of motion, consistent with the remarks in the beginning of section 2.3. The equation of motion reads

$$\begin{aligned}i\hbar\partial_t A^{\gtrless}(t,t-\tau) &= -i\hbar\gamma_{\rm cav}\left[A^{\gtrless}(t,t-\tau) - A^{\gtrless}_{\rm eq}(t,t-\tau)\right] \\ &+ \int_{-\infty}^{t} dt_1 \left[\left\{\sigma^{>}(t,t_1) - \sigma^{<}(t,t_1)\right\} A^{\gtrless}(t_1,t-\tau) - \left\{A^{>}(t,t_1) - A^{<}(t,t_1)\right\}\sigma^{\gtrless}(t_1,t-\tau)\right] \\ &- \int_{-\infty}^{t-\tau} dt_1 \left[\sigma^{\gtrless}(t,t_1)\left\{A^{>}(t_1,t-\tau) - A^{<}(t_1,t-\tau)\right\} - A^{\gtrless}(t,t_1)\left\{\sigma^{>}(t_1,t-\tau) - \sigma^{<}(t_1,t-\tau)\right\}\right],\end{aligned}$$

where a phenomenological decay term has been added, to take into account the interaction of the cavity photons with a reservoir through the decay rate $\gamma_{\rm cav}$. The effect of the decay term is to make sure that the photon Green's functions $A^{\gtrless}(t,t-\tau)$ return to their equilibrium values, $A^{\gtrless}_{\rm eq}(t,t-\tau)$, for sufficiently long times after the external pulse has acted. For $\tau > 0$ we[15] note that the integration domains in the memory integrals above overlap for $t_1 \in [t-\tau, -\infty[$, furthermore the structure of the integrands of the two memory integrals is rather similar, hence cancelations between the two could be expected. To anticipate this cancelation we split the first memory integral as $\int_{-\infty}^{t} dt_1 = \int_{t-\tau}^{t} dt_1 + \int_{-\infty}^{t-\tau} dt_1$ and rearrange to obtain

$$i\hbar\partial_t A^{\gtrless}(t,t-\tau) = \partial_t A^{\gtrless}(t,t-\tau)|_{\rm phen} + \partial_t A^{\gtrless}(t,t-\tau)|_{\rm scatt,I} + \partial_t A^{\gtrless}(t,t-\tau)|_{\rm scatt,II}, \quad (5.56)$$

where for notational simplicity we have defined the following three scattering terms

$$\begin{aligned}\partial_t A^{\gtrless}(t,t-\tau)|_{\rm phen} &= -i\hbar\gamma_{\rm cav}\left[A^{\gtrless}(t,t-\tau) - A^{\gtrless}_{\rm eq}(t,t-\tau)\right], \\ \partial_t A^{\gtrless}(t,t-\tau)|_{\rm scatt,I} &= \int_{t-\tau}^{t} dt_1 \left[\left\{\sigma^{>}(t,t_1) - \sigma^{<}(t,t_1)\right\} A^{\gtrless}(t_1,t-\tau) - \left\{A^{>}(t,t_1) - A^{<}(t,t_1)\right\}\sigma^{\gtrless}(t_1,t-\tau)\right], \\ \partial_t A^{\gtrless}(t,t-\tau)|_{\rm scatt,II} &= \int_{-\infty}^{t-\tau} dt_1 \Big[\left\{\sigma^{>}(t,t_1) - \sigma^{<}(t,t_1)\right\} A^{\gtrless}(t_1,t-\tau) - \left\{A^{>}(t,t_1) - A^{<}(t,t_1)\right\}\sigma^{\gtrless}(t_1,t-\tau) \\ &\qquad -\sigma^{\gtrless}(t,t_1)\left\{A^{>}(t_1,t-\tau) - A^{<}(t_1,t-\tau)\right\} + A^{\gtrless}(t,t_1)\left\{\sigma^{>}(t_1,t-\tau) - \sigma^{<}(t_1,t-\tau)\right\}\Big].\end{aligned}$$

[15] We only need to consider the case of $\tau > 0$, due to the fact that the values of the greater/lesser Green's function, on each side of the time diagonal, are related through complex conjugation. This was already pointed out in section 2.3 and is contained in eq. (5.49).

As expected no cancelations occur in $\partial_t A^{\gtrless}(t,t-\tau)|_{\text{scatt,I}}$, while for $\partial_t A^{\gtrless}(t,t-\tau)|_{\text{scatt,II}}$ the cancelations appear to depend on whether the greater or lesser component is considered, however, after actually performing the calculation one finds that $\partial_t A^{<}(t,t-\tau)|_{\text{scatt,II}} = \partial_t A^{>}(t,t-\tau)|_{\text{scatt,II}}$, in agreement with [39]. The simplified result is

$$\partial_t A(t,t-\tau)|_{\text{scatt,II}} = \int_{-\infty}^{t-\tau} dt_1 \Big[\sigma^{>}(t,t_1)A^{<}(t_1,t-\tau) - \sigma^{<}(t,t_1)A^{>}(t_1,t-\tau) \\ - A^{>}(t,t_1)\sigma^{<}(t_1,t-\tau) + A^{<}(t,t_1)\sigma^{>}(t_1,t-\tau)\Big],$$

where the greater/lesser superscript has been dropped as it is no longer necessary. We note that if we take the equal-time limit, $\tau = 0$, in $\partial_t A^{\gtrless}(t,t-\tau)|_{\text{scatt,I}}$ we find that this contribution to the total scattering term vanish due to the integration limits becoming equal. Hence both the greater and lesser Green's function obey the same equation of motion, as $\partial_t A^{<}(t,t-\tau)|_{\text{scatt,II}} = \partial_t A^{>}(t,t-\tau)|_{\text{scatt,II}}$. This might seem surprising, but is fully consistent with the exact relation eq. (5.52) between the greater and lesser Green's function. Furthermore we observe that the equation of motion reduce to the form given by eq. (2.50), as indeed it should.

To obtain explicit expressions for the two-time scattering terms we use the pair-bubble (PB) self-energy eq. (5.54), along with the slowly-varying transformation eq. (5.48). In all scattering terms we have further employed eq. (5.49) to limit the two-time functions to the subdiagonal half-plane, which simplifies the numerical labor significantly. We begin with the phenomenological decay term $\partial_t A^{\gtrless}(t,t-\tau)|_{\text{phen}}$ and readily obtain

$$\partial_t \tilde{A}^{\gtrless}(t,t-\tau)|_{\text{phen}} = -\gamma_{\text{cav}}\left[\tilde{A}^{\gtrless}(t,t-\tau) - \tilde{A}^{\gtrless}_{\text{eq}}(t,t-\tau)\right]$$

Regarding the form of $\tilde{A}^{\gtrless}_{\text{eq}}(t,t-\tau)$ we know from section 5.3.3 that the electronic and photonic degrees of freedom do not influence each other in equilibrium, at our level of approximation. Hence the photon Green's functions in equilibrium will be given by their free version, dressed with the decay rate γ_{cav}, from appendix A.6 we therefore find

$$\tilde{A}^{<}_{\text{eq}}(t,t-\tau) = 0, \quad \tilde{A}^{>}_{\text{eq}}(t,t-\tau) = e^{-\gamma_{\text{cav}}\tau},$$

where we have assumed $n_B(\hbar\omega_{\text{cav}}) = 0$, which is very reasonable at any temperatures normally considered in experiments. For the two-time photonic scattering terms we have employed the GKBA for the electronic Green's functions. For the term $\partial_t \tilde{A}^{>}(t,t-\tau)|^{\text{PB}}_{\text{scatt,I}}$ we get the following expression

$$\partial_t \tilde{A}^{>}(t,t-\tau)|^{\text{PB}}_{\text{scatt,I}} = \int_{t-\tau}^{t} dt_1 \sum_{\alpha_1} |\hbar g_{\alpha_1}|^2 \\ \times \Big[- G^{\text{c},r}_{\alpha_1}(t,t_1)\left[G^{\text{v},r}_{\alpha_1}(t,t_1)\right]^* e^{-i\omega_{\text{cav}}(t_1-t)}\{\rho^{\text{vv}}_{\alpha_1}(t_1) - \rho^{\text{cc}}_{\alpha_1}(t_1)\}\tilde{A}^{>}(t_1,t-\tau) \\ + G^{\text{c},r}_{\alpha_1}(t_1,t-\tau)\left[G^{\text{v},r}_{\alpha_1}(t_1,t-\tau)\right]^* e^{-i\omega_{\text{cav}}(t-\tau-t_1)}\{\tilde{A}^{>}(t,t_1) - \tilde{A}^{<}(t,t_1)\}[1-\rho^{\text{cc}}_{\alpha_1}(t-\tau)]\rho^{\text{vv}}_{\alpha_1}(t-\tau)\Big], \tag{5.57}$$

while for $\partial_t \tilde{A}^{<}(t,t-\tau)|^{\text{PB}}_{\text{scatt,I}}$ we obtain a similar expression

$$\partial_t \tilde{A}^{<}(t,t-\tau)|^{\text{PB}}_{\text{scatt,I}} = \int_{t-\tau}^{t} dt_1 \sum_{\alpha_1} |\hbar g_{\alpha_1}|^2 \\ \times \Big[- G^{\text{c},r}_{\alpha_1}(t,t_1)\left[G^{\text{v},r}_{\alpha_1}(t,t_1)\right]^* e^{-i\omega_{\text{cav}}(t_1-t)}\{\rho^{\text{vv}}_{\alpha_1}(t_1) - \rho^{\text{cc}}_{\alpha_1}(t_1)\}\tilde{A}^{<}(t_1,t-\tau) \\ + G^{\text{c},r}_{\alpha_1}(t_1,t-\tau)\left[G^{\text{v},r}_{\alpha_1}(t_1,t-\tau)\right]^* e^{-i\omega_{\text{cav}}(t-\tau-t_1)}\{\tilde{A}^{>}(t,t_1) - \tilde{A}^{<}(t,t_1)\}\rho^{\text{cc}}_{\alpha_1}(t-\tau)[1-\rho^{\text{vv}}_{\alpha_1}(t-\tau)]\Big]. \tag{5.58}$$

For the last term, $\partial_t \tilde{A}(t,t-\tau)|^{\mathrm{PB}}_{\mathrm{scatt,II}}$, we have a single expression for both the greater and lesser component

$$\begin{aligned}\partial_t \tilde{A}(t,t-\tau)|^{\mathrm{PB}}_{\mathrm{scatt,II}} &= \int_{-\infty}^{t-\tau} dt_1 \sum_{\alpha_1} |\hbar g_{\alpha_1}|^2 \\ &\times \Big[G^{\mathrm{c},r}_{\alpha_1}(t,t_1) \left[G^{\mathrm{v},r}_{\alpha_1}(t,t_1) \right]^* e^{-i\omega_{\mathrm{cav}}(t_1-t)} \{ -[1-\rho^{\mathrm{cc}}_{\alpha_1}(t_1)]\rho^{\mathrm{vv}}_{\alpha_1}(t_1)[\tilde{A}^<(t-\tau,t_1)]^* + \rho^{\mathrm{cc}}_{\alpha_1}(t_1)[1-\rho^{\mathrm{vv}}_{\alpha_1}(t_1)][\tilde{A}^>(t-\tau,t_1)]^* \} \\ &+ \left[G^{\mathrm{c},r}_{\alpha_1}(t-\tau,t_1) \right]^* G^{\mathrm{v},r}_{\alpha_1}(t-\tau,t_1) e^{-i\omega_{\mathrm{cav}}(t-\tau-t_1)} \{ \tilde{A}^>(t,t_1)\rho^{\mathrm{cc}}_{\alpha_1}(t_1)[1-\rho^{\mathrm{vv}}_{\alpha_1}(t_1)] - \tilde{A}^<(t,t_1)[1-\rho^{\mathrm{cc}}_{\alpha_1}(t_1)]\rho^{\mathrm{vv}}_{\alpha_1}(t_1) \} \Big].\end{aligned} \tag{5.59}$$

As used and mentioned several times in previous sections, all Green's functions of an equilibrium system only depend on the difference between their two different times, which was utilized heavily in section 5.3. All the non-equilibrium equations of motion derived in this and the previous section, are equations of motion propagating the Green's functions along the time diagonal or parallel to it. Along these straight lines the two times do not change relative to each other, and one would expect all source terms to these equations of motion to vanish in the case of an equilibrium system. Reminding ourselves that for a semiconductor in equilibrium we assume that all electrons are in the valence band, hence $\rho^{\mathrm{vv}}_{\alpha}(t) = 1$ and $\rho^{\mathrm{cc}}_{\alpha}(t) = 0$, and that no photons are thermally excited, $\tilde{A}^<(t,t-\tau) = 0$. Noting this it is relatively straight forward to see that all electronic scattering terms indeed vanish in equilibrium, due to the structure alone. For the photonic scattering terms in the GKBA, it is equally apparent that also these vanish for a system in equilibrium. However, the situation is not that clear cut for one of the the two-time scattering terms, namely eq. (5.57), while for the two other it is relatively easy to see that these are zero in equilibrium. After using the equilibrium values stated above and writing all functions as single-time quantities, we may basically write eq. (5.57) on the simplified form

$$\int_{t-\tau}^{t} dt_1 g(t_1 - t + \tau) a(t - t_1) - \int_{t-\tau}^{t} dt_1 g(t - t_1) a(t_1 - t + \tau).$$

To see that an integral of this type is indeed zero, one may perform a change of integration variable according to [37] $\tilde{t}_1 = 2t - t_1 + \tau$ in one of the integrals, after which it is clearly seen that this scattering term also vanish in equilibrium.

Path	Scattering term	function	memory time t_1
$C_{\mathrm{I},1}$	$\partial_t \tilde{A}^{\gtrless}(t,t-\tau)\|^{\mathrm{PB}}_{\mathrm{scatt,I}}$	$\tilde{A}^{\gtrless}(t_1,t-\tau)$	$[t-\tau,t]$
$C_{\mathrm{I},2}$	$\partial_t \tilde{A}^{\gtrless}(t,t-\tau)\|^{\mathrm{PB}}_{\mathrm{scatt,I}}$	$\tilde{A}^{\gtrless}(t,t_1)$	$[t-\tau,t]$
$C_{\mathrm{II},1}$	$\partial_t \tilde{A}(t,t-\tau)\|^{\mathrm{PB}}_{\mathrm{scatt,II}}$	$\tilde{A}^{\gtrless}(t-\tau,t_1)$	$]-\infty,t-\tau]$
$C_{\mathrm{II},2}$	$\partial_t \tilde{A}(t,t-\tau)\|^{\mathrm{PB}}_{\mathrm{scatt,II}}$	$\tilde{A}^{\gtrless}(t,t_1)$	$]-\infty,t-\tau]$

Table 5.2.: *Table explaining the integration paths shown in figure 5.5.*

Due to the significantly more difficult numerical procedure of solving the two-time equations of motion, as oppose to the single-time equations of motion, we briefly sketch the strategy for doing this. As mentioned above our equations of motion are formulated so that we propagate the Green's functions on or parallel to the time diagonal, which has the consequence that the difference time τ only enters the equations of motion as a parameter. This simplifies the numerical solution process, as we only have a single equation of motion, even though we have two independent times. Furthermore, this allows for a formulation that can be solved efficiently on a parallel computer. To illustrate the procedure, we show in figure 5.5 the steps needed to be taken to obtain the values of the two-time photonic Green's functions in a point $(t+\Delta t, t+\Delta t-\tau)$, where Δt is time discretization. The area in the figure between the two parallel lines is where we solve for the two-time Green's functions, and finite width of this strip illustrate the memory depth of the system, explicitly given by $\tau_{\max}$. Inspecting the scattering terms in eq. (5.56), we find that for the general case

of non-zero τ four different integration paths need to be followed. These originate from various argument arrangements in the photonic Green's functions, and are shown as the dashed lines in the figure and defined in detail in table 5.2. What should be noted from the figure, is that in order to increase t by Δt, all one must know is the values of the Green's functions in grey area in the figure, and this holds for any value of τ, which is the essential point. One does not have to start at $\tau = 0$, as could be expected as this is normally the case when time stepping, and hence the integrals can be calculated independently for each value of τ, allowing for parallelization, making large simulations possible. One does however have to solve for all τ's in the memory strip before t can be increased by yet another Δt.

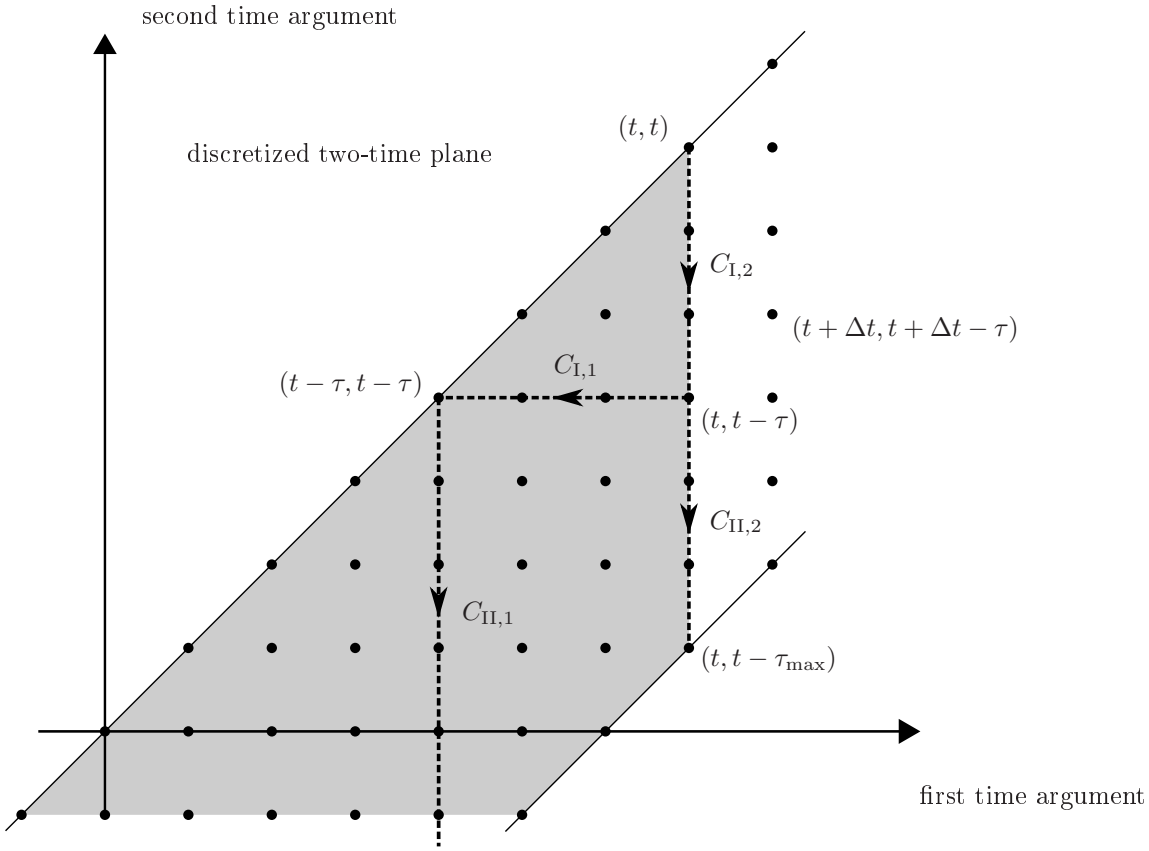

Figure 5.5.: *Schematic figure of the discretized two-time plane showing several important sets of time coordinates and four integration paths, the C's, followed in the photonic scattering terms.*

The equations of motion described above where solved using the numerical methods described in appendix A.4, further the slowly-varying versions of all source terms are presented in appendix A.9.

5.5. Summary

The main result of this chapter is final formulation of the equations of motion governing our non-equilibrium system. However, in order to get this far we performed a final set of approximations on the fundamental Hamiltonians of the system. Also, we treated the truncation of the various self-energies, which were all

kept in the lowest order, but self-consistent as dictated by particle conservation. The detailed derivation was performed in appendix A.5. A section was also devoted to studying the equilibrium properties of our system. These are important as knowledge of the equilibrium retarded Green's functions is very important for the application of the GKBA. The LO-phonon interaction was found to drastically change the properties of the non-interacting system, which were discussed for a few numerical examples. Surprisingly, the photon interaction was found not to alter the equilibrium properties of the electronic system, meaning that no correlations exists between the two species. In the last section we derived the kinetic equations for both the electronic and photonic degrees of freedom, in the general case applicable to a non-equilibrium situation. For the electronic equations the GKBA was applied everywhere, however for the photonic equations we presented two versions, namely one with and without application of the GKBA.

6. Results and Discussion

6.1. Introduction

In this chapter we present results of the numerical solution of the equations of motion derived in the previous chapter. The equations of motion will be applied to a number of interesting situations, which we think are relevant for obtaining an understanding of the effects of many-body interactions in our cQED system. A main task of this chapter will be the determination of the absorption spectra for our cQED system. This will be investigated for variety of different parameters and yield much information on the global spectral properties of the system. Another focus is the investigation of more specific situations where, under various circumstances, electrons are excited across the bandgap, and the subsequent population dynamics is analyzed in terms of time resolved series. These series display directly the interplay between electrons, phonons, and photons and allows one to obtain some intuition on the complicated many-body dynamics. In the last two sections we investigate properties specific to the photonic degrees of freedom, namely the emission spectra and indistinguishability of the photons emitted from the cavity. The numerical solution of the equations is in itself a significant task, and typical simulation times for the system configurations we have considered, tend to span from hours and up to one week. We will however not discuss the technicalities of the numerical solution process, as our focus is on analyzing the physics and theoretical model, and we only briefly discuss the numerical methods in appendix A.4.

6.2. Unphysical populations

During the verification and testing of the numerical implementation of the equations of motion presented in chapter 5, certain parameter sets were found to cause the failure of the diagonal elements of the density matrix, $\rho_\alpha^{bb}(t)$, to stay within the interval $[0;1]$. This result is of course unphysical as it ruins the statistical interpretation of the density matrix, and is an unacceptable result of a physical model. It is a known problem in the literature, that the "uncontrolled approximations" [70] which are involved when deriving approximate quantum kinetic equations, especially in non-equilibrium, can cause unphysical populations to appear. To our knowledge there do not exist any systematic way of choosing the self-energy, so that one is guarantied to obtain populations within $[0;1]$, as it is the case, e.g., with conservation of total particle number, see appendix A.5. In this section we will describe an example where this failure occurs and discuss its implications for the developed theory.

A system where the failure occurs is that described in section 5.3.2, which consists of purely discrete states. The scenario is the following; a weak pulse excites the system through eq. (5.38), while the electrons interact with LO-phonons through the scattering term eq. (5.44). We do not consider the Coulomb or electron-photon interaction. The temporal width of the pulse is 100 fs, it has its peak value at $t = 0.4$ ps, and we consider five different excitation energies. The Fourier transformed of the five pulses and the linear absorption spectrum of the system, calculated using the method described in section 6.3, are shown in figure 6.1. Here it is seen that we consider three cases of non-resonant excitation #1, #3, and #5 and two cases of resonant excitation #2 and #4, as it turns out that the failure depends very much on the excitation conditions.

In figure 6.2(a) we show the time evolution of the populations $\rho_\alpha^{bb}(t)$ for all states in both conduction and valence band, for the five excitation energies. After inspection of the solutions it is found that the populations describing the resonant excitations #2 and #4 behave physically, staying within the

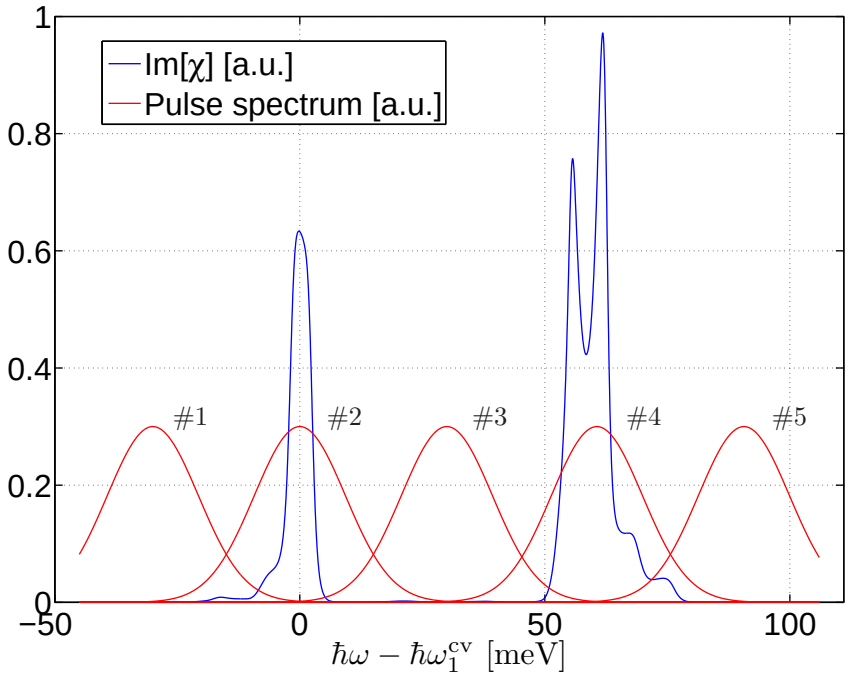

Figure 6.1.: *Figure showing the absorption spectra of the considered system (blue line) and the spectrums of the five different excitation pulses (red lines).*

[0; 1] interval, and eventually reach a quasi-thermal equilibrium after approximately 5 ps (not shown in figure 6.2(a)). For all the non-resonant excitations #1, #3, and #5 we do, however, observe unphysical populations below 0 and above 1, but on a longer timescale they all reach a quasi-thermal equilibrium with fully positive populations. The numbers in the figure show that the failure is quite substantial, especially for the conduction band, and hence indicates, along with the smoothness of the curves, that we are not dealing with some numerical noise issue. It should also be noted that the failure also occurs at stronger excitation where larger occupation probabilities are obtained. The first question that comes to mind is why does the theory only fail for the non-resonant excitations? To provide a possible answer for this, we have solved the equations without the LO-phonons, and the results are shown in figure 6.2(b). For the resonant cases we find what is expected, namely that the pulse excites some of the electrons which subsequently do not relax or dephase due to the lack of a decay mechanism. For the non-resonant cases we observe a phenomena known as adiabatic following [71, 72], where the populations are seen to basically follow the temporal shape of the pulse, hence the populations return to their equilibrium values after the pulse has passed. This phenomena occurs when the detuning between the excitation pulse and electronic transitions, is considerably larger than the spectral width of the pulse or any level broadenings. The adiabatic following of the populations, is thought to be the reason why the theory only fails when considering the non-resonant excitation cases. In these cases the populations in the conduction and valence band return to their extremal values of 0 and 1 respectively. As the approximate treatment of the LO-phonon interaction does not explicitly guarantee populations in the [0; 1] interval, exactly the cases where adiabatic following occur are thought to be extra sensitive to breaking the physical bounds of the populations. A quantity as the total particle number is, however, explicitly conserved through the use of self-consistent self-energies, and in our simulations we do indeed find that the particle number is conserved down to the numerical accuracy. The particle number conservation is taken as a strong indication that the equations of motion are solved correctly. It should be noted that including the Hartree energy renormalization eq. (5.40), does not change the solution to any significant degree, indicating that this correction is very small for the considered system.

The electronic single-particle wavefunctions used in these simulations are very similar for electrons in the

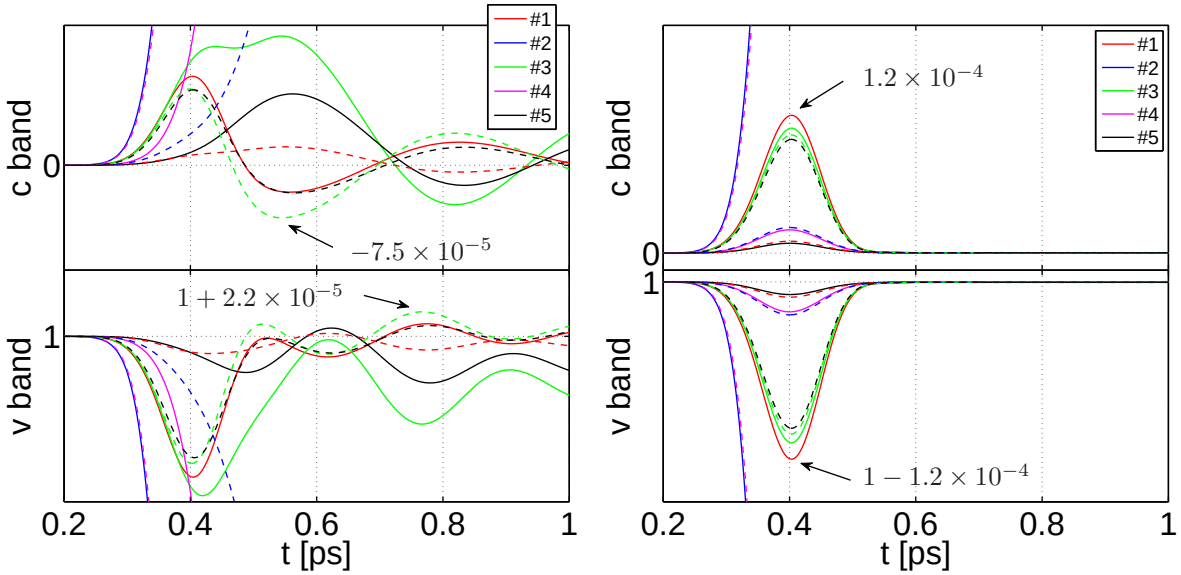

(a) Time evolution of the occupation probabilities with LO-phonon scattering.

(b) Time evolution of the occupation probabilities without LO-phonon scattering.

Figure 6.2.: *The different colored series are for different excitation energies, see figure 6.1, while the solid lines are* $\rho_1^{bb}(t)$ *and the dashed* $\rho_{2/3}^{bb}(t)$, $\rho_3^{bb}(t) = \rho_2^{bb}(t)$ *due to symmetry.*

conduction and valence band, which has the consequence that the Coulomb matrix elements that enter into the LO-phonon self-energy are very similar in magnitude for the electrons in both bands. Also the single-particle transition energies within each band are not far apart, we have $\hbar(\omega_2^{\mathrm{c}} - \omega_1^{\mathrm{c}}) = 36.17$ meV for the conduction band and $\hbar(\omega_1^{\mathrm{v}} - \omega_2^{\mathrm{v}}) = 24.44$ meV for the valence band, where we notice that the conduction band transition is almost perfectly resonant with a LO-phonon having an energy of 36.8 meV. This rather symmetric setup is a consequence of the band parameters we have chosen to describe the free electrons. They were chosen to yield an equal number of bound QD states for the electrons in both bands, which is desirable when only describing off-diagonal elements in the band index as we do (see discussion in section 5.4.1). To narrow down the origin of the population bound breaking another set of band parameters was tested, see appendix A.8 and section 6.3. This set resulted in more spatially localized valence band wavefunctions, yielding larger Coulomb matrix elements and smaller transition energies (≈ 15 meV), and much larger transition energies for the conduction band states ($\approx 2 \times \hbar\omega_{\mathrm{LO}}$). The same set of simulations as described above was performed on this new system, and it was found that no breaking of the population bounds occurred. To identify whether the reason for this new situation arose from the asymmetric matrix elements or the difference in transition energies compared to the first system, the transition energy of the conduction band was manually set to $\approx 1.5 \times \hbar\omega_{\mathrm{LO}}$. After this change the unphysical populations again started to occur, though not of the magnitude as seen in figure 6.2(a). We must therefore conclude that the present theory yields the worst results, sometimes even unphysical, when intra-band transitions are close to resonant with the LO-phonon energy. This conclusion is consistent with the findings of [73], who study a slightly different, but comparable system, in an exactly solvable model and makes comparisons to approximations similar to ours.

Negative populations can also occur as a result of the breakdown of the GKBA as investigated by [38]. This is however not thought to be the reason in our case, as we consider a material with a low LO-phonon coupling as opposed to [38], who consider a strong coupling material. The authors of [38] also raised the question of whether populations within [0;1] can be guaranteed on formal grounds, but knew of none work that could provide such a guarantee. More fundamentally the problems in our model are expected to arise due to the fact that we consider a purely discrete electronic system, i.e. we have neglected the WL continuum of delocalized states. This suspicion is supported by the fact that several others [41, 42, 74] have

obtained physical results for QD systems, coupled to a WL continuum, in the same self-energy approximation as considered here. Systematically going to higher orders in the LO-phonon self-energy should in principle remedy the problems concerning unphysical populations for the purely discrete system, that we consider. We suspect that the reason why the present self-energy approximation appear to be sufficient in the presence of a WL continuum, is connect to the presumably faster decay of higher order correlations (i.e. higher order self-energies), due to the access to the larger phase space provided by the continuum. However, as the ultimate goal is to include the WL continuum in the simulations, we will not pursue higher order corrections as the present order is expected to be sufficient, in the presence of a continuum [69]. Due to lack of time in the present project, inclusion of the WL is unrealistic and we will therefore continue with the material parameters not resulting in unphysical populations.

6.3. Absorption spectra

In this section we present calculations of the linear optical susceptibility for different temperatures in the range from 150 K to 300 K. The imaginary part of the susceptibility is known to be closely related to the absorption experienced by a weak probe field, see e.g. [56, p. 11], impinging on a system, and thus provides us with a valuable source of information on the effects the interactions have had on the free system. The spectrum will contain energy renormalizations and linewidth broadenings caused by the interactions, hence knowing this will make it much easier later on to perform specific narrow bandwidth excitations of the interacting system. The linear susceptibility is also an often treated quantity in the literature making comparison with other theories and models possible, that could help to verify our implementation.

As described in section 6.2 certain choices of parameters for the QD system resulted in unphysical populations. For this reason we will not continue our simulations with the system described in section 4.2.3 and section 5.3.2, but rather chose a new set of parameters not suffering from the unphysical populations. The band parameters of the new system are presented in table A.2, while the geometrical parameters of the new QD system are shown in table 6.1 (left), see figure 4.2. The size of the QD was tuned so that three clearly bound states formed in the conduction band. However due to the new set of band parameters[1] no symmetry in the number of bound states between the two bands exists, and the number of bound states in the valence band is much greater than that of the conduction band. This situation is illustrated schematically in figure 6.3, but for simplicity we will only consider the first three bound states in the valence band and all the bound states in the conduction band, indicated by the dashed box in the figure. We will also neglect the spin degrees of freedom, as we expect that including these will only cause minor

[1] Most significantly the larger heavy hole mass of the valence band electrons.

Quantity	Value	Unit	Quantity	Value	Unit	Quantity	Value	Unit
h	1.25	nm	$\hbar\omega_1^{\mathrm{c}}$	567.8	meV	V_{1111}^{cccc}	19.59	meV
d	1.25	nm	$\hbar\omega_2^{\mathrm{c}}$	650.5	meV	V_{2222}^{cccc}	13.76	meV
r_1	10	nm	$\hbar\omega_3^{\mathrm{c}}$	650.5	meV	V_{1111}^{vvvv}	27.05	meV
r_2	5	nm	$\hbar\omega_1^{\mathrm{v}}$	-270.5	meV	V_{2222}^{vvvv}	21.60	meV
R_0	50	nm	$\hbar\omega_2^{\mathrm{v}}$	-285.5	meV	V_{1111}^{cvcv}	22.41	meV
L_z	40	nm	$\hbar\omega_3^{\mathrm{v}}$	-285.5	meV	V_{2222}^{cvcv}	16.07	meV
						V_{1212}^{cccc}	15.35	meV
						V_{1212}^{vvvv}	22.98	meV
						V_{2112}^{cccc}	4.08	meV
						V_{2112}^{vvvv}	6.80	meV

Table 6.1.: *Table presenting various parameters: (left) geometrical parameters of the QD, (mid) free single-particle energies of the considered bound states in the QD, and (right) a representative selection of Coulomb matrix elements.*

changes. Indeed it is only the electron-electron Coulomb interaction that mixes subspaces of different spins in the Hamiltonian, which is not the interaction of main interest. The resulting energies of the levels are shown in table 6.1 (mid), along with a representative set of Coulomb matrix elements[2] in table 6.1 (right). The parameters describing the LO-phonons are given in table 5.1.

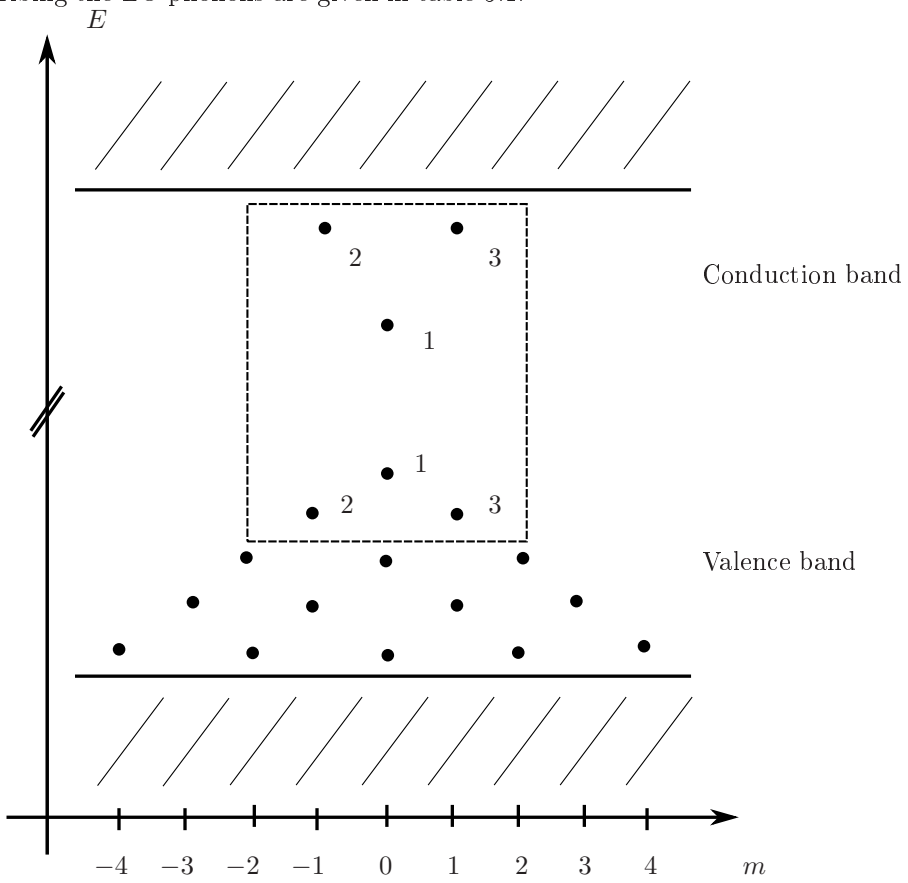

Figure 6.3.: *Schematic illustration of the level structure of the QD used in the simulations in section 6.3. The dashed box indicates the levels used in the simulations.*

Next we describe the theory needed to obtain the susceptibility for our system. The response of a system to a weak externally applied electric field, $E(t)$, can be described by an induced polarization of the medium. Within linear response theory the induced polarization can be written as [56]

$$P(t) = \int_{-\infty}^{t} dt' \chi(t,t') E(t'),$$

where $\chi(t,t')$ is the linear optical susceptibility that per definition is independent of $E(t)$, and only depends on the properties of the underlying system that is being probed. It should be noted that we assume pure scalar quantities and that $t > t'$ due to causality. The above form is completely general and $\chi(t,t')$ can describe any non-equilibrium system due to its two-time dependence, this form could, e.g., be used for

[2] The effective static dielectric constant ε enters the expression for the Coulomb interaction, which is a well known quantity for most bulk semiconductors. We do however deal with heterostructures, and here the situation is not as clear cut as for a bulk system. As we exclusively consider electronic states bound to the QD or WL, and not the surrounding barrier/bulk material, we choose the dielectric constant of the low bandgap material. In this thesis we only consider the ternary alloy $In_xGa_{x-1}As$ as the low bandgap material, and therefore we use the following expression for the effective dielectric constant: $1/\varepsilon_x = x/\varepsilon_{InAs} + (1-x)/\varepsilon_{GaAs}$, which seems appropriate for a heterostructure. The values of the binary compounds are found from [31] for GaAs, $\varepsilon_{GaAs}/\varepsilon_0 = 12.5$, and [75] for InAs, $\varepsilon_{InAs}/\varepsilon_0 = 14.61$. For $x = 0.6$ we get the value $\varepsilon_x/\varepsilon_0 = 13.68$ and for pure InAs, $x = 1$, the value is $\varepsilon_x/\varepsilon_0 = 14.61$. Prior to the discovery of the unphysical populations described in section 6.2, we used a $x = 0.6$ system and afterwards we switched to a $x = 1$ system as explained in the present section. Therefore the values presented in table 6.1 are for the $x = 1$ system.

describing the often performed pump-probe experiments. We are in the present section not interested in probing non-equilibrium systems, but rather systems in thermal equilibrium where it holds that the susceptibility is only a function of the time difference $\chi(t,t') = \chi(t-t')$, due to arguments similar to those of eq. (5.18). This yields a huge simplification in actually obtaining the susceptibility, as now we may write the formulae as

$$P(t) = \int_{-\infty}^{t} dt' \chi(t-t') E(t'), \tag{6.1}$$

which is nothing but a convolution integral that under Fourier transformation, eq. (5.1), transforms into an algebraic equation for the susceptibility which is easily solved as

$$\chi(\omega) = \frac{P(\omega)}{E(\omega)}. \tag{6.2}$$

The next task is to determine the "macroscopic" polarization from our microscopic model of the system. This is done by calculating the expectation value of the microscopic dipole operator as follows

$$P(t) = \mathrm{Tr}\left[\boldsymbol{D}\cdot\boldsymbol{e}_{\boldsymbol{E}}\rho(t)\right] = -\mathrm{Tr}\left[d\rho(t)\right] = -\sum_{bb'\alpha} d_\alpha^{bb'}\rho_\alpha^{b'b}(t),$$

where we use the dipole operator projected onto the direction of the excitation field, $d = -\boldsymbol{D}\cdot\boldsymbol{e}_{\boldsymbol{E}}$, as this is the only relevant quantity in a specific experiment, see eq. (3.21). Performing the sums over the band indices and using $d_\alpha = d_\alpha^{\mathrm{cv}} = d_\alpha^{\mathrm{vc}}$ we arrive at our final expression for the polarization

$$P(t) = -\sum_\alpha d_\alpha[\rho_\alpha^{\mathrm{cv}}(t) + \rho_\alpha^{\mathrm{vc}}(t)] = -\sum_\alpha d_\alpha[\tilde{\rho}_\alpha^{\mathrm{cv}}(t)e^{-i\omega_\alpha^{\mathrm{cv}}t} + \tilde{\rho}_\alpha^{\mathrm{vc}}(t)e^{-i\omega_\alpha^{\mathrm{vc}}t}]. \tag{6.3}$$

In the above expression we have also written the density matrix in terms of its slowly-varying components through the transformation

$$\rho_\alpha^{bb'}(t) = e^{-i\omega_\alpha^{bb'}t}\tilde{\rho}_\alpha^{bb'}(t),$$

that pulls out the fast oscillation due to the free evolution of the system. The actual numerical solution of the equations of motion was performed for the slowly-varying components, as this yields very significant advantages in terms of time discretization. See appendix A.9 for the slowly-varying versions of all equations of motion and appendix A.4 for a presentation of the numerical methods used.

The polarization eq. (6.3) is obtained by solving the equations of motion for the density matrix, after excitation by an ultra-short pulse of width 15 fs. Even though eq. (6.2) in principle holds for any electric field, it is in practise important that the pulse is temporally short enough to spectrally cover all resonances of the system, as otherwise numerical noise will become too much of a factor. For the Gaussian pulse used in our simulations, the Full Width Half Maximum (FWHM) width is in energy units given by $w_E = 4\ln(2)\hbar/\Delta t_{\mathrm{pulse}}$, which for $\Delta t_{\mathrm{pulse}} = 15$ fs yields $w_E = 122$ meV, being sufficient for our level scheme.

Our equations of motion are all derived from a theory that deals with reduced density matrices, and therefore they all contain memory integrals, linking the present state of the system to the past. All these memory integrals in principle extend from the present and back to the non-interacting past at $t = -\infty$, which is a situation that can not be treated numerically and fortunately we do not have to. Due to the interactions in our system, we expects correlations to decay when moving away from the time-diagonal. This is indeed the case as seen in section 5.3.2, where the finite width of the peaks in the spectrum of the electronic density of states, corresponds to decay in the time domain. For all electronic scattering terms it is exactly the equilibrium retarded Green's functions that set this so-called memory depth, due to the use of the GKBA, and similarly for the photons when the GKBA is used for these. In the simulations we present below, we have set the memory depth according to the criteria $\mathcal{G}_\alpha^b(\tau_{\mathrm{memory}}) < 10^{-4}$, with $\mathcal{G}_\alpha^b(\tau)$

T [K]	τ_{memory} [ps]
300	7
250	9
200	12
150	18

Table 6.2.: *Memory depths used in the absorption simulations performed in this section.*

being defined in eq. (5.29). As the retarded Green's functions always enter in pairs, this means that at a memory depth of τ_{memory}, the memory kernel will be suppressed by a factor of at least 10^{-8}, ensuring that all significant effects have been taken into account. For the specific system and temperatures we have considered in this section, we used the memory depths presented in table 6.2, which are determined according to the above mentioned criteria.

We note that being in the linear regime we do not formally induce any changes in the populations of the different electronic states, this can be deduced by an expansion in the excitation pulse. As such we need not solve for the diagonal elements of electronic density matrix, reducing the dimension of the equation system by a factor of 2/3. Furthermore we also note that from the slowly-varying version of eq. (6.3), we see that its Fourier transform will be peaked at the frequencies $\omega = \pm|\omega_\alpha^{\text{cv}}|$, thus having significant contributions at both positive and negative frequencies. The two parts of the spectrum are however mirror images of each other, and therefore essentially yields the same information. Also, only positive frequencies can be measured in experiments [76, p. 28], therefore we will only show spectrum at positive frequencies.

6.3.1. LO-phonons and Coulomb

In this subsection we will present and discuss absorption spectra for the free system described above with the effects of LO-phonons, described through eq. (5.44), and the HF Coulomb interaction between the electrons, described by eq. (5.39). The singular Hartree self-energy from the LO-phonons, eq. (5.40), does not contribute to the absorption spectra simulations as it only involves populations, that by construction do not contribute in equilibrium.

In figure 6.4 we show the imaginary part of the susceptibility for four temperatures between 150 K and 300 K, consistent with our choice of only considering LO-phonons, the top figure is with the HF Coulomb self-energy included and the bottom figure is without. When discussing the spectra we will adopt the terminology commonly used in atomic physics and denote the levels in our QD with the letters s, p, d and so on. Due to the size of our QD we only need s and p states, with s being the lowest/highest in the conduction/valence and p being the next lowest/highest in the conduction/valence band.

We start out discussing the spectra without the Coulomb interaction as this is the simplest. The most dominating features of the spectra are still the s and p transitions near the transition energies of the free system. These have obtained a finite width due to the dephasing caused by the interaction with LO-phonons and the transition energy has also been renormalized slightly to lower values. It is clear from the spectra that the lineshape of the s and p transitions are non-Lorentzian, bearing witness of non-exponential decay of the polarization in the time domain. This non-exponential decay arises due to the fact that our system has memory, but is limited to a short time span after the excitation by the external pulse. This time span is set by the decay of the memory kernel ([26, p. 40] and [56, p. 227]), i.e. the retarded Green's functions of the electrons. For times longer than the memory depth of the system, the polarization enters a regime of slow exponential decay, giving rise to the sharp resonances in the spectra having an approximately Lorentzian lineshape. The reason for the slower decay in the long-time limit, is due to the time-energy uncertainty relation $\Delta E \Delta t \geq \hbar/2$. This relation dictates that

the energy must be conserved to a higher degree in each scattering event, than was the case in the short-time regime. This yields less efficient scattering in the long-time limit, as oppose to the short-time limit where energy need not be conserved to such high degree and thus more processes contribute to scattering.

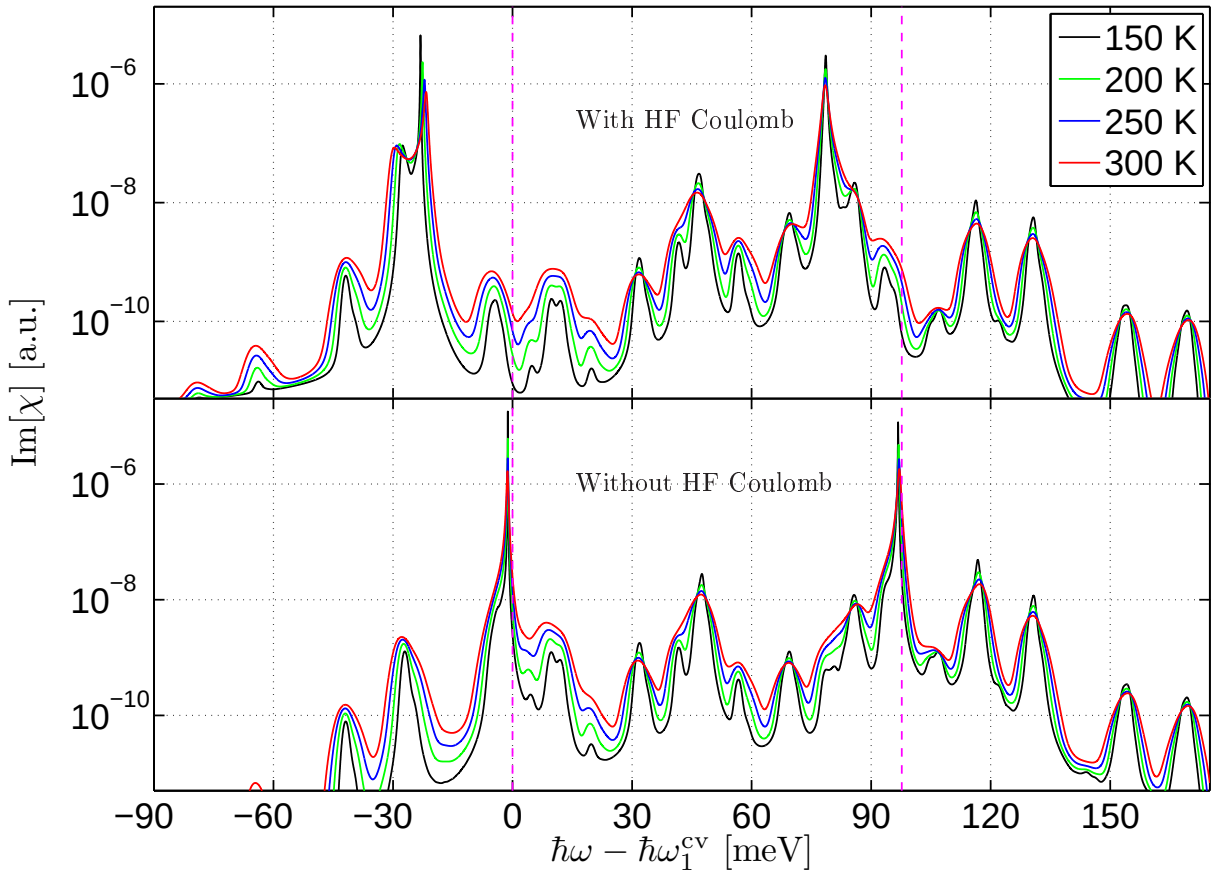

Figure 6.4.: *Absorption spectra of the system shown in figure 6.3 with the effects of LO-phonons and the Coulomb interaction. The transition energies of the free system are indicated by the dashed vertical lines.*

Apart from the main s and p transitions we observe a very rich structure of smaller peaks, positioned on the high and low energy sides of both main peaks. These are so-called LO-phonon-assisted transitions, and arise from processes where electrons having absorbed or emitted a number of LO-phonons, make optical transitions. To illustrate these LO-phonon dressed electrons, we show in figure 6.5 the equilibrium spectral density of the electron states involved in these simulations, through the GKBA. In principle we have transitions between every peak in the spectral densities, for equal[3] in-band quantum numbers (e.g. $A_1^{\mathrm{c}}(\hbar\omega)$ and $A_1^{\mathrm{v}}(\hbar\omega)$). However, due to the thermal broadening and the accuracy limits imposed by the numerics, many of these are too weak to be resolved. A general feature when considering the series for decreasing temperature is that the spectral features sharpen. This is indeed expected as the broadening is caused by the interaction with the LO-phonons, and as the thermal occupation of these decrease with temperature less scattering is expected to occur. There is a notable difference in the behavior of the peaks due to LO-phonon-assisted transitions as a function of temperature, some of them

[3] This is due to the fact that we only consider direct optical transitions, i.e. where the in-band quantum numbers α are equal. Allowing for "indirect" transitions would lead to a much more complicated spectrum, however, with smaller peak heights due to the smaller matrix element causing the transition.

increase and some decrease in peak height as the temperature is lowered. We expect this behavior to arise from the fact, that the LO-phonon-assisted transitions are between electron states either having absorbed or emitted a number of LO-phonons, and these behave differently on temperature. This is clearly illustrated in the case of the the valence band spectral densities in figure 6.5. Here the peaks on the high energy side decrease, corresponding to absorption, and those in the low energy side increase, corresponding to emission, as the temperature is decreased. We will therefore have three different kinds of LO-phonon-assisted transitions namely: 1) between two absorption sidebands which should therefore decrease the most for decreasing temperature, 2) between two emission sidebands which should increase for decreasing temperature, and 3) between an emission and absorption sideband where the height should be an intermediate between the two first. Predicting the relative strengths and positions of the LO-phonon-assisted transitions, would be a very complex and difficult procedure and one would have to analyze the LO-phonon scattering term in great detail. We are quite certain that the overall structure of the LO-phonon-assisted resonances, can be understood in terms of the above and we will therefore not go into further detail on this point.

A characteristic feature seen in many of the peaks at 300 K is that they appear to consist of a main peak and a shoulder on one of the sides, causing an apparent asymmetry of the resonance. For most of these, however, we observe, as temperature is lowered, that the shoulders are simply lesser pronounced resonances on their own, and not an asymmetry of the main peak. A curious feature is seen in the height of the s and p main resonances, where we notice that for all temperatures considered, the s peak is higher than the p peak. From a simple model of the system where, instead of LO-phonons, a constant dephasing rate is added to the off-diagonal elements of the density matrix, we expect the p resonance to have twice the maximum value of the s resonance. This is due to the fact that the p shell is doubly energy degenerate, and hence contributes twice to the total polarization, see eq. (6.3). In our model the height of the resonances is directly connected to the slow long-time decay of the polarization, where we can conclude that the s polarization decays slower than the total p polarization.

Having discussed the spectrum in the absence of the Coulomb interaction, we now consider the spectrum with this fundamental interaction turned on. In comparing the spectra with and without the Coulomb interaction, the most noticeable difference is the large negative shift of the s and p resonances, while other parts of the spectra appear largely unaffected. These shifts are well-known and are usually called exciton resonances [56, p. 188], and arise due to the effectively attractive interaction between an electron and a hole, that form the exciton quasi-particle. The magnitude of the exciton shifts can relatively easy be deduced from a simplified version of the equations of motions and we will briefly show how. We start by considering the Coulomb HF self-energy eq. (5.39), where we need only consider the band off-diagonal components, e.g. the cv component. After using the band selection rule of the Coulomb matrix element, eq. (4.18), we find that the Hartree contribution does not contribute, and that the Fock contribution reduces to

$$\Sigma_{\alpha}^{\mathrm{cv,ee,F}}(t) = -\sum_{\alpha_1} V_{\alpha\alpha_1\alpha_1\alpha}^{\mathrm{cvcv}} \rho_{\alpha_1}^{\mathrm{cv}}(t).$$

Using eq. (5.37a) we arrive at the equation of motion for $\rho_{\alpha}^{\mathrm{cv}}(t)$ including only the Coulomb interaction

$$\partial_t \rho_{\alpha}^{\mathrm{cv}}(t) = -i[\omega_{\alpha}^{\mathrm{cv}} - \hbar^{-1} V_{\alpha\alpha\alpha\alpha}^{\mathrm{cvcv}}]\rho_{\alpha}^{\mathrm{cv}}(t) - \gamma_{\alpha}\rho_{\alpha}^{\mathrm{cv}}(t) + i\hbar^{-1} \sum_{\alpha_1 \neq \alpha} V_{\alpha\alpha_1\alpha_1\alpha}^{\mathrm{cvcv}} \rho_{\alpha_1}^{\mathrm{cv}}(t) - i\hbar^{-1} U_{\alpha}^{\mathrm{cv}}(t), \tag{6.4}$$

where we have also added a small dephasing rate γ_{α} and an external excitation field $U_{\alpha}^{\mathrm{cv}}(t)$. From this equation it is easily seen that for a two-level system, we get an energy renormalization given by the direct exciton Coulomb matrix elements $V_{\alpha\alpha\alpha\alpha}^{\mathrm{cvcv}}$. On an intuitive level it does seems strange that one should obtain a Coulomb energy shift with only a single electron present in the system, as if the electron interacts with itself. We therefore suspect that it arises due to virtual processes, that are automatically taken into account in the Green's function formalism. We have not fully understood the origin of this shift, but we do think that it is an unphysical feature that should not appear. A strong possibility is that arises from the truncation of the self-energy, and therefore solving the problem with the exact self-energy would

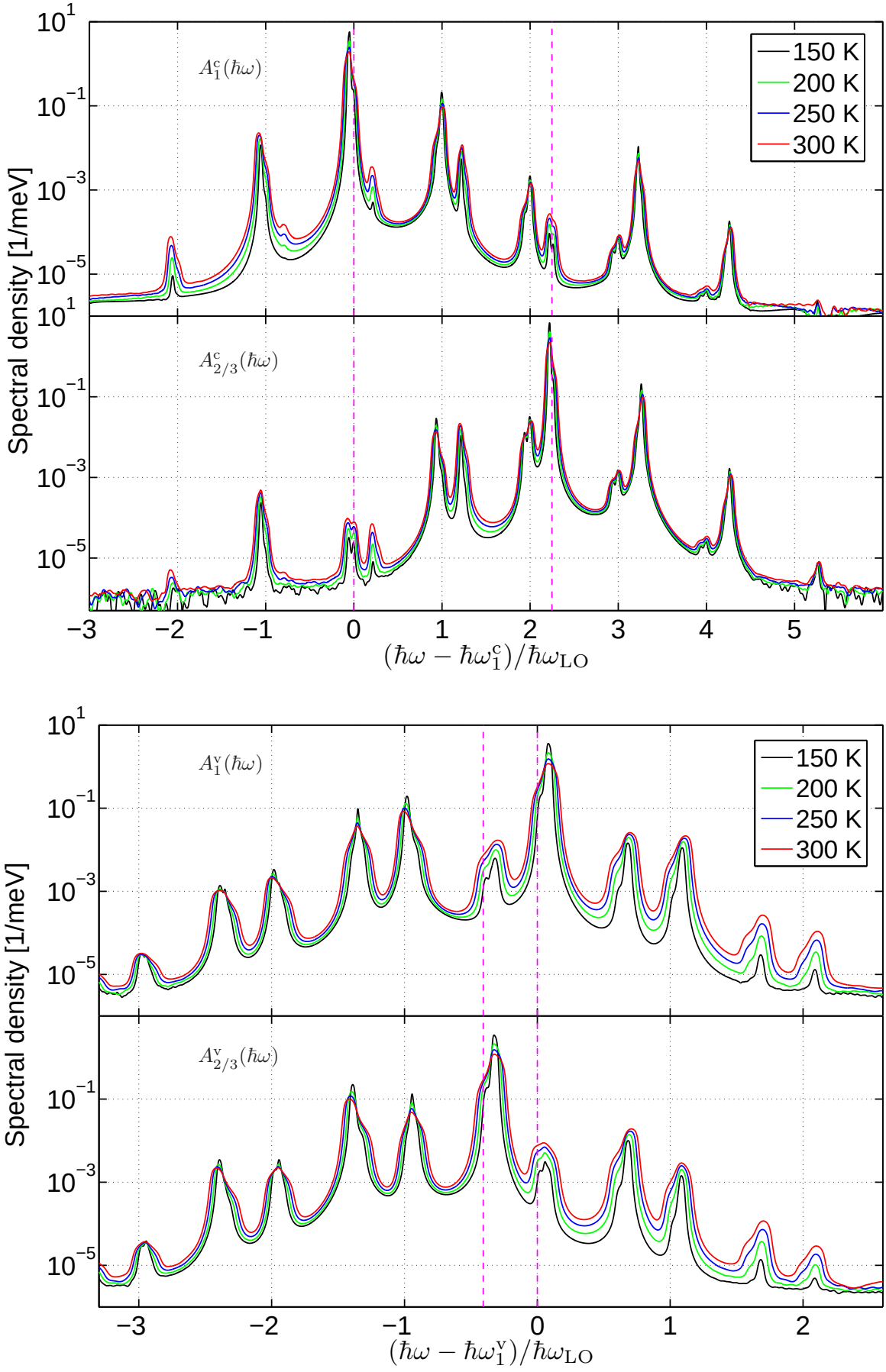

Figure 6.5.: *Plots of the spectral function, eq.* (5.31)*, for the electronic states.*

T [K]	Δ_{polaron} [meV]
300	-1.268
250	-1.200
200	-1.185
150	-1.185

Table 6.3.: *Temperature dependence of energy renormalization of the s transition, the polaron shift, deduced by inspecting the data from figure 6.4.*

somehow completely cancel the observed shift. For more than two levels the polarizations couple through the indirect exciton matrix elements in the third term, these are, however, usually several times smaller in magnitude than the direct ones, see table 6.1. Indeed solving the above equation of motion for our system, which can be done analytically exact, we find that the direct exciton matrix elements account for 98% and 97% of the entire exciton shift for the s and p transitions, respectively. Inspecting the data in figure 6.4 we find an excellent agreement with these simulations, when the polaron energy shift is taken into account.

A peculiar feature of the spectra is that the s resonance apparently split up into two peaks, when we turn on the Coulomb interaction. Splitting of spectral features is normally indicate that we have entered some sort of strong coupling regime for a given interaction, where the coupling strength exceeds the relevant linewidths. As this splitting appears when the Coulomb interaction is turned on, one might be tempted conclude that it is directly due to this interaction. However, due to the structure of eq. (6.4) and our experience with its solution, we do not think that the Coulomb interaction, at the HF level and in the linear regime, can give rise to the usual kind of interaction induced splitting. The only interaction that is included in these simulations besides the Coulomb, is the interaction with the LO-phonons, and hence we speculate that the splitting must somehow originate from this interaction. Indeed if we compare the spectra with and without Coulomb interactions, in the spectral region near the renormalized s resonance, we observe a rather pronounced LO-phonon-assisted transition in the spectra without Coulomb. This particular LO-phonon-assisted transition has a main peak and a small shoulder on the high energy side. We believe that by sheer coincidence (rooted in the specific system parameters of course), the s transition gets shifted and lands on top of this LO-phonon-assisted transition. This causes the LO-phonon-assisted transition to be magnified several orders of magnitude, and by coincidence it is the shoulder that gets magnified the most. The main peak is also magnified to a significant value, even though the exciton shift does not coincide exactly with this resonance, the reason being that the main peak was originally much more significant than the shoulder. The net result is what appears to be a Coulomb induced splitting, which in some sense it is, but fundamentally it is mediated by the LO-phonons.

The last observation we wish to note is that the exciton shift mainly occurs for the original s and p transitions, while all the LO-phonon-assisted transitions are only very weakly affected by the Coulomb interaction.

6.3.2. LO-phonons and photons

In this subsection we will discuss the absorption spectra for the same system as above, but now including the interaction with photons and not the Coulomb interaction. Even though we have derived equations of motion for the photon Green's functions in section 5.4.2, these will not be needed in the linear regime. This is because only electronic densities enter in the source terms of these equations of motion, and these are not affected in the linear regime, hence we will not change the photon Green's functions from their equilibrium values. The only way the photons enter the electronic equations, is through the singular Hartree self-energy, eq. (5.41), where the retarded photon Green's function may be taken in its equilibrium form due to the above arguments.

The properties of the cavity are treated fully on a parameter basis, which is reasonable as we only consider a single quasi-mode in the cavity. The first parameter is the energy of the cavity photon $\hbar\omega_{\text{cav}}$, which we in this section will always tune relatively close to the s transition in the QD. Therefore we write the energy as

$$\hbar\omega_{\text{cav}} = \hbar\omega_1^{\text{cv}} - |\Delta_{\text{polaron}}| + n \times 1 \text{ meV}, \tag{6.5}$$

where we have subtracted the small energy shift due to the electron-phonon interaction from the free energy of the s transition and n is a dimensionless parameters. This is done to be able to control the detuning of the cavity with respect to the LO-phonon dressed electronic system, and in table 6.3 we show the temperature dependence of the polaron shift of the s transition. The second parameter describes the finite lifetime of the photons in the quasi-mode of the cavity. We will usually talk about the linewidth $\hbar\gamma_{\text{cav}}$ of the photon, or its inverse counterpart the lifetime $\tau_{\text{cav}} = \gamma_{\text{cav}}^{-1}$, however, another commonly used measure is the Q-factor defined as $Q = \omega_{\text{cav}}/\gamma_{\text{cav}}$. In the following discussions we will use the quantity that best suits the given situation. The last parameter describes the coupling strength between the photons and electrons and is denoted $\hbar g_\alpha$. However, as discussed in section 4.4 it is reasonable within our model to consider a single strength for all transitions, and we may therefore drop the α subscript and simply refer to a single number $\hbar g$.

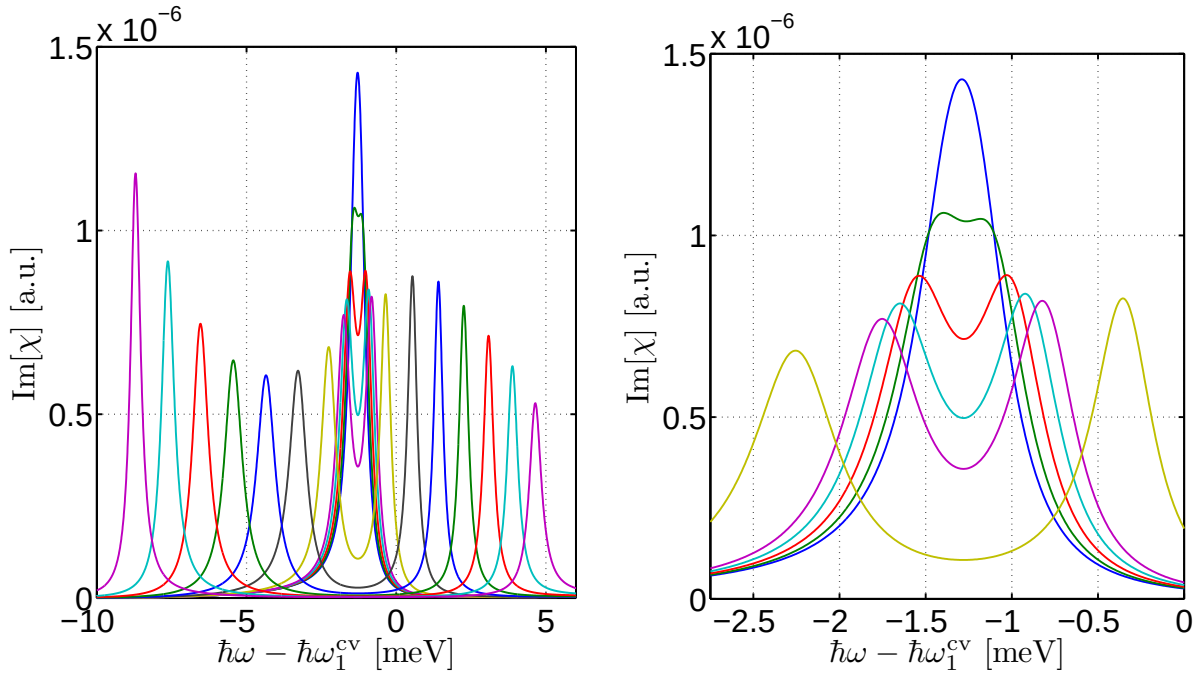

Figure 6.6.: *Figures showing the absorption spectra including the effects of LO-phonons and the cavity photons. These simulations were done for coupling strengths in the range* $\hbar g = [0.1, 0.2, 0.3, 0.4, 0.5, 1, 2, 3, 4, 5, 6, 7]$ meV*, with* $\hbar g = 0.1$ meV *being the blue center peak and* $\hbar g = 7$ meV *being the outer purple double peak. Other parameters in the simulations were:* $\hbar\omega_{\text{cav}} = \hbar\omega_1^{\text{cv}} - |\Delta_{\text{polaron}}|$, $\tau_{\text{cav}} = 2.36$ ps $\Rightarrow \hbar\gamma_{\text{cav}} = 0.28$ meV $\Rightarrow Q = 3000$*, and a temperature of 300 K.*

As in the case of the Coulomb interaction in the previous subsection, one may neglect the influence of the LO-phonons and come up with a much simpler set of equations, that in some cases can be solved analytically exact. These simpler models are sometimes useful in interpreting the results of more complicated numerical models, we will therefore briefly discuss such a model. As mentioned in the beginning of this subsection we need only consider the Hartree self-energy of the electrons due to the photons. Furthermore as the self-energy is purely off-diagonal in the band index, only the following element is

needed

$$\Sigma_\alpha^{\mathrm{cv,rad,H}}(t) = \int_{-\infty}^{t} dt' \sum_{\alpha_1} \hbar g_\alpha \hbar g_{\alpha_1} \rho_{\alpha_1}^{\mathrm{cv}}(t') A^r(t,t'), \tag{6.6}$$

where $A^r(t,t') = -i\hbar^{-1}\theta(t-t')e^{-i\omega_{\mathrm{cav}}(t-t')-\gamma_{\mathrm{cav}}|t-t'|}$ is the retarded photon Green's function[4]. Using eq. (5.37a) we obtain the equation of motion for the inter-band polarization

$$\partial_t \rho_\alpha^{\mathrm{cv}}(t) = -i\omega_\alpha^{\mathrm{cv}} \rho_\alpha^{\mathrm{cv}}(t) - \gamma_\alpha \rho_\alpha^{\mathrm{cv}}(t) - i\hbar^{-1} \int_{-\infty}^{t} dt' \sum_{\alpha_1} \hbar g_\alpha \hbar g_{\alpha_1} \rho_{\alpha_1}^{\mathrm{cv}}(t') A^r(t,t') - i\hbar^{-1} U_\alpha^{\mathrm{cv}}(t), \tag{6.7}$$

where a dephasing rate γ_α and an excitation field $U_\alpha^{\mathrm{cv}}(t)$ have been added. In our QD system the difference in transition energy between the s and p shells is above 90 meV, hence if we tune the cavity energy near the s transition we may neglect the influence of the p transitions, due to very large detuning. In this case of a two-level system we may solve eq. (6.7) analytically using the Laplace transform technique, if we assume a delta pulse excitation at $t = 0$. The solution yields the time-dependent polarization given explicitly by

$$\rho^{\mathrm{cv}}(t) = \frac{\rho^{\mathrm{cv}}(t=0)}{\lambda_+ - \lambda_-} \left([\lambda_+ + i\delta - \gamma_{\mathrm{cav}}]\, e^{\lambda_+ t} - [\lambda_- + i\delta - \gamma_{\mathrm{cav}}]\, e^{\lambda_- t} \right) e^{-i\omega_1^{\mathrm{cv}} t} \tag{6.8}$$

where $\delta = \omega_{\mathrm{cav}} - \omega_1^{\mathrm{cv}}$ is the detuning and $\lambda_\pm = \frac{1}{2}(-i\delta - \gamma - \gamma_{\mathrm{cav}} \pm i[4g^2 + (\delta + i[\gamma - \gamma_{\mathrm{cav}}])^2]^{1/2})$, the value of $\rho^{\mathrm{cv}}(t=0)$ is determined by the specifics of the excitation pulse but is relatively unimportant when considering absorption spectra. We note that only the dephasing rate γ does not enter in the full model and hence this is the only adjustable parameter.

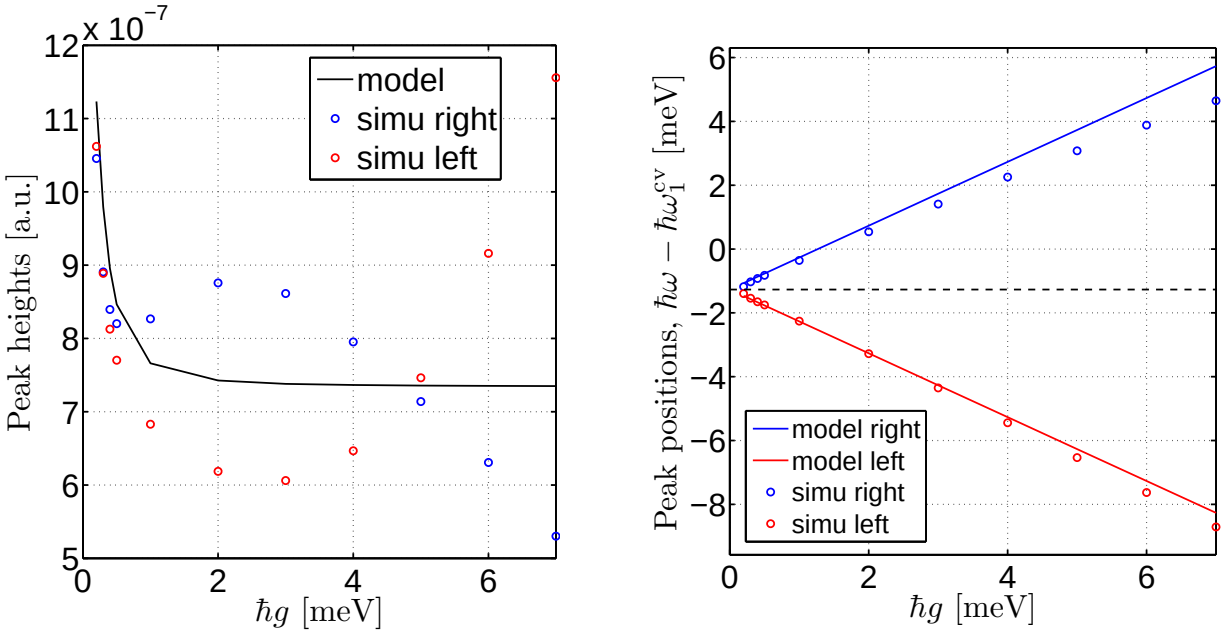

Figure 6.7.: *Two alternative representations of the data shown in figure 6.6, (left) shows the peak heights as a function of ħg for the simulation and two-level model, and (right) shows the positions of the peaks as a function of ħg for the simulation and two-level model, the black dashed line show the polaron shift.*

To start out the discussion we consider a situation where the photon energy is set so that we obtain a situation as close to the usual zero detuning case as possible, that is we put $n = 0$ in eq. (6.5), we choose a

[4] Alternatively one may introduce the difference time defined as $\tau = t - t'$, in terms of which eq. (6.6) transforms to: $\int_0^\infty d\tau \sum_{\alpha_1} \hbar g_\alpha \hbar g_{\alpha_1} \rho_{\alpha_1}^{\mathrm{cv}}(t-\tau) A^r(\tau)$, where τ can be interpreted as an absolute memory time.

Q-factor of 3000, and a temperature of 300 K. The coupling strength is varied from 0.1 meV to 7 meV (the step size is shown in the figure caption) and the resulting spectra are shown in figure 6.6. We only show the spectral region of the spectra near the energy of the cavity, as the other parts are basically unaffected by the presence of the coupling to the photons, which makes sense on an intuitive level. At the lowest value of $\hbar g$ we observe a single peak at the s transition energy, which is slightly broader and lower in maximum value compared to the spectra without photons. The fact that we see a single peak, indicates that we are in the so-called weak coupling regime, see the discussion in chapter 1. For the next few values of the coupling strength, we observe that the single peak gradually splits and becomes a double peak. The separation increases with the coupling strength, being expected behavior seen in simple textbook models as e.g. eq. (6.8). This is the regime of so-called strong coupling, see chapter 1. A behavior that is however not expected from simpler models, is the asymmetry in the peak heights in the double peak structure. We see through the different values of $\hbar g$ that neither the left or right peak remains dominant, but rather the maximum shifts several times. To quantify these observations, we show in figure 6.7 the peak heights and positions as a function of the coupling strength, along with the numbers predicted by eq. (6.8). It should be noted that the dephasing rate entering eq. (6.8), was chosen so that the peak heights were similar in magnitude, which coincidentally gave a dephasing rate very similar to the photon decay rate, reflecting the effective dephasing rate caused by the LO-phonons at this temperature. It is however not the goal of this discussion to extract dephasing rates, but rather to show qualitative differences, so we will not dwell on this point. In figure 6.7 we see that the spectral positions of the peaks in the strong coupling regime, follow rather closely the positions predicted by our simple model, although the right peak seems to drift a bit more than the left peak. In the case of the peak heights we see a much more dramatic departure from the predictions of the simple model. The simple model predicts that the left and right peaks should be of equal magnitude, due to the symmetric lineshape imposed by the constant dephasing rate, and tend toward a constant value for large $\hbar g$. Instead of an equal magnitude we observe that the data points from the simulation, actually cross each other twice in the range of coupling strengths we consider. This deviant behavior is, of course, caused by the interaction with the LO-phonons, and is the result of the complicated dynamics between the photons and the LO-phonon dressed electronic states. In order to more precisely determine the reason for this behavior, one should go back to the spectral functions in figure 6.5, and investigate exactly which of the LO-phonon and/or hybridization peaks, that give rise to spectral features near the s transition in the absorption spectra without photons. However, such an extensive analysis is beyond the scope of this thesis.

Now we will discuss a situation where we vary the detuning parameter n, see eq. (6.5), and fix the coupling strength at $\hbar g = 5$ meV, other parameters are as in figure 6.6. The spectra obtained from these simulations are shown in figure 6.8 for a wide range of detunings. Starting at $n = 0$ we see a clear double peak structure indicating that we are in the strong coupling regime. Furthermore, the left and right peaks are of approximately the same magnitude, which indeed they need not as can be seen in figure 6.6. In this situation we may not assign a specific peak to either the photon or electron. The system is in a strong superposition of the two, and it is not possible to distinguish them. We usually say that a polariton, an electron-photon quasi-particle, has formed. For increasing positive detuning we observe a clear monotonical increase for the left peak and decrease for the right peak, which is expected on the basis of our simple model. Having a situation where difference in peak magnitude is as large as for $n = 20$, corresponds to a departure from the strong coupling regime and into a regime where we may assign a peak to each of the involved particles. Here the left peak is the electron and the right is the photon, which can be seen from the fact that it is the most detuned of the two peaks. For increasing negative detuning we observe the same trend, but the other way around, until a detuning near $n = -12$ is reached, then the right peak is no longer increasing, but actually decreasing. In figure 6.9 the non-monotonical behavior is more clearly presented, and we see that the right peak continues to decrease for detunings larger than those shown in figure 6.8. Furthermore we also note a small increase in the left (photon) peak for the largest negative detuning considered, which might be due to the presence of LO-phonon assisted transition near this place in the spectrum, see figure 6.4. Comparing to what is predicted by our simple model, the disagreement is strongest for negative detunings, which is expected to originate from the spectral asymmetry introduced by the interaction with LO-phonons. In figure 6.9 we also show the peak positions as a function of the detuning, which are seen to rather closely resemble what is predicted

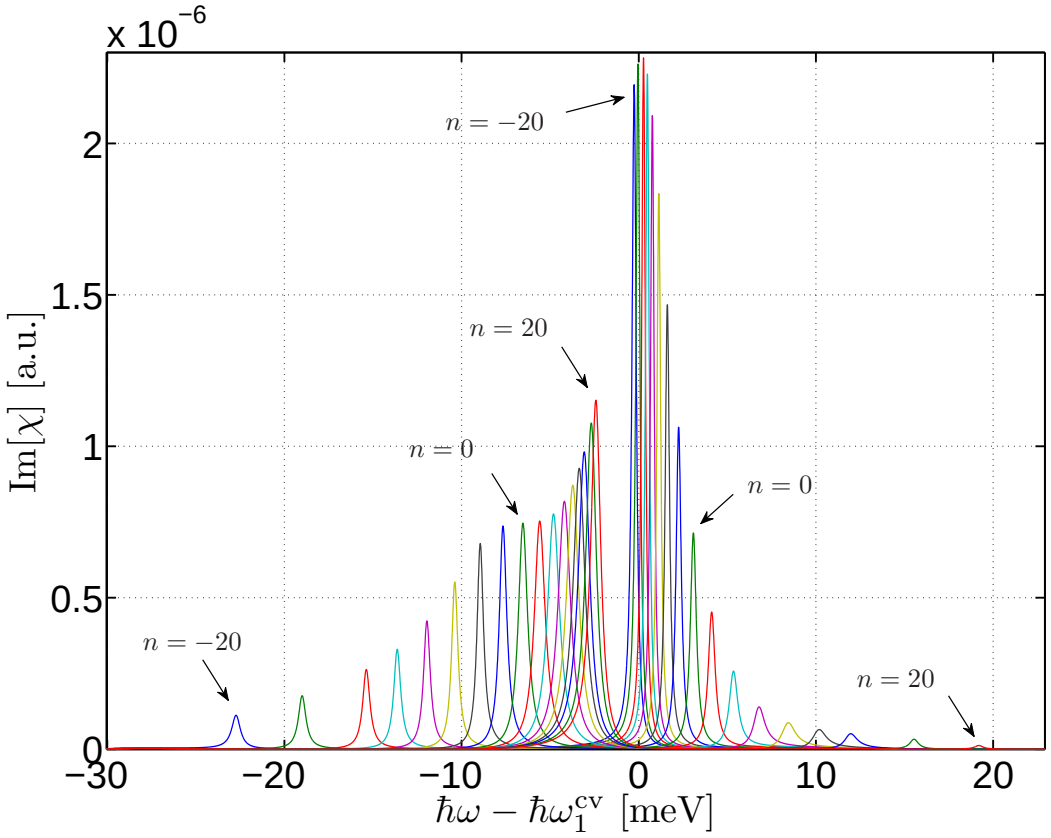

Figure 6.8.: *Figures showing the absorption spectra including the effects of LO-phonons and the cavity photons. These simulations were done for detunings in the range* $n = [-20, -16, -12, -10, -8, -6, -4, -2, 0, 2, 4, 6, 8, 10, 12, 16, 20]$, *see eq.* (6.5). *Other parameters in the simulations were:* $\hbar g = 5$ meV, $\tau_{\text{cav}} = 2.36$ ps $\Rightarrow \hbar\gamma_{\text{cav}} = 0.28$ meV $\Rightarrow Q = 3000$, *and a temperature of 300 K.*

by the two-level model.

Comparing the results of figures 6.7 and 6.9 we can conclude, that the spectral positions of the peaks in the strong coupling regime, are not much affected by having an explicitly many-body interaction causing the dephasing of the optical polarizations. The individual weights in the double peak structures are however very much affected by having dephasing modeled beyond simple constant dephasing rates, which can give an indication of when more detailed modeling of experiments is needed.

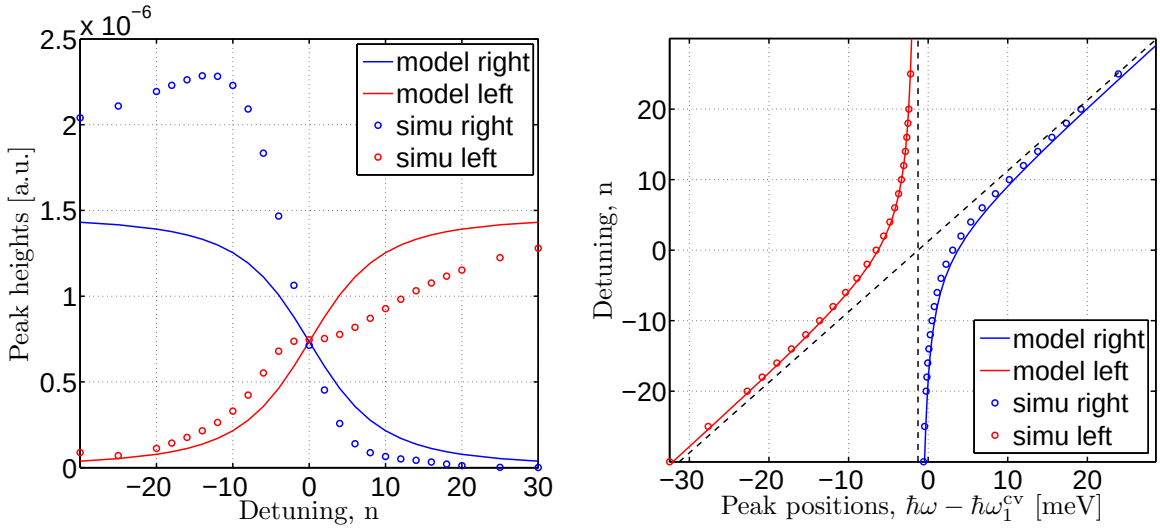

Figure 6.9.: *Two alternative representations of the spectra shown in 6.8, (left) presents peak heights as a function of the detuning parameter n for the simulation and model, (right) presents the peak positions as a function n for the simulation and model, further the black dashed lines are for the free systems.*

6.4. Time domain

In the previous section we discussed the absorption spectra of our QD system, which gave detailed spectral information on the electronic transitions and how these were affected by the various interactions we considered. However, the simulations were performed in the linear regime, where formally no population dynamics take place and we need only consider the equations of motion for the off-diagonal elements of the electronic density matrix. The theory developed throughout this thesis is, however, much more general and can treat a great range[5] non-equilibrium situations where the populations of the different states move away from their equilibrium values. Indeed, if one was solely interested in the linear absorption spectrum this can to a good approximation be deduced from the equilibrium properties of the system [26, p. 161], and a true non-equilibrium formalism need not be applied. As one of the main goals of this thesis is to develop a theory that is capable of describing non-equilibrium processes in semiconductors, this section will be devoted to discussing solutions of our equations of motion in the time domain under various circumstances where true non-equilibrium conditions are present.

6.4.1. LO-phonons

In this subsection we consider the time evolution of the electronic density matrix after excitation by an external pulse including only the interaction with LO-phonons, through the Hartree and Fock self-energies, eqs. (5.40) and (5.44), respectively. For simplicity we neglect the Coulomb interaction between the electrons and the interaction with photons, as including these interactions makes the analysis more difficult. Omitting these interactions of course makes the results less applicable to real physical systems, but it allows us to study the effect of LO-phonons exclusively. In fact in systems where photons occupy bulk sized volumes, it is well known that the radiative recombination times are on the order of nanoseconds, whereas the typical timescale for phonon dynamics is picoseconds. Hence in neglecting the photon interaction we may simply imagine considering such a system, where photons only become important on much longer timescales.

[5] Generally we are limited to the weak excitation regime. Going beyond the weak regime require us to take into account the effects of screening.

Excitation energy: $\hbar\omega_2^{\mathrm{cv}}$

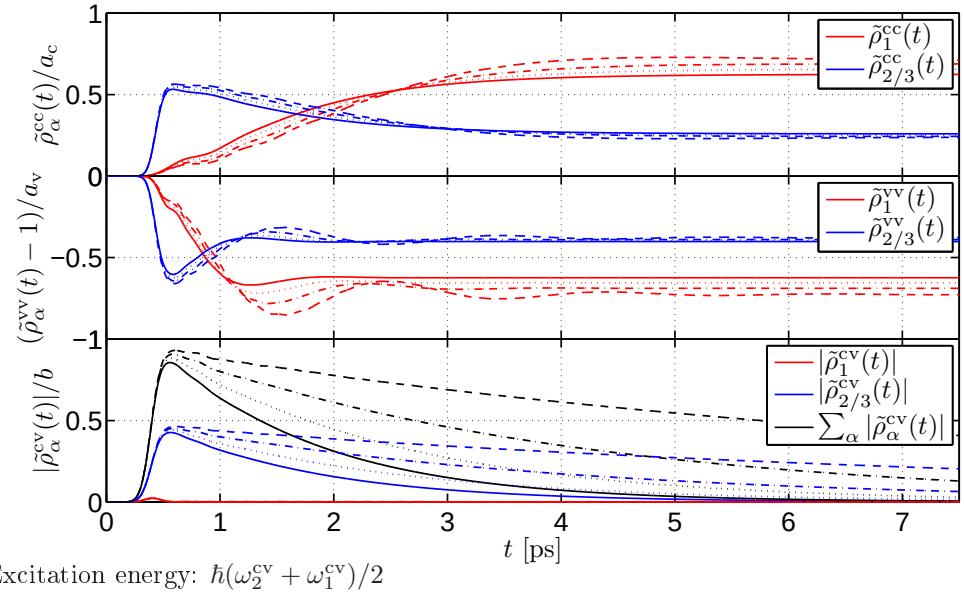

Excitation energy: $\hbar(\omega_2^{\mathrm{cv}}+\omega_1^{\mathrm{cv}})/2$

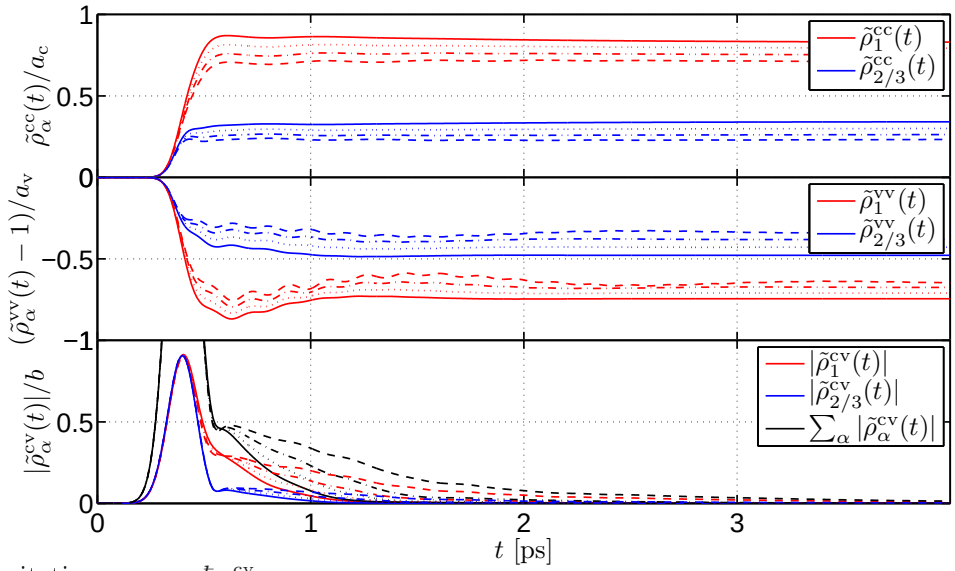

Excitation energy: $\hbar\omega_1^{\mathrm{cv}}$

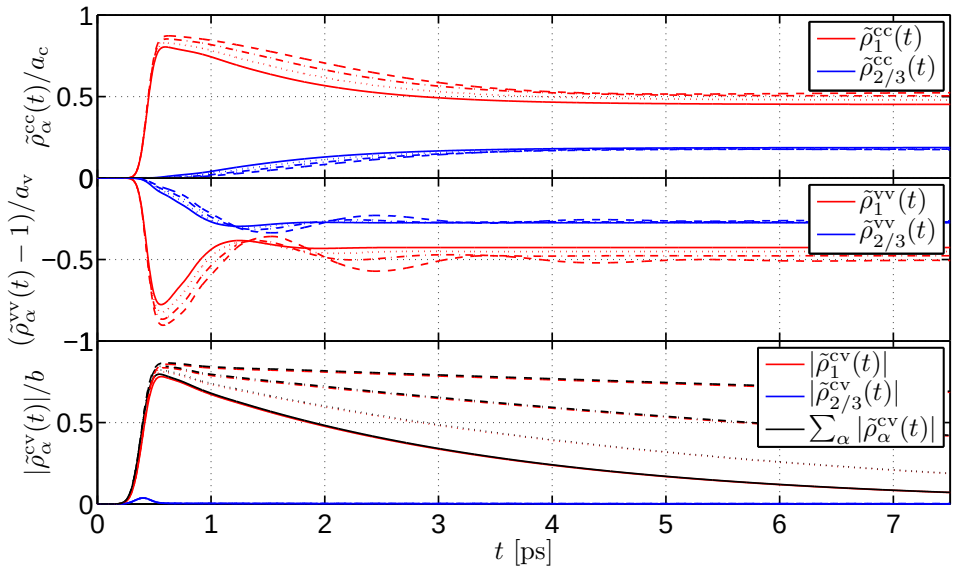

Figure 6.10.: *Figures showing the time evolution of the elements of the electronic density matrix for three different excitation energies and four different temperatures. In all figures the solid line is 300 K, the dotted 250 K, the dashed-dotted 200, and the dashed 150 K. The strength of the excitation pulse is the same for series. The scaling numbers* $\{a_{\mathrm{c}}, a_{\mathrm{v}}, b\}$ *for the plots are: top:* $\{1.5\times10^{-2}, 1.2\times10^{-2}, 1.9\times10^{-1}\}$*, middle:* $\{4.5\times10^{-4}, 4.0\times10^{-4}, 0.92\times10^{-2}\}$*, and bottom:* $\{1.3\times10^{-2}, 1.1\times10^{-2}, 1.2\times10^{-1}\}$.

Excitation energy	T [K]	$\sum_\alpha \tilde{\rho}^{cc}_\alpha(t = 10\text{ ps})$
$\hbar\omega_2^{cv}$	300	1.7127×10^{-2}
	250	1.7382×10^{-2}
	200	1.7610×10^{-2}
	150	1.7797×10^{-2}
$\hbar(\omega_2^{cv} + \omega_1^{cv})/2$	300	6.8058×10^{-4}
	250	6.2670×10^{-4}
	200	5.7419×10^{-4}
	150	5.2793×10^{-4}
$\hbar\omega_1^{cv}$	300	1.0728×10^{-2}
	250	1.0962×10^{-2}
	200	1.1168×10^{-2}
	150	1.1335×10^{-2}

Table 6.4.: *Table showing the total number of electrons excited into the conduction band,* $\sum_\alpha \tilde{\rho}^{cc}_\alpha(t = 10\text{ ps})$*, by the external excitation field.*

The first situation we wish to consider is the establishment of a quasi-thermal equilibrium state within each band, due to thermalization of the electrons through the interaction with the LO-phonons. We consider the same system as in section 6.3, where we excite the system with a 100 fs pulse of fixed amplitude and vary the photon energy of the pulse and temperature. The results of the simulations are shown in figure 6.10. The top figure is for a photon energy of $\hbar\omega_2^{cv}$ corresponding to the free p shell transition energy, the middle one is for an energy of $\hbar(\omega_2^{cv} + \omega_1^{cv})/2$ corresponding to right between the s and p transitions, and finally the bottom figure is for an energy of $\hbar\omega_1^{cv}$ corresponding to the free s transition. Thus we consider two cases of resonant excitation[6] and one case of off-resonant excitation. Each simulation was performed at four different temperatures, 300 K, 250 K, 200 K, and 150 K.

Generally we observe that all populations reach a quasi-equilibrium state within 4-7 ps. This is consistent with results obtained in the paper [41], even though they reach the quasi-equilibrium slightly faster, presumably due to the fact that they include a WL continuum that is expected to speed up the thermalization. The simulations all show the expected result, namely that electron states of lower energy are more populated than those of higher energy, being consistent with the general rule that a subsystem connected to a reservoir always tries to minimize its total energy. A slightly surprising result in the cases of the resonant excitations, is that the polarization decays on a significantly longer timescale than the timescale it takes the populations to reach the quasi-equilibrium. An increase in the lifetime of the polarizations is, however, observed as the temperature in lowered. Going through the populations at large times when the quasi-equilibrium has been established, we see a clear tendency of the electron occupation to shift towards higher/lower energy in the conduction/valence band as the temperature is increased. This is expected as for higher temperature, the probability of an electron to absorb a LO-phonon increases due to the thermal occupation factor of the LO-phonons. This trend is, however, not observed for the non-resonant excitation for reasons that will be explained shortly. As we learned in section 6.3 the absorbtion spectrum changes with temperature, and thus we can not expect the same number of electrons to be excited, for a fixed excitation pulse, as we vary the temperature. Inspecting the total number of electrons generated in the conduction band by the pulse, reveals that it does indeed depend on temperature, see table 6.4. Comparing the numbers for the two resonant excitations, we see that almost twice as many electrons are generated in the case of p shell excitation than in the case of the s shell. This is consistent with the fact the

[6] In the section on absorption spectra we were careful to subtract the small polaron energy shift from the energy of the cavity photon, in order to be able to have full resonance between the s transition and the photon. This is, however, not as important in this section, as we consider a 100 fs pulse corresponding to a FWHM energy width of 18.2 meV and thus the polaron shift of the order 1 meV is not important. The situation was different in the absorption simulations, where the high Q of the cavity made the photon linewidth of the order 0.1 meV, thus making the polaron shift important to account for.

p shell is double energy degenerate and hence in the free system one would expect this ratio to be exactly 2. However due to the effects of the LO-phonons this is not the case. For the case of the non-resonant excitation we see that the numbers depend strongly on temperature, explaining why we do not see the same trend as for the resonant cases. In fact the dependence of $\sum_\alpha \tilde{\rho}^{cc}_\alpha(t = 10 \text{ ps})$ on temperature is so strong that in order to confirm the above intuition regarding LO-phonon absorption, one should tune the excitation field so that an equal amount was excited for the different temperatures, or simply initiate the simulations with electrons already excited[7].

We will now turn to a discussion of the transient regime in figure 6.10, between the pulse has excited the system and the quasi-equilibrium has been reached. In the cases of resonant excitation, we observe an initial rapid change in the populations of the levels the pulse was tuned onto, however already during the short time span the pulse is in the system, scattering between the intra-band levels has already occurred. This shows that the LO-phonons influence the electron dynamics on timescales below the 100 fs mark. In the non-resonant case we are in the regime where one would expect to see the phenomena of adiabatic following, already discussed in section 6.2, due to very off-resonant character of the external pulse. Indeed for a free system, as shown in figure 6.2(b), we see how the populations simply follow the excitation pulse envelope, illustrating the adiabatic following. Whereas in the present simulations, the LO-phonons seem to "catch" the electrons near their quasi-equilibrium values, making the pulse unable to "follow" them back to their true equilibrium values. After the pulse has left the system, the electron populations approach their quasi-equilibrium values of qualitatively different ways, we observe both exponential-like monotonical decay and decay with rather powerful oscillations. The exponential-like monotonical decay occurs mainly in the conduction band and the oscillatory decay occurs mainly in the valence band. We expect this difference between the bands to arise from the difference in intra-band transition energies, as this is one of two quantities determining how efficient the electrons and LO-phonons couple, the other being the matrix element. Indeed from table 6.1 we read off the following intra-band transition energies: $\hbar\omega^{vv}_{12} = 0.4 \times \hbar\omega_{LO} = 15.0$ meV and $\hbar\omega^{cc}_{21} = 2.2 \times \hbar\omega_{LO} = 82.7$ meV. These clearly show that the intra-band transition in the valence band is much more resonant with a LO-phonon energy than the intra-band transition in the conduction band. Thus we expect a much stronger coupling in the valence band than in the conduction band. Indeed it has been pointed out in the literature [41, 61] that these oscillations are analogous to the Rabi oscillations[8] observed in optics in the strong coupling regime. Studying carefully the transient regime in the valence band, we notice a pronounced dependence of the oscillations on temperature, both in oscillation period, amplitude, and decay time. The oscillation period is seen to increase as the temperature is lowered, which is usually connect to a decrease in a coupling strength. In our case we expect that this lowering of the effective electron-phonon interaction, arises from the thermal occupation factors of the LO-phonons. These decrease along with the temperature and enters the LO-phonon Green's functions occurring in the self-energy determining the interaction. The damping of the oscillations is seen to increase along with temperature, which is also consistent with the fact that the effective electron-phonon interaction increases with increasing temperature. In the low temperature simulations for the off-resonant case, we observe a lot of small oscillations modulating the larger oscillation. We suspect that these small oscillations might arise from processes, where the inter-band polarization for both the s and p transitions enters, so-called P^2 terms see [26, p. 281] or [56, p. 229]. The reason for this suspicion is that it is only for the non-resonant case that the polarizations for both inter-band transitions have similar magnitude.

The simulations discussed above were all done in the weak excitation or linear regime where, as noted in section 6.3, only the off-diagonal elements of the electronic density matrix change significantly from their equilibrium value. This is due to the fact that these are first order in the external field, whereas the populations or diagonal elements are second order[9]. In this lowest order regime the qualitative shape of the solutions does not change, only the absolute magnitude does, and this scales linearly for off-diagonal elements and quadratically for the diagonal elements in the external field. Our model is however not limited to lowest order in the excitation field, in fact it contains all order of the excitation field, and we

[7] In the low excitation regime it is actually possible to obtain the quasi-thermal equilibrium populations only through knowledge of the true equilibrium retarded Green's functions, through the use of the fluctuation-dissipation theorem [38].
[8] This is actually not that surprising as photons and phonons are formally identical at our approximation level.
[9] This can be realized by performing a formal expansion in the external field, see [31].

will therefore spend some time discussing how the solutions change qualitatively as we move away from the linear regime. To illustrate the change we have plotted in figure 6.11 the incoherently summed polarization $\sum_\alpha |\tilde{\rho}^{\mathrm{cv}}_\alpha(t)|$ and the population of the s shell in the conduction band, for a range of different strengths of the excitation field. The simulations were performed with a 15 fs pulse and a temperature of 300 K. The reason for choosing such a short pulse, is that it creates solutions that are more oscillatory than a 100 fs pulse, making the point easier to illustrate. All solutions are scaled to facilitate comparison of the qualitative shape, even though their absolute values are quite different.

For the two sets of solutions with relative field strengths of 0.75 and 1 we are clearly in the linear regime, seen through the fact that these solution are of the same scaled shape. For the next two of strengths 2.5 and 5, we still see an overall agreement in the shape of the solutions, compared to the linear regime, however they do start to differ slightly. At relative strengths of 7.5 and 8.75 the departure from the linear regime is even more pronounced, especially for the solutions of the populations, whereas the incoherently summed polarization is not affected that much. For the largest relative strength considered, equal to 10, the qualitative shape of the solution for the population has totally changed, and again we see that the polarization is not as sensitive. Increasing the excitation strength even further, we enter a regime where Rabi oscillations start to occur, due to the interaction between the classical excitation field and the electrons. These are, however, not presented as the focus is on changes in the dynamics due to LO-phonons.

To understand the origin of these qualitative changes in the dynamics, one should look at the scattering terms originating from the electron-phonon interaction, the Hartree contribution 5.40 and the Fock contribution eq. (5.44). The Fock contribution is the more important of the two and therefore we will only treat this in the following. More specifically one should consider the factors in the scattering terms containing the electronic density matrix. Upon examination of eq. (5.44) we find that all these factors appear in the following forms: $[\delta_{b,b_1} - \rho^{bb_1}_{\alpha_1}(t_1)]\rho^{b_1b'}_{\alpha}(t_1)$ and $\rho^{bb_1}_{\alpha_1}(t_1)[\delta_{b_1,b'} - \rho^{b_1b'}_{\alpha}(t_1)]$. b, b', and α are fixed depending on which element of the density matrix is considered, while b_1 and α_1 are integration variables that should be summed over all their possible values. Considering the scattering term of the polarization, $b = \mathrm{c}$ and $b' = \mathrm{v}$, we get the following kinds of contributions

$$\begin{aligned} &\text{lowest order}: \quad \rho^{\mathrm{cv}}_{\alpha}(t_1) \\ &\text{higher order}: \quad \rho^{\mathrm{cc}}_{\alpha_1}(t_1)\rho^{\mathrm{cv}}_{\alpha}(t_1), \quad \rho^{\mathrm{vv}}_{\alpha_1}(t_1)\rho^{\mathrm{cv}}_{\alpha}(t_1) \end{aligned}$$

and for the conduction band population, $b = \mathrm{c}$ and $b' = \mathrm{c}$,

$$\begin{aligned} &\text{lowest order}: \quad \rho^{\mathrm{cv}}_{\alpha}(t_1)\rho^{\mathrm{vc}}_{\alpha_1}(t_1), \quad \rho^{\mathrm{cc}}_{\alpha}(t_1) \\ &\text{higher order}: \quad \rho^{\mathrm{cc}}_{\alpha}(t_1)\rho^{\mathrm{cc}}_{\alpha_1}(t_1) \end{aligned}$$

where we have arranged the different contributions according to their order in the excitation field. We note that the lowest order for the polarization is first and second for the population. In the linear regime the dynamics is governed by the lowest order contributions presented above, whereas the higher order contributions become significant when the strength of the excitation field is increased. Physically what happens in this weak to strong transition is that population dynamics start to become significant.

6.4.2. LO-phonons and photons

In this section we will describe and discuss solutions of our equations including LO-phonons, as in the previous subsection, and now with the electron-photon interaction also. In section 6.3 we have already considered the effect of adding photons to the equations of motion, but as these simulations were done in the linear regime, no electrons were excited and thus no real photons generated. In this section we will allow for excitation of electrons across the bandgap and hence for the generation of real photons. In section 5.4 we derived two versions of equations of motion containing photons, one where photons where treated in the GKBA and one where the full two-time photonic Green's functions were retained. In this

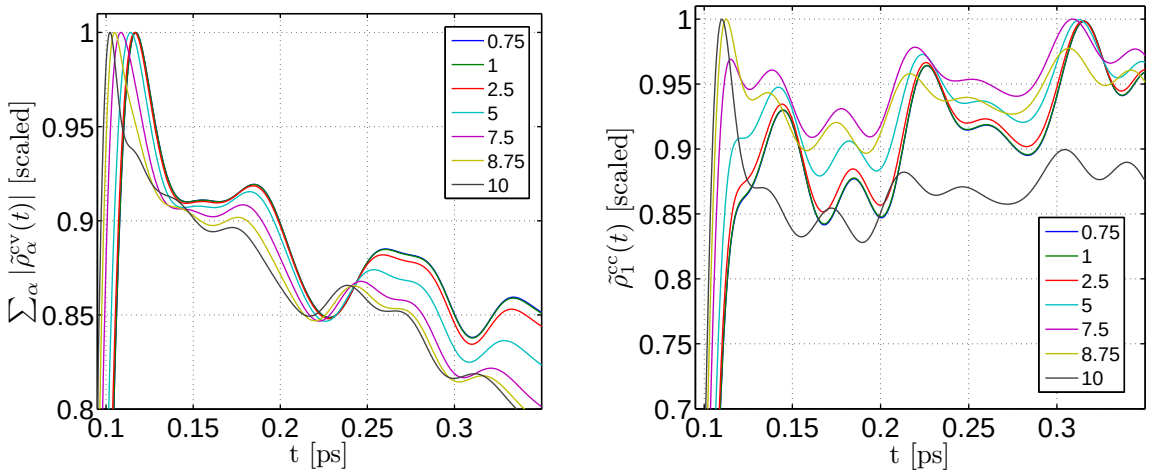

Figure 6.11.: *Figures illustrating the transition from the weak to the strong excitation regime, (left) shows the incoherently summed polarization and (right) shows the occupation of the s shell in the QD. The legends indicate the relative strength of the excitation field and further all solutions have been scaled to facilitate comparison. The simulations were performed with a 15 fs pulse at a temperature of 300 K.*

section we will only consider photon dynamics in the GKBA, the two-time version of the equations will be treated in later sections. To include photons in the electronic equations we add the following terms in the simulations: Eqs. (5.41), (5.46), and (5.47). In the GKBA for the photon, the only dynamical quantity is the photon density in the cavity, $A(t)$, which obeys the equation of motion given in eq. (5.55).

To illustrate the more interesting effects photons has on the dynamics of the system, we present simulations in the short-time regime where coherent effects are still present in the scattering processes taking place. More specifically we will look for Rabi oscillations, i.e. coherent exchange of energy between two subsystems, between the electrons and photons, as these are signatures of the electron-photon system being in the strong coupling regime. The strong coupling regime is where most of the interesting physics takes place and it is therefore of great interest to obtain a better theoretical understanding of this. We consider the same electronic system as in the previous sections, which we excite with a 100 fs pulse and we choose a rather strong pulse. We use a strong excitation pulse in order excite a significant number of electrons, that again is the prerequisite for generating enough real photons to make stimulated processes significant. Going into the strong excitation regime is actually not justified in our model, as in this regime the Coulomb interaction starts to become the dominant dephasing mechanism, which we can not describe in lowest order self-energy approximation. For simplicity we do however not include the Coulomb interaction in these simulations, and hence the simulations are not expected to yield results similar to what would be measured, but hopefully they highlight some general features in electron-photon-phonon dynamics.

In figure 6.12 we show the results of the simulations in the case of p and s shell excitation, and with the cavity tuned to the renormalized s transition, other parameters are given in the figure caption. Comparing the two different excitation conditions we observe a substantial difference in the dynamics, especially within the first 5 ps after excitation. In the case of p shell excitation we observe an initial rapid relaxation of electrons toward the s shells, where they are resonant with the cavity, and photons are generated in the cavity in a smooth way. Even though the s shells are populated very fast by the efficient LO-phonon scattering, we observe no significant signs of Rabi oscillations neither in the populations nor polarizations. We suspect that the reason for the absence of Rabi oscillations, is due to the very rapid dephasing of the s polarization, in which the resulting loss of coherence of the electrons, prevents the coherent energy exchange between electrons and photons. In figure 6.14 we see how the conduction band is gradually emptied of electrons, with the rate of decay increasing with increasing $\hbar g$ as expected. In the case of s shell excitation,

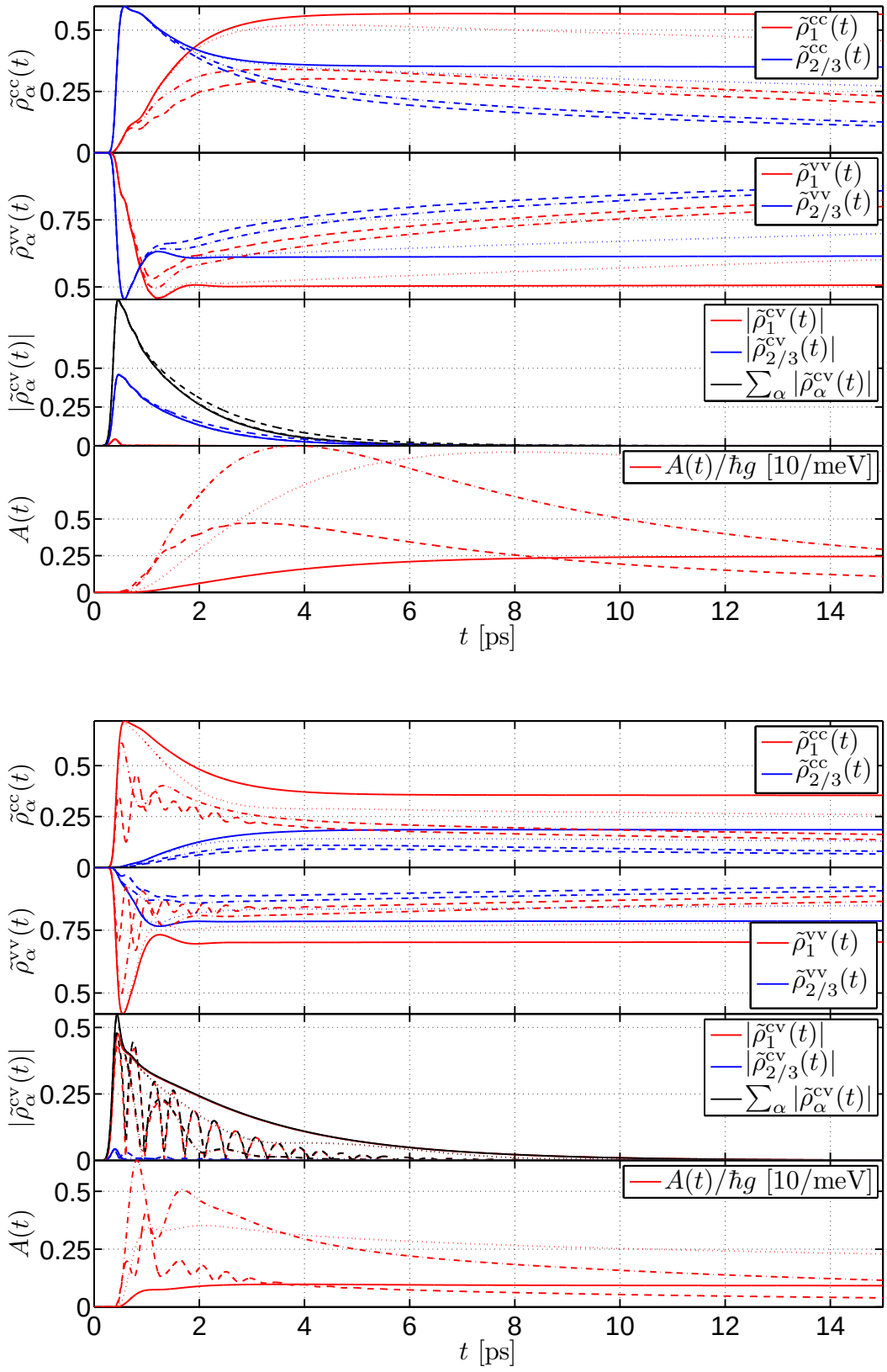

Figure 6.12.: *Figures showing the solution of all electron and photon quantities in our model. The pulse excitation energy is* $\hbar\omega_2^{cv}$ *(top) and* $\hbar\omega_1^{cv}$ *(bottom), and a strong pulse magnitude was used. The cavity is tuned so that* $\hbar\omega_{cav} = \hbar\omega_1^{cv} - |\Delta_{polaron}|$*. The different series are: (solid)* $\hbar g = 0.1$ meV*, (dotted)* $\hbar g = 0.5$ meV*, (dashed-dotted)* $\hbar g = 2$ meV*, and (dashed)* $\hbar g = 5$ meV*, and a Q-factor of 3000 was used. The temperature is 300* K*.*

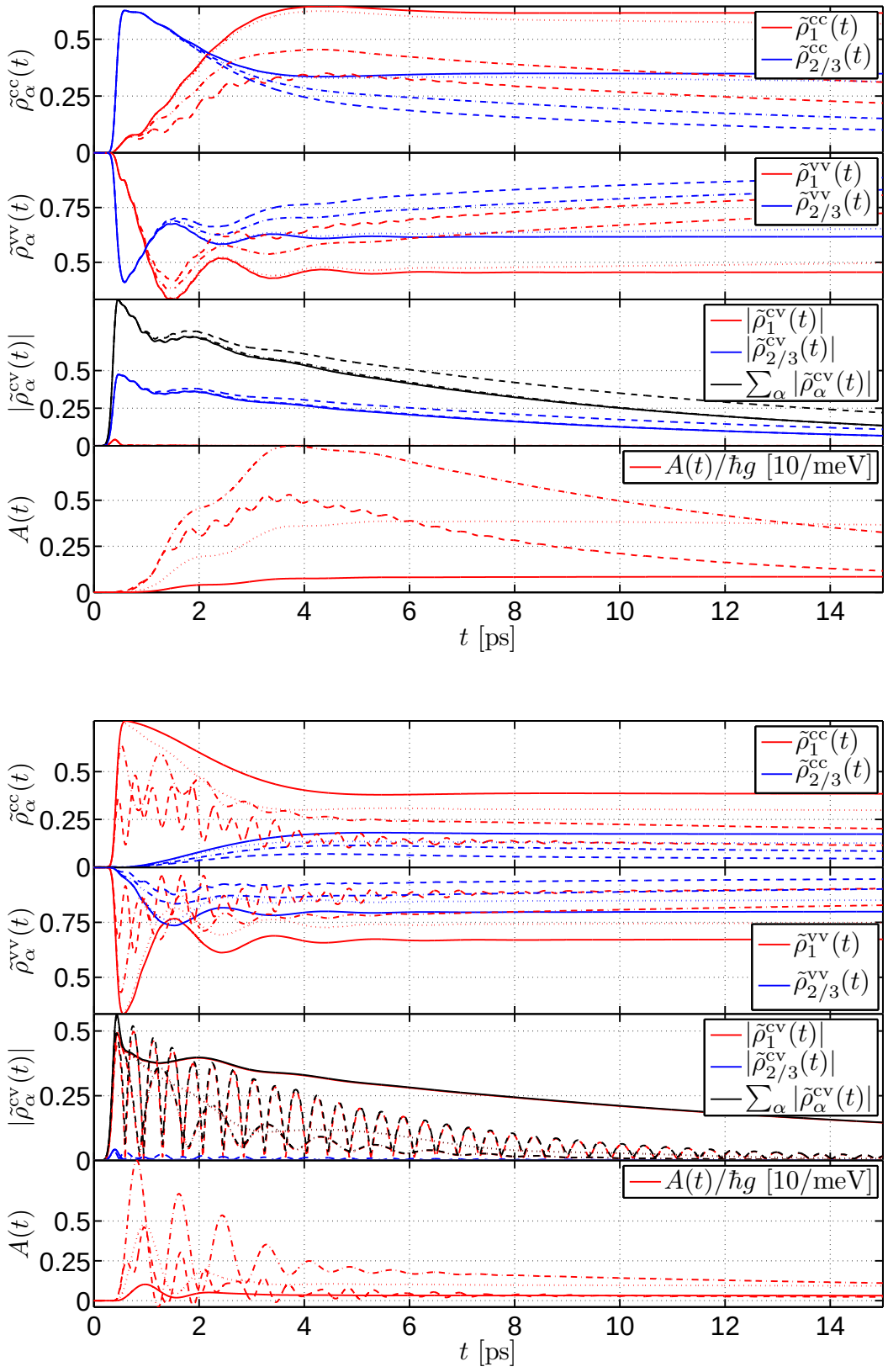

Figure 6.13.: *As in figure 6.12, but with a temperature of 150* K.

powerful Rabi oscillations are observed for the two highest values of the electron-photon coupling strengths considered. The fact that the slowly-varying s polarization is modulated with an oscillation depending on $\hbar g$ can understood in terms of eq. (6.8), where we see that in the strong coupling regime, oscillations are indeed expected in the time domain. As in the previous case the conduction band electrons decay into the valence band, however, at much lower rate, see figure 6.14 (top).

The origin of the lower decay rate for the s excitation, is expected to be found in the part of the scattering term describing spontaneous processes, the part with the blocking factor structure $\rho^{cc}_{\alpha_1}(t_1)\left[1-\rho^{vv}_{\alpha_1}(t_1)\right]$. These terms give relatively high values when the occupation in the conduction band is high and low in the valence band, i.e. right after the excitation pulse has excited the system. Whereas when the occupation in the conduction band decreases and the valence band increases, these terms give relatively low values. To support this argument a simulation was made where the conduction band occupation after p shell excitation, reached a level comparable to that of the s shell excitation. Figure 6.14 (bottom) shows that the rate of decay for the p shell excitation, drops dramatically once fewer electrons are present in the conduction band. This effect is most clearly illustrated when dealing with a two-level one electron system, where the relation $\rho^{cc}(t_1)+\rho^{vv}(t_1)=1$ holds yielding a blocking term of the form $(\rho^{cc}(t_1))^2$. This should be contrasted to the usual exponential decay known for a two-level system, arising from "blocking" terms of the form $\rho^{cc}(t_1)$, where no extra slow down is experienced when the occupation is low. This discrepancy between the two methods in the case of a two-level system is not fully understood yet, but we are certain that it is the Green's function approach which yields the incorrect result[10], manifested in a sort of artificial Pauli blocking. The blocking factor structure described above is also obtained in the cluster expansion scheme, however in this formalism the artificial blocking issue may be resolved as described in [68]. In the case of a system containing more than one electron, it is however clear that the various scattering terms must contain blocking terms of the form encountered in our theory, supported by the literature [68, 77].

The important difference between the two excitation cases is that in the present, coherent electrons are excited directly to states interacting through the cavity mode, whereas in the previous case the initially coherent electrons had to undergo scattering processes in order to arrive at the cavity resonant states. During these scattering processes they lost enough of their coherence, so that Rabi oscillations were not observable. This indicates that if we could maintain the coherence of the p shell excited electrons for a longer time, Rabi oscillations for this excitation case could become observable. Our handle for providing longer coherence time, is to lower the temperature and hence the amount of LO-phonons available to participate in scattering. In figure 6.13 we show simulations identical to those in figure 6.12, but with a temperature of 150 K, and indeed Rabi oscillations start to become visible for the p shell excitation. Oscillations due to LO-phonons also become more pronounced, especially for the valence band population, however, they have a larger period than those induced by the photons and can therefore be distinguished, compare with figure 6.10. For the s shell excitation the already existing Rabi oscillations have become greater in amplitude, in particular in photon density where we observe negative populations. This indicates the either the GKBA or lowest order self-energy approximation has broken down, and that lower $\hbar g$ values should be used to obtain sensible results.

Comparison with numerically exact solution

To be able to formulate and solve the equations of motion for the Green's functions as done above, we have applied two major approximations, namely the truncation of the various (self-consistent) self-energies and the employment of the GKBA. The exact validity and range of either of these approximations are not fully understood yet in a formal rigorous sense, and thus it is always interesting to compare with other solution methods. In this section we will perform such a comparison, with a simplified version of the cQED system considered above that can be solved numerically exact.

The first simplification we employ is to neglect the interaction with the LO-phonons, which is done to be able to span the Hilbert space with a finite set of basis vectors. This removes the basic dissipation

[10] Or our inability to apply it correctly.

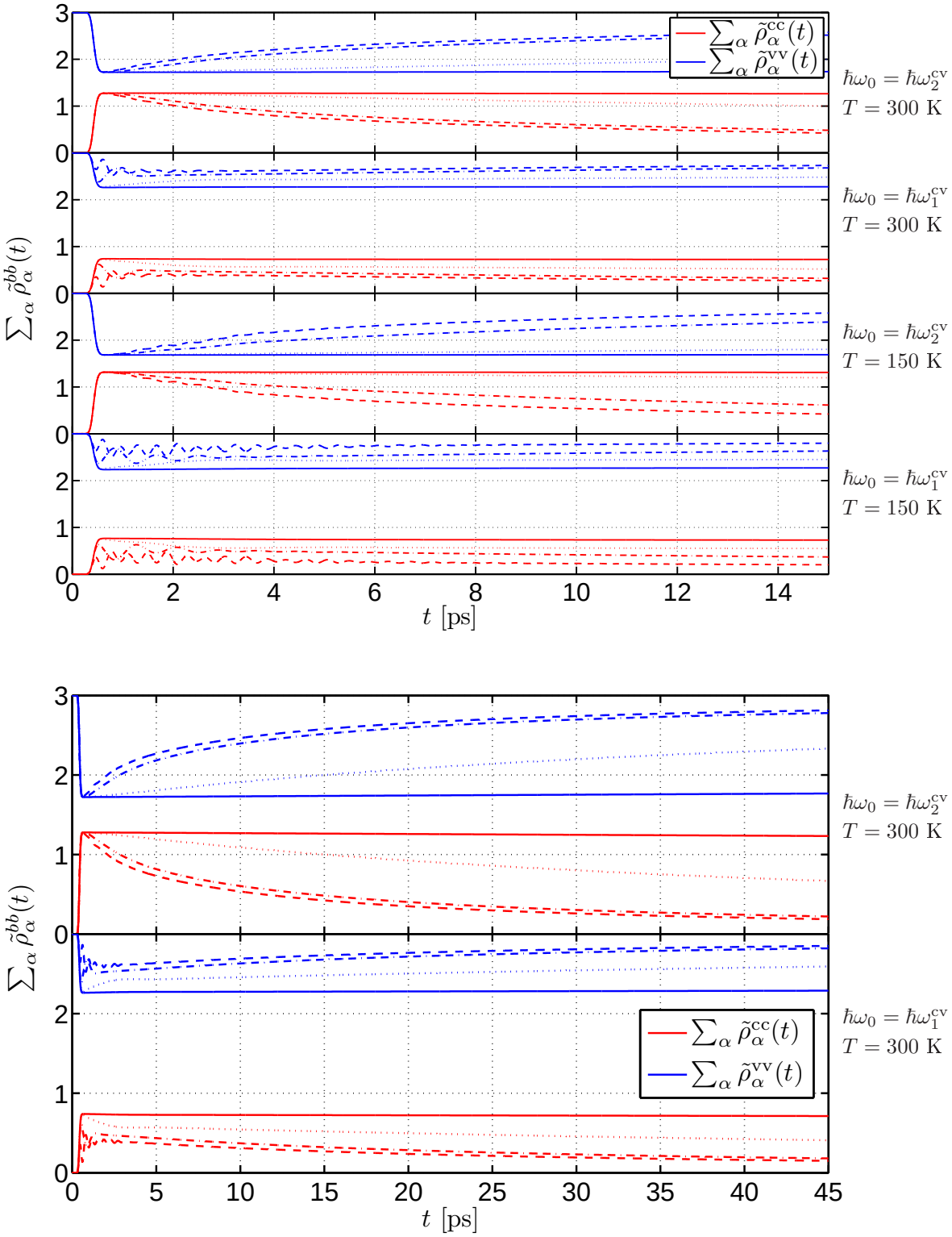

Figure 6.14.: *The total population in each of the bands, $\sum_\alpha \tilde{\rho}^{bb}_\alpha(t)$, for all the simulations presented in figures 6.12 and 6.13. The lower figure is the same as 6.12, but for a longer simulation time.*

mechanism and thus no dephasing or relaxation will occur, unless it is added phenomenologically. Next we limit ourselves to only considering the s shells of our QD, hence we only treat two electronic states. This system is described by the following Hamiltonian

$$H = \hbar\omega^{\mathrm{c}} c_{\mathrm{c}}^\dagger c_{\mathrm{c}} + \hbar\omega^{\mathrm{v}} c_{\mathrm{v}}^\dagger c_{\mathrm{v}} + \hbar\omega_{\mathrm{cav}} a^\dagger a + \hbar g(c_{\mathrm{c}}^\dagger c_{\mathrm{v}} a + a^\dagger c_{\mathrm{v}}^\dagger c_{\mathrm{c}}) + \hbar\frac{dE_0(t)}{2}(c_{\mathrm{c}}^\dagger c_{\mathrm{v}} e^{-i\omega_0 t} + c_{\mathrm{v}}^\dagger c_{\mathrm{c}} e^{+i\omega_0 t}),$$

in the case where no loss processes are present. To include losses one may use a master equation approach as the Lindblad form, see [78]. Here the equation of motion for the reduced density operator of the system described by the lossless Hamiltonian above reads

$$\partial_t \rho(t) = \frac{1}{i\hbar}[H, \rho(t)] - \frac{1}{2}\sum_k \left(L_k^\dagger L_k \rho(t) + \rho(t) L_k^\dagger L_k - 2L_k \rho(t) L_k^\dagger \right). \tag{6.9}$$

In this formula $L_{a,b} = \sqrt{\gamma_{a,b}}\,|a\rangle\langle b|$ are Lindblad operators, describing a loss process occurring at a rate $\gamma_{a,b}$ in the transition from state b to a. In this formalism pure dephasing can easily be added by including Lindblad operators of the form $L_{a,a} = \sqrt{\gamma_{a,a}}\,|a\rangle\langle a|$, that can be thought of as a virtual transition, not changing the occupation of level a. Now in order to perform a comparison between the Green's function approach and a solution obtained through that Lindblad master equation, we can not include losses that can not be unambiguously included in both formalisms. This rules out adding pure dephasing, as it is not clear how it should be included in the Green's function approach. One might naively think that a simple term like $-\gamma_{\mathrm{deph}}\rho^{\mathrm{cv}}(t)$ could be added to the equation of motion for the polarization. However, as we have learned in the previous sections, decay mechanisms also affect the retarded Green's functions entering the GKBA, and it is not clear how these functions should be modified to include pure dephasing. The situation is quite different for the case of the cavity loss rate, γ_{cav}, which can easily be included in both the Lindblad formalism and Green's function approach.

To proceed with the solution eq. (6.9), we need to span a Hilbert space capable of describing the physical situation we wish to consider. The situation is the usual, in which the electron is initially in the ground state and at some point it is excited by the external field, and the system is left to evolve according to the rest of the Hamiltonian. Due to the application of the RWA for the light-matter interaction, and the assumption that we only excite that system once with a ultra-fast pulse, we may limit the Hilbert space to only contain basis states with at maximum a single photon added. Choosing the set $\left\{|1\rangle = c_{\mathrm{v}}^\dagger|0\rangle, |2\rangle = a^\dagger c_{\mathrm{v}}^\dagger|0\rangle, |3\rangle = c_{\mathrm{c}}^\dagger|0\rangle\right\}$ we may expand the operator equation eq. (6.9) and by including the Lindblad operator $L_{\gamma_{\mathrm{cav}}} = \sqrt{\gamma_{\mathrm{cav}}} c_{\mathrm{v}}^\dagger c_{\mathrm{v}} a$, loss is introduces for the cavity photons. We obtain the following equations for the reduced density matrix

$$\begin{aligned}
\partial_t \rho_{11}(t) &= \gamma_{\mathrm{cav}}\rho_{22} + \frac{i}{2}dE_0(t)[\tilde{\rho}_{13}(t)e^{-i\delta_0 t} - \text{c.c.}],\\
\partial_t \rho_{22}(t) &= -\gamma_{\mathrm{cav}}\rho_{22} + ig[\rho_{23}(t) - \text{c.c.}],\\
\partial_t \rho_{33}(t) &= -ig[\rho_{23}(t) - \text{c.c.}] - \frac{i}{2}dE_0(t)[\tilde{\rho}_{13}(t)e^{-i\delta_0 t} - \text{c.c.}],\\
\partial_t \tilde{\rho}_{12}(t) &= -\frac{\gamma_{\mathrm{cav}}}{2}\tilde{\rho}_{12}(t) + ig\tilde{\rho}_{13}(t)e^{-i\delta t} - \frac{i}{2}dE_0(t)\rho_{23}^*(t)e^{-i\delta' t},\\
\partial_t \tilde{\rho}_{13}(t) &= ig\tilde{\rho}_{12}(t)e^{i\delta t} + \frac{i}{2}dE_0(t)e^{i\delta_0 t}[\rho_{11}(t) - \rho_{33}(t)],\\
\partial_t \rho_{23}(t) &= -\frac{\gamma_{\mathrm{cav}}}{2}\rho_{23}(t) - i\delta\rho_{23}(t) + ig[\rho_{22}(t) - \rho_{33}(t)] + \frac{i}{2}dE_0(t)\tilde{\rho}_{12}^*(t)e^{-i\delta' t},
\end{aligned}$$

where we have defined the following detunings $\delta = \omega - \omega^{\mathrm{cv}}$, $\delta_0 = \omega_0 - \omega^{\mathrm{cv}}$, and $\delta' = \omega - \omega_0$, and the slowly-varying functions $\rho_{13}(t) = e^{i\omega^{\mathrm{cv}}t}\tilde{\rho}_{13}(t)$ and $\rho_{12}(t) = e^{i\omega t}\tilde{\rho}_{12}(t)$. In the case of the Green's functions we use the equations described in the beginning of this subsection. In the GKBA for the electrons we employ free retarded Green's functions, which is actually exact in this case where only the photon interaction is considered. This we know from section 5.3.3, where it was established that there are no correlations between the electrons and photons in equilibrium, and thus no initial correlations need to be included through the retarded Green's functions.

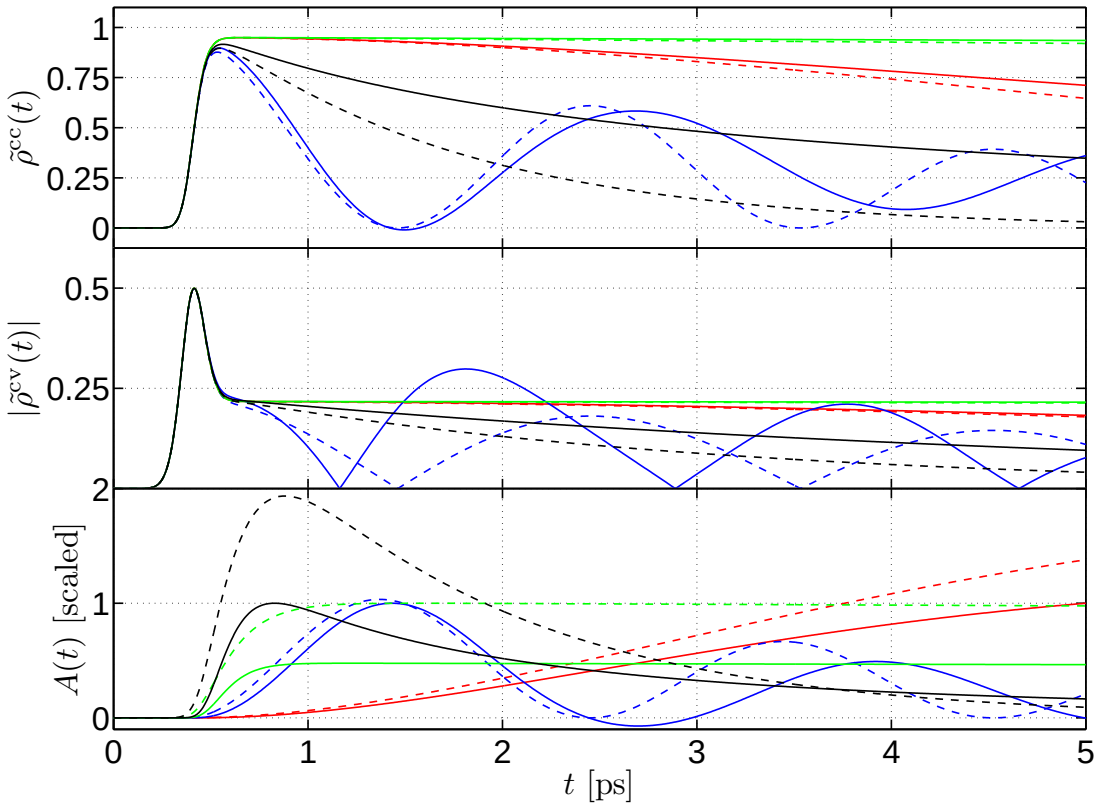

Figure 6.15.: *Figures comparing the solution of the Jaynes-Cummings model using an exact method (dashed) and our Green's function method (solid). The excitation was done with a 100 fs pulse with a large magnitude and the colors are for: (red)* $Q = 3000$ *and* $\hbar g = 0.1$ meV*, (blue)* $Q = 3000$ *and* $\hbar g = 1$ meV*, (green)* $Q = 100$ *and* $\hbar g = 0.1$ meV*, and (black)* $Q = 100$ *and* $\hbar g = 1$ meV*. The detuning between the photon energy and electronic transition is in all cases zero.*

In figure 6.15 we show the results simulations using the two different methods. We consider four representative parameters sets combining a large/small coupling strength $\hbar g$ and high/low damping through the Q-factor. The exact numbers are given in the figure caption. We show the population of the conduction band state, the valence band population can be obtained through particle conservation, the polarization, and the photon density. The agreement appears to be best for the red series describing both a low coupling strength and damping. The agreement is worst for the case of high coupling strength and low damping, which could intuitively have been expected, as formally we consider an expansion in $\hbar g$. For certain times we even have negative populations for both the electrons and photons, see section 6.2 for more on this feature of the theory. The overall conclusion of this brief comparison is that we can only expect qualitative agreement in the case of the electron-photon interaction, however, quantitative agreement can not be expected on the basis of this investigation. For the full system where the LO-phonons are also included, we do not expect the disagreement with the exact result to be as large is in this particular situation. This is due to the fact that dissipative processes, introduced by the LO-phonons, tend to make higher order correlations decay faster. This hopefully lowers the need to go to higher order in the self-energy in order to avoid unphysical populations. Also the present system is a two level one electron system, where the effects of the artificial Pauli blocking discussed in section 6.4.2 are expected to be most severe.

6.5. Emission spectra

In this section we will describe and discuss our attempts to model the emission spectrum of the cavity photons in our semiconductor cQED system. This is an interesting quantity as it is often measured in experiments, see e.g. [16, 79].

We begin with an expression for the emission spectrum [44, p. 299] for an idealized two-level detector. Assuming an infinite detection time, the expression reads

$$S(\boldsymbol{R},\omega_S) \propto \int_{-\infty}^{+\infty} dt' \int_{-\infty}^{+\infty} dt e^{-i\omega_S(t'-t)} \left\langle E^{(-)}(\boldsymbol{R},t')E^{(+)}(\boldsymbol{R},t)\right\rangle ,$$

where $\boldsymbol{R}$ is the position of the detector, ω_S is the detection frequency, and $E^{(\pm)}(\boldsymbol{R},t)$ are the electric field operators, assumed to be scalars. Note that we have neglected an unimportant prefactor and therefore we only write "proportional to" at the moment. In principle the electric field operators contain a sum over all modes, including those in the far field where the emitted photons are actually measured, these modes can be important to obtain agreement with experiment. It is, however, beyond the scope of this thesis to describe all these modes and we limit ourselves to only considering the local cavity mode, as also done in appendix A.1, which greatly reduces the complexity of calculating the spectra. This corresponds to the rather unrealistic experiment where the detector is placed inside the cavity, or to the case where the photon propagates without changing its properties from the cavity to the detector in the far field. In any case it does not make much sense, to assign any significance to the mode function of the cavity that enter the expression for the field operator, and we will simply neglect this overall prefactor and therefore also the dependence on the detector position $\boldsymbol{R}$. The emission spectrum is now expressed only in terms of the creation and annihilation operators of the cavity, and this expression will be used in the rest of the thesis

$$\begin{aligned} S(\omega_S) &= \int_{-\infty}^{+\infty} dt' \int_{-\infty}^{+\infty} dt e^{-i\omega_S(t'-t)} \left\langle a^\dagger(t')a(t)\right\rangle \\ &= \int_{-\infty}^{+\infty} dt' \int_{-\infty}^{+\infty} dt e^{-i(\omega_S-\omega_{\text{cav}})(t'-t)} \tilde{A}^<(t,t'), \end{aligned} \tag{6.10}$$

where in the second line we have expressed the photon bracket in terms of the slowly-varying lesser Green's function defined in eq. (5.48). The two time integrals in eq. (6.10) cover the entire two-time plane and thus the two-time photon Green's function is needed at all these points. However, due to the symmetry relation eq. (5.49), that relates the values of the lesser Green's function above and below the time diagonal, it is possible to reduce the double time integral to run over either the half plane above or below the time diagonal. Choosing below the time diagonal we may derive the following expression

$$S(\omega_S) = 2\text{Re}\left\{ \int_0^{+\infty} d\tau e^{i(\omega_S-\omega_{\text{cav}})\tau} \int_{-\infty}^{+\infty} dt \tilde{A}^<(t,t-\tau)\right\}, \tag{6.11}$$

using eq. (5.49).

As a first approximation one may attempt to use the GKBA version of the two-time photonic Green's function as given by eq. (5.53), where the retarded Green's function is taken in its equilibrium form. In the GKBA the slowly-varying lesser Green's function has the form

$$\tilde{A}^<(t,t-\tau) = \exp(-\gamma_{\text{cav}}\tau)A(t-\tau), \tag{6.12}$$

where $A(t-\tau)$ is simply the photon density and we have assumed $\tau > 0$. Inserting this form into eq. (6.11) we get

$$S(\omega_S) = 2\text{Re}\left\{ \int_0^{+\infty} d\tau e^{i(\omega_S-\omega_{\text{cav}})\tau-\gamma_{\text{cav}}\tau} \int_{-\infty}^{+\infty} dt A(t-\tau)\right\}.$$

The integral over t deals only with the photon density, and due to the functional dependence of A on τ we may change the integration variable $t \to t - \tau$ so that we get the integral $\int_{-\infty}^{+\infty} dt A(t)$, which is clearly independent of τ and we will simply denote it by the real constant $\mathcal{A}$. Performing the integral over the remaining exponential and taking the real part yields

$$S(\omega_S) = 2\mathcal{A}\frac{\gamma_{\text{cav}}}{(\omega_S - \omega_{\text{cav}})^2 + \gamma_{\text{cav}}^2}, \tag{6.13}$$

revealing a Lorentzian lineshape centered around the cavity frequency. We note that the only requirement for performing this calculation, is that the retarded Green's function used in the GKBA only depends on the time difference. This result tells us that one can only obtain a Lorentzian emission spectrum, if the GKBA is used as an approximation for the two-time photon Green's function. All information on how the electrons were initially excited, and exactly how the photons were emitted is all contained in the constant $\mathcal{A}$. This simple constant only scales the magnitude of the Lorentzian lineshape, and hence application of the GKBA will be of very little use in interpreting experimental emission spectra. The fact that the GKBA fails spectacularly for this type of calculation, is perhaps a bit surprising since it is an approximation, that is very often used in the literature. It has, however, mainly been applied in situations where the object of primary interest was the equal-time lesser Green's function of the electrons. In these situations knowledge of the Green's function outside the time-diagonal is as such redundant. The situation here is very different, in that the quantity we wish to determine depends strongly on the values of the Green's function outside the time diagonal. Considering that all propagation outside the time diagonal in the GKBA is handled by the retarded Green's function, it might not be that surprising after all that the properties of the retarded Green's function, will be very significant in quantities depending strongly on the off-diagonal values of the two-time lesser Green's function. On the basis of this discussion, we must conclude that in order to calculate emission spectra of light emitted under strong non-equilibrium conditions, the full two-time machinery must be set in motion, at least for the photonic Green's functions.

6.5.1. Present stage results

As discussed above we have to work with the two-time versions of the equations of motion for the photonic Green's functions, as oppose to the one-time GKBA version, in order to obtain meaningful emission spectra. This is a significantly more complicated task, both formally, as seen by comparing eqs. (5.55) and (5.56), and especially numerically. In the GKBA one should only perform a single memory integral for each discretized t value, while in the two-time formalism a memory integral must be performed for each discretized t and τ value. Furthermore, this should be done for both the greater and lesser photonic Green's function, as these are both independent functions in the two-time formalism. Depending on the required memory depth of the memory integrals, the computationally demands are increased many times, and as a consequence of this the implementation and verification process becomes more difficult and more time consuming. This stage of the project was not initialized until the very end of the assigned time period, and therefore enough time was not available to obtain a completely satisfactory result. We will, however, describe the present stage of our progress and discuss what further steps need to be taken.

To start off the discussion we in figure 6.16 show our solutions for the two-time photonic Green's functions. To reduce the computationally demands we only consider the two s shells of our QD, and excite the system on resonance with a strong 100 fs pulse, other parameters are given in the figure caption. The solution for the lesser Green's function shows a behavior that is somewhat expected, in that we observe an initial increase in magnitude, due to the electron and hole recombining by photon emission, and afterwards a decay in both the t and τ is seen. For the greater Green's function the behavior is much different and we observe a strong increase in the τ direction, where we would expect a decay on physical grounds. The apparent plateaus in the figure are artificial and represent areas where the magnitude is larger than the color scale. Indeed, we are quite certain that this behavior is not physical, and arises from numerical instabilities that eventually would lead to a blow up of the solution. This kind of behavior is usually a sign that one should lower the discretization size until a converged result is reached. Due to very long integration

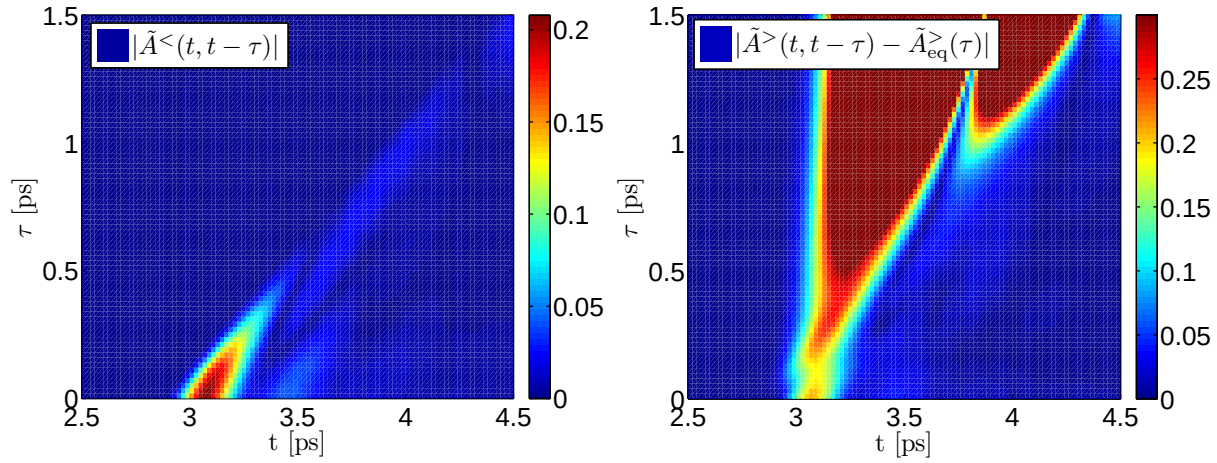

Figure 6.16.: *Solutions of the two-time photonic Green's functions for the following parameters:* $\hbar\omega_{\mathrm{cav}} = \hbar\omega_1^{\mathrm{cv}}$, $Q = 100 \Rightarrow \hbar\gamma_{\mathrm{cav}} = 8.38$ meV, $\hbar g = 8$ meV, *and* $T = 300$ K. *Note that the pixellation does not represent the time discretization used in the simulations, where* $\Delta t = \Delta\tau = 1$ fs *was used.*

times, such a systematic study was not performed for the present set of parameters. We did, however, take another route and increased the physical damping in the system, through lowering the Q-factor from 100 to 30. This was done expecting that it would help to prevent the numerical instabilities from occurring. In figure 6.17 we show our solution for the Q-factor of 30. The excitation was performed with a 50 fs pulse, instead of 100 fs, other parameters are as in figure 6.16. The figure shows that the numerical instabilities are indeed damped significantly, even though one still observes some bands in the τ direction near $t = 2.2$ ps and $t = 2.6$ ps for the greater Green's function that do not appear physical. The magnitude of the bands does, however, decrease for increasing τ, and hence we do not expect that this solution would blow up if one calculated it for larger τ values than considered here.

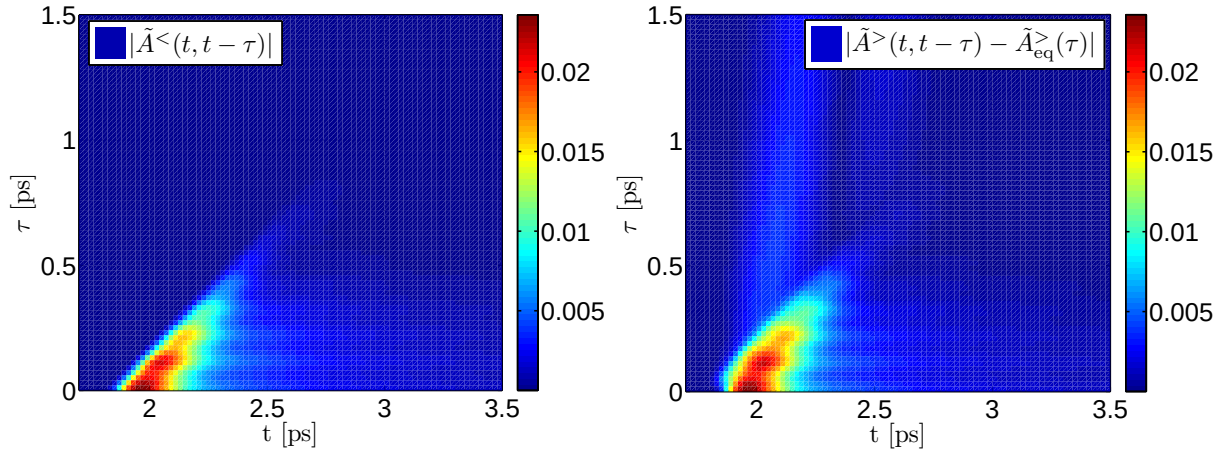

Figure 6.17.: *Solutions of the two-time photonic Green's functions with parameters as in figure 6.16, except for* $Q = 30 \Rightarrow \hbar\gamma_{\mathrm{cav}} = 27.94$ meV *and the use of a* 50 fs *pulse for excitation.*

These observations hint that the problem is at least partly due to numerical instabilities, that in principle can be cured by decreasing the time discretization, and not due to flaws in our theory or implementation. Indeed it is reasonable to think that a finer time discretization is needed in a two-time calculation, than would be necessary in a single-time calculation, due to the much more progressive accumulation of errors. This is so as we basically solve a differential equation for each discretized value of τ, each of which has an numerical error and an accumulated error due to the memory integral. Each of these solutions are used

every time we increase t, and the net result is a much larger error on the overall solution, which could easily lead to the instabilities we observe. We would like to point out that the solutions satisfy particle conservation and fulfil the relation $\tilde{A}^{>}(t,t) - \tilde{A}^{<}(t,t) = 1$, see eq. (2.31). This indicates that our theory and implementation at least to some extent are correct. In order to get rid of the numerical instabilities, one could perform a thorough analysis of the error as a function of the time discretization, and compare it to a formal error analysis of the equations, to see if the two agree.

Even though we are quite convinced that the two-time solutions presented above, do not represent the true solutions to our equations, we have still calculated the emission spectrum according to eq. (6.11) to see if some physical signatures could be identified. The results are shown in figure 6.18 for the considered cases. Both spectra display a large emission near the free cavity frequency, where the renormalized cavity frequency is slightly lower than the free. The set of sidebands situated on each side of the main peak are signatures of LO-phonons, confirmed through the fact that appear approximately a LO-phonon energy on each side of the main peak. Furthermore, the spectrum for the highest Q-factor also display a splitting of the main peak, which shows that this system is in the strong coupling regime, see chapter 1. The small ripples in this spectrum are expected to occur, as we have basically performed a Fourier transformation of a function that has not fully decayed in a smooth manner.

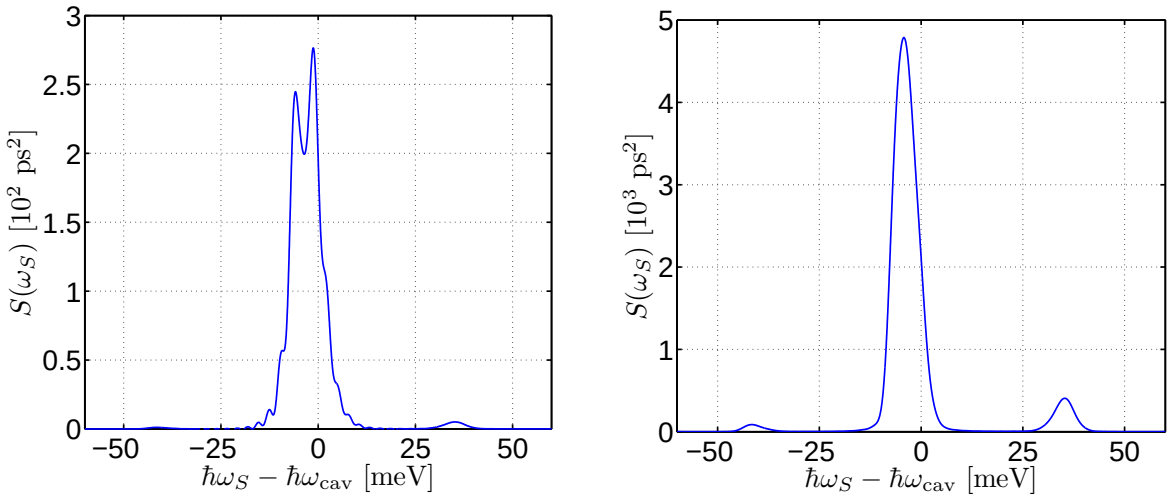

Figure 6.18.: *Emission spectra calculated from eq.* (6.11) *using the solutions in figure 6.16 (left) and figure 6.17 (right).*

6.6. Indistinguishability

In order for a single-photon source to be used in a quantum computer, it is essential that the single photons it emits are indistinguishable, as otherwise one will not be able to make them interfere. This makes it very important to obtain an understanding of what physical processes, causes the single photons to become distinguishable. In this section we will discuss how to define and determine the indistinguishability of the single photons emitted from our cQED system.

As discussed in chapter 1, one way to quantify the indistinguishability is to perform a Hong-Ou-Mandel (HOM) interference experiment as shown in figure 1.3(a). The result of such a measurement is a coincidence histogram for photon detection events, in the two photon detectors on each of the output arms of the BS, as shown in the bottom of the figure. Two perfectly indistinguishable photons would coalesce into a two-photon state, when impinging simultaneously on the two input arms of a BS. Therefore one would not observe simultaneous clicks in both detectors for this case, leading to the vanishing of the peak near $\tau = 0$ in the histogram. Real single photons are, however, always slightly distinguishable, due to interactions

with the environment, causing the peak at $\tau = 0$ to not vanish completely. We may therefore use the magnitude of the peak near $\tau = 0$ as a measure of the indistinguishability [15, 17], normalized in an appropriate way. To quantify this proposal we denote the function describing the coincidence histogram, as a function of the delay time τ, with the symbol $G^{(2)}_{\text{exp}}(\tau)$. With this quantity we may define the degree of indistinguishability I in the following way

$$I = 1 - \frac{\int_{\text{peak near } \tau=0} d\tau G^{(2)}_{\text{exp}}(\tau)}{\int_{\text{peak away from } \tau=0} d\tau G^{(2)}_{\text{exp}}(\tau)}, \tag{6.14}$$

where the normalization must be chosen as the integral over a peak sufficiently far away from the center peak at $\tau = 0$, so that no two-photon interference occurs. The peaks far away from $\tau = 0$ are basically what would be measured with no BS in the experiment.

Next one needs to relate the experimental function $G^{(2)}_{\text{exp}}(\tau)$ to a function that can be calculated theoretically. The relevant function is the second order correlation function for the photon [17], which is proportional to the probability of detecting a photon at one space-time point and another photon at some other (or the same) space-time point. In our case the two different space points are the two detectors in the HOM experiment, and the two times are the arrival times of the photons on the detectors. We denote this function as $G^{(2)}(t, t') = G^{(2)}(t, t-\tau)$, where reference to the space points has been omitted and further we have employed the time transformation used throughout the thesis. The second order correlation function is, however, a true two-time function and not an effective single-time function as $G^{(2)}_{\text{exp}}(\tau)$. It turns out that in order to obtain the experimental function one must average the time t, as this is what is done with the experimental data[11], due to large uncertainties in t. Performing the averaging we obtain

$$G^{(2)}_{\text{exp}}(\tau) \propto \frac{1}{2T} \int_{-T}^{+T} dt G^{(2)}(t, t-\tau), \tag{6.15}$$

where T must be chosen large enough so that $G^{(2)}(t, t-\tau)$ has fully decayed, furthermore only "proportional to" can be used due to several unknown prefactors pertaining to the experimental setup.

The above approach for defining and obtaining the indistinguishability was motivated by the experimental procedure. We may however choose a simpler approach as we work with pure theory and are not limited by the technicalities of the experiment. The motivation is the fact that $G^{(2)}(t, t-\tau)$ vanishes everywhere for two perfectly indistinguishable photons, in the case of a single[12] simultaneous excitation of the two single-photon sources. The degree on indistinguishability may then be defined as

$$I = 1 - \frac{\int_{-\infty}^{+\infty} dt \int_{-\infty}^{+\infty} d\tau G^{(2)}(t, t-\tau)}{\int_{-\infty}^{+\infty} dt \int_{-\infty}^{+\infty} d\tau G^{(2)}_{\text{no BS}}(t, t-\tau)}, \tag{6.16}$$

where we have chosen the normalization as the integral over $G^{(2)}(t, t-\tau)$ with no BS present, and thus no interference effects. With this definition one obtains $I = 1$ for perfectly indistinguishable photons and $I = 0$ when no interference occurs at all, with the extreme being the case of no BS present in the experiment.

Returning to the second order correlation function we note that it is a special case of the two-particle Green's function for the photon, which is a difficult object to handle in a many-body formalism. Fortunately it turns out that due to the specifics of our system, we may to a good approximation express the two-particle Green's function in terms of single-particle Green's functions. An expression for $G^{(2)}(t, t-\tau)$,

[11] We thank Henri Thyrrestrup Nielsen and Toke Lund-Hansen of DTU Fotonik for enlightening discussions.

[12] It is important that the single-photon sources are only excited once, as otherwise one would get peaks away from $\tau = 0$ similar to those in figure 1.3(a). The peaks in this experiment [14] are due to technicalities of the experiment, i.e. the need to build up a proper statistics through many identical excitations of the emitter.

appropriate for our experiment, has been derived in appendix A.1 and is given by

$$G^{(2)}(t_3,t_4) = \langle a^\dagger(t_3)a(t_3)\rangle \langle a^\dagger(t_4)a(t_4)\rangle - \langle a^\dagger(t_3)a(t_4)\rangle \langle a^\dagger(t_4)a(t_3)\rangle + \langle a^\dagger(t_3)a^\dagger(t_4)a(t_4)a(t_3)\rangle$$
$$+ \frac{1}{\sqrt{2}}\left[\langle a^\dagger(t_3)a^\dagger(t_4)a(t_3)\rangle \langle a(t_4)\rangle + \langle a^\dagger(t_3)a(t_4)a(t_3)\rangle \langle a^\dagger(t_4)\rangle \right.$$
$$\left. - \langle a^\dagger(t_3)a^\dagger(t_4)a(t_4)\rangle \langle a(t_3)\rangle - \langle a^\dagger(t_4)a(t_4)a(t_3)\rangle \langle a^\dagger(t_3)\rangle\right].$$

The two first terms in this expression are proportional to single-particle photonic Green's functions, while the third is a two-particle Green's function and the rest represent other contributions. In appendix A.2 it was shown that in the RWA it is well justified to neglect all other terms than the two first in the above expression. Hence we end up with a much more manageable object

$$\begin{aligned} G^{(2)}(t,t-\tau) &= \langle a^\dagger(t)a(t)\rangle \langle a^\dagger(t-\tau)a(t-\tau)\rangle - \langle a^\dagger(t)a(t-\tau)\rangle \langle a^\dagger(t-\tau)a(t)\rangle \\ &= \tilde{A}^<(t,t)\tilde{A}^<(t-\tau,t-\tau) - |\tilde{A}^<(t,t-\tau)|^2, \end{aligned} \tag{6.17}$$

where in the last line we have used the definition of the slowly-varying photon Green's function eq. (5.48) and also the symmetry eq. (2.32) to write the second term as an absolute value. The second order correlation function with no BS introduced in eq. (6.16), may be found from eq. (6.17) by simply removing the last term

$$G^{(2)}_{\text{no BS}}(t,t-\tau) = \tilde{A}^<(t,t)\tilde{A}^<(t-\tau,t-\tau), \tag{6.18}$$

as this is what introduces correlations between the photons. For a proper formal derivation of this result, one may go back to eq. (A.4) and realize that without the action of the BS, one may simply factor this expectation value right away, due to the assumption of independence of the two emitters.

As done in section 6.5, where we found that the determination of the emission spectrum required the full two-time lesser Green's function of the photon, we may attempt to use the GKBA to express the two-time Green's function in the expression eq. (6.17). To apply the GKBA we simply have to insert eq. (6.12) into eq. (6.17) which yields the following

$$G^{(2)}(t,t-\tau) = A(t-\tau)\left[A(t) - e^{-2\gamma_{\text{cav}}\tau}A(t-\tau)\right],$$

where we have used that both the decaying exponential and the photon density are real functions. In section 6.5 the GKBA was found to be of no use as the replacement for the true two-time Green's function, however at first sight the situation does not look as critical here as in the case of the emission spectrum. A further investigation has unfortunately not yet been performed.

6.6.1. Present stage results

In the section we present calculations of $G^{(2)}(t,t-\tau)$ and $G^{(2)}_{\text{exp}}(\tau)$ based on the two-time solutions already introduced in section 6.5.1. As the solutions themselves have already been discussed we will simply make a brief comments on the obtained results for $G^{(2)}(t,t-\tau)$ and $G^{(2)}_{\text{exp}}(\tau)$.

In figure 6.19 we show the results of calculating $G^{(2)}(t,t-\tau)$ based on the formulae eq. (6.17). The first thing one notices is the fact that the values become negative. This is clearly unphysical as $G^{(2)}(t,t-\tau)$ expresses a probability, which is another indication that the two-time solutions presented section 6.5.1 are not the actual physical solutions to the equations. Other than this unacceptable property, we notice that the value goes to zero for $\tau = 0$, being consistent with eq. (6.17), and that it decays in both the t and τ directions.

The corresponding $G^{(2)}_{\text{exp}}(\tau)$ functions are shown figure 6.20. These also display negative values, due to the fact that $G^{(2)}(t,t-\tau)$ does, again being an unphysical property. The red curves display the so-called HOM dip, which is a sign that interference has occurred. The blue curves illustrate $G^{(2)}_{\text{exp}}(\tau)$ with no BS present, eq. (6.18), and for this reason they do not display any signs of correlation.

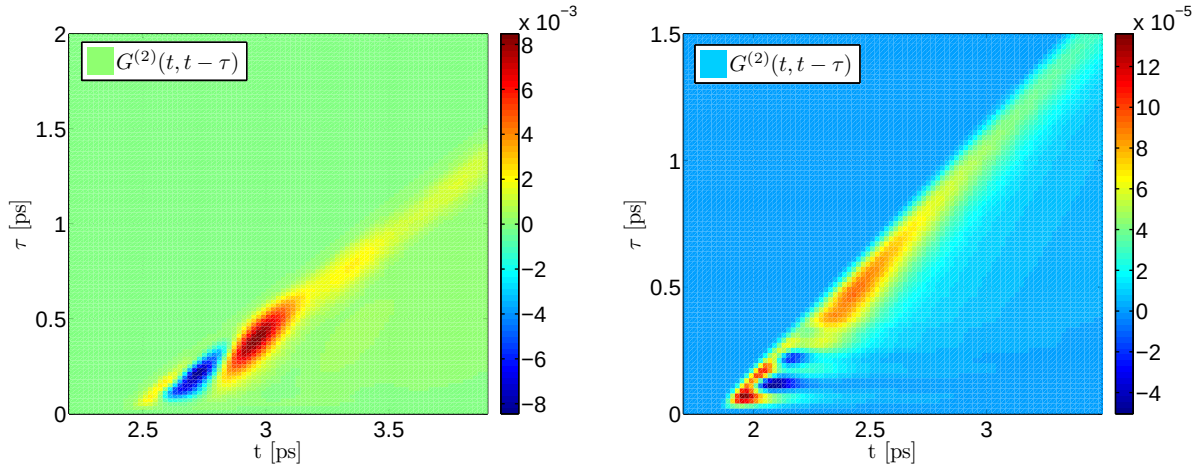

Figure 6.19.: $G^{(2)}(t,t-\tau)$ *calculated from eq.* (6.17) *for the solutions shown in figure 6.16 to the left and figure 6.17 to the right.*

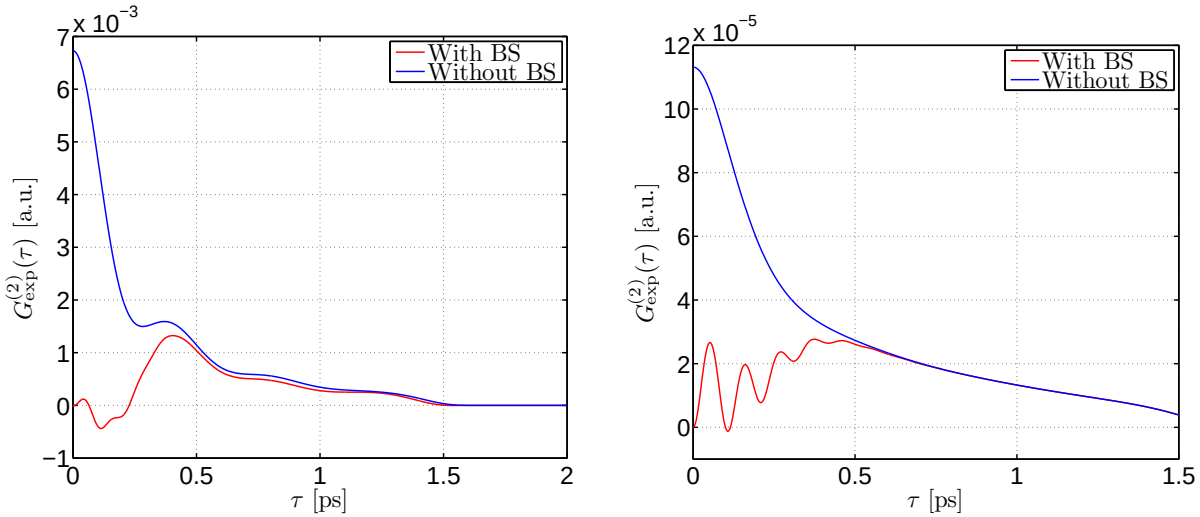

Figure 6.20.: *calculated from eq.* (6.17) *for the solutions shown in figure 6.16 to the left and figure 6.17 to the right.*

6.7. Summary

In this chapter we have applied the equations of motion derived in the previous chapter, to a number of specific situations, including probing the equilibrium system in linear response theory and investigating the full non-equilibrium dynamics of our cQED system. Below we go through the findings and results of the different sections in the chapter.

In section 6.2 we discussed the occurrence of unphysical populations within our theory. These occur for certain excitation schemes, when conditions for very efficient coupling are present within the bands. We suspect that these unphysical features are due to a break down of the GKBA and/or the lowest order self-energy approximation, a suspicion which is supported by the literature. Using a level structure with transitions less resonant with the LO-phonon energy, did, however, provide us with a quick fix of the problem, but more work is needed to fully resolve this issue in a satisfactory manner.

The linear absorption spectrum was treated in section 6.3, where the effects of all many-body interactions were systematically investigated. Only including the LO-phonon interaction, we found that the main s and p transitions were broadened and slightly shifted. Beside the renormalizations of the main peaks, a

very rich structure of lesser pronounced peaks arose. It turns out that the rich peak structure can be understood in terms of the spectral functions of the polaron quasi-particles, where a number of sidebands and hybridization effects enter in a dramatic way. The quasi-particles give rise to so-called LO-phonon-assisted transitions, manifesting themselves as a complicated background of peaks. Including the Coulomb interaction mainly resulted in a large negative shift of the s and p transitions, known as exciton shifts. The magnitude of the shifts could be explained using a relatively simple model. The combined effects of both the LO-phonons and photons was also investigated, and several parameters controlling the electron-photon coupling were systematically varied. The results from the numerical simulations, were compared to a simple model where dephasing was treated in the constant decay rate approximation. In the strong coupling regime, the transition resonant with cavity photon developed into a double peak, as expected, and the positions and relative weights of the two peaks were compared to the simple model. It was found that the spectral positions of the peaks could be relatively well explained by the model, whereas the relative weights could not, due to symmetric Lorentzian lineshape implicitly assumed in the constant decay rate approximation.

In section 6.4 time domain solutions to our equations were investigated. The first part dealt with the approach to a quasi-equilibrium state, due to LO-phonon scattering after excitation by a short optical pulse. In all considered cases a quasi-equilibrium state was reached within a time span of 5 ps. Furthermore Rabi oscillations between the electrons in valence band and LO-phonons was observed, which are analogous to well-known Rabi oscillations between electrons and photons. In the second part we considered a similar situation, but now photons were included in the equations, and in this investigation we looked specifically for Rabi oscillations between the electrons and photons. The occurrence of Rabi oscillations was found, not surprisingly, to depend on temperature, which is reasonable as the number of LO-phonons causing dephasing decreases with temperature. A much stronger dependence was, however, found on exactly how the electrons were excited, and the strongest Rabi oscillations were found for excitation directly into the levels being resonant with the cavity photon. In the last part we compared our Green's function approach to a numerically exact solution to a simplified system. Quantitatively the agreement was not overwhelming, but qualitatively the agreement was reasonable. It is, however, difficult to gauge the accuracy of solutions obtained using Green's functions for more realistic systems, as exact solutions to many-body problems are in general very difficult to obtain.

In the last couple of sections, 6.5 and 6.6, we discussed how to determine the emission spectrum and indistinguishability of the emitted photons using the Green's function formalism. In the case of the emission spectrum, it was found that in order to obtain lineshapes other than Lorentzians, the GKBA could not be employed for the photonic Green's functions. This called for the use of the full two-time photonic Green's function theory, which is much more complicated than the effective single-time version provided by the GKBA. The present stage of progress on solving the two-time theory was discussed in section 6.5.1. Even though it was concluded that we had not yet obtained the correct physical solution, the solutions that had been obtained, still produced emission spectra containing some of the expected physics, such as the strong coupling splitting and sidebands due to LO-phonons. In section 6.6 two-time findings in connection to indistinguishability were discussed, but these were to a large degree unphysical and therefore inconclusive.

7. Summary and Outlook

In this thesis we have investigated many-body effects in self-assembled semiconductor QDs, with the main motivation of describing relaxation and dephasing processes beyond a simple constant decay rate picture. The main emphasis has been on the interaction between electrons and LO-phonons, which is known to be the main scattering mechanism in the low excitation and high temperature regime. To model a single-photon source the QD has been placed in an optical cavity, in which the interaction with photons becomes important on short time-scales. To describe the dynamics, a many-body formalism has been employed, which is based on non-equilibrium Green's functions. Invoking complicated theoretical methods is necessary in order to correctly describe a true many-body system, which a semiconductor QD is. The governing equations derived using the many-body formalism, have been solved numerically and the solutions analyzed and discussed for a range of parameters. Below we go through the individual chapters and summarize the results obtained in these in greater detail.

A general introduction to the subject is given in chapter 1, where we have tried to motivate the present work and give an introduction to the physical system being considered.

In chapter 2 we took on the task of introducing the reader to the formal theory of non-equilibrium Green's functions. We started from a basic calculation of an ensemble average for a non-equilibrium system written as an infinite series, and ended up with the celebrated Dyson equation, formulated in terms of the contour ordered Green's function and its corresponding self-energy. From this we were able to formulate a set of equations for various real time Green's functions, that are capable of describing physically observables. The equations are the foundation for almost all calculations performed in this thesis. Last we introduced an extremely important approximation known as the Generalized Kadanoff-Baym Ansatz (GKBA), that in some cases enables us to reduce the general two-time structure of the Green's functions to an effective single-time structure.

The most fundamental ingredient in any quantum theory, namely the Hamiltonian operator, was treated in chapter 3 for a general semiconductor system. Even though this is normally regarded as textbook material, we went through many of the steps necessary to go from a fully general Hamiltonian, to a form more appropriate for practical calculations. This was done in order to gain an overview and understanding of the many different Hamiltonians that enter many-body physics. We have at least to some degree succeeded in doing this.

The more practical problem of obtaining a sufficient description of the electronic single-particle states, and the computationally demanding task of subsequent calculating of the various interaction matrix elements, was treated in chapter 4. In this chapter we set up a simple model for the combined QD and WL system, that captures the essential features of the self-assembled QDs grown in the laboratory. We numerically solved the model for a specific geometry and discussed the qualitatively different states. Next we proposed two ways of calculating Coulomb matrix elements on the basis of the states obtained from our model. One which is exact but slow and one which is approximate but much faster. The need for a fast and efficient method is paramount, as the number of Coulomb matrix elements grows extremely fast with the number of basis states. The two methods were compared and for most elements the relative error of the approximative method was below 1 %.

In chapter 5 we performed a last set of approximations on the Hamiltonians and truncated the many-body self-energies, further we formulated the final versions of equations describing our equilibrium and non-equilibrium system. The self-energies were truncated at the lowest order level, but made self-consistent in the electronic and photonic Green's functions, as dictated by the particle conservation law in the case of the electrons. An analysis of the equilibrium properties of our system was performed, and it was found that the coupling to the LO-phonons strongly modified the spectral properties of the electrons, compared

to the free or slightly lifetime broadened case. These quasi-particle properties are very important to incorporate into the non-equilibrium theory, as otherwise the initial or equilibrium correlations will be missing in the non-equilibrium dynamics. In contrast to the LO-phonons, the photons were found not to have any equilibrium correlations with the electrons, at least at our level of approximation. This was a bit surprising due to the formal similarities between phonons and photons. In the last part of the chapter the non-equilibrium equations of motion were derived. In these derivations the main approximation was employment of the GKBA. The GKBA was applied to all electronic Green's functions, whereas for the photonic Green's functions we presented two versions, one in the GKBA and one where we retained the full two-time form of the Green's functions.

The application of the equations of motion to non-equilibrium situations was treated in chapter 6. Due to the size of this chapter, we will only summarize a few of the main results obtained here, referring the reader to section 6.7 for a more complete summary. A large part of this chapter was devoted to studying many-body effects on the linear absorption spectrum of our system. The most dramatic effect occurred due to inclusion of LO-phonons into the Hamiltonian. A very rich spectrum resulted where beside the already existing the main s and p transitions, a large number of lesser pronounced peaks came into existence. It was established that these smaller peaks were manifestations of LO-phonon-assisted transitions, arising due to transitions between LO-phonon dressed electron states, illustrated clearly through the polaron spectral functions. Including photons into the theory, we were able to study the effects of LO-phonons on the vacuum Rabi splitting, that appears in the spectrum in the strong coupling regime. We systematically varied the coupling strength $\hbar g$ and detuning, between the cavity and s transition, and compared the results to a simple analytical model. We found that the spectral positions of the two peaks characterizing the vacuum Rabi splitting, were well described by the simple model, however the relative weights of the peaks were not. Another main focus was the investigation of population dynamics after excitation by a short optical pulse, displaying the full power of the non-equilibrium theory developed in this thesis. The approach to a quasi-thermal equilibrium state was studied, and it was found that this state was established within 5 ps for all the cases considered. Furthermore, Rabi oscillations between the LO-phonons and valence band electrons was observed, indicating that these couple strongly for the considered system. The occurrence of Rabi oscillations due to the electron-photon interaction was also treated, and we investigated under which conditions these were most pronounced. Not surprisingly it was confirmed that lowering the temperature made it more likely to observe these coherent exchanges of energy. This is consistent with the fact that the thermal occupation of LO-phonons decreases for decreasing temperature, and hence the decoherence caused by them. More surprisingly it was found that the Rabi oscillations depended much stronger on exactly how the electrons were excited. More specifically the more powerful oscillations were observed when electrons were excited into the shell being resonant with the cavity. We expect this to be due to the electrons losing their coherence while relaxing into the cavity resonant s shell, and thereby not being able to interact coherently with the photons.

7.1. Outlook

In the limited time span of this project we have not been able to pursue all the directions and ideas we would have liked to. In the following we describe several extensions of the present work, that would be natural to investigate in the future.

One of the most obvious improvements of the present theory would be the inclusion of the electronic states in the WL continuum, that we know are part of the real physical system we are trying to describe. At elevated temperatures it is known that electrons are thermally excited into the WL states [42], hence making these important for a proper description. Although the WL continuum has been taken into account in several many-body calculations [41, 55], this was done in a scheme where the bound and unbound states of the QD and WL respectively, were not treated on the same footing, which could potentially be a serious problem. A consistent solution to this problem would be the implementation of the WL states described in section 4.2.3, into the theory developed in this thesis. It is further expected that adding an electronic continuum would remedy the issues we have experienced regarding the unphysical populations described

in section 6.2, in that they would provide more efficient scattering making the application of the lowest order self-energy sufficient.

Many quantum optical experiments are performed at very low temperatures, where it is known that LA-phonons become the dominant dephasing mechanism. It would indeed be very interesting to include LA-phonons into our theory, as this would enable us to help interpreting many of the experiments currently being performed around the world, some of which even in the Quantum Photonics group at DTU Fotonik. Going to low temperatures would furthermore drastically lower the amount of electrons being thermally excited, that could serve as an argument for neglecting the WL continuum. The fact that LA-phonons constitute an energy continuum could possibly, in analog to adding a electronic continuum, help us avoid unphysical populations, due to the increased scattering efficiency.

A more practical improvement, but no less important, would be to implement the numerical code in a low level programming language such as Fortran or C. The present implementation of the theory has been done in the commercial script language MATLAB, which offers easy access to complicated functionality and relatively easy debugging capabilities, however often at the cost computational efficiency. Implementation in a low level language would offer great speed and the opportunity to use existing parallelization packages, making large scale computations possible. A faster implementation of the theory, would also ease the analysis of the unresolved issues remaining in the two-time theory of the photonic Green's functions described in sections 6.5 and 6.6.

The ultimate goal for future developments of the work presented in this thesis, is to provide a practical theory that takes into account all the important many-body interactions in a cQED system. From this theory it should be is possible to extract all wanted information on the emitted photons, which is the most important property to describe as it is what is being measured in experiments. We have initiated this by setting up a theory for the two-time photonic Green's functions, but as has been reported much work still remains to be done.

A. Appendix

A.1. Second order correlation function for a Hong-Ou-Mandel type experiment

As mentioned in chapter 1 we are interested in determining the indistinguishability of single photons emitted from a semiconductor cQED system, for this we may perform an interference experiment as interference and quantum indistinguishability are intimately connected. Indeed it is known [15, 17] that if two perfectly indistinguishable photons are interfered on a BS, these will coalesce into a two-photon state. The corresponding coincidence detection probability in a Hong-Ou-Mandel (HOM) two-photon interference experiment [80] will be zero. The experiment we wish to describe is shown schematically in figure A.1. It consists of two systems, denoted 1 and 2, that are capable of emitting photons, which are directed onto a beam-splitter (BS) where they may interfere and the output arms of the BS are equipped with photon detectors.

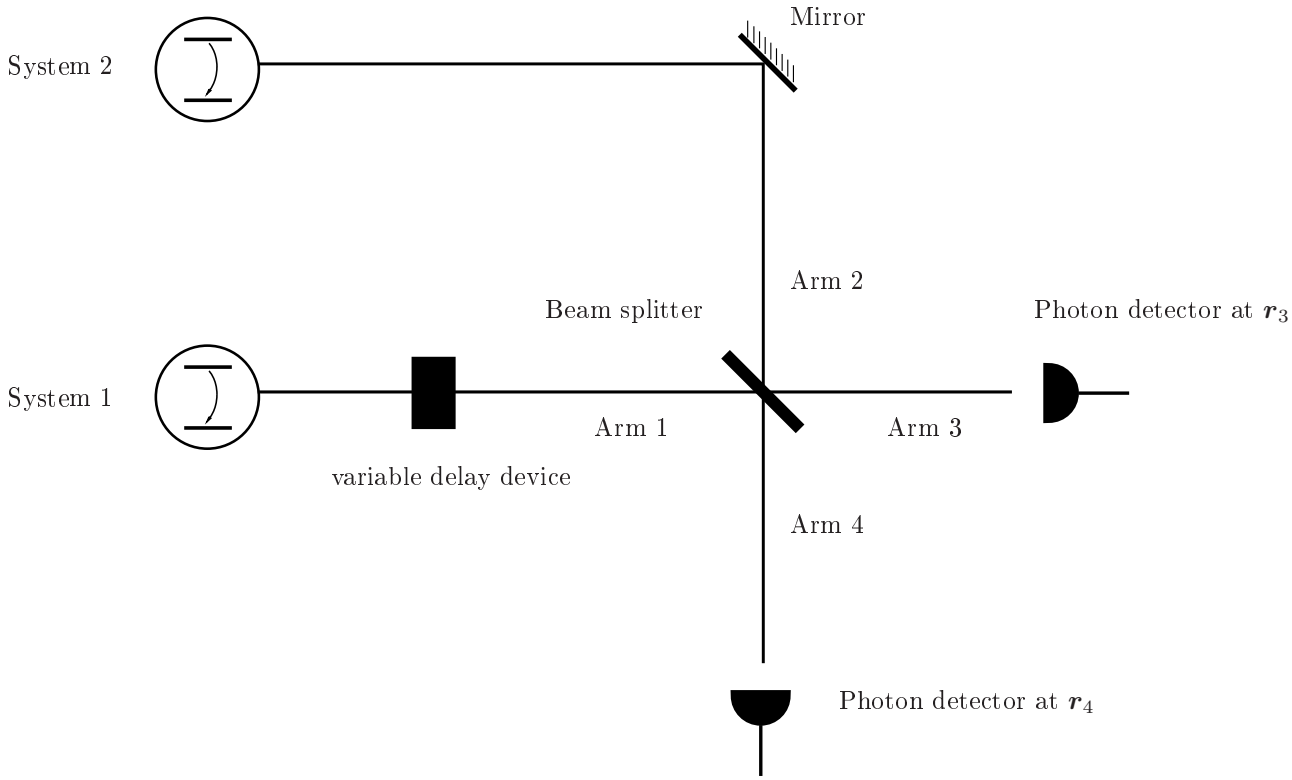

Figure A.1.: *Schematic illustration of the experiment designed to measure* $G^{(2)}(\boldsymbol{r}_3 t_3, \boldsymbol{r}_4 t_4; \boldsymbol{r}_4 t_4, \boldsymbol{r}_3 t_3)$. *The variable delay device is inserted to adjust the path length for the photons from system 1, so that one may control the arrival times for the photons from system 1 on the BS.*

Theoretically the relevant quantity for describing such an experiment is the second order correlation function of the quantized electric field [45, p. 564], with its spatial coordinates evaluated at the detector

positions in each of the output arms 3 and 4. The explicit expression for the second order correlation function is

$$G^{(2)}(\boldsymbol{r}_3 t_3, \boldsymbol{r}_4 t_4; \boldsymbol{r}_4 t_4, \boldsymbol{r}_3 t_3) = \langle E^{(-)}(\boldsymbol{r}_3, t_3) E^{(-)}(\boldsymbol{r}_4, t_4) E^{(+)}(\boldsymbol{r}_4, t_4) E^{(+)}(\boldsymbol{r}_3, t_3) \rangle \,, \tag{A.1}$$

where the positive and negative frequency parts of the quantized electric field are given by

$$E^{(+)}(\boldsymbol{r}, t) = \sum_m \mathcal{E}_m a_m(t) u_m(\boldsymbol{r}), \quad E^{(-)}(\boldsymbol{r}, t) = \sum_m \mathcal{E}_m a_m^\dagger(t) u_m(\boldsymbol{r}), \tag{A.2}$$

and the mode functions and expansion coefficients are assumed to be real. For simplicity we will assume that the fields on the output side of the BS can be represented by a single mode in each arm so that we may write the field as

$$E^{(-)}(\boldsymbol{r}, t) = E_3^{(-)}(\boldsymbol{r}, t) + E_4^{(-)}(\boldsymbol{r}, t) = \mathcal{E}_3 a_3^\dagger(t) u_3(\boldsymbol{r}) + \mathcal{E}_4 a_4^\dagger(t) u_4(\boldsymbol{r}), \tag{A.3}$$

where only the negative frequency part is shown. The reason for making this assumption is that we only wish to model a single quasi-mode of the cavity, from which the photons originate, and therefore also the input side of the BS will be represented by a simple two mode field as above. In this approximation we only solve for the local cavity mode and through this we implicitly assume that propagation effects from the cavity to the detectors are neglectable. This often used assumption has recently been questioned [81], for some types of photonic structures, and may therefore not be valid in all cases, but it is beyond the scope of this thesis to improve upon this approximation. To proceed we insert eq. (A.3) into eq. (A.1) which results in a total of $2^4 = 16$ contributions. Fortunately most of these can be neglected as they contain spatial cross terms of the type $u_3(\boldsymbol{r}_4)$ or $u_4(\boldsymbol{r}_3)$, where a spatially localized mode function is evaluated at the detector position in the other output arm, which can safely neglected. After throwing all these cross terms away we end up with the expression

$$G^{(2)}(\boldsymbol{r}_3 t_3, \boldsymbol{r}_4 t_4; \boldsymbol{r}_4 t_4, \boldsymbol{r}_3 t_3) \approx |\mathcal{E}_3 u_3(\boldsymbol{r}_3)|^2 |\mathcal{E}_3 u_4(\boldsymbol{r}_4)|^2 \langle a_3^\dagger(t_3) a_4^\dagger(t_4) a_4(t_4) a_3(t_3) \rangle \,,$$

where we may further remove the constant prefactors. This is allowed due to the fact that the considered second order correlation function is only proportional to the probability we are looking for, and hence it must be normalized at some point anyway. We may now simply the notation and write the second order correlation function as follows

$$G_{34}^{(2)}(t_3, t_4) = \langle a_3^\dagger(t_3) a_4^\dagger(t_4) a_4(t_4) a_3(t_3) \rangle \,. \tag{A.4}$$

The next thing is to relate the output photon operators to those on the input side, which is done with a standard BS relation of the form [17]

$$\begin{bmatrix} a_3(t) \\ a_4(t) \end{bmatrix} = \begin{bmatrix} \cos(\xi) & -e^{-i\phi}\sin(\xi) \\ e^{i\phi}\sin(\xi) & \cos(\xi) \end{bmatrix} \begin{bmatrix} a_1(t) \\ a_2(t) \end{bmatrix}, \tag{A.5}$$

that performs the BS action as a unitary operation. The number ξ determines the reflection and transmission of the BS and ϕ is an arbitrary phase. To express $G_{34}^{(2)}(t_3, t_4)$ in terms of the input photon operators we use eq. (A.5) on eq. (A.4) which generates $2^4 = 16$ terms of four-operator brakets in the photon operators for the two input arms. We assume the photon operators of the input to be equal to the photon operators of system 1 and 2, respectively. To simplify this expression and the further analysis of the problem, we will assume that system 1 and 2 are identical and independent. The identical part means that their respective Hamiltonians are equal, except for the index, and the independence means that their Hamiltonians commute, $[H_1, H_2] = 0$, i.e. do not interact. The fact that their Hamiltonians commutes, has the consequence that any expectation value involving operators of the two subsystems may be factored into an expectation value for each of the subsystems, e.g. $\langle a_2^\dagger(t_3) a_1^\dagger(t_4) a_1(t_4) a_2(t_3) \rangle = \langle a_2^\dagger(t_3) a_2(t_3) \rangle \langle a_1^\dagger(t_4) a_1(t_4) \rangle$. The fact that the are equal means that after the factorization we may simply remove the subscript referring to the individual subsystems, so that effectively we only consider a single system. In practise this situation can realized by using the same system as both system 1 and 2. The first emitted photon could be sent on

a longer path, while the system returned to equilibrium and could be excited again to emit the second photon. Performing the steps described above and specializing to the case of a 50/50 BS, obtained by setting $\xi = \pi/4$, and choosing the arbitrary phase as $\phi = \pi/4$ we arrive at

$$\begin{aligned} G^{(2)}_{34}(t_3,t_4) &= \langle a^\dagger(t_3)a(t_3)\rangle \langle a^\dagger(t_4)a(t_4)\rangle - \langle a^\dagger(t_3)a(t_4)\rangle \langle a^\dagger(t_4)a(t_3)\rangle + \langle a^\dagger(t_3)a^\dagger(t_4)a(t_4)a(t_3)\rangle \\ &+ \frac{1}{\sqrt{2}}\left[\langle a^\dagger(t_3)a^\dagger(t_4)a(t_3)\rangle \langle a(t_4)\rangle + \langle a^\dagger(t_3)a(t_4)a(t_3)\rangle \langle a^\dagger(t_4)\rangle \right. \\ &\left. - \langle a^\dagger(t_3)a^\dagger(t_4)a(t_4)\rangle \langle a(t_3)\rangle - \langle a^\dagger(t_4)a(t_4)a(t_3)\rangle \langle a^\dagger(t_3)\rangle\right], \end{aligned} \tag{A.6}$$

where an overall factor of 1/2 has been removed. The two first terms in this expression are first order correlation functions or single-particle Green's functions and are expected to play an important role as we are considering single-photon states. The third term is a second order correlation function, or two-particle Green's function, and is not expected to yield significant contributions due to its two particle nature. This may sound strange as we are interfering two photons, however, we have expressed the two-photon detection probability in terms of quantities of the single emitter, where only a single photon is generated. The last four terms are more difficult to have an intuition about, as they are not directly related to photon detection probabilities as the first three terms are. The importance of all terms will be investigated further in appendix A.2.

A.2. Higher Order Correlation Functions

The purpose of this appendix is to estimate the relative magnitude of the various photon correlation functions appearing in the expression for $G^{(2)}_{34}(t_3,t_4)$, see eq. (A.6), and show or argue that higher order correlation functions are identically zero or negligible. For reference we reproduce the expression for $G^{(2)}_{34}(t_3,t_4)$ below

$$\begin{aligned} G^{(2)}_{34}(t_3,t_4) &= \langle a^\dagger(t_3)a(t_3)\rangle \langle a^\dagger(t_4)a(t_4)\rangle - \langle a^\dagger(t_3)a(t_4)\rangle \langle a^\dagger(t_4)a(t_3)\rangle + \langle a^\dagger(t_3)a^\dagger(t_4)a(t_4)a(t_3)\rangle \\ &+ \frac{1}{\sqrt{2}}\left[\langle a^\dagger(t_3)a^\dagger(t_4)a(t_3)\rangle \langle a(t_4)\rangle + \langle a^\dagger(t_3)a(t_4)a(t_3)\rangle \langle a^\dagger(t_4)\rangle \right. \\ &\left. - \langle a^\dagger(t_3)a^\dagger(t_4)a(t_4)\rangle \langle a(t_3)\rangle - \langle a^\dagger(t_4)a(t_4)a(t_3)\rangle \langle a^\dagger(t_3)\rangle\right] \end{aligned} \tag{A.7}$$

To avoid having to deal with the full solid-state system, see section 3.2.3, we will focus on a much simpler system, namely the well known Jaynes-Cummings model[1] (JCM). The JCM describes a system of a single electron interacting with a single cavity mode through the dipole coupling, for a illustration see figure A.2. The Hamiltonian for the JCM is given by

$$H = H_0 + H_{\rm i}, \quad H_0 = \sum_{i=1,2} \hbar\omega_i c_i^\dagger c_i + \hbar\omega(a^\dagger a + 1/2), \quad H_{\rm i} = \sum_{i\neq j} \hbar g c_i^\dagger c_j (a^\dagger + a), \tag{A.8}$$

where ω_i is the frequency of electron state i, ω is the frequency of the cavity mode, and g is the coupling constant between the two systems which we assume to be real. The operators $c_i^\dagger$, c_i, $a^\dagger$, and a are the standard second quantization operators for fermions and bosons. We note that the rotating wave approximation (RWA) has not been applied, as it is partly the validity of this we wish to examine, also the spin index of the electron has been omitted for notational simplicity. The part of the Hamiltonian for the full system which is responsible photon emission into the cavity is exactly given by the JCM Hamiltonian. The extra terms occurring, all lead to various forms of the decay. On this basis, we can expect the JCM to exhibit stronger photon correlations than the full system, and hence it can be used as an ideal system to investigate higher order correlations. We will then assume that photon correlation functions, which are zero or negligible for the JCM will be of even smaller significance for the full system, and hence can be omitted in the full analysis.

[1] See e.g. chapter 6 in [44].

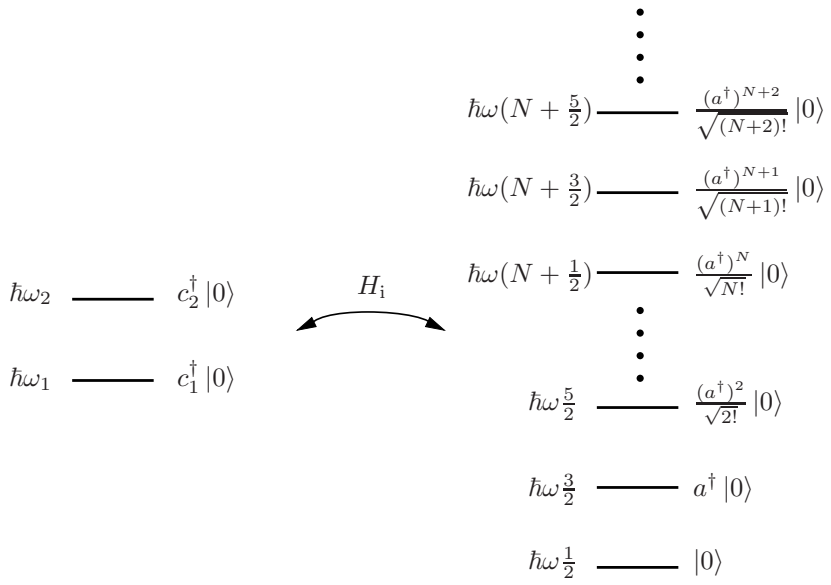

Figure A.2.: *Schematic illustration of the Jaynes-Cummings model, with the electronic and photonic systems interacting through* H_i.

In order to obtain the photon correlation functions we need to determine the time evolution of the photon operators (a and $a^\dagger$) in the Heisenberg picture. This is given by

$$a(t) = u^\dagger(t,t_0)au(t,t_0), \tag{A.9}$$

where $u(t,t_0)$ is the time evolution operator

$$i\hbar\partial_t u(t,t_0) = Hu(t,t_0) \Rightarrow u(t,t_0) = \exp\left(-iH(t-t_0)/\hbar\right),$$

and where the initial condition $u(t_0,t_0)=1$ has been used. In the following we will set $t_0=0$ and drop the second time argument in $u(t,t_0)$. The explicit form of $u(t)$ is most easily obtained by diagonalizing H, as $u(t)$ will be diagonal in the eigenstates of H.

The next step is to choose a suitable basis for our system. A general basis vector containing one electron and N photons will be of the form

$$|n_1,n_2;N\rangle = (c_1^\dagger)^{n_1}(c_2^\dagger)^{n_2}\frac{(a^\dagger)^N}{\sqrt{N!}}|0\rangle, \quad \text{where} \quad n_1,n_2=0,1 \quad \text{and} \quad N=0,1,2\ldots \tag{A.10}$$

Usually when considering the JCM, in the RWA, the basis $\{|1,0;1\rangle, |0,1;0\rangle\}$ is used, as this generates a closed set of equations for the initial state $|\psi(t=0)\rangle = |0,1;0\rangle$. However due to the fact that we have not applied the RWA, the same initial condition will couple to states containing more than one photon, and in general generate an infinite set of equations. These other states contain virtual photons, that is photons that would not be allowed to exist if strict energy conservation was to hold. In quantum mechanics strict energy conservation does not hold, due to the energy-time uncertainty relation[2] $\Delta E\Delta t \geq \hbar/2$, and breaking energy conservation is allowed within small time spans. The main reason for going beyond the RWA is to examine the effect of the virtual photons on the higher order terms in $G^{(2)}_{34}(t_3,t_4)$.

[2]For a critical comment on the usual interpretation of the energy-time uncertainty relation see [45, p. 343]. The comment is based on the fact that there does not exist a time operator in quantum mechanics and hence an energy-time uncertainty relation, in the usual sense, cannot be derived.

As a truncated basis we will choose the following five states, denoted the bare basis,

$$|1\rangle = |1,0;0\rangle = c_1^\dagger |0\rangle , \tag{A.11a}$$
$$|2\rangle = |1,0;1\rangle = c_1^\dagger a^\dagger |0\rangle , \tag{A.11b}$$
$$|3\rangle = |0,1;0\rangle = c_2^\dagger |0\rangle , \tag{A.11c}$$
$$|4\rangle = |0,1;1\rangle = c_2^\dagger a^\dagger |0\rangle , \tag{A.11d}$$
$$|5\rangle = |1,0;2\rangle = c_1^\dagger \frac{(a^\dagger)^2}{\sqrt{2}} |0\rangle . \tag{A.11e}$$

These are chosen as they possess the two lowest free transition energies for a system initially in the $|3\rangle$ state, assuming a zero detuning setup, $\omega_2 - \omega_1 = \omega$. The free transition energy between two states is given by: $|H_0(|\text{final}\rangle - |\text{initial}\rangle)|$, so that for our basis we get

$$H_0(|2\rangle - |3\rangle) = 0, \quad |H_0(|1\rangle - |3\rangle)| = H_0(|4\rangle - |3\rangle) = H_0(|5\rangle - |3\rangle) = \hbar\omega.$$

This way we allow the initial excitation to propagate into states which are energetically unfavorable, but nevertheless occur as we have not applied the energy-conserving RWA. In the case of having applied the RWA there would be no need to expand the basis beyond $\{|2\rangle , |3\rangle\}$, as these are the only states conserving energy for a system initially in state $|2\rangle$ or $|3\rangle$.

The matrix representation of H in the basis $\{|1\rangle , |2\rangle , |3\rangle , |4\rangle , |5\rangle\}$ is given by

$$H = \begin{bmatrix} \hbar\omega_1 & 0 & 0 & \hbar g & 0 \\ 0 & \hbar(\omega_1+\omega) & \hbar g & 0 & 0 \\ 0 & \hbar g & \hbar\omega_2 & 0 & 0 \\ \hbar g & 0 & 0 & \hbar(\omega_2+\omega) & \sqrt{2}\hbar g \\ 0 & 0 & 0 & \sqrt{2}\hbar g & \hbar(\omega_1+2\omega) \end{bmatrix},$$

where the zero-point energy of the photons has been neglected, as it only corresponds to a shift of $\hbar\omega/2$ to all energy levels and hence is without any dynamical significance. Finding eigenvalues- and vectors of this 5×5 matrix can be done analytically, as the solution of the characteristic equation for determining the eigenvalues only involves a third order polynomial. The explicit form of the eigenvalues- and vectors is however not very important in the present context and would take up a lot of space, so these will not be shown. Instead we present the general form of the solution and argue on the basis of this.

The eigenvalues- and vectors will be represented by the following symbols

$$\hbar\Omega_i, \quad |\Omega_i\rangle = \begin{bmatrix} \langle 1|\Omega_i\rangle \\ \langle 2|\Omega_i\rangle \\ \langle 3|\Omega_i\rangle \\ \langle 4|\Omega_i\rangle \\ \langle 5|\Omega_i\rangle \end{bmatrix},$$

respectively and the vectors have been normalized, i.e. $\langle\Omega_i|\Omega_j\rangle = \delta_{ij}$. Representing the Hamiltonian in the basis of its eigenstates, the dressed states, diagonalizes the matrix form of H. Mathematically the diagonalization is performed by applying the following transformation to H

$$H' = V^{-1}HV \Rightarrow (H')_{ij} = \hbar\Omega_i\delta_{ij}.$$

Here the prime ($'$) signifies representation in the dressed basis and V is a unitary transformation matrix, which columns are given by the eigenvectors of H, i.e. $(V)_{ij} = \langle i|\Omega_j\rangle$. Having diagonalized the Hamiltonian, it is easy to obtain the time evolution operator as this is also diagonal in the dressed basis

$$u'(t) = \exp(-iH't/\hbar) \Rightarrow (u'(t))_{ij} = \exp(-i\Omega_i t)\delta_{ij}.$$

We could proceed to work in the dressed basis, but we will transform back to the more intuitive bare basis, eq. (A.11), where the time evolution operator is given by the inverse transformation

$$u(t) = Vu'(t)V^{-1}.$$

The last thing needed to calculate the photon correlation functions is to determine the matrix representation of the photon operators a and $a^\dagger$. The elements of a are found by writing a general matrix element of a in two states of the form eq. (A.10)

$$\begin{aligned}\langle m_1, m_2; M|a|n_1, n_2; N\rangle &= \langle 0|\frac{a^M}{\sqrt{M!}}c_2^{m_2}c_1^{m_1}a(c_1^\dagger)^{n_1}(c_2^\dagger)^{n_2}\frac{(a^\dagger)^N}{\sqrt{N!}}|0\rangle \\ &= \langle M|a|N\rangle\,\delta_{m_1,n_1}\delta_{m_2,n_2} \\ &= \sqrt{N}\delta_{M,N-1}\delta_{m_1,n_1}\delta_{m_2,n_2},\end{aligned}$$

where in the last line we have used $a\,|N\rangle = \sqrt{N}\,|N-1\rangle$. The matrix representing a can now be written as

$$a = \begin{bmatrix} 0 & 1 & 0 & 0 & 0 \\ 0 & 0 & 0 & 0 & \sqrt{2} \\ 0 & 0 & 0 & 1 & 0 \\ 0 & 0 & 0 & 0 & 0 \\ 0 & 0 & 0 & 0 & 0 \end{bmatrix}.$$

The matrix form of $a^\dagger$ is easily found from the above by the definition of Hermitian conjugation $(a^\dagger)_{ij} = [(a)_{ji}]^*$.

Obtaining the time evolution of the various correlation functions in $G_{34}^{(2)}(t_3, t_4)$, eq. (A.7), is now a simple matter of matrix multiplication as seen from eq. (A.9). One last thing that needs to be discussed is the meaning of the brackets in eq. (A.7). The usual meaning of the bracket is that of taking the expectation value of a certain operator $O(t)$, that is $\langle O(t)\rangle = \mathrm{Tr}\,[\rho_0 O(t)]$, where ρ_0 is the initial density matrix of the system. For a pure state the density matrix can be written as $\rho_0 = |\psi_0\rangle\,\langle\psi_0|$, so that the expectation value of $O(t)$ can rewritten as follows

$$\langle O(t)\rangle = \mathrm{Tr}\,[\rho_0 O(t)] = \mathrm{Tr}\,[|\psi_0\rangle\,\langle\psi_0|\,O(t)] = \langle\psi_0|O(t)|\psi_0\rangle\,,$$

where $|\psi_0\rangle$ is the initial state vector of the system. This means that we simply have to take the matrix element of the product of operator matrices corresponding to the desired initial state. To mimic the situation in an optically excited semiconductor intended for single photon production, we choose the state corresponding to a single excited electron, $|\psi_0\rangle = |3\rangle$.

We will start by considering the correlation functions on the second and third line of eq. (A.7), containing an uneven number of photon operators inside the brackets. It can be shown explicitly by multiplying all the various matrices and in the end taking the $\langle 3|\cdots|3\rangle$ element, that both brackets of single and three photon operators are identically zero for all times. None of the other terms in $G_{34}^{(2)}(t_3, t_4)$ are identically zero, but we have still achieved a major simplification and we are down to brackets of two and four photon operators

$$G_{34}^{(2)}(t_3,t_4) = \underbrace{\langle a^\dagger(t_3)a(t_3)\rangle\,\langle a^\dagger(t_4)a(t_4)\rangle - \langle a^\dagger(t_3)a(t_4)\rangle\,\langle a^\dagger(t_4)a(t_3)\rangle}_{\text{single-particle contributions}} + \underbrace{\langle a^\dagger(t_3)a^\dagger(t_4)a(t_4)a(t_3)\rangle}_{\text{two-particle contributions}}. \tag{A.12}$$

The correlation function with four operators constitutes a two-particle Green's function, which is a much more difficult object to handle than the correlation functions with two photon operators, single-particle Green's functions. Due to this fact we are interested in examining the importance of the two-particle Green's function contributions, relative to the contributions from the one-particle Green's functions.

To start off the discussion of the last remaining terms in $G^{(2)}_{34}(t_3,t_4)$, it is useful to mention a few properties of the JCM in the RWA. When applying the RWA to the JCM Hamiltonian we remove the term $\hbar g(c_2^\dagger c_1 a^\dagger + c_1^\dagger c_2 a)$, as this corresponds to the creation of virtual photons, see [44, p. 196]. The justification for performing the RWA, rests on the assumption that coupling energy $\hbar g$ is small compared to the transition energies of the free system, i.e. $\hbar\omega$ and $\hbar(\omega_2-\omega_1)$. This is certainly the case for present semiconductor nanostructures [82]. Applying the RWA has the consequence that the elements H_{14} and H_{41} of the Hamiltonian become zero, which leads to a new matrix form of H

$$H=\begin{bmatrix}\hbar\omega_1 & 0 & 0 & 0 & 0\\ 0 & \hbar(\omega_1+\omega) & \hbar g & 0 & 0\\ 0 & \hbar g & \hbar\omega_2 & 0 & 0\\ 0 & 0 & 0 & \hbar(\omega_2+\omega) & \sqrt{2}\hbar g\\ 0 & 0 & 0 & \sqrt{2}\hbar g & \hbar(\omega_1+2\omega)\end{bmatrix}.$$

It is clearly seen that the new system consists of three independent subsystems, which do not mix due to the RWA. For this Hamiltonian all correlation functions, except those composed of single-particle Green's functions, are identically zero for all times. On the basis of this, one could therefore expect that the contributions from $\langle a^\dagger(t_3)a^\dagger(t_4)a(t_4)a(t_3)\rangle$ would become negligible for small g for the full JCM. However, it was found not to be the case. For the following set of parameters[3]: $\hbar\omega_2=2\hbar\omega_1=2\hbar\omega=2.64$ eV and $\hbar g=85$ μeV, the single- and two-particle contributions in eq. (A.12) were of the same order of magnitude. However, the absolute value of the single-particle Green's functions was much larger than for the two-particle Green's functions . This picture did not change for even lower g, down to $\hbar g=15$ μeV. To be able to see the expected behavior, the bare basis was extended by the following two basis states

$$|6\rangle=|0,1;2\rangle=c_2^\dagger\frac{(a^\dagger)^2}{\sqrt{2}}|0\rangle,$$
$$|7\rangle=|1,0;3\rangle=c_1^\dagger\frac{(a^\dagger)^3}{\sqrt{3!}}|0\rangle,$$

thereby allowing for the creation of another pair of virtual photons, breaking the strict energy conservation by $2\hbar\omega$. This enlargement of the basis did not cause any visible changes in the single-particle contributions, but it did cause small changes in the two-particle contributions, not in magnitude but rather shifting various oscillations in the two-time plane. It was indeed expected that the inclusion of more virtual photons would change the two-particle contributions, but not have much effect on the single-particle ones. Due to this observation and the strong expectation that enough virtual photon processes[4] and sufficiently low g will cause us to reach the RWA limit of vanishing two-particle contributions, we will assume that the two-particle contributions in $G^{(2)}_{34}(t_3,t_4)$ can be neglected.

A.3. From $\boldsymbol{A}\cdot\boldsymbol{p}$ to $\boldsymbol{d}\cdot\boldsymbol{E}_{\mathrm{T}}$ interaction

In this appendix we will rewrite the electron-photon interaction from the $\boldsymbol{A}\cdot\boldsymbol{p}$ to the $\boldsymbol{D}\cdot\boldsymbol{E}_{\mathrm{T}}$ form. To do this we employ a relatively simple heuristic approach, more rigorous methods [31, 43, 46] can be used involving unitary transformations but the result is basically the same, hence we will use the more transparent simple approach. We consider the $\boldsymbol{A}\cdot\boldsymbol{p}$ interaction between a classical field[5] and a single electron in the electric dipole approximation

$$H_{\mathrm{i}}=\frac{e}{m}\boldsymbol{A}(0)\cdot\boldsymbol{p}.$$

[3] Representative for present day semiconductor nanostructures, see [82].

[4] Enough virtual photon processes could mean taking certain processes to infinite order and would therefore not be practically possible in the present approach of diagonalizing a Hamiltonian matrix.

[5] Basically the same argument can be performed with a quantized field of the form $\boldsymbol{E}_{\mathrm{T}}(0)=\frac{\boldsymbol{E}_0}{2}(a^\dagger+a)$.

To connect the two different forms a relation between the momentum, $\boldsymbol{p}$ and position, $\boldsymbol{r}$, is needed. This is found by using the definition of momentum [31, p. 26] as the time derivative of the position times the (free) mass of the electron

$$\boldsymbol{p} = m\partial_t \boldsymbol{r} = \frac{m}{i\hbar}\left[\boldsymbol{r}, H_0\right],$$

where H_0 is the single-electron Hamiltonian, whose eigenstates we use as basis $H_0\left|n\right\rangle = \hbar\omega_n\left|n\right\rangle$. We proceed by taking an arbitrary matrix element of H_{i}

$$\langle j|H_{\mathrm{i}}|k\rangle = \frac{e}{m}\boldsymbol{A}(0)\cdot\langle j|\boldsymbol{p}|k\rangle = \frac{e}{m}\boldsymbol{A}(0)\cdot\left\{\langle j|\frac{m}{i\hbar}\left(\boldsymbol{r}H_0 - H_0\boldsymbol{r}\right)|k\rangle\right\} = -i\omega_{jk}\boldsymbol{D}_{jk}\cdot\boldsymbol{A}(0), \tag{A.13}$$

where $\omega_{jk} = \omega_j - \omega_k$ and $\boldsymbol{D} = -e\boldsymbol{r}$ is the electrons dipole. The connection between $\boldsymbol{A}$ and $\boldsymbol{E}_{\mathrm{T}}$ is given by the gauge relation eq. (3.3)

$$\boldsymbol{E}_{\mathrm{T}}(0,t) = -\partial_t\boldsymbol{A}(0,t) \Rightarrow \boldsymbol{A}(0,t) = -\int d\tilde{t}\boldsymbol{E}_{\mathrm{T}}(0,\tilde{t}).$$

Assuming that we have a classical electric field for which dominating time-dependence is given by

$$\boldsymbol{E}_{\mathrm{T}}(0,t) = \frac{\boldsymbol{E}_0}{2}(e^{i\omega t} + e^{-i\omega t}),$$

the corresponding vector potential becomes

$$\boldsymbol{A}(0,t) = -\frac{\boldsymbol{E}_0}{i\omega 2}(e^{i\omega t} - e^{-i\omega t}).$$

Inserting this into the matrix elements above yields

$$\langle j|H_{\mathrm{i}}|k\rangle = \frac{\omega_{jk}}{\omega}\boldsymbol{D}_{jk}\cdot\frac{\boldsymbol{E}_0}{2}(e^{i\omega t} - e^{-i\omega t}).$$

To show that these matrix elements are identical to those of $H_{\mathrm{i}} = -\boldsymbol{D}\cdot\boldsymbol{E}_{\mathrm{T}}$, and hence that it is the same operator, we consider the cases $\omega_{jk} > 0$ and $\omega_{jk} < 0$ separately. The case $\omega_{jk} > 0$ corresponds to the excitation of the electron, and hence the dominating contribution will come from the term where a photon is absorbed, so that

$$\langle j|H_{\mathrm{i}}|k\rangle \approx -\frac{\omega_{jk}}{\omega}\boldsymbol{D}_{jk}\cdot\frac{\boldsymbol{E}_0}{2}e^{-i\omega t}. \tag{A.14}$$

The case $\omega_{jk} < 0 \Rightarrow \omega_{jk} = -\omega_{kj}$ corresponds to the deexcitation of the electron, and therefore the dominating contribution comes from the term where a photon is emitted yielding

$$\langle j|H_{\mathrm{i}}|k\rangle \approx -\frac{\omega_{kj}}{\omega}\boldsymbol{D}_{jk}\cdot\frac{\boldsymbol{E}_0}{2}e^{i\omega t}. \tag{A.15}$$

For both cases we consider only the resonant part of the interaction, so that the fraction containing the transition frequency and field frequency is very close to unity. This completes the derivation and we have shown that the $\boldsymbol{A}\cdot\boldsymbol{p}$ and $\boldsymbol{D}\cdot\boldsymbol{E}_{\mathrm{T}}$ interactions are identical within the approximations used above. Considering only resonant contributions in the electron-photon interaction is commonly known as the rotating-wave approximation (RWA), thus in order for the arguments stated in this appendix to hold, the RWA should be applied in every electron-photon interaction Hamiltonian. The more advanced derivations referred to in the beginning, do however not make use of the RWA to prove equivalence between the two forms, hence using the $\boldsymbol{D}\cdot\boldsymbol{E}_{\mathrm{T}}$ interaction and not applying the RWA will still be a consistent choice.

A possible issue should be noted regarding the current approach. The unitary transformation applied in the references [46, p. 636] generates a dipole-dipole interaction of the form $\boldsymbol{D}\cdot\boldsymbol{D}$ in the transformed Hamiltonian, which does not appear in our derivation performed above. This indicates that the approximations we have used correspond to neglecting this dipole-dipole interaction. The validity of this approximation can be assessed by comparing two review articles written by the same main authors [25, 83]. In the oldest article the dipole-dipole term is kept in the calculations, whereas in the more recent article this term has been neglected. The calculations were performed on semiconductor nanostructures comparable to those we are considering, indicating that the neglection of the dipole-dipole interaction is hopefully justified.

A.4. Numerics

The numerical methods for solving the equations of motion of the Green's functions are an extremely important aspect of performing many-body simulations. This is due to the often huge computations that need to be performed and choosing the wrong method can easily result in several orders of magnitude longer computation time. Of similar importance is how the algorithms are implemented on a computer system, we will however not describe this part of the project. For the above reason we will briefly describe different methods used in the numerical solution of our equations.

The differential equations we need to solve are all of the following general form

$$\partial_t u(t) = g(t) + \int_{-\infty}^{t} dt' k(t,t')u(t') = f(t), \tag{A.16}$$

where for simplicity we write it is a scalar, generalization to a more general matrix form is straight-forward. In the above differential equation $u(t)$ is function we solve for, $g(t)$ is some general function, and the last term is a memory integral with a memory kernel $k(t,t')$. In the following we will denote the entire RHS as a single source term $f(t)$.

The goal in numerics is to achieve as high a degree of computational efficiency as possible, i.e. obtain a sufficiently accurate solution in the least amount of time, which is what guides ones choice of method. Accuracy is generally obtained through the use of high order methods, while the time consumption is kept low by minimizing the number of function evaluations. We are not in search of extremely accurate solutions, but we do have the rather special problem that our source term $f(t)$ is often very expensive to evaluate. This is due to the presence of many sums in the self-energies and especially the memory integral over the past. Fortunately there exists a class of methods known as linear multistep or Adams methods, that are designed to minimize the number of source evaluations, while still being available to high order. For our type of problem a specific set of schemes have proved themselves useful [26, p. 284], these are known as predictor-corrector (PC) schemes. A particular choice is the so-called Adams-Bashforth-Moulton (ABM) procedure [84, p. 943] which is a third order method. The time-stepping formulas are given by two contributions, a predictor and a corrector part

$$\text{predictor}: \quad u_{n+1} = u_n + \frac{h}{12}(23f_n - 16f_{n-1} + 5f_{n-2}) + \mathcal{O}(h^4), \tag{A.17}$$

$$\text{corrector}: \quad u_{n+1} = u_n + \frac{h}{12}(5f_{n+1} + 8f_n - f_{n-1}) + \mathcal{O}(h^4). \tag{A.18}$$

In these formulas h is the distance between two consecutive time discretization points, the integer n refers to the discrete time axis, and $\mathcal{O}(h^{p+1})$ is an order of magnitude error term with p being the order of the method. The predictor part is an explicit method in that u_{n+1} only depends on quantities at previous times, whereas the corrector part is an implicit method as u_{n+1} depends on the source term at the present time $n+1$. The reason for combining these two methods is that the explicit predictor is easy to implement but has bad stability properties, while the implicit method is difficult[6] to implement but has good stability properties. The strategy is then to calculate an initial estimate of u_{n+1} using the predictor, and then calculate a better estimate using the corrector, using at each n the predictor guess to evaluate the unknown source f_{n+1}. This procedure can be repeated many times, but usually only a single iteration is performed, the rather subtle reason for this is explained in [84, p. 944]. The great advantage of Adams methods is, as mentioned, that it minimizes the number of source evaluations needed. This can be realized by considering the RHS of eqs. (A.18) and (A.17) where reference is to previous grid points only (except for f_{n+1} in the predictor), meaning that these evaluations can be reused by employing a bit of bookkeeping. This is in contrast to e.g. high order Runge-Kutta methods, where several intermediate source evaluations are needed in between the actual grid points. The memory of the Adams method is in general an advantage, but it does cause some problems for the first few initial steps of the algorithm,

[6] Eq. (A.18) is actually an implicit equation in u_{n+1}, through f_{n+1}, that would have to be solved somehow, which would be very time consuming.

as basically one has to known the solution in the first few grid points in order to start the time stepping. This is not a problem for the non-equilibrium simulations performed in chapter 6, where prior to the arrival of the excitation pulse the solution is known and all source terms are zero. For the simulations of the retarded Green's function performed in section 5.3 we are however not that fortunate, and we have to apply some other method to solve the problem or somehow obtain the solution in first few grid points. One solution is to use the most simple of all the Adams methods, namely the well-known Euler formulae

$$u_{n+1} = u_n + hf_n + \mathcal{O}(h^2).$$

Being a first order method a very small h is often needed in order to obtain a desired accuracy, hence solution of the full problem using the Euler scheme is often not feasible. An alternative strategy is to use the Euler scheme to obtain the solution in the grid points needed to initiate the PC ABM procedure and subsequently use this method, with a feasible h, for the rest of the time stepping. This strategy has been applied whenever needed. A more serious drawback of the Adams is the fact that they rely on equidistant time grids, thus making adaptive time grids difficult to implement.

During the implementation and testing of the PC ABM procedure, the numerical solution was for some situations found to be subjected to numerical dispersion, that is damping of the solution not related to any physical damping mechanisms but purely due to the numerical method. The numerical dispersion was however only an issue during time spans when energy was being put into the system through the excitation pulse, after the pulse had passed no significant numerical dispersion was observed. This could become a serious issue for certain excitation conditions that occur over long periods of time, e.g. continuous wave excitation, but for our system where only short pulses are considered it was no practical problem.

So far we discussed the solution of eq. (A.16) assuming that the source term could be evaluated without any special effort, this is not the case as an integral has to be evaluated. The memory kernel and solution are both discrete functions, hence one of the easiest and most intuitive ways of performing the integral, would be using the trapezoid rule [84]

$$\int_{hn}^{h(n+1)} dtu(t) = \frac{h}{2}(u_n + u_{n+1}) + \mathcal{O}(h^3),$$

as it integrates piecewise linear functions exactly. Being a second order method one could speculate whether using the trapezoid rule for calculating the source term, would ruin the advantage of using the third order ABM method for the time stepping, as the second order method in principle should introduce a larger error than the third order in each time step. To test this the Simpson's rule [84]

$$\int_{hn}^{h(n+2)} dtu(t) = \frac{h}{3}(u_n + 4u_{n+1} + u_{n+2}) + \mathcal{O}(h^5),$$

which is of fourth order was tested, but turned out to yield the same result as using the trapezoid rule. For this reason the trapezoid rule was used in the simulations, as it has the advantage of being able to integrate both an even and odd number of grid points, as oppose to the Simpson rule which can only integrate an odd number.

A.5. Self-energies

In this appendix we will derive the self-energies to be used in this thesis. To keep the theory as simple as possible only lowest order self-energies will be considered, which means that the self-energy can be identified from the second non-zero term in the expansion of the contour ordered Green's functions, see eq. (2.22),

$$G_{\alpha\beta}(\tau,\tau') = G^0_{\alpha\beta}(\tau,\tau') + \int_C d\tau_2 d\tau_1 \sum_{\alpha_1\beta_1} G^0_{\alpha\beta_1}(\tau,\tau_2)\Sigma^{(1)}_{\beta_1\alpha_1}(\tau_2,\tau_1)G^0_{\alpha_1\beta}(\tau_1,\tau') + \cdots \tag{A.19}$$

The superscript on the self-energy signifies that this is a lowest/first order self-energy. It should be noted that this approach for obtaining the self-energy can be applied for both fermions and bosons, as long as the Green's function is defined according to eq. (2.19). All the self-energies derived in this appendix will be made self-consistent, in the sense that all free Green's functions appearing will be replaced by the corresponding full Green's functions, $G^0 \to G$, except for the phonons which are treated as a reservoir. The procedure for making the self-energy self-consistent, is to include a wide enough subclass of diagrams into $\Sigma^{(1)}_{\beta_1\alpha_1}(\tau_2, \tau_1)$ in eq. (A.19), until one can replace all free Green's functions with the corresponding full ones. This has the consequence that the self-consistent self-energy has infinite many terms, whereas the corresponding non-self-consistent self-energy only has a single term. This is illustrated for a Fock type self-energy in figure A.3, where all terms up to third order are shown and a few of fourth order. The self-consistent scheme ensures that the different subsystems couple and also that the self-energies satisfy important physical conservation laws, such as particle number [85]. The physical justifications, and limitations, for only considering lowest order self-energies are given in the main text, see section 5.2.2, hence this appendix will only present the formal details with the physics postponed.

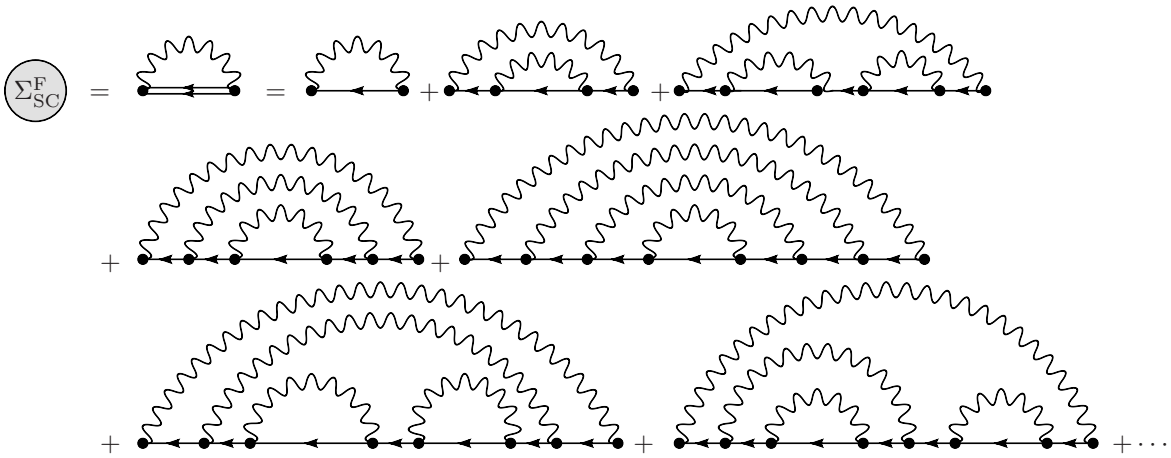

Figure A.3.: *Diagrams illustrating a self-consistent Fock self-energy for electrons interacting with phonons.*

Below we will go through the self-energies arising from the various interactions presented in generic form in section 3.2.3. The following symbols will be used to the denote the various Green's functions: G for electrons, A for photons, and D for phonons. Their diagrammatic counterparts are shown in figure A.4.

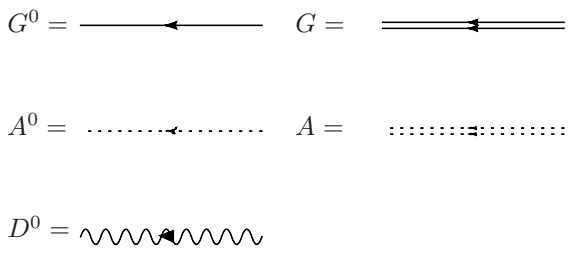

Figure A.4.: *Diagrams used for the various Green's functions; G is for electrons, A is for photons, and D is for phonons.*

Excitation pulse

The semi-classical interaction between the electrons and the classical excitation pulse is given eq. (3.21)

$$U(t) = \sum_{\nu\nu'} d_{\nu\nu'} E_{\mathrm{cl}}(t) c^\dagger_\nu c_{\nu'}.$$

According to eq. (2.22) the first two terms in the expansion of the electron Green's function are given by

$$\begin{aligned} G_{\nu\nu'}(\tau,\tau') &= G^0_{\nu\nu'}(\tau,\tau') + (-i\hbar^{-1})^2 \int_C d\tau_1 \, \langle T_C\{\hat{U}(\tau_1)\hat{c}_\nu(\tau)\hat{c}^\dagger_{\nu'}(\tau')\}\rangle_{0,\mathrm{con}} + \cdots \\ &= G^0_{\nu\nu'}(\tau,\tau') + \int_C d\tau_1 \sum_{\nu_1\nu_1'} d_{\nu_1\nu_1'} E_{\mathrm{cl}}(\tau_1)(-i\hbar^{-1})^2 \, \langle T_C\{\hat{c}^\dagger_{\nu_1}(\tau_1)\hat{c}_{\nu_1'}(\tau_1)\hat{c}_\nu(\tau)\hat{c}^\dagger_{\nu'}(\tau')\}\rangle_{0,\mathrm{con}} + \cdots \end{aligned}$$

Wick's theorem, eq. (2.21), can now be applied to the two-particle Green's function in the second term above, this results in a connected and a disconnected diagram. Keeping only the connected diagram yields for the second term

$$\int_C d\tau_1 \sum_{\nu_1\nu_1'} G^0_{\nu\nu_1}(\tau,\tau_1) \left[d_{\nu_1\nu_1'} E_{\mathrm{cl}}(\tau_1)\right] G^0_{\nu_1'\nu'}(\tau_1,\tau'),$$

comparing to eq. (A.19) we can identify the (singular) self-energy as the content of the square brackets

$$U_{\nu_1\nu_1'}(\tau_1) = d_{\nu_1\nu_1'} E_{\mathrm{cl}}(\tau_1). \tag{A.20}$$

It should be noted that as this interaction is a one-body interaction, it does not generate anymore terms to its self-energy and is therefore treated exactly. A diagrammatic representation is shown in figure A.5.

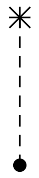

Figure A.5.: *Diagram used for the singular self-energy eq.* (A.20).

Electron-electron

The Coulomb interaction between the electrons is given by eq. (3.17)

$$H_{\mathrm{e-e}} = \frac{1}{2} \sum_{\substack{\nu_1\nu_2 \\ \nu_3\nu_4}} V_{\nu_4\nu_3,\nu_1\nu_2} c^\dagger_{\nu_4} c^\dagger_{\nu_3} c_{\nu_2} c_{\nu_1}.$$

The first two terms in the expansion of the electron Green's function are given by

$$G_{\nu\nu'}(\tau,\tau') = G^0_{\nu\nu'}(\tau,\tau') + (-i\hbar^{-1})^2 \int_C d\tau_1 \, \langle T_C\{\hat{H}_{\mathrm{e-e}}(\tau_1)\hat{c}_\nu(\tau)\hat{c}^\dagger_{\nu'}(\tau')\}\rangle_{0,\mathrm{con}} + \cdots$$

For the second term we further get

$$\int_C d\tau_1 \frac{(-i\hbar^{-1})^{-1}}{2} \sum_{\substack{\nu_1\nu_2 \\ \nu_3\nu_4}} V_{\nu_4\nu_3,\nu_1\nu_2} (-i\hbar^{-1})^3 \, \langle T_C\{\hat{c}^\dagger_{\nu_4}(\tau_1)\hat{c}^\dagger_{\nu_3}(\tau_1)\hat{c}_{\nu_2}(\tau_1)\hat{c}_{\nu_1}(\tau_1)\hat{c}_\nu(\tau)\hat{c}^\dagger_{\nu'}(\tau')\}\rangle_{0,\mathrm{con}}.$$

Applying Wick's theorem to the three-particle Green's function we obtain six diagrams, two of which are disconnected, and therefore disregarded, and four connected diagrams. Of the four connected diagrams there are only two that are topologically different, each occurring in pairs, hence the "double counting" $\frac{1}{2}$ factor cancels. For the first connected diagram we get

$$\int_C d\tau_1 \sum_{\nu_1\nu_4} G^0_{\nu\nu_4}(\tau,\tau_1)\left[-i\hbar\sum_{\nu_2\nu_3} V_{\nu_4\nu_3,\nu_1\nu_2} G^0_{\nu_2\nu_3}(\tau_1,\tau_1^+)\right] G^0_{\nu_1\nu'}(\tau_1,\tau'),$$

where $\tau_1^+ = \tau_1 + 0^+$ so that $\tau_1^+ >_C \tau_1$. This interpretation of the equal-time contour ordered Green's function, $G^0_{\nu\nu'}(\tau,\tau)$, as slightly contour time shifted, $G^0_{\nu\nu'}(\tau,\tau^+)$, is necessary to make sure that the operators in the Hamiltonian are ordered correctly, i.e. that creation operators stand to the left of annihilation operators[7]. This has the consequence that $G^0_{\nu\nu'}(\tau,\tau^+)$ becomes an equal-time lesser Green's functions $G^{0,<}_{\nu\nu'}(t,t)$ no matter where τ is located on the Keldysh contour. The self-consistent self-energy can now be identified as

$$\Sigma^{\mathrm{e-e,H}}_{\nu_4\nu_1}(\tau_1) = -i\hbar\sum_{\nu_2\nu_3} V_{\nu_4\nu_3,\nu_1\nu_2} G_{\nu_2\nu_3}(\tau_1,\tau_1^+),$$

which is usually called the Hartree self-energy or direct interaction. The second connected diagram yields

$$\int_C d\tau_1 \sum_{\nu_2\nu_4} G^0_{\nu\nu_4}(\tau,\tau_1)\left[i\hbar\sum_{\nu_1\nu_3} V_{\nu_4\nu_3,\nu_1\nu_2} G^0_{\nu_1\nu_3}(\tau_1,\tau_1^+)\right] G^0_{\nu_2\nu'}(\tau_1,\tau'),$$

from which we get the self-consistent self-energy

$$\Sigma^{\mathrm{e-e,F}}_{\nu_4\nu_2}(\tau_1) = i\hbar\sum_{\nu_1\nu_3} V_{\nu_4\nu_3,\nu_1\nu_2} G_{\nu_1\nu_3}(\tau_1,\tau_1^+),$$

this self-energy is usually called the Fock self-energy or exchange interaction. These two contributions look formally quite similar and by interchanging ν_1 and ν_2 in the Fock part they can be collected into the well known Hartree-Fock self-energy

$$\Sigma^{\mathrm{e-e,HF}}_{\nu_4\nu_1}(\tau_1) = i\hbar\sum_{\nu_2\nu_3} \left(V_{\nu_4\nu_3,\nu_2\nu_1} - V_{\nu_4\nu_3,\nu_1\nu_2}\right) G_{\nu_2\nu_3}(\tau_1,\tau_1^+). \tag{A.21}$$

A diagrammatic representation is shown in figure A.6.

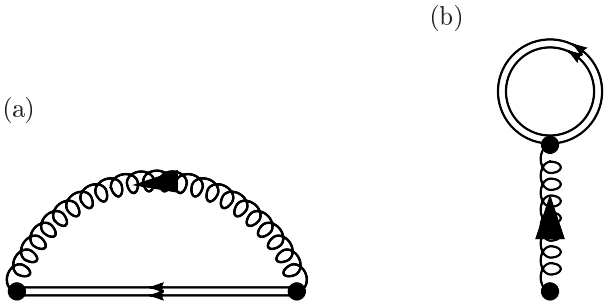

Figure A.6.: *Diagrams used for (a) the Coulomb Fock self-energy and (b) the Coulomb Hartree self-energy, see eq.* (A.21).

[7] See e.g. [24, p. 97-98] or [28, p. 227]

Electron-photon

The interaction between the electrons and photons is given by eq. (3.19)

$$H_{\mathrm{e-rad}} = \sum_{\nu\nu' m} \hbar g^m_{\nu\nu'} c^\dagger_\nu c_{\nu'} (a^\dagger_m + a_m).$$

The first three terms in the electronic Green's function are

$$G_{\nu\nu'}(\tau,\tau') = G^0_{\nu\nu'}(\tau,\tau') + (-i\hbar^{-1})^2 \int_C d\tau_1 \left\langle T_C\{\hat{H}_{\mathrm{e-rad}}(\tau_1)\hat{c}_\nu(\tau)\hat{c}^\dagger_{\nu'}(\tau')\}\right\rangle_{0,\mathrm{con}} + \frac{(-i\hbar^{-1})^3}{2!}\int_C d\tau_1 d\tau_2 \left\langle T_C\{\hat{H}_{\mathrm{e-rad}}(\tau_1)\hat{H}_{\mathrm{e-rad}}(\tau_2)\hat{c}_\nu(\tau)\hat{c}^\dagger_{\nu'}(\tau')\}\right\rangle_{0,\mathrm{con}} + \cdots$$

The second term in this expansion is identically zero due to the fact that the electron-photon interaction does not conserve the number photons. More specifically one gets terms of the form $\langle c^\dagger_1 c_2 c_3 c^\dagger_3 (a^\dagger + a)\rangle_0$, which can be factored into an electron and a photon part, $\langle c^\dagger_1 c_2 c_3 c^\dagger_4\rangle_0 \langle a^\dagger + a\rangle_0$, as H_0 for the electrons and photons commute. The photon factor is identically zero as the brackets denote thermal averaging, where each contribution to the trace has the same number of photons in it. This has the consequence that one has to go to second order in the interaction Hamiltonian to obtain a non-zero contribution. The second order term becomes

$$\int_C d\tau_1 d\tau_2 \sum_{\substack{\nu_1\nu'_1 m_1\\ \nu_2\nu'_2 m_2}} (-i\hbar^{-1})^{-1}\hbar g^{m_1}_{\nu_1\nu'_1}\hbar g^{m_2}_{\nu_2\nu'_2}(-i\hbar^{-1}) \left\langle T_C\{\left[\hat{a}^\dagger_{m_1}(\tau_1) + \hat{a}_{m_1}(\tau_1)\right]\left[\hat{a}^\dagger_{m_2}(\tau_2) + \hat{a}_{m_2}(\tau_2)\right]\}\right\rangle_0 \times \frac{1}{2!}(-i\hbar^{-1})^3 \left\langle T_C\{\hat{c}^\dagger_{\nu_1}(\tau_1)\hat{c}_{\nu'_1}(\tau_1)\hat{c}^\dagger_{\nu_2}(\tau_2)\hat{c}_{\nu'_2}(\tau_2)\hat{c}_\nu(\tau)\hat{c}^\dagger_{\nu'}(\tau')\}\right\rangle_{0,\mathrm{con}}.$$

In the photon bracket on the first line it would be natural to simply define the entire object as the photon Green's function, as is usually done for phonons (see last part of this section). However to set the stage for solving the Dyson equation for the photon Green's functions, we choose to write out the big bracket into two Green's functions of the usual form $A_{m_1m_2}(\tau_1,\tau_2) = -i\hbar^{-1}\langle T_C\left\{a_{m_1}(\tau_1)a^\dagger_{m_2}(\tau_2)\right\}\rangle$. We do however keep the symbol $\mathcal{A}$ for the sum for notational reasons, hence we write

$$\begin{aligned}\mathcal{A}^0_{m_1m_2}(\tau_1,\tau_2) &= -i\hbar^{-1}\left\langle T_C\{\left[\hat{a}^\dagger_{m_1}(\tau_1) + \hat{a}_{m_1}(\tau_1)\right]\left[\hat{a}^\dagger_{m_2}(\tau_2) + \hat{a}_{m_2}(\tau_2)\right]\}\right\rangle_0 \\ &= A^0_{m_1m_2}(\tau_1,\tau_2) + A^0_{m_2m_1}(\tau_2,\tau_1).\end{aligned}$$

It should be noted that this relation does not hold for a general non-thermal state, as in this case terms like $\langle a^\dagger a^\dagger\rangle$ and $\langle aa\rangle$ are not necessarily zero. The three-particle electron Green's function is evaluated using Wick's theorem and yields two disconnected diagrams, that are disregarded, and four connected diagrams. As in the electron-electron case only two of these diagrams are topologically different, canceling the $\frac{1}{2!}$ factor. The first connected contribution to the second order term is

$$\int_C d\tau_1 \sum_{\nu_1\nu'_1} G^0_{\nu\nu_1}(\tau,\tau_1)\left[-i\hbar\int_C d\tau_2 \sum_{\substack{m_1m_2\\ \nu_2\nu'_2}} \hbar g^{m_1}_{\nu_1\nu'_1}\hbar g^{m_2}_{\nu_2\nu'_2} G^0_{\nu'_2\nu_2}(\tau_2,\tau_2^+)\mathcal{A}^0_{m_1m_2}(\tau_1,\tau_2)\right] G^0_{\nu'_1\nu'}(\tau_1,\tau'),$$

where the self-energy can then be identified as the content of the square brackets. This self-energy is usually called the Hartree part, due to its diagrammatical similarity to the Hartree part for the electron-electron interaction and the self-consistent version is given by

$$\Sigma^{\mathrm{e-rad,H}}_{\nu_1\nu'_1}(\tau_1) = -i\hbar\int_C d\tau_2 \sum_{\substack{m_1m_2\\ \nu_2\nu'_2}} \hbar g^{m_1}_{\nu_1\nu'_1}\hbar g^{m_2}_{\nu_2\nu'_2} G_{\nu'_2\nu_2}(\tau_2,\tau_2^+)\mathcal{A}_{m_1m_2}(\tau_1,\tau_2). \tag{A.22}$$

As we integrate over τ_2 this self-energy becomes singular and will therefore not cause any relaxation or dephasing, but will only act as an instantaneous renormalization quantity. The second connected contribution is the following

$$\int_C d\tau_1 d\tau_2 \sum_{\nu_1\nu_2'} G^0_{\nu\nu_1}(\tau,\tau_1)\left[i\hbar \sum_{\substack{m_1m_2\\ \nu_2\nu_1'}} \hbar g^{m_1}_{\nu_1\nu_1'}\hbar g^{m_2}_{\nu_2\nu_2'} G^0_{\nu_1'\nu_2}(\tau_1,\tau_2)\mathcal{A}^0_{m_1m_2}(\tau_1,\tau_2)\right] G^0_{\nu_2'\nu'}(\tau_2,\tau'),$$

where the self-consistent self-energy, usually called the Fock part again due to its diagrammatical appearance, can be identified and is given by

$$\Sigma^{\mathrm{e-rad,F}}_{\nu_1\nu_2'}(\tau_1,\tau_2) = i\hbar \sum_{\substack{m_1m_2\\ \nu_2\nu_1'}} \hbar g^{m_1}_{\nu_1\nu_1'}\hbar g^{m_2}_{\nu_2\nu_2'} G_{\nu_1'\nu_2}(\tau_1,\tau_2)\mathcal{A}_{m_1m_2}(\tau_1,\tau_2). \tag{A.23}$$

For diagrammatic illustrations of these contributions to the self-energy see figure A.7.

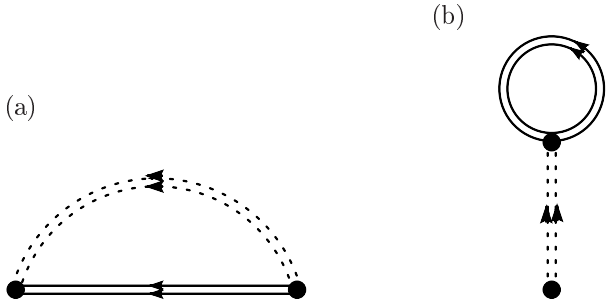

Figure A.7.: *Diagrams used for the electron-photon interaction, where (a) is the Fock-type self-energy and (b) is the Hartree-type self-energy, see eqs. (A.23) and (A.22) respectively.*

In practise we will employ the RWA in the interaction Hamiltonian between the electrons and photons that is given by eq. (5.6)

$$H_{\mathrm{e-rad}} = \sum_{\alpha\alpha' m} \hbar g^m_{\alpha\alpha'}(c^\dagger_{\mathrm{c},\alpha}c_{\mathrm{v},\alpha'}a_m + a^\dagger_m c^\dagger_{\mathrm{v},\alpha}c_{\mathrm{c},\alpha'}). \tag{A.24}$$

The above derivation can be repeated for this Hamiltonian and the result for the Fock contribution is

$$\begin{aligned}\Sigma^{bb',\mathrm{e-rad,F}}_{\alpha_1\alpha_2'}(\tau_1,\tau_2) = i\hbar \sum_{\substack{m_1m_2\\ \alpha_2\alpha_1'}} \hbar g^{m_1}_{\alpha_1\alpha_1'}\hbar g^{m_2}_{\alpha_2\alpha_2'} \\ \times \left\{G^{\mathrm{vv}}_{\alpha_1'\alpha_2}(\tau_1,\tau_2)A_{m_1m_2}(\tau_1,\tau_2)\delta_{b,\mathrm{c}} + G^{\mathrm{cc}}_{\alpha_1'\alpha_2}(\tau_1,\tau_2)A_{m_2m_1}(\tau_2,\tau_1)\delta_{b,\mathrm{v}}\right\}\delta_{b,b'},\end{aligned} \tag{A.25}$$

while for the Hartree contribution we get

$$\begin{aligned}\Sigma^{bb',\mathrm{e-rad,H}}_{\alpha_1\alpha_1'}(\tau_1) = -i\hbar\int_C d\tau_2 \sum_{\substack{m_1m_2\\ \alpha_2\alpha_2'}} \hbar g^{m_1}_{\alpha_1\alpha_1'}\hbar g^{m_2}_{\alpha_2\alpha_2'} \\ \times \left\{G^{\mathrm{cv}}_{\alpha_2'\alpha_2}(\tau_2,\tau_2^+)A_{m_1m_2}(\tau_1,\tau_2)\delta_{b,\mathrm{c}}\delta_{b',\mathrm{v}} + G^{\mathrm{vc}}_{\alpha_2'\alpha_2}(\tau_2,\tau_2^+)A_{m_2m_1}(\tau_2,\tau_1)\delta_{b,\mathrm{v}}\delta_{b',\mathrm{c}}\right\}.\end{aligned} \tag{A.26}$$

We note that due to the selection rules of g and the application of the RWA, the Fock self-energy is purely diagonal in the band indices and the Hartree self-energy is purely off-diagonal in the band indices.

Photon-electron

In the previous section we calculated the self-energy of the electrons due to the interaction with the photons, here we determine the self-energy of the photons arising from the interaction with the electrons. This means that it is of course the same interaction Hamiltonian, but now we consider the photon Green's function to second order

$$A_{mm'}(\tau,\tau') = A^0_{mm'}(\tau,\tau') + (-i\hbar^{-1})^2 \int_C d\tau_1 \, \langle T_C\{\hat{H}_{\mathrm{e-rad}}(\tau_1)\hat{a}_m(\tau)\hat{a}^\dagger_{m'}(\tau')\}\rangle_{0,\mathrm{con}} + \\ \frac{(-i\hbar^{-1})^3}{2!}\int_C d\tau_1 d\tau_2 \, \langle T_C\{\hat{H}_{\mathrm{e-rad}}(\tau_1)\hat{H}_{\mathrm{e-rad}}(\tau_2)\hat{a}_m(\tau)\hat{a}^\dagger_{m'}(\tau')\}\rangle_{0,\mathrm{con}} + \cdots$$

The first order term is zero due to basically the same reason as above, i.e. after factorization of the electron and photon brackets, we obtain terms like $\langle aaa^\dagger\rangle_0$ and $\langle a^\dagger aa^\dagger\rangle_0$ which are identically zero. For the second order term we get

$$\int_C d\tau_1 d\tau_2 \sum_{\substack{\nu_1\nu_1' m_1 \\ \nu_2\nu_2' m_2}} (-i\hbar^{-1})^{-1}\hbar g^{m_1}_{\nu_1\nu_1'}\hbar g^{m_2}_{\nu_2\nu_2'}(-i\hbar^{-1})^2 \, \langle T_C\{\hat{c}^\dagger_{\nu_1}(\tau_1)\hat{c}_{\nu_1'}(\tau_1)\hat{c}^\dagger_{\nu_2}(\tau_2)\hat{c}_{\nu_2'}(\tau_2)\}\rangle_{0,\mathrm{con}} \\ \times \frac{1}{2!}(-i\hbar^{-1})^2 \, \langle T_C\{\left[\hat{a}^\dagger_{m_1}(\tau_1)+\hat{a}_{m_1}(\tau_1)\right]\left[\hat{a}^\dagger_{m_2}(\tau_2)+\hat{a}_{m_2}(\tau_2)\right]\hat{a}_m(\tau)\hat{a}^\dagger_{m'}(\tau')\}\rangle_{0,\mathrm{con}}\,.$$

Through Wick's theorem the electron bracket gives a connected and disconnect diagram, where only the connected is kept. Multiplying out the two square brackets in photon bracket yields two equal contributions, which can be realized by relabeling the integration variables, thus canceling the $\frac{1}{2!}$. Further application of Wick's theorem gives a connected and disconnect diagram, where only the connected is kept. In the end the second order term can be written as

$$\int_C d\tau_1 d\tau_2 \sum_{m_1 m_2} A^0_{mm_2}(\tau,\tau_2)\left[-i\hbar\sum_{\substack{\nu_1\nu_1' \\ \nu_2\nu_2'}}\hbar g^{m_1}_{\nu_1\nu_1'}\hbar g^{m_2}_{\nu_2\nu_2'}G^0_{\nu_2'\nu_1}(\tau_2,\tau_1)G^0_{\nu_1'\nu_2}(\tau_1,\tau_2)\right]A^0_{m_1m'}(\tau_1,\tau'),$$

where the self-energy can be identified and in its self-consistent form it is given by

$$\Sigma^{\mathrm{e-rad,PB}}_{m_2m_1}(\tau_2,\tau_1) = -i\hbar\sum_{\substack{\nu_1\nu_1' \\ \nu_2\nu_2'}}\hbar g^{m_1}_{\nu_1\nu_1'}\hbar g^{m_2}_{\nu_2\nu_2'}G_{\nu_1'\nu_2}(\tau_1,\tau_2)G_{\nu_2'\nu_1}(\tau_2,\tau_1). \tag{A.27}$$

Due to its diagrammatic form this self-energy is often called a pair-bubble term, for an illustration see figure A.8. As mentioned in the previous section we in practise employ the RWA form of the electron-photon interaction eq. (A.24), for this interaction Hamiltonian we get the following photon self-energy

$$\Sigma^{\mathrm{e-rad,PB}}_{m_2m_1}(\tau_2,\tau_1) = -i\hbar\sum_{\substack{\alpha_1\alpha_1' \\ \alpha_2\alpha_2'}}\hbar g^{m_1}_{\alpha_1\alpha_1'}\hbar g^{m_2}_{\alpha_2\alpha_2'}G^{\mathrm{cc}}_{\alpha_2'\alpha_1}(\tau_2,\tau_1)G^{\mathrm{vv}}_{\alpha_1'\alpha_2}(\tau_1,\tau_2). \tag{A.28}$$

Electron-phonon

The interaction between the electrons and phonons is given by eq. (3.23)

$$H_{\mathrm{e-ph}} = \sum_{\nu\nu'\mu} M^\mu_{\nu\nu'}c^\dagger_\nu c_{\nu'}(b^\dagger_{\bar{\mu}} + b_\mu),$$

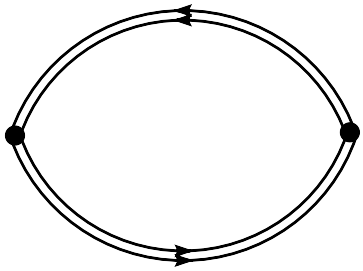

Figure A.8.: *Diagram used for the photon-electron interaction, see eq.* (A.27).

and is seen to be formally equivalent to the electron-photon interaction, eq. (3.19), this has the consequence that the self-energy must be the same also. Referring to eqs. (A.22) and (A.23) we can immediately write down the two first order contributions to the self-energy of the electrons due to interaction with phonons

$$\Sigma^{\mathrm{e-ph,H}}_{\nu_1\nu_1'}(\tau_1) = -i\hbar \int_C d\tau_2 \sum_{\nu_2\nu_2'\mu} M^{\mu}_{\nu_1\nu_1'} M^{\bar{\mu}}_{\nu_2\nu_2'} G_{\nu_2'\nu_2}(\tau_2,\tau_2^+) D^0_{\mu\bar{\mu}}(\tau_1,\tau_2), \tag{A.29}$$

and

$$\Sigma^{\mathrm{e-ph,F}}_{\nu_1\nu_2'}(\tau_1,\tau_2) = i\hbar \sum_{\nu_1'\nu_2\mu} M^{\mu}_{\nu_1\nu_1'} M^{\bar{\mu}}_{\nu_2\nu_2'} G_{\nu_1'\nu_2}(\tau_1,\tau_2) D^0_{\mu\bar{\mu}}(\tau_1,\tau_2). \tag{A.30}$$

Where we have defined the free phonon Green's function as follows

$$D^0_{\mu_1\mu_2}(\tau_1,\tau_2) = -i\hbar^{-1} \left\langle T_C\{[\hat{b}^\dagger_{\bar{\mu}_1}(\tau_1) + \hat{b}_{\mu_1}(\tau_1)][\hat{b}^\dagger_{\bar{\mu}_2}(\tau_2) + \hat{b}_{\mu_2}(\tau_2)]\}\right\rangle_0, \tag{A.31}$$

note that we do not make this self-energy self-consistent in the phonon Green's function, as the phonons are treated as a reservoir, i.e. the phonons are assumed to in thermal equilibrium at all times. For the free phonon Green's function we have the following nice property

$$D^0_{\mu_1\mu_2}(\tau_1,\tau_2) = D^0_{\mu_1\bar{\mu}_1}(\tau_1,\tau_2)\delta_{\bar{\mu}_1\mu_2},$$

which has been used to simplify the above self-energies. For diagrammatic illustrations of these self-energies see figure A.9.

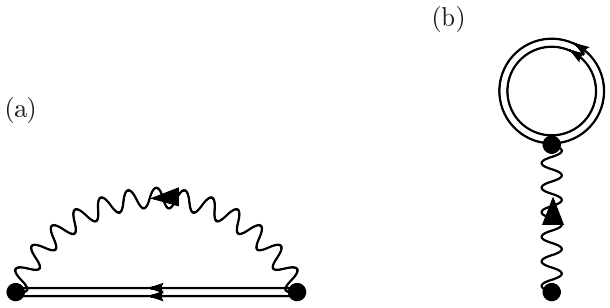

Figure A.9.: *Diagrams used for the electron-phonon interaction, where (a) is the Fock-type self-energy and (b) is the Hartree-type self-energy, see eqs. (A.30) and (A.29) respectively.*

A.6. Free real-time Green's functions

In this appendix we derive explicit expressions for free (non-interacting) real-time Green's functions. These can be found in any textbook, but are used frequently in this thesis, hence this appendix.

The Green's functions we are looking for are defined by eq. (2.24)

$$
\begin{aligned}
G^{0,>}_{\alpha\beta}(t,t') &= -i\hbar^{-1}\left\langle O_\alpha(t)O^\dagger_\beta(t')\right\rangle_0,\\
G^{0,<}_{\alpha\beta}(t,t') &= \pm i\hbar^{-1}\left\langle O^\dagger_\beta(t')O_\alpha(t)\right\rangle_0,\\
G^{0,r}_{\alpha\beta}(t,t') &= -i\hbar^{-1}\theta(t-t')\left\langle [O_\alpha(t),O^\dagger_\beta(t')]_\pm\right\rangle_0,\\
G^{0,a}_{\alpha\beta}(t,t') &= i\hbar^{-1}\theta(t'-t)\left\langle [O_\alpha(t),O^\dagger_\beta(t')]_\pm\right\rangle_0,
\end{aligned}
$$

where the $+$ is for fermions and the $-$ for bosons. The procedure we are about to go through can be performed simultaneously for both fermions and bosons, when minding a few signs underway. For a non-interacting system the Hamiltonian is quadratic and time-independent and can without loss of generality be chosen to be diagonal, hence we write it as

$$H_0 = \sum_\alpha \hbar\omega_\alpha O^\dagger_\alpha O_\alpha.$$

To obtain the time evolution of the operators comprising the Green's functions, we need to solve the Heisenberg equation of motion for these quantities, namely

$$i\hbar\partial_t O_\alpha(t) = [O_\alpha(t),H_0(t)] = [O_\alpha,H_0]\,(t) = \sum_\beta \hbar\omega_\beta [O_\alpha, O^\dagger_\beta O_\beta](t).$$

Evaluating the remaining commutator as $[O_\alpha, O^\dagger_\beta O_\beta] = O_\beta\delta_{\alpha\beta}$ is easily done using the (anti)commutator relations for the O_α's

$$[O_\alpha, O^\dagger_\beta]_\pm = \delta_{\alpha\beta}, \quad [O_\alpha, O_\beta]_\pm = [O^\dagger_\alpha, O^\dagger_\beta]_\pm = 0, \tag{A.33}$$

where again $+$ is for fermions and $-$ for bosons. The equation of motions becomes

$$i\hbar\partial_t O_\alpha(t) = \hbar\omega_\alpha O_\alpha(t),$$

which is solved using the initial condition $O_\alpha(t=0) = O_\alpha$ to give

$$O_\alpha(t) = e^{-i\omega_\alpha t}O_\alpha \Rightarrow O^\dagger_\alpha(t) = e^{+i\omega_\alpha t}O^\dagger_\alpha, \tag{A.34}$$

applying for both fermions and bosons.

These solutions can now be plugged into the definitions of the Green's functions. We start with the greater Green's function

$$
\begin{aligned}
G^{0,>}_{\alpha\beta}(t,t') &= -i\hbar^{-1}e^{-i\omega_\alpha(t-t')}[1-n_F(\hbar\omega_\alpha)]\delta_{\alpha\beta}, \quad \text{Fermions}\\
G^{0,>}_{\alpha\beta}(t,t') &= -i\hbar^{-1}e^{-i\omega_\alpha(t-t')}[1+n_B(\hbar\omega_\alpha)]\delta_{\alpha\beta}, \quad \text{Bosons.}
\end{aligned}
$$

The distribution functions $n_{F/B}$, the Fermi-Dirac and Bose-Einstein functions respectively, arise when performing thermal averaging over the number operator $n_\alpha = O^\dagger_\alpha O_\alpha$, see eq. (2.18). The lesser Green's function yields

$$
\begin{aligned}
G^{0,<}_{\alpha\beta}(t,t') &= +i\hbar^{-1}e^{-i\omega_\alpha(t-t')}n_F(\hbar\omega_\alpha)\delta_{\alpha\beta}, \quad \text{Fermions}\\
G^{0,<}_{\alpha\beta}(t,t') &= -i\hbar^{-1}e^{-i\omega_\alpha(t-t')}n_B(\hbar\omega_\alpha)\delta_{\alpha\beta}, \quad \text{Bosons.}
\end{aligned}
$$

The retarded and advanced Green's functions are equal for the fermions and bosons and are given by

$$
\begin{aligned}
G^{0,r}_{\alpha\beta}(t,t') &= -i\hbar^{-1}\theta(t-t')e^{-i\omega_\alpha(t-t')}\delta_{\alpha\beta},\\
G^{0,a}_{\alpha\beta}(t,t') &= +i\hbar^{-1}\theta(t'-t)e^{-i\omega_\alpha(t-t')}\delta_{\alpha\beta}.
\end{aligned}
$$

Two important common features of all the free Green's functions are that they 1) only depend on their time difference, effective being one-time functions and not two-time, and 2) that they are diagonal in their quantum numbers. The time difference dependence can in fact be shown to hold for any equilibrium Green's function, regardless of what interactions might be present. This feature makes equilibrium retarded and advanced Green's functions very attractive to use in connection with the GKBA, see section 2.5.

We make use of one last free Green's function which is not defined the same way as above. This is the free phonon Green's function introduced in eq. (A.31)

$$D^0_{\mu\mu'}(\tau,\tau') = -i\hbar^{-1}\left\langle T_C\{[b^\dagger_{\bar{\mu}}(\tau)+b_\mu(\tau)][b^\dagger_{\bar{\mu}'}(\tau')+b_{\mu'}(\tau')]\}\right\rangle_0.$$

To obtain its real-time components we put it on a more familiar form by defining $B_\mu(\tau)\equiv b^\dagger_{\bar{\mu}}(\tau)+b_\mu(\tau)=B^\dagger_{\bar{\mu}}(\tau)$, so that we may write

$$D^0_{\mu\mu'}(\tau,\tau') = -i\hbar^{-1}\left\langle T_C\{B_\mu(\tau)B^\dagger_{\bar{\mu}'}(\tau')\}\right\rangle_0.$$

The greater and lesser Green's functions are thus given by

$$D^{0,>}_{\mu\mu'}(t,t') = -i\hbar^{-1}\left\langle B_\mu(t)B^\dagger_{\bar{\mu}'}(t')\right\rangle_0,$$
$$D^{0,<}_{\mu\mu'}(t,t') = -i\hbar^{-1}\left\langle B^\dagger_{\bar{\mu}'}(t')B_\mu(t)\right\rangle_0.$$

The time evolution of $B_\mu(t)$ is easily found from eq. (A.34) and we get

$$D^{0,>}_{\mu\mu'}(t,t') = -i\hbar^{-1}\left\{e^{i\omega_\mu(t-t')}n_B(\hbar\omega_\mu)+e^{-i\omega_\mu(t-t')}[n_B(\hbar\omega_\mu)+1]\right\}\delta_{\bar{\mu}',\mu}, \tag{A.35a}$$
$$D^{0,<}_{\mu\mu'}(t,t') = -i\hbar^{-1}\left\{e^{-i\omega_\mu(t-t')}n_B(\hbar\omega_\mu)+e^{i\omega_\mu(t-t')}[n_B(\hbar\omega_\mu)+1]\right\}\delta_{\bar{\mu}',\mu}. \tag{A.35b}$$

From these expressions the following relations are seen holds between the greater and lesser phonon Green's functions

$$D^{0,\gtrless}_{\mu\mu'}(t,t') = D^{0,\lessgtr}_{\mu'\mu}(t',t) = -[D^{0,\lessgtr}_{\mu\mu'}(t,t')]^*, \tag{A.36}$$

this redundancy in Green's functions is due to the way the phonon Green's function is defined eq. (A.31).

A.7. Analytical basis set for the electronic single-particle states

The purpose of this appendix is to describe how to obtain the basis functions used in section 4.3.2 to expand the numerical solutions from COMSOL. The most important properties of a basis is that it must be complete and further that it must satisfy the same outer boundary conditions as the function it is to expand. The simplest way to satisfy both of these requirements is to use the same geometry as for the COMSOL solution, see figure 4.2, but simply for a homogenous medium and impose the same zero boundary conditions on the outer boundaries. This empty cylinder is schematically shown in A.10.

As for the COMSOL solution we deal with rotationally symmetric system and thus the angular dependence can readily be obtained as in section 4.2.2, and we are left with an equation of the form eq. (4.4) for the two remaining directions. Due to the fact that we have no internal boundaries, it is reasonable to assume that we may further factorize the remaining function into a part for the radial coordinate, ρ, and for the z-direction, $f(\rho,z)=R(\rho)Z(z)$. Substituting this into eq. (4.4) we end up with a Schrödinger equation of the form

$$-\frac{\hbar^2}{2m^*}\left(\frac{1}{\rho}\partial_\rho\left[\rho\partial_\rho\right]+\frac{m^2}{\rho^2}+\partial_{zz}\right)R(\rho)Z(z) = ER(\rho)Z(z).$$

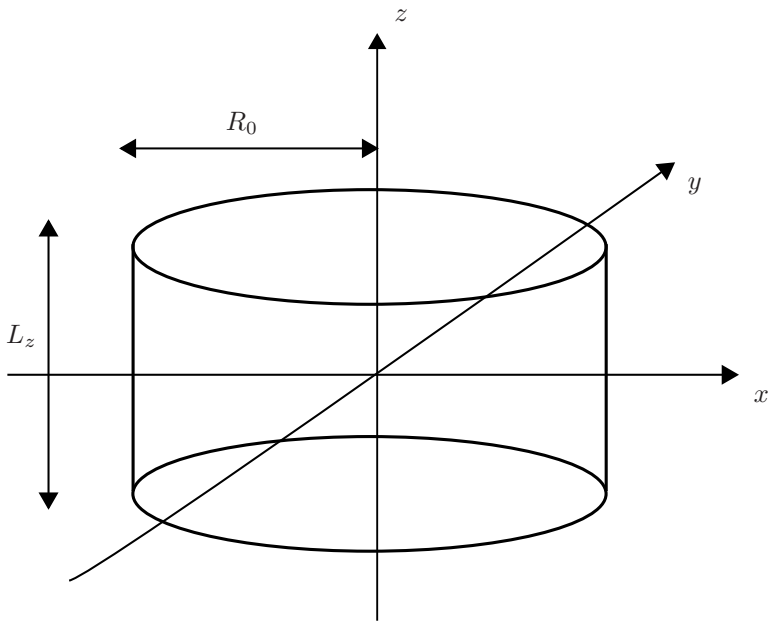

Figure A.10.: *Figure of the geometry used to obtain the free basis functions.*

This kind of equation may be solved using the separation of variables technique and is done in any textbook on partial differential equations, see e.g. [86], and we will therefore simply state the solution satisfying the boundary conditions given in eqs. (4.5) and (4.6). The full solution may be written on the following form

$$B_{mln_z}(\boldsymbol{r}) = \Phi_m(\varphi) R_{|m|l}(\rho) Z_{n_z}(z),$$

where the explicit form of each of the three functions will be briefly described below. For the angular part we obtain

$$\Phi_m(\varphi) = \frac{1}{\sqrt{2\pi}} e^{im\varphi}, \quad m = 0, \pm 1, \pm 2, \pm 3, \ldots$$

which are the well-known eigenstates of the z-component of the angular momentum operator. For the radial part we have

$$R_{|m|l}(\rho) = \frac{\sqrt{2}}{R_0 J_{|m|+1}(\gamma_{|m|l})} J_{|m|}(k_{|m|l}\rho), \quad k_{|m|l} = \frac{\gamma_{|m|l}}{R_0}, \quad l = 1, 2, 3, \ldots \tag{A.37}$$

where $\gamma_{|m|l}$ is the l'th root of $J_{|m|}$, with $J_{|m|}$ being the Bessel function of the first kind. For illustration we show a few of the radial functions in figure A.11. For the z-direction we get

$$Z_{n_z}(z) = \frac{1}{\sqrt{L_z/2}} \sin\left(\frac{\pi n_z}{L_z} z + \frac{\pi n_z}{2}\right), \quad n_z = 1, 2, 3, \ldots$$

Each of the above functions have been normalized and hence the full product form is also normalized. The eigenenergy is given by the following expression

$$E_{mln_z} = \frac{\hbar^2}{2m^*}\left((k_{|m|l})^2 + (k_{n_z})^2\right) = \frac{\hbar^2}{2m^*}\left(\left[\frac{\gamma_{|m|l}}{R_0}\right]^2 + \left[\frac{\pi}{L_z} n_z\right]^2\right),$$

where we notice the degeneracy in m, due to the rotational symmetry of the system.

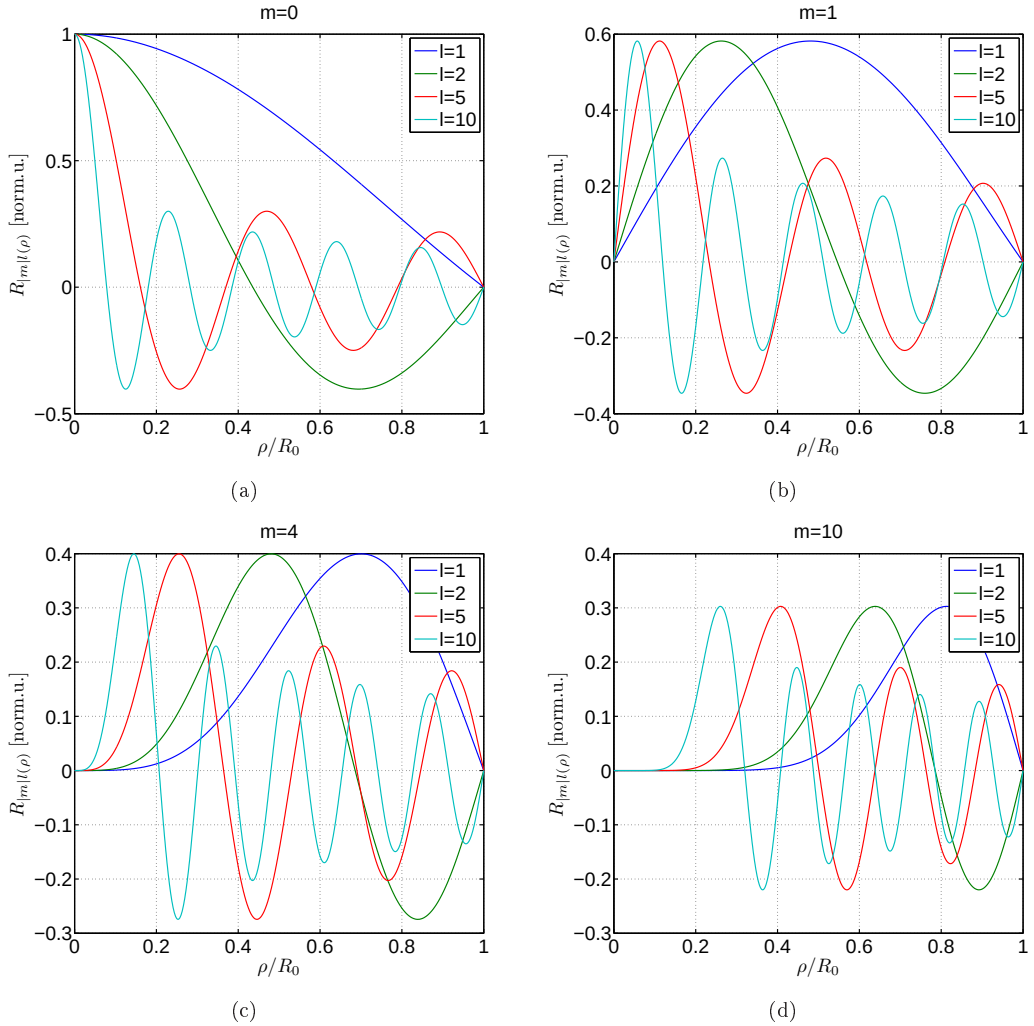

Figure A.11.: *Figures showing a few of the radial basis functions eq.* (A.37).

A.8. Semiconductor band parameters

In this appendix we will briefly discuss the parameters that enter in the one-band effective mass Schrödinger equation, we use to obtain the electronic wavefunctions, see eq. (4.4). Figure A.12 illustrates the energy landscape we are considering. We use an uncoupled two-band model with a conduction and valence band, where II (I) denotes the high (low) bandgap material. It should be emphasized that no effects due to strain or piezo electric effects are explicitly taken into account, apart of course from the fact that we have a QD that have formed due to strain/surface tension. This is a huge approximation and the calculated energies and wavefunctions should therefore only be considered as crude estimates to the real quantities. Hopefully the calculated physical quantities will still display qualitatively correct behavior. Apart from the various energies shown in figure A.12 we also need to know the effective masses of the electrons and holes.

We will use GaAs as the high bandgap material and $In_xGa_{x-1}As$ as the low bandgap material, with[8] $x = 0.60$ to simulate the diffusion of Ga into the shallow InAs QD and WL. We will adopt bulk values for all parameters, except for the hole masses which need special attention due to anisotropy in $\boldsymbol{k}$-space

[8] Obtained through personal communication with Søren Stobbe of DTU Fotonik.

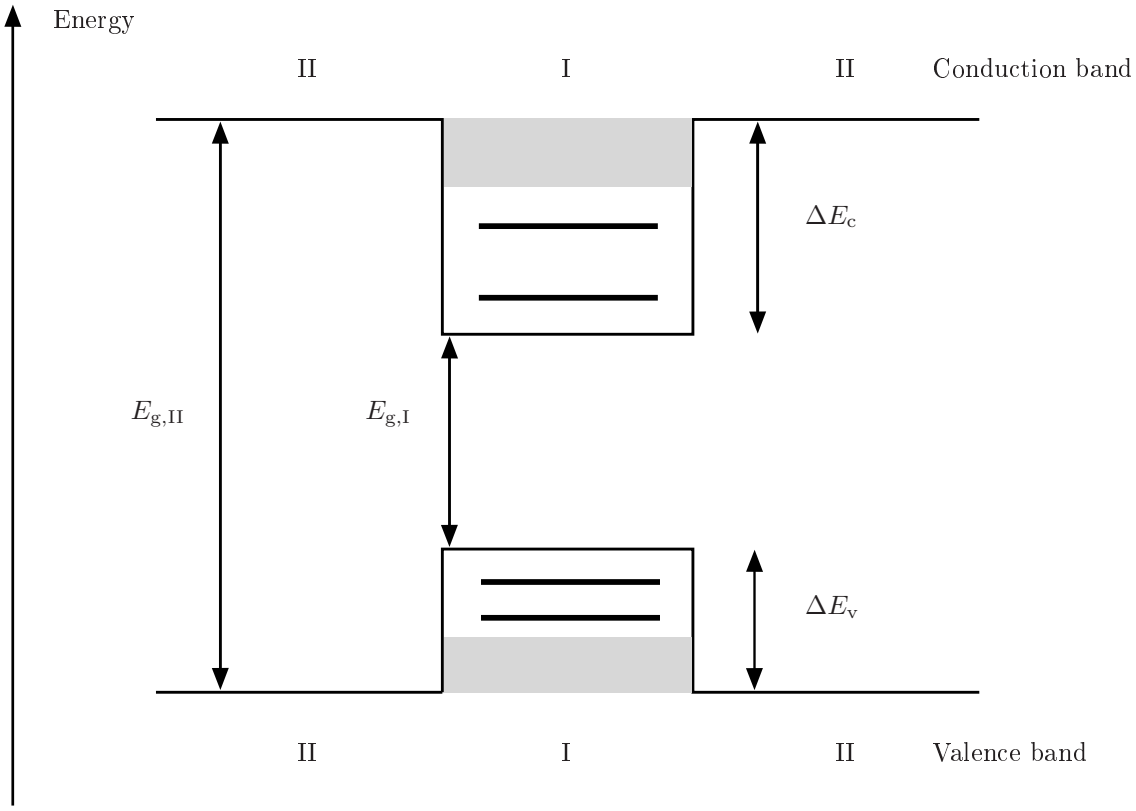

Figure A.12.: *Schematic illustration of the energy landscape in the QD/WL system. In the potential well the horizontal lines indicate bound QD states, while the grey box indicate the WL energy continuum.*

for the valence band. The parameters for the high bandgap material are tabulated in table A.1, while those for the low bandgap material are obtained using interpolation formulas, to take into account the Ga concentration in the InAs. For the bandgap we use the formulae [87]

$$E_{g,I} = xE_{g,InAs} + (1-x)E_{g,GaAs} - x(1-x)C_{g,GaInAs},$$

where $C_{g,GaInAs}$ is known as a bowing parameter. The so-called conduction band offset (CBO), ΔE_c, and valence band offset (VBO), ΔE_v, are assumed to be given by the 60/40 ratio so that

$$\Delta E_c = 0.60 \times (E_{g,II} - E_{g,I}),$$
$$\Delta E_v = 0.40 \times (E_{g,II} - E_{g,I}).$$

For the hole mass we use the heavy hole (hh) mass and choose the component the in-plane direction, (x, y)-plane in real space, as this is where most of our dynamics is. Furthermore we adopt the hh mass appropriate for quantum well structures as our QD/WL system is very similar to this, this choice is supported in the literature see e.g. [88]. It is however an open question what input parameters to use when performing simulations using effective descriptions, like the effective mass Schrödinger equation, on semiconductor heterostructures and there is no broad consensus on this point in the scientific literature. We take the hh mass as given by [89, p. 171]

$$\left[\frac{m_0}{m^*_{hh}}\right]^{[110]}_{QW} = \gamma_1 + \gamma_2.$$

The high bandgap material hh mass is readily obtained, while for the low bandgap material we use the

Quantity	Value	Unit	Reference	Quantity	Value	Unit
$\gamma_{1,\mathrm{GaAs}}$	6.98	1	[87]	$E_{\mathrm{g,II}}$	1.519	eV
$\gamma_{2,\mathrm{GaAs}}$	2.06	1	[87]	$E_{\mathrm{g,I}}$	0.7433	eV
$\gamma_{3,\mathrm{GaAs}}$	2.93	1	[87]	ΔE_{c}	0.465	eV
$\gamma_{1,\mathrm{InAs}}$	20.0	1	[87]	ΔE_{v}	0.310	eV
$\gamma_{2,\mathrm{InAs}}$	8.5	1	[87]	$m^*_{\mathrm{c,II}}$	0.067	m_0
$\gamma_{3,\mathrm{InAs}}$	9.2	1	[87]	$m^*_{\mathrm{c,I}}$	0.0344	m_0
$m^*_{\mathrm{e,GaAs}}$	0.067	m_0	[87]	$m^*_{\mathrm{v,II}}$	0.111	m_0
$m^*_{\mathrm{e,InAs}}$	0.026	m_0	[87]	$m^*_{\mathrm{v,I}}$	0.0483	m_0
$E_{\mathrm{g,GaAs}}$	1.519	eV	[87]			
$E_{\mathrm{g,InAs}}$	0.417	eV	[87]			
$C_{\mathrm{g,GaInAs}}$	0.477	eV	[87]			

Table A.1.: *First set of the band parameters used in the effective mass Schrödinger equation simulations.*

Quantity	Value	Unit
$E_{\mathrm{g,II}}$	1.424	eV
$E_{\mathrm{g,I}}$	0.359	eV
ΔE_{c}	0.697	eV
ΔE_{v}	0.368	eV
$m^*_{\mathrm{c,II}}$	0.0665	m_0
$m^*_{\mathrm{c,I}}$	0.027	m_0
$m^*_{\mathrm{v,II}}$	0.38	m_0
$m^*_{\mathrm{v,I}}$	0.34	m_0

Table A.2.: *Second set of the band parameters used in the effective mass Schrödinger equation simulations. All values are taken from [53].*

following interpolation formulae

$$\left[\frac{m_0}{m^*_{\mathrm{hh}}}\right]^{[110]}_{\mathrm{QW,I}} = x\left[\frac{m_0}{m^*_{\mathrm{hh}}}\right]^{[110]}_{\mathrm{QW,InAs}} + (1-x)\left[\frac{m_0}{m^*_{\mathrm{hh}}}\right]^{[110]}_{\mathrm{QW,GaAs}}.$$

All the parameters are summarized in table A.1.

After it was realized that the set of parameters described above yielded unphysical population for some excitation conditions, see section 6.2, another set was chosen that did not suffer from this problem. We will briefly describe the new set in the following. The materials are the same as above, but now we use pure InAs as the low bandgap material, i.e. $x = 1$. Furthermore we use the effective mass in the [001], z, direction, as oppose to the [110] direction above, which is considerably larger, leading in general to more confined valence band states. For the CBO and VBO we choose a slightly different ratio given by 0.654/0.346 so that

$$\Delta E_{\mathrm{c}} = 0.654 \times (E_{\mathrm{g,GaAs}} - E_{\mathrm{g,InAs}}),$$
$$\Delta E_{\mathrm{v}} = 0.346 \times (E_{\mathrm{g,GaAs}} - E_{\mathrm{g,InAs}}),$$

where the number of digits has historical reasons. The new parameters are summarized in table A.2.

A.9. Slowly-varying equations

In this appendix we list the slowly-varying versions of the equations of motion presented in chapter **??**, which are the quantities that are solved for numerically. We define the slowly-varying transformation for the electronic density matrix as follows

$$\rho_\alpha^{bb'}(t) = e^{-i\omega_\alpha^{bb'}t}\tilde{\rho}_\alpha^{bb'}(t), \tag{A.38}$$

that removes the fast underlying oscillations in the off-diagonal elements of the density matrix due to the free evolution of the system. Eq. (A.38) transforms the equation of motion for the density matrix, eq. (5.34), into the form

$$\partial_t\tilde{\rho}_\alpha^{bb'}(t) = \partial_t\tilde{\rho}_\alpha^{bb'}(t)|_{\text{coh}} + \partial_t\tilde{\rho}_\alpha^{bb'}(t)|_{\text{scatt}}.$$

Below we list each of the contributions to the coherent and scattering terms used in the simulations in their slowly-varying version

A.9.1. Coherent terms

The coherent source term, eq. (5.35), transforms into

$$\partial_t\tilde{\rho}_\alpha^{bb'}(t)|_{\text{coh}} = -i\hbar^{-1}\sum_{b_1}\left[\left\{e^{i\omega_\alpha^{bb_1}t}\Sigma_\alpha^{bb_1,\text{s}}(t)\right\}\tilde{\rho}_\alpha^{b_1b'}(t) - \tilde{\rho}_\alpha^{bb_1}(t)\left\{e^{i\omega_\alpha^{b_1b'}t}\Sigma_\alpha^{b_1b',\text{s}}(t)\right\}\right],$$

were the term due to the free evolution has disappeared and hence the fast oscillations associated with it.

Now we list the slowly-varying transformed of the terms in eq. (5.36):

Eq. (5.38):

$$U_\alpha^{bb'}(t) = \begin{cases} 0, & b = b' = \text{c, v} \\ d_\alpha^{\text{cv}}\frac{E_0(t)}{2}e^{-i\omega_0 t}, & b = \text{c}, \quad b' = \text{v} \\ d_\alpha^{\text{vc}}\frac{E_0(t)}{2}e^{i\omega_0 t}, & b = \text{v}, \quad b' = \text{c} \end{cases}$$

Eq. (5.39):

$$\Sigma_\alpha^{bb',\text{HF}}(t) = \sum_{\substack{b_1b_2\\ \alpha_1}}\left(V_{\alpha\alpha_1\alpha\alpha_1}^{bb_2b'b_1} - V_{\alpha\alpha_1\alpha_1\alpha}^{bb_2b_1b'}\right)e^{-i\omega_{\alpha_1}^{b_1b_2}t}\left[\tilde{\rho}_{\alpha_1}^{b_1b_2}(t) - \delta_{b_1,\text{v}}\delta_{b_2,\text{v}}\right]$$

Eq. (5.40):

$$\Sigma_\alpha^{bb',\text{LO,H}}(t) = \int_{-\infty}^{t}dt'\sum_{b_1\alpha_1}\frac{\hbar\omega_{\text{LO}}}{2\varepsilon^*/\varepsilon}V_{\alpha_1\alpha\alpha_1\alpha}^{b_1bb_1b}\left[\tilde{\rho}_{\alpha_1}^{b_1b_1}(t') - \delta_{b_1,\text{v}}\right]D_{\text{LO}}^{0,r}(t,t')\delta_{b,b'},$$

Eq. (5.41):

$$\Sigma_\alpha^{bb',\text{rad,H}}(t) = \int_{-\infty}^{t}dt'\sum_{\alpha_1}\hbar g_\alpha\hbar g_{\alpha_1}\left[e^{-i\omega_{\alpha_1}^{\text{cv}}t'}\tilde{\rho}_{\alpha_1}^{\text{cv}}(t')A^r(t,t')\delta_{b,\text{c}}\delta_{b',\text{v}} + e^{-i\omega_{\alpha_1}^{\text{vc}}t'}\tilde{\rho}_{\alpha_1}^{\text{vc}}(t')[A^r(t,t')]^*\delta_{b,\text{v}}\delta_{b',\text{c}}\right].$$

A.9.2. Electronic scattering terms

LO-phonons: Eq. (5.44):

$$\begin{aligned}
&\partial_t \tilde{\rho}_\alpha^{bb'}(t)|_{\text{scatt}}^{\text{F,LO}} = \\
&e^{i\omega_\alpha^{bb'}t}\int_{-\infty}^{t} dt_1 \sum_{b_1\alpha_1}\Big(G_{\alpha_1}^{b,r}(t,t_1)\left[G_\alpha^{b',r}(t,t_1)\right]^* e^{-i(\omega_{\alpha_1}^{bb_1}+\omega_\alpha^{b_1b'})t_1} \\
&\times\Big\{-D_{\alpha\alpha_1}^{bb_1,>}(t,t_1)[\delta_{b,b_1}-\tilde{\rho}_{\alpha_1}^{bb_1}(t_1)]\tilde{\rho}_\alpha^{b_1b'}(t_1)+D_{\alpha\alpha_1}^{bb_1,<}(t,t_1)\tilde{\rho}_{\alpha_1}^{bb_1}(t_1)[\delta_{b_1,b'}-\tilde{\rho}_\alpha^{b_1b'}(t_1)]\Big\} \\
&+G_\alpha^{b,r}(t,t_1)\left[G_{\alpha_1}^{b',r}(t,t_1)\right]^* e^{-i(\omega_\alpha^{bb_1}+\omega_{\alpha_1}^{b_1b'})t_1} \\
&\qquad\times\Big\{[\delta_{b,b_1}-\tilde{\rho}_\alpha^{bb_1}(t_1)]\tilde{\rho}_{\alpha_1}^{b_1b'}(t_1)D_{\alpha\alpha_1}^{b_1b',>}(t,t_1)-\tilde{\rho}_\alpha^{bb_1}(t_1)[\delta_{b_1,b'}-\tilde{\rho}_{\alpha_1}^{b_1b'}(t_1)]D_{\alpha\alpha_1}^{b_1b',<}(t,t_1)\Big\}\Big)
\end{aligned}$$

RWA GKBA photons: Eq. (5.46):

$$\begin{aligned}
\partial_t\tilde{\rho}_\alpha^{bb}(t)|_{\text{scatt}}^{\text{rad,F}} = -2\text{Re}\Big[\int_{-\infty}^{t} dt_1 G_\alpha^{\text{v},r}(t,t_1)\left[G_\alpha^{\text{c},r}(t,t_1)\right]^*\left(i\hbar|\hbar g_\alpha|^2 A^r(t,t_1)\right) \\
\times\left\{A(t_1)\left[\tilde{\rho}_\alpha^{\text{cc}}(t_1)-\tilde{\rho}_\alpha^{\text{vv}}(t_1)\right]+\tilde{\rho}_\alpha^{\text{cc}}(t_1)\left[1-\tilde{\rho}_\alpha^{\text{vv}}(t_1)\right]\right\}(\delta_{b,\text{c}}-\delta_{b,\text{v}})\Big].
\end{aligned}$$

Eq. (5.47):

$$\begin{aligned}
&\partial_t\tilde{\rho}_\alpha^{\text{cv}}(t)|_{\text{scatt}}^{\text{rad,F}} = -e^{i\omega_\alpha^{\text{cv}}t}\int_{-\infty}^{t} dt_1\left(i\hbar|\hbar g_\alpha|^2 A^r(t,t_1)\right)e^{-i\omega_\alpha^{\text{cv}}t_1}\Big(\\
&|G_\alpha^{\text{v},r}(t,t_1)|^2\left\{A(t_1)\tilde{\rho}_\alpha^{\text{cv}}(t_1)+\tilde{\rho}_\alpha^{\text{cv}}(t_1)[1-\tilde{\rho}_\alpha^{\text{vv}}(t_1)]\right\}+|G_\alpha^{\text{c},r}(t,t_1)|^2\left\{A(t_1)\tilde{\rho}_\alpha^{\text{cv}}(t_1)+\tilde{\rho}_\alpha^{\text{cv}}(t_1)\tilde{\rho}_\alpha^{\text{cc}}(t_1)\right\}\Big).
\end{aligned}$$

RWA two-time photons: Eq. (5.50):

$$\begin{aligned}
\partial_t\tilde{\rho}_\alpha^{bb}(t)|_{\text{scatt}}^{\text{rad,F}} = -2\text{Re}\Big[\int_{-\infty}^{t} dt_1|\hbar g_\alpha|^2 G_\alpha^{\text{v},r}(t,t_1)\left[G_\alpha^{\text{c},r}(t,t_1)\right]^* e^{-i\omega_{\text{cav}}(t-t_1)} \\
\times\Big\{[1-\tilde{\rho}_\alpha^{\text{vv}}(t_1)]\tilde{A}^{>}(t,t_1)\tilde{\rho}_\alpha^{\text{cc}}(t_1)-\tilde{\rho}_\alpha^{\text{vv}}(t_1)\tilde{A}^{<}(t,t_1)[1-\tilde{\rho}_\alpha^{\text{cc}}(t_1)]\Big\}(\delta_{b,\text{c}}-\delta_{b,\text{v}})\Big].
\end{aligned}$$

Eq. (5.51):

$$\begin{aligned}
&\partial_t\tilde{\rho}_\alpha^{\text{cv}}(t)|_{\text{scatt}}^{\text{rad,F}} = -e^{i\omega_\alpha^{\text{cv}}t}\int_{-\infty}^{t} dt_1|\hbar g_\alpha|^2 e^{-i\omega_\alpha^{\text{cv}}t_1}e^{-i\omega_{\text{cav}}(t-t_1)}\Big(\\
&|G_\alpha^{\text{v},r}(t,t_1)|^2\Big\{[1-\tilde{\rho}_\alpha^{\text{vv}}(t_1)]\tilde{A}^{>}(t,t_1)\tilde{\rho}_\alpha^{\text{cv}}(t_1)+\tilde{\rho}_\alpha^{\text{vv}}(t_1)\tilde{A}^{<}(t,t_1)\tilde{\rho}_\alpha^{\text{cv}}(t_1)\Big\} \\
&\qquad+|G_\alpha^{\text{c},r}(t,t_1)|^2\Big\{\tilde{\rho}_\alpha^{\text{cv}}(t_1)\tilde{\rho}_\alpha^{\text{cc}}(t_1)\tilde{A}^{>}(t,t_1)+\tilde{\rho}_\alpha^{\text{cv}}(t_1)[1-\tilde{\rho}_\alpha^{\text{cc}}(t_1)]\tilde{A}^{<}(t,t_1)\Big\}\Big).
\end{aligned}$$

A.9.3. Photonic scattering terms

As only electronic populations enter these terms, the slowly-varying versions are identical to those presented in the main section and however for completeness we repeat them here.

Eq. (5.59):

$$\partial_t \tilde{A}(t,t-\tau)|^{\mathrm{PB}}_{\mathrm{scatt,II}} = \int_{-\infty}^{t-\tau} dt_1 \sum_{\alpha_1} |\hbar g_{\alpha_1}|^2$$
$$\times \Big[G^{\mathrm{c},r}_{\alpha_1}(t,t_1) \left[G^{\mathrm{v},r}_{\alpha_1}(t,t_1)\right]^* e^{-i\omega_{\mathrm{cav}}(t_1-t)} \{-[1-\tilde{\rho}^{\mathrm{cc}}_{\alpha_1}(t_1)]\tilde{\rho}^{\mathrm{vv}}_{\alpha_1}(t_1)[\tilde{A}^{<}(t-\tau,t_1)]^* + \tilde{\rho}^{\mathrm{cc}}_{\alpha_1}(t_1)[1-\tilde{\rho}^{\mathrm{vv}}_{\alpha_1}(t_1)][\tilde{A}^{>}(t-\tau,t_1)]^*\}$$
$$+ \left[G^{\mathrm{c},r}_{\alpha_1}(t-\tau,t_1)\right]^* G^{\mathrm{v},r}_{\alpha_1}(t-\tau,t_1) e^{-i\omega_{\mathrm{cav}}(t-\tau-t_1)} \{\tilde{A}^{>}(t,t_1)\tilde{\rho}^{\mathrm{cc}}_{\alpha_1}(t_1)[1-\tilde{\rho}^{\mathrm{vv}}_{\alpha_1}(t_1)] - \tilde{A}^{<}(t,t_1)[1-\tilde{\rho}^{\mathrm{cc}}_{\alpha_1}(t_1)]\tilde{\rho}^{\mathrm{vv}}_{\alpha_1}(t_1)\}\Big],$$

Eq. (5.57):

$$\partial_t \tilde{A}^{>}(t,t-\tau)|^{\mathrm{PB}}_{\mathrm{scatt,I}} = \int_{t-\tau}^{t} dt_1 \sum_{\alpha_1} |\hbar g_{\alpha_1}|^2$$
$$\times \Big[- G^{\mathrm{c},r}_{\alpha_1}(t,t_1) \left[G^{\mathrm{v},r}_{\alpha_1}(t,t_1)\right]^* e^{-i\omega_{\mathrm{cav}}(t_1-t)} \{\tilde{\rho}^{\mathrm{vv}}_{\alpha_1}(t_1) - \tilde{\rho}^{\mathrm{cc}}_{\alpha_1}(t_1)\}\tilde{A}^{>}(t_1,t-\tau)$$
$$+ G^{\mathrm{c},r}_{\alpha_1}(t_1,t-\tau) \left[G^{\mathrm{v},r}_{\alpha_1}(t_1,t-\tau)\right]^* e^{-i\omega_{\mathrm{cav}}(t-\tau-t_1)} \{\tilde{A}^{>}(t,t_1) - \tilde{A}^{<}(t,t_1)\}[1-\tilde{\rho}^{\mathrm{cc}}_{\alpha_1}(t-\tau)]\tilde{\rho}^{\mathrm{vv}}_{\alpha_1}(t-\tau)\Big],$$

Eq. (5.58):

$$\partial_t \tilde{A}^{<}(t,t-\tau)|^{\mathrm{PB}}_{\mathrm{scatt,I}} = \int_{t-\tau}^{t} dt_1 \sum_{\alpha_1} |\hbar g_{\alpha_1}|^2$$
$$\times \Big[- G^{\mathrm{c},r}_{\alpha_1}(t,t_1) \left[G^{\mathrm{v},r}_{\alpha_1}(t,t_1)\right]^* e^{-i\omega_{\mathrm{cav}}(t_1-t)} \{\tilde{\rho}^{\mathrm{vv}}_{\alpha_1}(t_1) - \tilde{\rho}^{\mathrm{cc}}_{\alpha_1}(t_1)\}\tilde{A}^{<}(t_1,t-\tau)$$
$$+ G^{\mathrm{c},r}_{\alpha_1}(t_1,t-\tau) \left[G^{\mathrm{v},r}_{\alpha_1}(t_1,t-\tau)\right]^* e^{-i\omega_{\mathrm{cav}}(t-\tau-t_1)} \{\tilde{A}^{>}(t,t_1) - \tilde{A}^{<}(t,t_1)\}\tilde{\rho}^{\mathrm{cc}}_{\alpha_1}(t-\tau)[1-\tilde{\rho}^{\mathrm{vv}}_{\alpha_1}(t-\tau)]\Big],$$

Bibliography

[1] E. Knill, R. Laflamme, and G. J. Milburn, Nature **409**, 46 (2001).

[2] B. Lounis and M. Orrit, Reports on Progress in Physics **68**, 1129 (2005).

[3] T. C. Ralph, Reports on Progress in Physics **69**, 853 (2006).

[4] `www.fotonik.dtu.dk`.

[5] H. Thyrrestrup, Photonic crystal nano-cavities, Master's thesis, Technical University of Denmark, 2008.

[6] W. Seifert et al., Progress in Crystal Growth and Characterization of Materials **33**, 423 (1996).

[7] K. J. Vahala, Nature **424**, 839 (2003).

[8] P. Michler, editor, Single Quantum Dots, Topics in Applied Physics Vol. 90/2003 (Springer Berlin / Heidelberg, 2003).

[9] E. M. Purcell, H. C. Torrey, and R. V. Pound, Phys. Rev. **69**, 37 (1946).

[10] S. Varoutsis et al., Phys. Rev. B **72** (2005).

[11] V. S. C. M. Rao and S. Hughes, Phys. Rev. B **75**, 205437 (2007).

[12] G. Lecamp, P. Lalanne, and J. P. Hugonin, Physical Review Letters **99**, 023902 (2007).

[13] T. Lund-Hansen et al., arXiv:0805.3485v2 (2008).

[14] C. Santori, D. Fattal, J. Vuckovic, G. S. Solomon, and Y. Yamamoto, Nature **419**, 594 (2002).

[15] J. Bylander, I. Robert-Philip, and I. Abram, The European Physical Journal D **22**, 295 (2003).

[16] J. P. Reithmaier et al., Nature **432**, 197 (2004).

[17] A. Kiraz, M. Atatüre, and A. Imamoğlu, Phys. Rev. A **69**, 032305 (2004).

[18] G. Cui and M. G. Raymer, Phys. Rev. A **73** (2006).

[19] A. Naesby, T. Suhr, P. T. Kristensen, and J. Mørk, Influence of pure dephasing on emission spectra from single photon sources, Submitted to PRL., 2008.

[20] I. Wilson-Rae and A. Imamoğlu, Phys. Rev. B **65**, 235311 (2002).

[21] J. Larson and H. Moya-Cessa, arXiv:cond-mat/0703552v4 (2008).

[22] A. Nazir and S. D. Barrett, arXiv:0806.1164v1 [quant-ph] (2008).

[23] F. Milde, A. Knorr, and S. Hughes, Physical Review B (Condensed Matter and Materials Physics) **78**, 035330 (2008).

[24] G. D. Mahan, Many-particle physics, 2nd ed. (Plenum Press, 1993).

[25] M. Kira and S. Koch, Progress in Quantum Electronics **30**, 155 (2006).

[26] H. Haug and A.-P. Jauho, Quantum Kinetics in Transport and Optics of Semiconductors, Second ed. (Springer, 2008).

[27] V. Axt and T. Kuhn, Reports on Progress in Physics **67**, 433 (2004).

[28] H. Bruus and K. Flensberg, Many-Body Quantum Theory in Condensed Matter Physics (Oxford University Press, 2004), second reprint.

[29] R. Binder and S. W. Koch, Pogress in Quantum Electronics **19**, 307 (1995).

[30] P. Danielewicz, Annals of Physics **152**, 239 (1984).

[31] W. Schäfer and M. Wegener, Semiconductor Optics and Transport Phenomena (Springer, 2002).

[32] T. R. Nielsen, Carrier-Carrier and Carrier-Phonon Scattering in Self-Assembled Quantum Dots, PhD thesis, University of Bremem, 2005.

[33] T. Frederiksen, Inelastic electron transport in nanosystems, Master's thesis, Technical University of Denmark, 2004, PDF version available at `www.mic.dtu.dk`.

[34] J. Rammer, Quantum Field Theory of Non-equilibrium States, First ed. (Cambridge University Press, 2007).

[35] H. Haug and A.-P. Jauho, Quantum Kinetics in Transport and Optics of Semiconductors, 1st ed. (Springer, 1996).

[36] H. Haug and A.-P. Jauho, Quantum Kinetics in Transport and Optics of Semiconductors, 2nd ed. (Springer, 2007), Preprint notes.

[37] P. Gartner, L. Banyai, and H. Haug, Phys. Rev. B **60**, 14234 (1999).

[38] P. Gartner, J. Seebeck, and F. Jahnke, Phys. Rev. B **73**, 115307 (2006).

[39] M. Hartmann and W. Schäfer, physica status solidi (b) **173**, 165 (1992).

[40] P. Lipavský, V. Špička, and B. Velický, Phys. Rev. B **34**, 6933 (1986).

[41] J. Seebeck, T. Nielsen, P. Gartner, and F. Jahnke, Phys. Rev. B **71**, 125327 (2005).

[42] J. Seebeck, T. R. Nielsen, P. Gartner, and F. Jahnke, The European Physical Journal B **49**, 167 (2006).

[43] R. Loudon, The Quantum Theory of Light, Third ed. (Oxford University Press, 2000).

[44] M. O. Scully and S. Zubairy, Quantum Optics (Cambridge University Press, 1997), third reprint.

[45] L. E. Ballentine, Quantum Mechanics - A Modern Development (World Scientific, 1998), fourth reprint.

[46] C. Cohen-Tannoudji, J. Dupont-Roc, and G. Grynberg, Atom-Photon Interactions (Wiley, 1992).

[47] N. Liu, J. Tersoff, O. Baklenov, A. L. Holmes, and C. K. Shih, Phys. Rev. Lett. **84**, 334 (2000).

[48] I. Kegel et al., Phys. Rev. Lett. **85**, 1694 (2000).

[49] K. Jacobi, Progress in Surface Science **71**, 185 (2003).

[50] R. Melnik and M. Willatzen, Nanotechnology **15**, 1 (2004).

[51] T. Markussen, P. Kristensen, B. Tromborg, T. Berg, and J. Mørk, Physical Review B **74** (2006).

[52] P. K. Nielsen, H. T. Nielsen, J. Mørk, and B. Tromborg, Optics Express **15** (2007).

[53] L. A. Coldren and S. W. Corzine, Diode Lasers and Photonic Integrated Circuits (Wiley, 1995).

[54] G. Bastard, Wave mechanics applied to semiconductor heterostructures (Les éditions de physique, 1990).

[55] T. R. Nielsen, P. Gartner, and F. Jahnke, Physical Review B **69** (2004).

[56] H. Haug and S. W. Koch, Quantum Theory of Optical and Electronic Properties of Semiconductors, Fourth ed. (World Scientific, 2004).

[57] G. B. Arfken and H. J. Weber, Mathematical Methods For Physicists (Harcourt - Academic Press, 2001).

[58] I. S. Gradshteyn and I. M. Ryshik, Table of Integrals, Series, and Products (Academic Press, 2007).

[59] K. Kunc and R. M. Martin, Phys. Rev. Lett. **48**, 406 (1982).

[60] T. Inoshita and H. Sakari, Physcal Review B **46**, 7260 (1992).

[61] T. Inoshita and H. Sakari, Physcal Review B **56**, 4355 (1997).

[62] P. Borri et al., Phys. Rev. Lett. **87**, 157401 (2001).

[63] M. Lorke, T. R. Nielsen, J. Seebeck, P. Gartner, and F. Jahnke, Physical Review B **73**, 085324 (2006).

[64] M. A. Stroscio and M. Dutta, Phonons in Nanostructures (Cambridge University Press, 2004).

[65] A. V. Uskov, A.-P. Jauho, B. Tromborg, J. Mørk, and R. Lang, Phys. Rev. Lett. **85**, 1516 (2000).

[66] G. Cui and M. G. Raymer, Physical Review B **73**, 053807 (2006).

[67] L. Banyai, H. Haug, and P. Gartner, Eur. Phys. J. B **1**, 209 (1998).

[68] N. Baer, C. Gies, J. Wiersig, and F. Jahnke, The European Physical Journal B **50**, 411 (2006).

[69] T. Stauber, R. Zimmermann, and H. Castella, Phys. Rev. B **62**, 7336 (2000).

[70] V. Meden, C. Wöhler, J. Fricke, and K. Schönhammer, Phys. Rev. B **52**, 5624 (1995).

[71] M. D. Crisp, Phys. Rev. A **8**, 2128 (1973).

[72] R. Binder, S. W. Koch, M. Lindberg, N. Peyghambarian, and W. Schäfer, Phys. Rev. Lett. **65**, 899 (1990).

[73] R. Zimmermann and J. Wauer, Journal of Luminescence **58**, 271 (1994).

[74] Q. T. Vu, H. Haug, and S. W. Koch, Physical Review B (Condensed Matter and Materials Physics) **73**, 205317 (2006).

[75] X.-X. Liang and X. Wang, Phys. Rev. B **43**, 5155 (1991).

[76] M. Wegener, Extreme Nonlinear Optics - An introduction (Springer, 2005).

[77] M. Schwab et al., Physical Review B (Condensed Matter and Materials Physics) **74**, 045323 (2006).

[78] H. J. Carmichael, An Open Systems Approach to Quantum Optics (Springer, 1993).

[79] K. Hennessy et al., Nature **445**, 896 (2007).

[80] C. K. Hong, Z. Y. Ou, and L. Mandel, Phys. Rev. Lett. **59**, 2044 (1987).

[81] S. Hughes, On the "quantum nature of a strongly coupled single quantum dot-cavity system", CLEO/QELS, 2008, QWF3.

[82] G. Khitrova, H. Gibbs, M. Kira, S. Koch, and A. Scherer, Nature Physics **2**, 81 (2006).

[83] M. Kira, F. Jancke, W. Hoyer, and S. Koch, Progress in Quantum Electronics **23**, 189 (1999).

[84] W. H. Press, S. A. Teukolsky, W. T. Vetterling, and B. P. Flannery, Numerical Recipes - The Art of Scientific Computing, Third ed. (Cambridge University Press, 2007).

[85] G. Baym and L. P. Kadanoff, Phys. Rev. **124**, 287 (1961).

[86] N. H. Asmar, Partial Differential Equations (Pearson, 2005).

[87] I. Vurgarftman, J. Meyer, and L. Ram-Mohan, Journal of Applied Physics **89**, 5815 (2001).

[88] M. Grundmann, O. Stier, and D. Bimberg, Physical Review B **52**, 11969 (1995).

[89] W. Chow and S. Koch, Semiconductor-Laser Fundamentals - Physics of the Gain Materials (Springer, 1999).